

AFRL-ML-TY-TR-2002-4549



**Development of a Carbon Dioxide-Based Field Deployable
Environmental Control Unit to Replace HCFC-22 or HFC-
134a Units**

Joo Seok Baek, Eckhard A. Groll, PhD, Patrick B. Lawless, PhD

Purdue University
Sponsored Programs Services
Hovde Hall
West Lafayette, IN 47907

20020919 018

Approved for Public Release; Distribution Unlimited

**AIR FORCE RESEARCH LABORATORY
MATERIALS & MANUFACTURING DIRECTORATE
AIR EXPEDITIONARY FORCES TECHNOLOGIES DIVISION
139 BARNES DRIVE, STE 2
TYNDALL AFB FL 32403-5323**

NOTICES

USING GOVERNMENT DRAWINGS, SPECIFICATIONS, OR OTHER DATA INCLUDED IN THIS DOCUMENT FOR ANY PURPOSE OTHER THAN GOVERNMENT PROCUREMENT DOES NOT IN ANY WAY OBLIGATE THE US GOVERNMENT. THE FACT THAT THE GOVERNMENT FORMULATED OR SUPPLIED THE DRAWINGS, SPECIFICATIONS, OR OTHER DATA DOES NOT LICENSE THE HOLDER OR ANY OTHER PERSON OR CORPORATION; OR CONVEY ANY RIGHTS OR PERMISSION TO MANUFACTURE, USE, OR SELL ANY PATENTED INVENTION THAT MAY RELATE TO THEM.

THIS REPORT IS RELEASABLE TO THE NATIONAL TECHNICAL INFORMATION SERVICE
5285 PORT ROYAL RD.

SPRINGFIELD VA 22 161

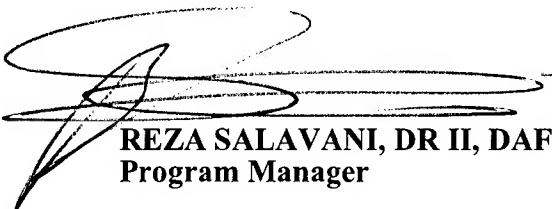
TELEPHONE 703 487 4650; 703 4874639 (TDD for the hearing-impaired)

E-MAIL orders@ntis.fedworld.gov

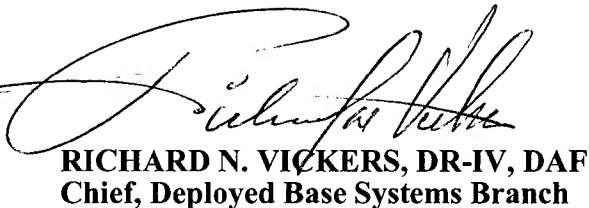
WWW <http://www.ntis.gov/index.html>

AT NTIS, IT WILL BE AVAILABLE TO THE GENERAL PUBLIC, INCLUDING FOREIGN NATIONS.

THIS TECHNICAL REPORT HAS BEEN REVIEWED AND IS APPROVED FOR PUBLICATION.



REZA SALAVANI, DR II, DAF
Program Manager



RICHARD N. VICKERS, DR-IV, DAF
Chief, Deployed Base Systems Branch



DONALD R. HUCKLE, JR., Lt. Col, USAF
Chief, Air Expeditionary Forces Technologies Division

Do not return copies of this report unless contractual obligations or notice on a specific document requires its return.

AQM02-12-3141

REPORT DOCUMENTATION PAGE			Form Approved OMB No. 0704-0188	
maintaining the data needed, and completing and reviewing the collection of information. Send comments regarding this burden estimate or any other aspect of this collection of information, including suggestions for reducing this burden, to Washington Headquarters Services, Directorate for Information Operations and Reports, 1215 Jefferson Davis Highway, Suite 1204, Arlington, VA 22202-4302, and to the Office of Management and Budget, Paperwork Reduction Project (0704-0188), Washington, DC 20503.				
1. AGENCY USE ONLY (Leave blank)		2. REPORT DATE 31 March 2002		3. REPORT TYPE AND DATES COVERED Final Report 02 March 2000 – 31 March 2002
4. TITLE AND SUBTITLE Development of a Carbon Dioxide-Based Field Deployable Environmental Control Unit to Replace HCFC-22 or HFC-134a Units			5. CONTRACT NUMBERS F08637-00-C-6001	
6. AUTHOR (S) Joo Seok Baek; Eckhard A. Groll, PhD; Patrick B. Lawless, PhD				
7. PERFORMING ORGANIZATION NAMES (S) AND ADDRESS (ES) Purdue University Sponsored Programs Services Hovde Hall West Lafayette, IN 47907			8. PERFORMING ORGANIZATION REPORT NUMBER HL 2002-10	
9. SPONSORING/MONITORING AGENCY NAME (S) AND ADDRESS (ES) AFRL/MLQD 139 Barnes Drive, Suite 2 Tyndall AFB FL 32403-5323			10. SPONSORING/MONITORING AGENCY REPORT NUMBER AFRL-ML-TY-TR-02-4547	
11. SUPPLEMENTARY NOTES				
12a. DISTRIBUTION/AVAILABILITY STATEMENT Approved for public release, distribution unlimited			12b. DISTRIBUTION CODE A	
13. ABSTRACT (Maximum 200 words) This document reports on the design, construction, and testing of a piston-cylinder type expansion device with output work (ED-WOW) to be used in a transcritical carbon dioxide air conditioning system that is intended to replace R-22-based or R-134a-based Field Deployable Environmental Control Units (FDECUs). The ED-WOW is based on a highly modified small four-cycle, two-piston engine with a displacement of $2 \times 13.26 \text{ cm}^3$ that is commercially available. The ED-WOW replaced the expansion valve in an experimental transcritical CO_2 cycle and increased the system performance by up to 10%. In addition, this document reports on the development of simulation models for the ED-WOW as well as for the transcritical CO_2 cycle. The ED-WOW model was used to verify the proper operation of the device in the prototype application and to identify the major losses of the device. The model can be used to re-design the next generation ED-WOW. The cycle model was used to predict the performance of several modifications to the transcritical CO_2 cycle and identify which modification is most suitable for implementation in a carbon dioxide-based FDECU.				
14. SUBJECT TERMS Carbon dioxide, Expansion device with output work (ED-WOW), Transcritical cycle, Experimental systems, Simulations models			15. NUMBER OF PAGES 204	
			16. PRICE CODE	
17. SECURITY CLASSIFICATION OF REPORT Unclassified	18. SECURITY CLASSIFICATION OF REPORT Unclassified	19. SECURITY CLASSIFICATION OF REPORT Unclassified	20. LIMITATION OF ABSTRACT UL	

TABLE OF CONTENTS

	Page
LIST OF FIGURES	v
LIST OF TABLES	xi
NOMENCLATURE.....	xiii
ABSTRACT	xxxi
 1 INTRODUCTION.....	 1
1.1 Background	1
1.2 Basic Transcritical CO ₂ Cycle	3
1.3 Cycle Improvements	4
1.3.1 Transcritical CO ₂ Cycles with Expansion Device with Work Extraction.....	5
1.3.2 Transcritical CO ₂ Cycle with Other Options.....	8
1.4 Research Objectives	10
1.5 Organization of This Document.....	11
 2 TECHNICAL APPROACH.....	 19
2.1 Cycle Analysis	19
2.1.1 Assumptions	20
2.1.2 Transcritical CO ₂ Cycles with an Economizer and Intercooler	20
2.1.2.1 Calculation Methods	22
2.1.2.1.1 Calculation Method for Base Cycle	22
2.1.2.1.2 Calculation Method for Economizer Cycle.....	23
2.1.2.1.3 Calculation Method for Intercooler Cycle	25
2.1.3 Transcritical CO ₂ Cycles with Work Extraction	27
2.1.3.1 Calculation Method	27
2.2 Expansion Device.....	28
2.2.1 Overview	28
2.2.2 Thermodynamic Processes of the Piston Expander	31
2.2.3 Theoretical Modeling of the ED-WOW Device	31
2.2.3.1 Basic Loss Mechanisms	32

	Page
2.2.3.1.1 Minor Flow Losses.....	32
2.2.3.1.1.1 Single-Phase Minor Losses	32
2.2.3.1.1.2 Two-Phase Minor Losses	34
2.2.3.1.2 Piston Ring Scuffing and Lubrication.....	37
2.2.3.1.2.1 Piston Ring Scuffing	38
2.2.3.1.2.2 Piston Ring Lubrication	39
2.2.3.2 Fluid Mechanic Model for the ED-WOW Device	40
2.2.3.2.1 Modeling for Mass Flow into Chamber	41
2.2.3.2.1.1 Pressure Loss due to Sudden Contraction	42
2.2.3.2.1.2 Pressure Loss due to Miter Bend.....	42
2.2.3.2.1.3 Pressure Loss due to Sudden Enlargement	43
2.2.3.2.1.4 Pressure Loss due to Exit	44
2.2.3.2.2 Calculation Method for Mass Flow into Chamber.....	44
2.2.3.2.3 Determination of Discharge Coefficient of Sudden Contraction.....	45
2.2.3.2.4 Modeling for Mass Flow Out from Chamber	46
2.2.3.3 Modeling for Piston Ring Lubrication	47
2.2.3.3.1 Theoretical Model	47
2.2.3.3.1.1 Governing Equation	47
2.2.3.3.2 Geometry of Piston Ring.....	48
2.2.3.3.3 Boundary Conditions	48
2.2.3.3.4 Initial Condition	49
2.2.3.3.5 Piston Ring Elastic Characteristics	49
2.2.3.3.6 Method of Solution	50
2.2.3.3.6.1 Pressure Distribution	50
2.2.3.3.6.2 Friction Force	52
2.2.3.3.6.3 Power Loss	53
2.2.3.3.7 Numerical Scheme	53
2.2.3.3.8 Validation of the Model for the Piston Ring Lubrication	54
2.2.3.4 Modeling for Thermodynamic Processes.....	56
2.2.3.4.1 Intake Process.....	56
2.2.3.4.2 Calculation Procedure	57
2.2.3.4.3 Determination of Thermodynamic Properties.....	57
2.2.3.4.4 Expansion Process.....	59
2.2.3.4.5 Exhaust Process.....	61
2.2.3.4.6 Total Power Loss and Net Work Output.....	62
2.3 Experiments for Cycle with ED-WOW Device	62
2.3.1 Description of Testing Procedure.....	63
3 DESIGN OF ED-WOW EXPANSION DEVICE.....	88
3.1 Design of Control Valves.....	88
3.1.1 Experiments for the Characteristics of the Solenoid Valve	89
3.1.2 Example of Valve Control.....	91

	Page
3.2 Design of Expander Cylinder, Piston, and Crank	91
3.3 Design of Top of Expander Cylinder	92
3.4 Design of Enclosure	93
3.5 Design of Loading Device	95
3.5.1 Calibration of Hydraulic Pump	95
3.6 Establishment of Input Timings for the Intake and Exhaust Valves.....	97
3.7 Determination of Revolution Speed of the Expansion Device	98
4 RESULTS.....	118
4.1 Results of Analysis for Cycles with an Economizer or Intercooler	118
4.1.1 Comparison of COPs of Base, Economizer, and Intercooler Cycles	118
4.1.1.1 Economizer and Base Cycles	118
4.1.1.2 Intercooler and Base Cycles.....	119
4.1.2 Effects of Pressure Ratios on COP.....	121
4.1.3 Effect of Low-Side Pressure on COP.....	124
4.1.3.1 Economizer Cycle	124
4.1.3.2 Intercooler Cycle	125
4.1.4 Effect of High-Side Pressure on COP	126
4.1.5 Summary for Cycles with an Economizer or Intercooler.....	128
4.2 Results of Analysis for Cycles with Work Extraction	129
4.2.1 Constant Pressure Ratios across Compressors	129
4.2.2 Different Pressure Ratios across Compressors.....	132
4.3 Results of Theoretical Model for ED-WOW Device	133
4.3.1 Chamber Pressure.....	134
4.3.2 Work Done by CO ₂	135
4.3.3 Minimum Film Thickness Under the Piston Ring	136
4.3.4 Power Loss	136
4.4 Experimental Results for Cycle with ED-WOW Device.....	137
4.4.1 Experimental Test Conditions	137
4.4.2 Cycle Performance	138
4.4.3 Uncertainty Analysis	141
4.5 Analysis of the ED-WOW as Installed in Cycle.....	147
5 SUMMARY, CONCLUSIONS, AND RECOMMENDATIONS.....	183
5.1 Summary of Results	183
5.1.1 Cycle Analysis Conclusions.....	184
5.1.2 Cycle with Work Extraction.....	184
5.2 Recommendations	185
5.2.1 Design Improvements	185
LIST OF REFERENCES	187

APPENDICES.....	192
-----------------	-----

LIST OF FIGURES

Figure	Page
1.1: Schematic of basic transcritical carbon dioxide cycle	13
1.2: Temperature-entropy diagram of transcritical carbon dioxide cycle	13
1.3: Schematic of transcritical CO ₂ cycle with expansion device with output of work (ED-WOW) replacing expansion valve	14
1.4: Free piston expander-compressor-unit [Heyl et al., 1988]	14
1.5: Schematic of transcritical CO ₂ cycle with liquid-to-suction line (internal) heat exchanger	15
1.6: Temperature-entropy diagram of transcritical CO ₂ cycle with internal heat exchange	15
1.7: Schematic of transcritical CO ₂ cycle with an economizer	16
1.8: Temperature-entropy diagram of transcritical CO ₂ cycle with an economizer	16
1.9: Two-stage compression with intercooling [Moran and Shapiro, 1992]	17
1.10: Schematic of transcritical CO ₂ cycle with two-stage compression with intercooling	17
1.11: Temperature-entropy diagram of transcritical CO ₂ cycle with two-stage compression with intercooling	18
2.1: Basic transcritical CO ₂ cycle (Base cycle) – Case 1	67
2.2: Base cycle with ED-WOW – Case 2	67

Figure	Page
2.3: Base cycle with internal heat exchanger (IHX cycle) – Case 3	68
2.4: IHX cycle with ED-WOW – Case 4	68
2.5: Intercooler cycle – Case 5 and Case 8.....	69
2.6: Intercooler cycle with ED-WOW – Case 6 and Case 9	69
2.7: Economizer cycle – Case 7 and Case 10.....	70
2.8: Piston-cylinder device with the related components and piston positions.....	70
2.9: Piston processes with assumption of ideal process	71
2.10: Schematic of connection of the solenoid valve to the fitting and cylinder chamber	71
2.11: Loss coefficients for flow through sudden area changes [Fox and McDonald, 1992]	72
2.12: Entrance loss	72
2.13: Entrance loss coefficients [Evetts and Liu, 1987]	73
2.14: Exit loss	73
2.15: Flow losses in a gradual conical expansion region [Evetts and Liu, 1987].	74
2.16: Representative total resistance (L_e/D) for miter bends [Fox and McDonald, 1992].	74
2.17: Sudden enlargement in two-phase flow	75
2.18: Sudden contraction in two-phase flow	75
2.19: Flow diameter of the computer program modeling.....	76
2.20: Pressure losses.....	77
2.21: Flow diagram for calculation of mass flow into the chamber.....	78
2.22: Determination of discharge coefficient for sudden contraction	79

Figure	Page
2.23: Piston ring geometry	79
2.24: Pressure distribution under the piston ring during the intake and expansion stroke	80
2.25: Piston speed versus crank angle for 2000 rpm engine speed	80
2.26: Combustion chamber pressure versus crank angle	81
2.27: Minimum film thickness predicted by models of Jeng and Radkovic and Khonsari [Radkovic and Khonsari, 1997].....	81
2.28: Power losses predicted by model of Radkovic and Khonsari [Radkovic and Khonsari, 1997].....	82
2.29: Minimum film thickness versus crank angle.....	82
2.30: Power loss versus crank angle.....	83
2.31: Intake process	83
2.32: Expansion process	84
2.33: Exhaust process	84
2.34: Schematic of CO ₂ based ECU test setup	85
2.35: Schematic of experimental setup for transcritical CO ₂ cycle with ED-WOW	86
2.36: Schematic of the connection of the hydraulic pump system to the expansion device producing work	87
3.1: Schematic of test stand to determine the opening time of the intake valve	103
3.2: Filling behaviors of CO ₂ in the chamber with the intake valve (D _{orifice} =3/64 in).....	103
3.3: Comparison of filling behaviors for similar pressure differences, but with different p_{1s}	104
3.4: Timings for input signals to the solenoid valves.....	104
3.5: Crankshaft of the expansion device producing work	105

Figure	Page
3.6: Assembly of a piston, piston ring and connecting rod	105
3.7: Several views of the head of the piston-cylinder device	106
3.8: Top and bottom views of the cylinder head	107
3.9: Bottom and cut-way views of the cylinder head	108
3.10: Cut view of the designed enclosure with expansion device in scale.....	109
3.11: Several view of the enclosure.....	110
3.12: Fabricated enclosure.....	111
3.13: Front and side views of the expansion device and hydraulic pump.....	112
3.14: Schematic of set-up for torque measurement using spring scale and string	113
3.15: Connection of hydraulic pump to expansion device producing work.....	114
3.16: Schematic of the test stand for the establishment of the input timings for the intake and exhaust valves	115
3.17: Valve on/off timing of 1 st intake and 2 nd exhaust valves	116
3.18: Valve on/off timing of 2 nd intake and 1 st exhaust valves	116
3.19: Desired timing table to control all solenoid valves	117
4.1: Comparison of COPs of Economizer cycle and Base cycle.....	161
4.2: Comparison of COPs of Intercooler cycle and Base cycle	161
4.3: COP and compression work of Intercooler cycle.....	162
4.4: COP of Intercooler cycle with different pressure ratios across the 1 st -stage and 2 nd -stage compressors.....	162
4.5: Behavior of compression works of Intercooler cycle over intermediate pressure.....	163
4.6: Processes of Intercooler cycle on pressure-enthalpy diagram	163

Figure	Page
4.7: Effect of pressure at the inlet to the evaporator on COP of Economizer cycle...	164
4.8: Effect of pressure at the inlet to the evaporator on heat removal capacity of Economizer cycle	164
4.9: Effect of pressure at the inlet to the evaporator on COP of Intercooler cycle	165
4.10: Comparison of COPs of transcritical CO ₂ cycles for $T_{H1}=26.7^{\circ}\text{C}$ and $T_{air} = 27.8^{\circ}\text{C}$	165
4.11: Comparison of COPs of transcritical CO ₂ cycles for $T_{H1}=26.7^{\circ}\text{C}$ and $T_{air} = 35.0^{\circ}\text{C}$	166
4.12: Comparison of COPs of transcritical CO ₂ cycles for $T_{H1}=26.7^{\circ}\text{C}$ and $T_{air} = 40.6^{\circ}\text{C}$	166
4.13: Comparison of COPs of transcritical CO ₂ cycles for $T_{H1}=26.7^{\circ}\text{C}$ and $T_{air} = 46.1^{\circ}\text{C}$	167
4.14: Comparison of COPs of transcritical CO ₂ cycles for $T_{H1}=26.7^{\circ}\text{C}$ and $T_{air} = 51.7^{\circ}\text{C}$	167
4.15: Thermodynamic characteristics of CO ₂ on P-h diagram.....	168
4.16: Comparison of COPs of transcritical CO ₂ cycles for $T_{H1}=32.2^{\circ}\text{C}$ and $T_{air} = 35^{\circ}\text{C}$	168
4.17: Comparison of COPs of transcritical CO ₂ cycles for $T_{H1}=32.2^{\circ}\text{C}$ and $T_{air} = 40.6^{\circ}\text{C}$	169
4.18: Comparison of COPs of transcritical CO ₂ cycles for $T_{H1}=32.2^{\circ}\text{C}$ and $T_{air} = 46.1^{\circ}\text{C}$	169
4.19: Comparison of COPs of transcritical CO ₂ cycles for $T_{H1}=32.2^{\circ}\text{C}$ and $T_{air} = 51.7^{\circ}\text{C}$]	170
4.20: Behavior of COP of Intercooler cycle for $T_{H1}=26.7^{\circ}\text{C}$ and $T_{air}=27.8^{\circ}\text{C}$	170
4.21: Behavior of COP of Intercooler cycle for $T_{H1}=26.7^{\circ}\text{C}$ and $T_{air}=35.0^{\circ}\text{C}$	171
4.22: Behavior of COP of Intercooler cycle for $T_{H1}=26.7^{\circ}\text{C}$ and $T_{air}=40.6^{\circ}\text{C}$	171

Figure	Page
4.23: Behavior of COP of Intercooler cycle for $T_{H1}=26.7^{\circ}\text{C}$ and $T_{air}=46.1^{\circ}\text{C}$	172
4.24: Behavior of COP of Intercooler cycle for $T_{H1}=26.7^{\circ}\text{C}$ and $T_{air}=51.7^{\circ}\text{C}$	172
4.25: Piston speed versus crank angle of the ED-WOW	173
4.26: Repeat of the same trends of the pressure behavior for 120RPM and 240RPM.....	173
4.27: CO_2 pressure in the chamber versus crank angle	174
4.28: Work done by CO_2 versus crank angle (120 RPM)	174
4.29: Minimum film thickness under the piston ring (120 RPM)	175
4.30: Power loss due to friction of the piston ring (120 RPM)	175
4.31: Pressure-enthalpy diagram of the processes of the system	176
4.32: Pressure behavior inside the cylinder of the ED-WOW with the assumption of zero leakage of CO_2	177
4.33: Pressure behavior inside the cylinder of the ED-WOW with the assumption of leakage of CO_2 through piston rings.....	178
4.34: Predicted work produced with zero leakage assumption	179
4.35: Predicted work produced and required with the assumption of leakage	180
4.36: Predicted minimum film thickness of the lubricant	181
4.37: Predicted power loss due the friction between the piston ring and the cylinder wall	182
A.1: Flow under a piston ring.....	197

LIST OF TABLES

Table	Page
2.1: Operating conditions for a typical expansion device in the transcritical CO ₂ cycle.....	65
2.2: Loss coefficients for gradual contractions: Round and rectangular ducts [Fox and McDonald, 1992]	65
2.3: Relation between the coefficient of contraction C_c and area ratio σ [Collier, 1972].	66
2.4: Relevant engine parameters	66
3.1: Valve fully opening and closing timings for the solenoid valve with 3/64 in orifice	100
3.2: Dimensions of the expansion device producing work	100
3.3: Summary of the design of the enclosure	101
3.4: Power measurement using torque of the expansion device producing work	101
3.5: Power measurement of the hydraulic pump and its efficiency	102
3.6: Revolution speed of the expansion device versus the time to reach LOE	102
4.1: Total compression works of the Economizer cycle for low-side pressures	153
4.2: Maximum COP values, pressure ratio and high-side pressure at which the maximum COP occurs	153
4.3: Results of thermodynamic analysis for several CO ₂ cycles (For two stage cycles, fixed pressure ratios are considered across compressors).....	154

Table	Page
4.4: Results of thermodynamic analysis for intercooler and economizer cycles to find pressure ratios across compressors that give maximum system performance.....	155
4.5: Input values for simulation of the expansion device producing work	156
4.6: Test conditions to investigate the performance of the ED-WOW	157
4.7: Results of the experiments with ED-WOW in a transcritical CO ₂ cycle	158
4.8: Increases of the evaporator capacity and COP	158
4.9: Uncertainties of measurements	159
4.10: Calculated Results and associating uncertainties (Case 3).....	159
4.11: Results of the ED-WOW simulation for the experimental test conditions	160
4.12: Calculation of leakage area of CO ₂ through the piston ring for Case 3	160

NOMENCLATURE

Symbols

Main variables

A	area
A_c	area of vena contracta
A_1	upstream flow area or area at position 1
A_2	downstream flow area or area at position 2
A_3	area at position 3
A_4	area at position 4
A_5	area at position 5
B	diameter of cylinder wall
b	width of piston ring
C	radial deflection of piston ring
C_c	coefficient of contraction
C_D	discharge coefficient for sudden contraction
$C_{D,e}$	discharge coefficient for sudden enlargement
C_R	crown height of piston ring
C_1	constant or sonic velocity in liquid phase
C_2	constant

Main variables (cont.)

C_3	constant
COP	coefficient of performance
COP _B	COP of base cycle
COP _E	COP of Economizer cycle
COP _{ED-1}	COP based on expansion through the ED-WOW (by considering only lower enthalpy effect)
COP _{ED-2}	COP based on expansion through the ED-WOW (by considering both of lower enthalpy and work output effects)
COP _{EXV}	COP based on isenthalpic expansion
COP _I	COP of Intercooler cycle
D	diameter
D_e	equivalent diameter
D_{exh}	orifice diameter of exhaust valve
D_{fit}	inner diameter of fittings
D_{int}	orifice diameter of intake valve
e	surface roughness
E	Young's modulus of piston ring or energy
E_{CV}	energy in a control volume
F	friction force or function
F_{mass}	force due to the mass
F_{scale}	force measured by spring scale
F'	derivative of function F
f	friction coefficient

Main variables (cont.)

G	mass velocity
G_c	mass velocity defined as $\frac{G_2}{C_c}$
G_1	upstream mass velocity
G_2	downstream mass velocity
h	film thickness of lubricant or enthalpy
h_{B1}	enthalpy at the inlet to the compressor in the Base cycle
h_{B2}	enthalpy at the inlet to the gas cooler in the Base cycle
h_{B3}	enthalpy at the outlet of the gas cooler in the Base cycle
h_{B4}	enthalpy at the inlet to the evaporator in the Base cycle
$h_{com,ext}$	enthalpy at the outlet of the compressor
$h_{com,in}$	enthalpy at the inlet to the compressor
$h_{comp,in}$	enthalpy at the inlet to the compressor
$h_{comp,out}$	enthalpy at the outlet of the compressor
$h_{comp,out,s}$	enthalpy at the outlet of the compressor for an isentropic process
$h_{ED,i}$	enthalpy at the inlet of the ED-WOW
$h_{ED-WOW,in}$	enthalpy at the inlet to the ED-WOW
$h_{ED-WOW,out}$	enthalpy at the outlet of the ED-WOW
$h_{ED-WOW,out,s}$	enthalpy at the outlet of the ED-WOW for an isentropic process
$h_{evap,i}$	enthalpy at the inlet of the evaporator
$h_{evap,o}$	enthalpy at the outlet of the evaporator
h_{exh}	enthalpy at the outlet of the expansion device

Main variables (cont.)

h_{E1}	enthalpy at the inlet to the 1 st -stage compressor in the Economizer cycle
$h_{E1'}$	enthalpy at the outlet of the 1 st -stage compressor in the Economizer cycle
$h_{E1''}$	enthalpy at the inlet to the 2 nd -stage compressor in the Economizer cycle
h_{E2}	enthalpy at the inlet to the gas cooler in the Economizer cycle
h_{E3}	enthalpy at the outlet of the gas cooler in the Economizer cycle
$h_{E3'}$	enthalpy at the inlet to the accumulator in the Economizer cycle
$h_{E3''}$	enthalpy of liquid phase CO ₂ at the accumulator in the Economizer cycle
h_{E4}	enthalpy at the inlet to the evaporator in the Economizer cycle
h_{E5}	enthalpy of vapor phase CO ₂ at the accumulator in the Economizer cycle
h_{in}	enthalpy at the inlet to the intake valve
h_{I1}	enthalpy at the inlet to the 1 st -stage compressor in the Intercooler cycle
$h_{I1'}$	enthalpy at the outlet of the 1 st -stage compressor in the Intercooler cycle
h_{I2}	enthalpy at the inlet to the gas cooler in the Intercooler cycle
h_{I3}	enthalpy at the outlet of the gas cooler in the Intercooler cycle
h_{I4}	enthalpy at the inlet to the evaporator in the Intercooler cycle
h_{lm}	head loss
h_m	minimum film thickness of lubricant
h_{m1}	minimum film thickness of lubricant calculated by using internal halving method for comparison

Main variables (cont.)

h_{m2}	minimum film thickness of lubricant
h_s	piston ring face profile
$h_{s,ED,o}$	enthalpy at the outlet of the ED-WOW for the isentropic expansion process
h_∞	film thickness of lubricant far away from slippery bearing
h_m^{n-1}	minimum film thickness of lubricant at (n-1) th iteration step
h_m^n	minimum film thickness of lubricant at n th iteration step
\dot{H}_{cap}	heat removal capacity of the evaporator
I_1	analytical integration term
I_2	analytical integration term
I_3	analytical integration term
k	constant
K_c	minor loss coefficient for sudden contraction
K_e	minor loss coefficient for sudden enlargement
K_{exit}	loss coefficient for exit
L	length of pipe or length of connecting rod
m	mass inside chamber
m_{in}	amount of mass flowing into the chamber
m_{out}	amount of mass flowing out from the chamber
m_1	mass inside chamber before the piston movement
m_2	mass inside chamber after the piston movement
\dot{m}	mass flow rate

Main variables (cont.)

\dot{m}_{CO_2}	mass flow rate of CO ₂
\dot{m}_{CO_2-leak}	CO ₂ leakage rate through the piston rings
\dot{m}_{in}	mass flow rate into the chamber
\dot{m}_{out}	mass flow rate from the chamber
n_{in}	number of intake valves
n_{exh}	number of exhaust valves
p	pressure of lubricant
p_{bot}	pressure at trailing edge of piston ring
p_{bk}	pressure at the back side of piston ring
p_{B1}	pressure at the inlet to the compressor in the Base cycle
p_{B2}	pressure at the inlet to the gas cooler in the Base cycle
p_{B3}	pressure at the outlet of the gas cooler in the Base cycle
p_{crk}	pressure inside enclosure
$P_{c,in}$	pressure at the inlet of the compressor
$P_{c,out}$	pressure at the outlet of the compressor
$P_{ED,i}$	pressure at the inlet of the ED-WOW
$P_{ED,in}$	pressure at the inlet of the ED-WOW
$P_{ED,o}$	pressure at the outlet of the ED-WOW
$P_{ED,out}$	pressure at the outlet of the ED-WOW
p_{el}	piston ring elastic pressure
p_{exh}	pressure at the outlet of the expansion device

Main variables (cont.)

$P_{evap,o}$	pressure at the out of the evaporator
$P_{evap,out}$	pressure at the out of the evaporator
p_{E1}	pressure at the inlet to the 1 st -stage compressor in the Economizer cycle
$p_{E1'}$	pressure at the outlet of the 1 st -stage compressor in the Economizer cycle
$p_{E1''}$	pressure at the inlet to the 2 nd -stage compressor in the Economizer cycle
p_{E2}	pressure at the inlet to the gas cooler in the Economizer cycle
p_{E3}	pressure at the outlet of the gas cooler in the Economizer cycle
$p_{E3'}$	pressure at the inlet to the accumulator in the Economizer cycle
$p_{E3''}$	liquid pressure in the accumulator in the Economizer cycle
p_{E4}	pressure at the inlet to the evaporator in the Economizer cycle
p_{E5}	vapor pressure in the accumulator in the Economizer cycle
$P_{gc,in}$	pressure at the inlet of the gas cooler
$P_{gc,out}$	pressure at the outlet of the gas cooler
p_{high}	high-side pressure
p_{in}	pressure at the inlet to the intake valve or inlet pressure of the ED-WOW
p_{I1}	pressure at the inlet to the 1 st -stage compressor in the Intercooler cycle
$p_{I1'}$	pressure at the outlet of the 1 st -stage compressor in the Intercooler cycle
p_{I2}	pressure at the inlet to the gas cooler in the Intercooler cycle
$p_{I2'}$	pressure at the inlet to the 2 nd -stage compressor in the Intercooler cycle

Main variables (cont.)

p_{I3}	pressure at the outlet of the gas cooler in the Intercooler cycle
p_{I4}	pressure at the inlet to the evaporator in the Intercooler cycle
p_M	external mean hydrodynamic pressure
P_{out}	outlet pressure of the ED-WOW
P_{pp}	power of the hydraulic pump
$P_{p,in}$	inlet pressure of the hydraulic pump
$P_{p,out}$	outlet pressure of the hydraulic pump
P_{ss}	power calculated using the torque of the ED-WOW
p_{top}	pressure at leading edge of piston ring
$p_{pump,i}$	static pressure at the inlet of the pump
$p_{pump,o}$	static pressure at the outlet of the pump
p_1	upstream pressure or pressure at position 1
p_2	downstream pressure or pressure at position 2
p_3	pressure at position 3
p_4	pressure at position 4
p_5	pressure at position 5
p_1^n	pressure at position 1 at the n^{th} iteration
p_2^n	pressure at position 2 at the n^{th} iteration
p_2^{n-1}	pressure at position 2 at the $(n-1)^{th}$ iteration
p_2^{n+1}	pressure at position 2 at the $(n-1)^{th}$ iteration
p_5^n	pressure at position 5 at the n^{th} iteration

Main variables (cont.)

p'	uniform internal gas pressure
\dot{Q}	heat loss rate or volumetric water flow rate
q_{IHX}	heat transfer from hot CO ₂ to cold CO ₂ through the internal heat exchanger per unit mass
\dot{Q}_{ED}	evaporator capacity rate with expansion through the ED-WOW
\dot{Q}_{isenth}	evaporator capacity rate with isenthalpic process
$q_{IHX,max}$	maximum heat transfer from hot CO ₂ to cold CO ₂ through the internal heat exchanger per unit mass
$Q_{e,B}$	heat capacity of evaporator in the Base cycle
$Q_{e,E}$	heat capacity of evaporator in the Economizer cycle
$Q_{e,I}$	heat capacity of evaporator in the Intercooler cycle
R	crank radius
r	radius of piston ring, or cylinder bore radius, or radius of rod
S	engine speed
s_{B1}	entropy at the inlet to the compressor in the Base cycle
$s_{ED,i}$	entropy at the inlet of the ED-WOW
$s_{E1'}$	entropy at the outlet of the 1 st -stage compressor in the Economizer cycle
$s_{E1''}$	entropy at the inlet to the 2 nd -stage compressor in the Economizer cycle
s_{E2}	entropy at the inlet to the gas cooler in the Economizer cycle
s_{E3}	entropy at the outlet of the gas cooler in the Economizer cycle
$s_{E3'}$	entropy at the inlet to the accumulator in the Economizer cycle

Main variables (cont.)

$s_{E3''}$	entropy of liquid phase CO ₂ in the accumulator in the Economizer cycle
s_{E4}	entropy at the inlet to the evaporator in the Economizer cycle
s_{E5}	entropy of vapor phase CO ₂ at the accumulator in the Economizer cycle
s_{I1}	entropy at the inlet to the 1 st -stage compressor in the Intercooler cycle
$s_{I1'}$	entropy at the outlet of the 1 st -stage compressor in the Intercooler cycle
s_{I2}	entropy at the inlet to the gas cooler in the Intercooler cycle
$s_{I2'}$	entropy at the inlet to the 2 nd -stage compressor in the Intercooler cycle
STD	standard deviation
T	tangential ring tension
T_{air}	air temperature
T_{B1}	temperature at the inlet to the compressor in the Base cycle
T_{B2}	temperature at the inlet to the gas cooler in the Base cycle
T_{B3}	temperature at the outlet of the gas cooler in the Base cycle
$T_{c,in}$	temperature at the inlet of the compressor
$T_{c,out}$	temperature at the outlet of the compressor
$T_{ED,i}$	temperature at the inlet of the ED-WOW
$T_{ED,in}$	temperature at the inlet of the ED-WOW
T_{evap}	evaporation temperature
$T_{evap,o}$	temperature at the outlet of the evaporator
$T_{evap,out}$	temperature at the outlet of the evaporator

Main variables (cont.)

T_{exh}	temperature at the outlet of the expansion valve
T_{E1}	temperature at the inlet to the 1 st -stage compressor in the Economizer cycle
$T_{E1'}$	temperature at the outlet of the 1 st -stage compressor in the Economizer cycle
$T_{E1''}$	temperature at the inlet to the 2 nd -stage compressor in the Economizer cycle
T_{E2}	temperature at the inlet to the gas cooler in the Economizer cycle
T_{E3}	temperature at the outlet of the gas cooler in the Economizer cycle
$T_{E3'}$	temperature at the inlet to the accumulator in the Economizer cycle
$T_{E3''}$	liquid temperature in the accumulator in the Economizer cycle
T_{E4}	temperature at the inlet to the evaporator in the Economizer cycle
T_{E5}	vapor temperature in the accumulator in the Economizer cycle
$T_{gas-out}$	CO ₂ temperature at the gas cooler outlet
$T_{gc,in}$	temperature at the inlet of the gas cooler
$T_{gc,out}$	temperature at the outlet of the gas cooler
T_{in}	temperature at the inlet to the intake valve or inlet temperature of the ED-WOW
T_{indoor}	indoor temperature
T_{I1}	temperature at the inlet to the 1 st -stage compressor in the Intercooler cycle
$T_{I1'}$	temperature at the outlet of the 1 st -stage compressor in the Intercooler cycle
T_{I2}	temperature at the inlet to the gas cooler in the Intercooler cycle

Main variables (cont.)

T_{I2}	temperature at the inlet to the 2 nd -stage compressor in the Intercooler cycle
T_{I3}	temperature at the outlet of the gas cooler in the Intercooler cycle
T_{n-1}	temperature at (n-1) th iteration step
T_n	temperature at n th iteration step
T_{n+1}	temperature at (n+1) th iteration step
T_{out}	outlet temperature of the ED-WOW
$T_{outdoor}$	outdoor temperature
T_q	torque
t_r	piston ring thickness
T_{sat}	CO ₂ saturation temperature
T_1	temperature at position 1
T_2	temperature at position 2
T_3	temperature at position 3
T_4	temperature at position 4
U	piston speed
U_1	impact velocity
u	x-component of velocity
u_{f1}	upstream velocity of liquid phase
u_{f2}	downstream velocity of liquid phase
u_{g1}	upstream velocity of vapor phase
u_{g2}	downstream velocity of vapor phase

Main variables (cont.)

u_1	internal energy inside chamber before the piston movement
u_2	down stream velocity or internal energy inside chamber after the piston movement
$V(t)$	velocity of piston ring in y-coordinate
V	chamber volume
v	velocity or y-component of velocity
\dot{V}	volumetric flow rate of water
V_{BDC}	chamber volume at bottom dead center
v_f	specific volume of liquid phase
v_{fg}	specific volume difference between vapor and liquid phases
v_g	specific volume of vapor phase
V_{fit}	volume of fitting attached to the intake and exhaust valves
V_{TDC}	chamber volume at top dead center
V_1	chamber volume before piston movement
V_2	chamber volume after piston movement
v_2	velocity at position 2
$v_{2,f}$	specific volume of liquid downstream
$v_{2,fg}$	specific volume difference between vapor and liquid phases downstream
v_3	velocity at position 3
v_4	velocity at position 4
\bar{v}	flow velocity
\bar{v}_1	flow velocity at position 1

Main variables (cont.)

\bar{v}_2	flow velocity at position 2
W	load imposed on piston ring, or work done by system, or mass flow rate
\dot{W}	work per unit time done by CO ₂
w_A	total uncertainty associated with the dependent variable A
\dot{W}_{com}	compression power
\dot{W}_{comp}	compression work
w_{comp}	specific compression work
$w_{comp,s}$	specific compression work for an isentropic process
w_{COP}	uncertainty for COP
$W_{c,B}$	compression work in the Base cycle per unit mass
$W_{c1,E}$	compression work of the 1 st -stage compressor in the Economizer cycle
$W_{c2,E}$	compression work of the 2 nd -stage compressor in the Economizer cycle
$W_{c1,I}$	compression work of the 1 st -stage compressor in the Intercooler cycle per unit mass
$W_{c2,I}$	compression work of the 2 nd -stage compressor in the Intercooler cycle per unit mass
w_d	compression work with different pressure ratio
\dot{W}_{ED}	power extracted through the ED-WOW
w_{ED-WOW}	specific work extracted through the ED-WOW
$w_{ED-WOW,s}$	specific work extracted through the ED-WOW with isentropic process
W_f	mass flow rate of liquid phase

Main variables (cont.)

w_f	specific compression work with fixed pressure ratio
W_g	mass flow rate of vapor phase
$w_{h_{ED,i}}$	uncertainty for the enthalpy at the inlet of the ED-WOW
$w_{h_{evap,o}}$	uncertainty for the enthalpy at the outlet of the evaporator
$w_{\dot{m}}$	uncertainty for the CO ₂ mass flow rate
W_{net}	net work output done by CO ₂
$w_{\dot{W}_{ED}}$	uncertainty for the work produced through the ED-WOW
$w_{p_{ED,i}}$	uncertainty for the pressure at the inlet of the ED-WOW
$w_{p_{ED,o}}$	uncertainty for the pressure at the outlet of the ED-WOW
$w_{p_{pump,i}}$	uncertainty for pressure at the inlet of the pump
$w_{p_{pump,o}}$	uncertainty for pressure at the outlet of the pump
$w_{\dot{Q}_{ED}}$	uncertainty for the heat capacity of the evaporator
$\dot{W}_{s,ED}$	ideal work output in an isentropic expansion process
$w_{s,h_{ED,o}}$	uncertainty for the enthalpy at the outlet of the ED-WOW for the isentropic expansion process
$w_{s_{ED,i}}$	uncertainty for the entropy at the inlet of the ED-WOW
$w_{T_{ED,i}}$	uncertainty for the temperature at the inlet of the ED-WOW
$w_{\dot{V}}$	uncertainty for the volumetric water flow rate
$w_{\dot{W}_{s,ED}}$	uncertainty for the ideal work produced through the ED-WOW

Main variables (cont.)

w_z	uncertainty for variable z_i
w_τ	uncertainty for the torque of the compressor
w_ω	uncertainty for the rotational speed of the compressor
x	quality of CO ₂ or x direction in rectangular coordinate
y	y direction in rectangular coordinate
z_i	independent variable which affects the dependent variable A

Greek

α	void fraction
α_1	upstream void fraction
α_2	downstream void fraction
Δp	pressure difference across the hydraulic pump
Δp_{bend}	pressure loss due to bending
Δp_f	frictional pressure loss across a sudden contraction
Δp_{pump}	pressure difference across the hydraulic pump
Δp_{total}	total pressure loss
$\Delta p_{1 \rightarrow 2}$	pressure loss due to sudden contraction
$\Delta p_{2 \rightarrow 3}$	pressure loss due to sudden enlargement from position 2 to position 3
$\Delta p_{3 \rightarrow 4}$	pressure loss due to sudden enlargement from position 3 to position 4

Greek (cont.)

$\Delta p_{4 \rightarrow 5}$	pressure loss at exit
Δt	time step
Δt_{intake}	intake valve opening time
ΔU	change of internal energy
ΔV	change of chamber volume
Δx	mesh size
ε	convergence tolerance
ε_{ED}	isentropic efficiency of the ED-WOW
ε_{IHX}	effectiveness of the internal heat exchanger
η_{comp}	isentropic efficiency of the compressor
η_{ED-WOW}	isentropic efficiency of the work producing expansion device
η_{pump}	efficiency of the pump
π	constant
θ	radial direction in cylindrical coordinate
ρ	density
ρ_1	density of liquid phase
ρ_2	density at position 2 or density after piston movement
ρ_3	density at position 3
ρ_4	density at position 4
μ	viscosity

Greek (cont.)

μ_c	coefficient of friction
P	power loss
P_{tot}	total power loss
σ	area ratio or composite roughness
σ_e	material limiting stress
τ	shear stress acting on piston ring or torque of the compressor
ω	revolutionary speed
ω_{ED}	revolutionary speed of ED-WOW

Executive Summary

Develop an advanced lightweight highly efficient Environmental Control Unit (ECU) by utilizing CO₂ cycle technology for AEF applications that reduces airlift and logistics requirements. The technical challenges in the development of this technology include development of compact evaporator and gas cooler based on micro-channel technology, development of an energy recovery expansion device, and integration of the expansion device and compressor into a hermetically sealed package.

This report include the design, construction, and testing of a piston-cylinder type expansion device with output work (ED-WOW) to be used in a trans-critical carbon dioxide (CO₂) air conditioning system that is intended to replace R-22-based or R-134a-based Field Deployable Environmental Control Units (FDECUs). The ED-WOW is based on a highly modified small four-cycle, two-piston engine with a displacement of $2 \times 13.26 \text{ cm}^3$ that is commercially available. The ED-WOW replaced the expansion valve in an experimental trans-critical CO₂ cycle and increased the system performance by up to 10%. In addition, this document reports on the development of simulation models for the ED-WOW as well as for the trans-critical CO₂ cycle. The ED-WOW model was used to verify the proper operation of the device in the prototype application and to identify the major losses of the device. The model can be used to re-design the next generation ED-WOW. The cycle model was used to predict the performance of several modifications to the trans-critical CO₂ cycle and identify which modification is most suitable for implementation in a carbon dioxide-based FDECU.

ABSTRACT

Baek, Joo Seok. Ph.D., Purdue University, August 2002. Development of a Work Producing Expansion Device for a Transcritical Carbon Dioxide Cycle. Major Professors: Dr. Eckhard A. Groll and Dr. Patrick B. Lawless, School of Mechanical Engineering.

Because of its high volumetric heat capacity, CO₂ offers the potential for reduced weight and volume in packaged systems, which is a major focus for automobile and military applications. The proceeding literature review, however, has shown that the overall efficiency of the transcritical CO₂ cycle decreases as the weight and volume of the system is decreased. System improvements must be achieved to meet the goals of the reduction of weight and volume, while still retaining competitive efficiency.

A thermodynamic analysis was performed for several modified transcritical CO₂ cycles, with a goal of determining the proper configuration to achieve the optimum system performance. The analysis shows that the system efficiency of the transcritical CO₂ cycle can be dramatically increased by modifications of the system configuration, and that the optimum performance is a strong function of the operating conditions.

The system efficiency of the transcritical CO₂ cycle is increased considerably by nearly 100 % when the low-side pressure increases from 2.5 MPa to 4.5 MPa. There is a specific high-side pressure at which the maximum COP occurs in the CO₂ cycle. There

are also specific pressure ratios across the compressors for the minimum compression work and the maximum COP for the two-compressor system.

The employment of a work extraction device in the role of an expander is expected to give the largest improvement of the system efficiency. This device will not only increase the heat removal capacity of the evaporator but also can reduce the compression work. As part of this research, an expansion device with output work (ED-WOW) was designed, constructed and installed in a prototype transcritical CO₂ refrigeration system, replacing the simple throttling valve. During cycle tests, the use of the device provided between 7% and 10% improvement in COP. These figures are considered to be highly conservative, as the work extraction measurement was biased toward a lower value due to uncertainty in the load device performance.

1 INTRODUCTION

1.1 Background

Many nations of the world have agreed on regulations prohibiting the use of chlorofluorocarbons (CFCs) and hydrochlorofluorocarbons (HCFCs) as refrigerants due to their potential to destroy the ozone layer of the earth's atmosphere. Hydrofluorocarbons (HFCs) are considered as the replacements for CFC and HCFC refrigerants since they have zero ozone depletion potential. However, HFCs still have a significant global warming potential. Therefore, substances with no ozone depletion potential and negligible global warming potential, e.g., natural fluids, are being considered as alternative refrigerants. Carbon dioxide, ammonia, hydrocarbons, water, and air are gaining more and more attention. Some of these refrigerants, i.e., hydrocarbons and ammonia, show unfavorable safety behaviors due to their toxicity and/or flammability. Carbon dioxide (CO₂) is nontoxic and non-flammable and has zero ozone depletion potential and negligible global warming potential as a refrigerant. It thus is close to being the ideal working medium for applications like air conditioning and heat pump systems.

Carbon dioxide is also receiving strong consideration for automobile and military applications due to its high volumetric heat capacity and the elimination of recovery and recycling equipment and procedures. Because of its high volumetric heat capacity, CO₂

offers the potential for reduced weight and volume in packaged systems, which is a major focus for transportable field units in the military. For example, the U.S. Army is seeking an air conditioning system with significant weight and size reduction and higher efficiency, resulting in reducing tactical power generator sizes [Patil, 1998].

In order to reduce the weight and volume of the system, the weights and volumes of the evaporator and gas cooler need to decrease. However, the overall system efficiency will also decrease if the heat exchanger sizes are reduced due to the increase in approach temperatures between the refrigerant and the heat sink and source fluids. Robinson and Groll compared the 'Coefficient Of Performances' (COPs) of a packaged air conditioner using HCFC-22 as the refrigerant with those of a carbon dioxide based packaged air conditioner by using a computer model [Robinson and Groll, 2000]. Their analysis showed that for a packaged air conditioner application using the same evaporator size and capacity, the transcritical CO₂ air conditioner will operate with a COP which is similar to the simulated (not actual) performance of an U.S. Army packaged air conditioner which uses HCFC-22. As previously mentioned, however, if the size of the evaporator is reduced, the heat removal capacity of the evaporator decreases, which would result in a reduction in the thermodynamic system performance.

Robinson conducted a parametric study which compared the actual performance of an HFC-134a based automobile air conditioner and the performance of a carbon dioxide based automobile air conditioner [Robinson, 2000]. His analysis showed that for an automobile application, the prototype transcritical CO₂ cycle system introduced by Pettersen [Pettersen, 1995] will operate with a COP which is 66-75% (average 70%) of

the experimentally determined COP of a production HFC-134a based automobile air conditioner while providing the same evaporator capacity.

As discussed above, the performance of a carbon dioxide based air conditioning system may be less than that of an HFC or HCFC based air conditioning system, especially if the size of the system is reduced. System improvements, therefore, need to be realized to meet the goal of the reduction of weight and volume while still maintaining the same or higher system efficiency. There are several approaches to increase the system efficiency. These include an increase of heat exchanger frontal area, the addition of a liquid-to-suction line heat exchanger, the use of two-stage compression with an intercooler or an economizer, and the use of an expansion device that provides for work extraction. The concepts behind these improvements are explained in detail in the following sections.

1.2 Basic Transcritical CO₂ Cycle

Figure 1.1 shows a schematic of the basic transcritical CO₂ cycle and Figure 1.2 illustrates the cycle on a T-s diagram. As shown in Figure 1.1, the basic transcritical CO₂ cycle consists of a compressor, a gas cooler, an expansion valve, and an evaporator. The cycle is composed of four basic processes; compression (1-2), heat rejection (2-3), expansion (3-4) and heat absorption (4-1) as shown in Figure 1.2. In the expansion process, the paths 3-4s, 3-4h and 3-4w represent isentropic expansion, isenthalpic expansion, and expansion through an expansion device with output work (ED-WOW), respectively. In the compression process, the paths 1-2s and 1-2 stand for the isentropic and actual processes, respectively.

The process that differs most from current conventional refrigeration systems is the supercritical heat rejection process. The critical temperature and pressure of CO₂ are 30.82°C and 7.353MPa [ASHRAE, 1997]. During hot weather periods, the temperature outside may be higher than the critical temperature of CO₂. Therefore, since the CO₂ temperature in the gas cooler must be higher than the outside temperature to reject heat to atmosphere, the CO₂ temperature needs to be much higher than the critical temperature (i.e. in a supercritical state). Hence, the heat will be rejected from CO₂ during a supercritical process while the heat is rejected from the conventional fluorocarbon-based refrigerant during a constant temperature and pressure two-phase process. During the supercritical heat rejection process the thermodynamic properties of CO₂ will change from a 'vapor-like' to a 'liquid-like' fluid.

1.3 Cycle Improvements

In order to increase the efficiency (or performance) of the basic cycle shown in Figure 1.1, some processes need to be modified or additional processes need to be added to the basic cycle. A literature review was conducted on studies of the transcritical CO₂ cycle in cases where the expansion valve was replaced by an expansion device producing work, and in cases where the transcritical CO₂ cycle was modified to achieve better system performance.

1.3.1 Transcritical CO₂ Cycles with Expansion Device with Work Extraction

Little research has focused on the topic of using work-producing expansion devices instead of the conventional expansion valve. Those studies available are reviewed and summarized in this section.

Robinson and Groll have suggested the possibility of using a two-phase expansion turbine in place of the expansion valve [Robinson and Groll, 1998]. The authors developed a thermodynamic computer model to analyze the transcritical CO₂ cycle with and without an expansion work recovery turbine. They discovered from their analysis that replacing the expansion valve with an expansion work recovery turbine reduced the process's contribution to total cycle irreversibility by 35% and the COP was on average of 25% higher than the COP of the transcritical CO₂ cycle with an expansion valve and maximum internal heat exchanger.

Li et al. introduced a vortex tube expansion device and expansion device producing work [Li et al., 2000]. Carbon dioxide leaving a gas cooler enters a vortex tube. The vortex tube separates the carbon dioxide into saturated liquid and superheated vapor at evaporation pressure due to the Ranque-Hilsch effect. The superheated vapor enters an auxiliary heat exchanger, dissipates heat to the environment and then mixes with the saturated liquid. The quality of the CO₂ becomes less than that of isenthalpic expansion so that the capacity of the evaporator increases. The authors also suggested a piston-cylinder type expansion device instead of the expansion valve that recovers some energy while CO₂ expands through the device. The energy can be used to recover mechanical shaft work that either directly drives a compressor or that could be utilized to generate electric power.

Figure 1.3 shows the schematic of the transcritical CO₂ cycle with a work-producing expansion device substituted for the expansion valve. For simplicity, the work producing device will be referred to as the ED-WOW (Expansion Device With Output Work). If CO₂ is expanded through the ED-WOW (process 3-4w), the enthalpy at the inlet to the evaporator will be lower than the case of isenthalpic expansion through an ordinary expansion valve (process 3-4h), as shown in Figure 1.2, so that the capacity of the evaporator will increase. When energy is extracted from the CO₂ through the ED-WOW during the expansion process and used to assist the compression process, the compression work will be reduced and the COP of the system will increase significantly.

Li et al. developed a computer model and performed thermodynamic calculations of the transcritical CO₂ cycle using three expansion options [Li et al., 2000]. The authors discussed that the COPs of the cycles with a vortex tube and an ED-WOW are increased by 37% (with the expansion work output device at an isentropic efficiency of 0.9 and with the vortex tube expansion process at an efficiency of 0.5) compared to that of the cycle with an expansion valve. It was concluded that the vortex tube and piston-cylinder type expansion device have good potential for cycle improvement.

Maurer and Zinn experimentally investigated axial, swash-plate piston expanders and internal gear expanders in a specially constructed liquid-loop test stand [Maurer and Zinn, 1999]. Both expanders were first tested as off-the-shelf components. Based on the experiences gathered during the first round of testing the design of both expanders was modified. The suction port of the axial, swash-plate piston expander was redesigned and better piston rings were introduced. With respect to internal gear expander, the tolerance of the sealing gap between the gears and the housing was reduced. After these

modifications were implemented, the isentropic and volumetric efficiencies that were achieved with both expanders were up to 50%.

Heyl et al. proposed an expander-compressor unit to improve the thermodynamic efficiency of the transcritical CO₂ cycle [Heyl et al., 1998]. Figure 1.4 shows the expander-compressor unit. As shown in the figure, this unit is constructed as a free piston machine with two double-acting pistons, which are connected by a piston rod. During the piston movement from left to right in cylinder 1, the refrigerant is expanded from the gas cooler pressure to the evaporator pressure. In cylinder 2, the refrigerant is first compressed then discharged. In cylinder 3, the remaining refrigerant is expanded and additional refrigerant is taken in for the next compression process. In cylinder 4 the expanded refrigerant is swept out. The authors mentioned, however, that the piston would stop due to the balance of the four forces in the cylinders of Figure 1.4. For the continuous operation of the piston, the authors proposed to terminate the expansion by opening the exhaust valve in a position of the stroke where the resulting balance of forces stops the movement of the piston. The expander operates according to the 'full pressure principle'. The authors mentioned that the resulting balance of forces of the expander-compressor unit operating with the 'full pressure principle' was positive over the entire piston stroke and they ensured the functioning of the unit. In this case, however, the expansion remains incomplete. There is unavoidable loss in the operating method proposed instead of a complete expansion. The authors discussed that the calculated efficiency of the unit was 78% in relation to a complete expansion due to the loss.

1.3.2 Transcritical CO₂ Cycle with Other Options

Instead of replacing the expansion valve with a work producing expansion device, many other authors suggested other modifications of the transcritical CO₂ cycle to improve the system performance.

Lorentzen and Pattersen introduced the idea of an internal heat exchanger for a transcritical CO₂ cycle [Lorentzen and Pattersen, 1993]. Figures 1.5 and 1.6 show a schematic of the transcritical CO₂ cycle with an internal heat exchanger and the cycle on a T-s diagram, respectively. The CO₂ exiting the gas cooler rejects heat to the CO₂ exiting the evaporator through the internal heat exchanger (also known as a 'liquid-to-suction line' heat exchanger). In the figures the processes 3'-3 and 1-1' correspond to the internal heat exchange. There are two major functions of the internal heat exchanger [Robinson, 2000]: 1) It ensures that the fluid entering the compressor is devoid of any entrained liquid CO₂; 2) It reduces the temperature of the fluid prior to expansion that results in lower vapor quality of the CO₂ entering the evaporator. This in turn increases the capacity of the evaporator.

G.T. Voorhees proposed a transcritical CO₂ cycle with an economizer in 1905 that is also known as the 'Multiple-Effect cycle' [Voorhees, 1979]. Figure 1.7 illustrates this cycle. The expansion process occurs through two expansion valves with an accumulator that separates vapor phase CO₂ from liquid phase CO₂. The vapor phase CO₂ mixes with the superheated CO₂ exiting the 1st-stage compressor and the mixture enters the 2nd-stage compressor. The liquid phase CO₂ expands again and enters the evaporator as shown in Figures 1.7 and 1.8. Figure 1.8 shows the system on T-s diagram.

As shown in Figure 1.8, the enthalpy of CO_2 entering the evaporator is reduced and it results in increased capacity of the evaporator.

The compressor work input can also be reduced by means of multistage compression with intercooling. Figure 1.9 illustrates a two-stage compressor with an intercooler [Moran and Shapiro, 1992]. The accompanying p-v and T-s diagrams show the states for internally reversible processes. Process 1-c denotes an isentropic compression from state 1 to state c where the pressure is p_i . In process c-d the gas is cooled at constant pressure from temperature T_c to T_d . Process d-2 is an isentropic compression from state d to state 2. The work input per unit mass flow is represented on the p-v diagram by area 1-c-d-2-a-b-1. Without intercooling the gas would be compressed isentropically in a single stage from state 1 to state 2' and the work would be represented by area 1-2'-a-b-1. The crosshatched area on the p-v diagram represents the reduction in work that would be achieved with intercooling. The size of the crosshatched area on the p-v diagram of Figure 1.9 representing the reduction of compression work depends on both the temperature T_d at the exit of the intercooler and the intercooler pressure p_i . By properly selecting T_d and p_i , the total work input to the compressor can be minimized. This concept can be applied to the transcritical CO_2 cycle.

Figure 1.10 shows a schematic of the transcritical CO_2 cycle with two-stage compression with intercooling. Figure 1.11 illustrates the T-s diagram of the system. The compression work will be reduced with this cycle as discussed above but the capacity of the evaporator does not change. Therefore, the coefficient of performance (COP) of this cycle will increase compared to the basic transcritical CO_2 cycle.

Heyl et al. analyzed several modifications of the basic transcritical CO₂ cycle [Heyl et al., 1998]. The author considered single-stage and two-stage compressions. The single-stage compression cycle included the basic transcritical CO₂ cycle (Figure 1.1), the basic cycle with an internal heat exchanger (Figure 1.5), the transcritical CO₂ cycle with an expander (Figure 1.3), and the transcritical CO₂ cycle with an expander and an internal heat exchanger. The two-stage compression cycle included the transcritical CO₂ cycle with two-stage compressions and intercooling (Figure 1.10), the transcritical CO₂ cycle with an economizer (Figure 1.7), and the transcritical CO₂ cycle with an expander, two compressors, and intercooling. Their analysis showed that the COP increased with the modification of the basic cycle and the COP became the maximum when the work output extracted during the CO₂ expansion was used to run the 2nd-stage compressor. The COP improvement was about 65% compared the basic transcritical CO₂ cycle.

1.4 Research Objectives

Because of its high volumetric heat capacity, CO₂ offers the potential for reduced weight and volume in packaged systems, which is a major focus for automobile and military applications. The proceeding literature review, however, has shown that the overall efficiency of the transcritical CO₂ cycle decreases as the weight and volume of the system decrease. System improvements must be achieved to meet the goals of the reduction of weight and volume, while still retaining competitive efficiency.

As previously discussed, the employment of a work extraction device in the role of an expander is expected to give the largest improvement of the system efficiency. This device will not only increase the heat removal capacity of the evaporator but also can

reduce the compression work. Most of the research above suggested the conceptual design of the expansion device. However, only Heyl tested on expander in a transcritical CO₂ cycle which had several limitations as outlined above [Heyl, 2000]. A major objective of this research was to design, construct, test, and analyze a work extraction expansion device. This device was installed in a prototype transcritical CO₂ refrigeration system, replacing the simple throttling valve. Experiments were performed to characterize the effect of the expansion device on the cycle performance. This data was compared to analytical predictions of the cycle performance.

Another objective of this research is to perform thermodynamic analyses for the transcritical CO₂ cycles using an economizer (Economizer cycle) and an intercooler (Intercooler cycle), which are described above, with the goal to determine the configuration that achieves optimum system performance. Especially, intermediate pressures were investigated for two compressor systems which gave the maximum system efficiency. Such an analysis of the optimum intermediate pressure of the transcritical CO₂ cycle with intercooling has not been published to date.

1.5 Organization of This Document

In Chapter 1, the background of this research is mentioned and the literature review has been calculated on the topic of the improvement of the thermodynamic system performance of the transcritical CO₂ cycles. The objectives of this research are discussed in Chapter 1 as well. In Chapter 2, the technical approach to conduct this research is described. First, the methods of the cycle analyses are given for transcritical CO₂ cycles with an economizer, an intercooler, and an expansion device producing work. Then, the

determination of a work producing expansion device is discussed. A detailed description of a theoretical model for the expansion device is also given in Chapter 2. In addition, Chapter 2 provides a summary of the literature review on the topics of the minor flow losses, piston ring scuffing, and lubrication. Furthermore, the testing procedure for the experiments with the expansion device in a transcritical CO₂ cycle is explained in Chapter 2. The design of the expansion device is discussed in detail in Chapter 3. The results of cycle analyses are discussed in Chapter 4. The results of the experiments are also discussed in detail in Chapter 4. The expansion device is analyzed using the theoretical model for its design. The experimental and simulation results are compared in Chapter 4 as well. A summary and conclusions of the research accomplishments and recommendations for design improvements of the expansion device are given in Chapter 5.

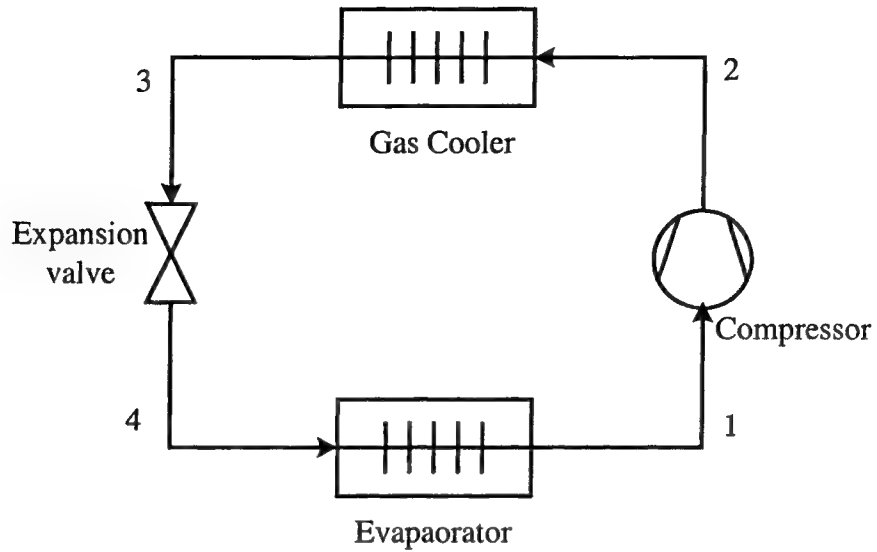


Figure 1.1: Schematic of basic transcritical carbon dioxide cycle.

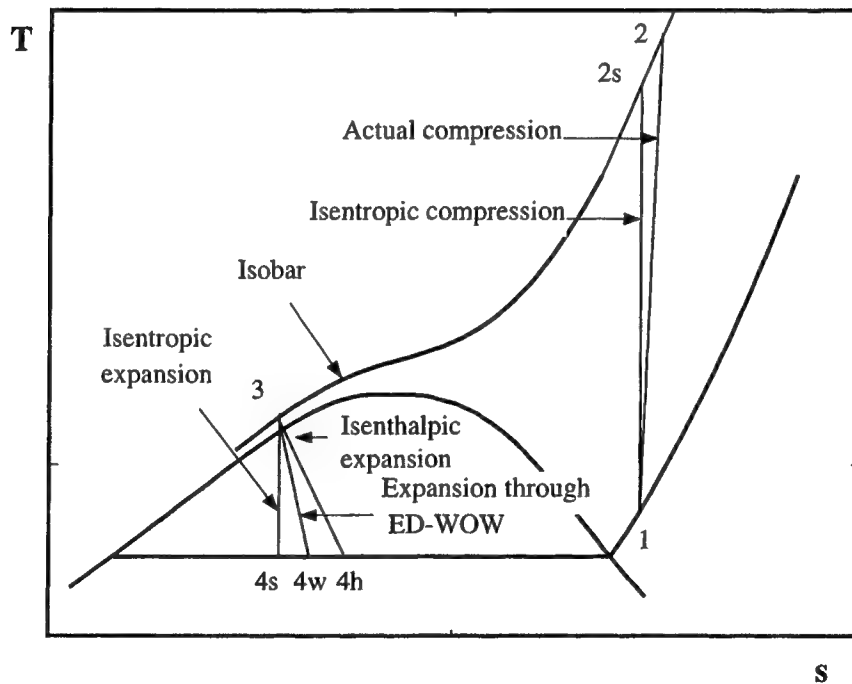


Figure 1.2: Temperature-entropy diagram of transcritical carbon dioxide cycle.

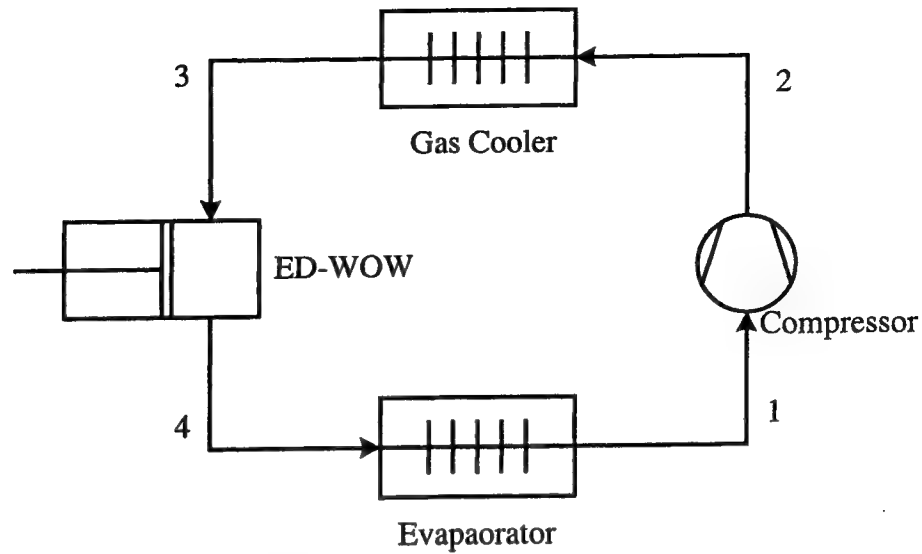


Figure 1.3: Schematic of transcritical CO₂ cycle with expansion device with output work (ED-WOW) replacing expansion valve.

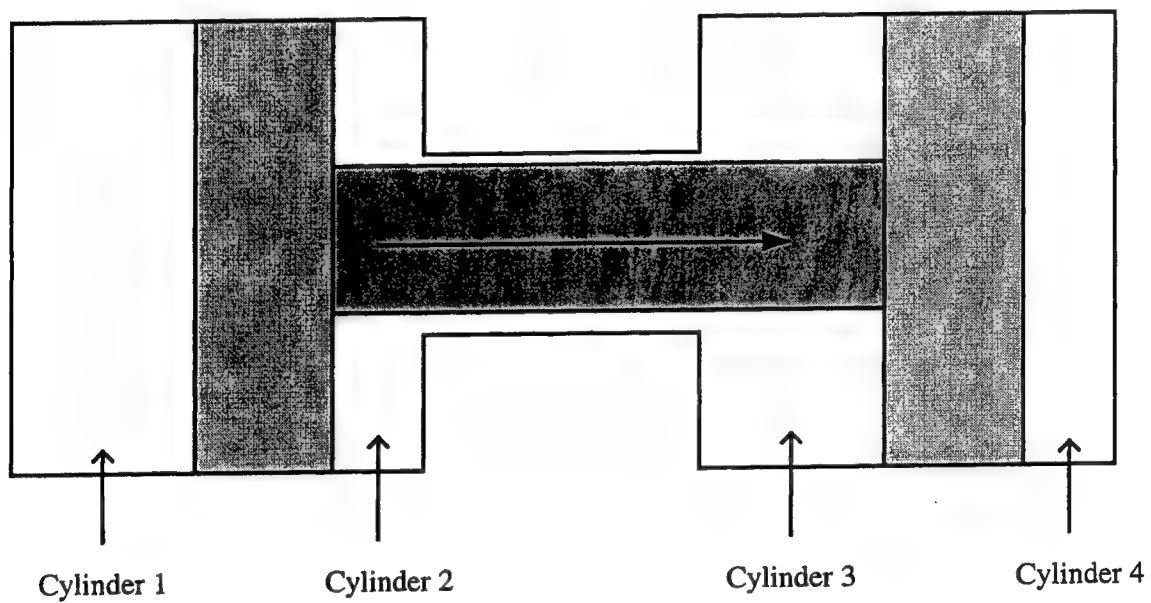


Figure 1.4: Free piston expander-compressor-unit [Heyl et al., 1988].

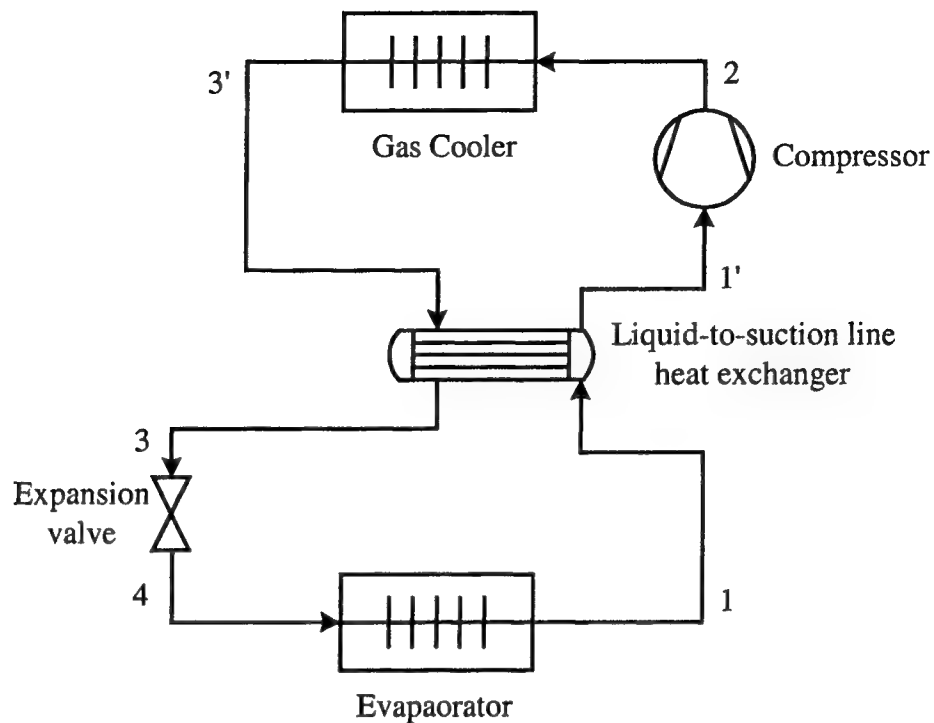


Figure 1.5: Schematic of transcritical CO₂ cycle with liquid-to-suction line (internal) heat exchanger.

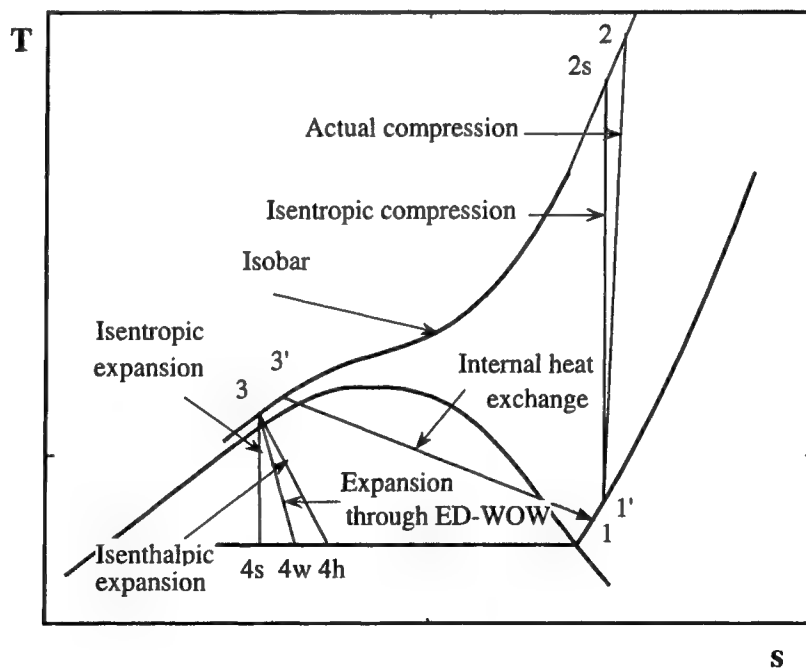


Figure 1.6: Temperature-entropy diagram of transcritical CO₂ cycle with internal heat exchange.

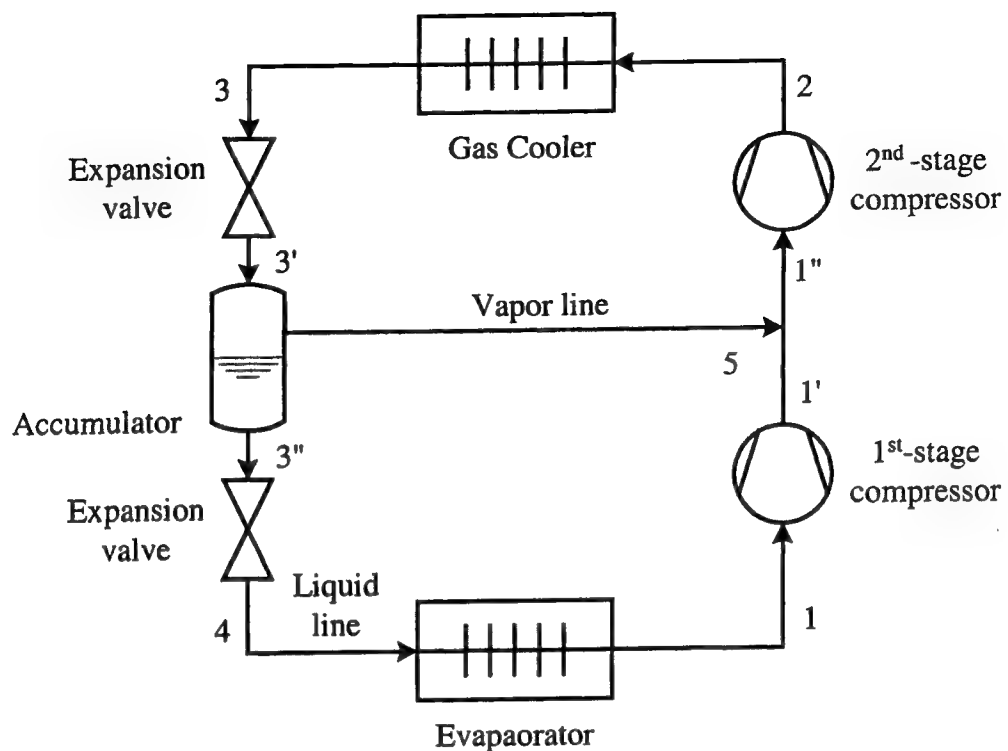


Figure 1.7: Schematic of transcritical CO₂ cycle with an economizer.

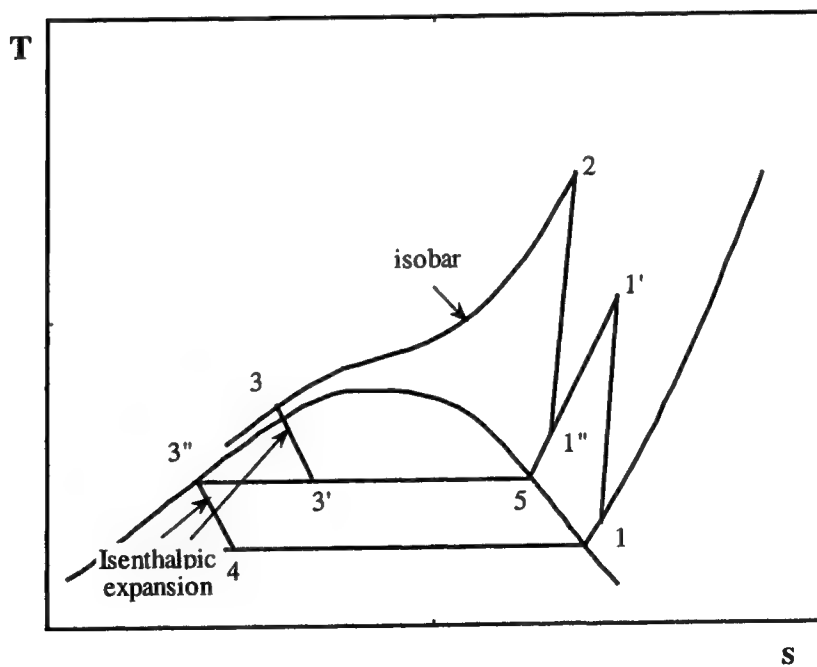


Figure 1.8: Temperature-entropy diagram of transcritical CO₂ cycle with an economizer.

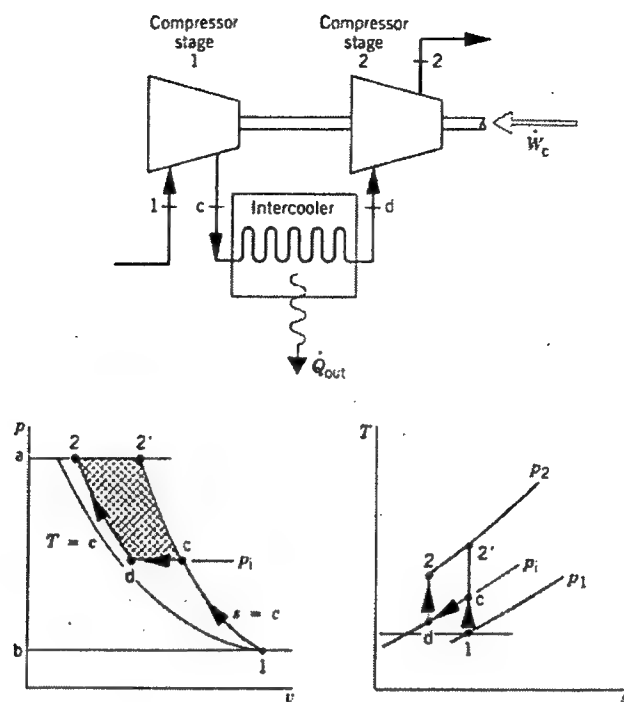


Figure 1.9: Two-stage compression with intercooling [Moran and Shapiro, 1992].

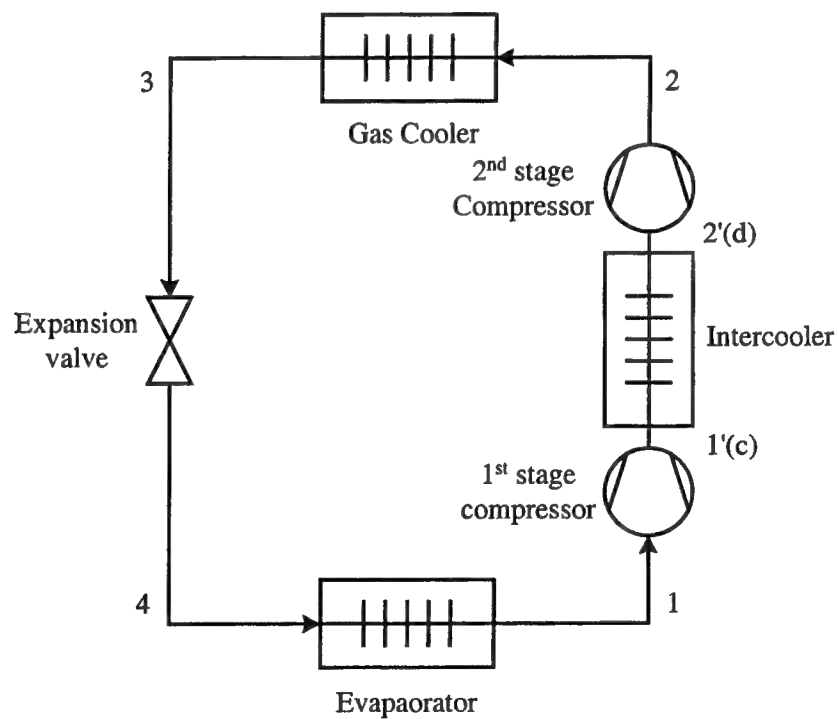


Figure 1.10: Schematic of transcritical CO_2 cycle with two-stage compression with intercooling.

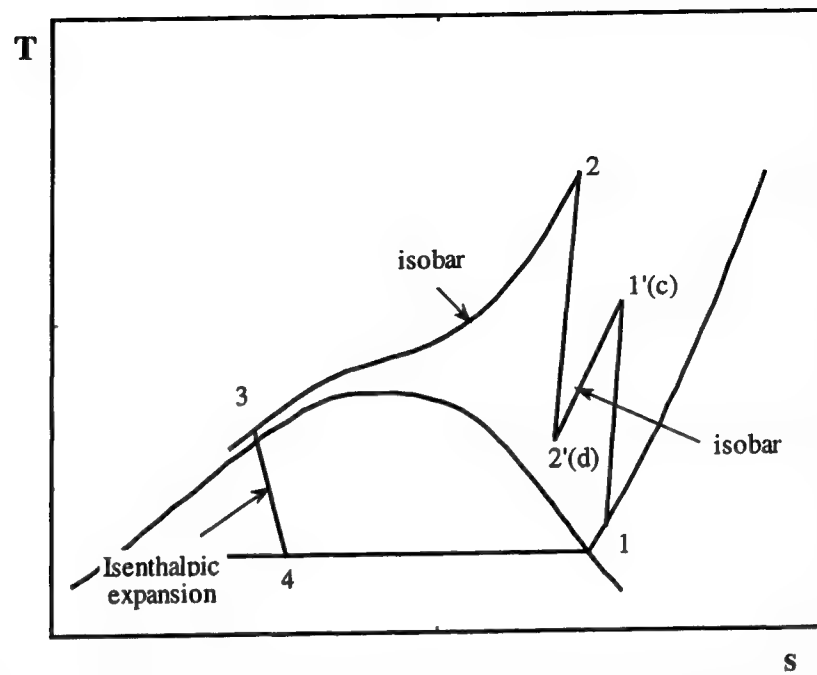


Figure 1.11: Temperature-entropy diagram of transcritical CO_2 cycle with two-stage compression with intercooling.

2 TECHNICAL APPROACH

2.1 Cycle Analysis

One of the objectives of this research was to perform the thermodynamic analyses to investigate the thermodynamic behavior of the transcritical CO₂ cycle and to find the optimum operating conditions for the maximum system performance. A thermodynamic model was developed to perform these analyses.

The analyses have been performed in two parts. In the first part, the cycles without the expansion device producing work have been considered. A transcritical CO₂ cycle with an economizer (Economizer cycle) or an intercooler (Intercooler cycle) has been analyzed. Since pressure is one of the most important parameters in the air conditioning system, the pressure effects are examined in detail. Especially, the effects of the pressure ratios across the compressors, the low-side pressure, and the high-side pressure on the system performance of the transcritical CO₂ cycle are investigated.

In the second part, the effect of an expansion device with output of work (ED-WOW) on the system performance of the transcritical CO₂ cycles has been analyzed. There are two advantages in using the ED-WOW instead of a throttling expansion valve on the system performance. The first advantage is that lower enthalpy can be obtained at the inlet of the evaporator. The other one is that work can be extracted through the

expansion device. If this work is used to run the compressor, the input work for the compression of carbon dioxide can be reduced. In the analysis, these effects have been considered. First, the use of the work output extracted from CO₂ during the expansion process has not been considered. That is, only the enthalpy decrease through the expansion device has been considered. Secondly, the work output through the ED-WOW has also been considered with the decrease of the enthalpy and it has been assumed that the work is used to run the compressor.

2.1.1 Assumptions

The main assumptions for the analysis of the thermodynamic performance are as follows:

1. Flow is steady state.
2. Compression processes is isentropic but the expansion process is isenthalpic.
3. There are no pressure losses in the heat exchangers and piping.
4. The atmosphere is the heat sink. The CO₂ temperature equilibrates with the ambient air temperature due to the heat transfer through the gas cooler and intercooler.

2.1.2 Transcritical CO₂ Cycles with an Economizer and Intercooler

When the transcritical CO₂ cycle features a two-stage compression system, the COP can be optimized by choosing different pressure ratios for each stage. The system performances of the Economizer cycle and Intercooler cycle were examined and compared with that of the Base cycle. The investigated parameters are the effect of the

pressure ratios across the compressors, the effect of low-side pressure, and the effect of high-side pressure on system performance.

Two basic CO₂ cycles are analyzed here; namely the transcritical CO₂ cycle with an economizer (Economizer cycle, Figure 1.7) and the transcritical CO₂ cycle with an intercooler (Intercooler cycle, Figure 1.10). Both cycles include two compressors. As discussed in Chapter 1, both cycles are modified from the basic transcritical CO₂ cycle (Base cycle) of Figure 1.1. The Base cycle consists of a compressor, a gas cooler, an evaporator, and an expansion valve.

The Economizer cycle is composed of two compressors, a gas cooler, an evaporator, two expansion valves and an accumulator. After the first expansion, the saturated vapor of CO₂ at the intermediate pressure in the accumulator flows to the inlet to the 2nd-stage compressor and mixes with the CO₂ coming from the outlet of the 1st-stage compressor. The saturated liquid CO₂ expands again through another expansion valve. Following this valve, the two-phase flow of carbon dioxide enters the evaporator. The enthalpy of the carbon dioxide at the inlet to the evaporator decreases as shown in Figure 1.8 and it will increase the capacity of evaporator. This results in an increase of COP of the CO₂ cycle.

Figure 1.10 represents the Intercooler cycle. As shown in this figure, the Intercooler cycle comprises two compressors, a gas cooler, an expansion valve, an evaporator and an intercooler. The CO₂ coming from the outlet of the 1st-stage compressor is cooled down by removing heat through the intercooler. Then it flows to the inlet to the 2nd-stage compressor. As discussed in Chapter 1, it results in saving the compression work and increase of COP.

2.1.2.1 Calculation Methods

The calculation methods for the thermodynamic performance of the CO₂ cycles are given below. The method depends on the type of transcritical CO₂ cycle being analyzed.

2.1.2.1.1 Calculation Method for Base Cycle

In this analysis, the subscript 'B' is used on all variables to represent the Base cycle (Figure 1.1).

The CO₂ temperature and pressure at the inlet to the compressor (T_{B1} and p_{B1}) and the air temperature (T_{air}) are given as input variables. The temperature T_{B1} is higher than or equal to the saturated temperature (T_{sat}) at p_{B1} . The entropy (s_{B1}) and enthalpy (h_{B1}) at T_{B1} and p_{B1} are found using the CO₂ thermodynamic property data by Span and Wagner [Span and Wagner, 1996]. In the Base cycle, the high-side pressure (p_{B2}) is the same as the pressure (p_{E2} or p_{I2} , see the following sections) at the outlet of the 2nd-stage compressor of the Economizer cycle or Intercooler cycle. For the Base cycle

$$p_{B2} = p_{B1} \times (\text{pressure ratio})^2. \quad (2-1)$$

The temperature after compression (T_{B2}) is found for the same s_{B1} and p_{B2} using the thermodynamic property data [Span and Wagner, 1996]. Then the enthalpy (h_{B2}) at the outlet of the compressor is found at T_{B2} and p_{B2} . The compression work per unit mass flow is calculated by subtracting the enthalpy of CO₂ at the inlet to the compressor from the enthalpy at the outlet of the compressor as follows:

$$W_{c,B} = h_{B2} - h_{B1}. \quad (2-2)$$

After heat rejection to the ambient atmosphere through the gas cooler, the CO₂ temperature (T_{B3}) becomes T_{air} . Then the enthalpy (h_{B3}) at the outlet of the gas cooler is found at T_{B3} and $p_{B3} = p_{B2}$. The enthalpy after expansion, h_{B4} , at p_{B1} becomes the same as h_{B3} based on the assumption of isenthalpic expansion process. Then, the heat capacity of the evaporator is calculated as follows:

$$Q_{e,B} = h_{B1} - h_{B4} . \quad (2-3)$$

The COP of the Base cycle then becomes

$$\text{COP}_B = \frac{Q_{e,B}}{W_{c,B}} . \quad (2-4)$$

2.1.2.1.2 Calculation Method for Economizer Cycle

The subscript 'E' is employed to represent the Economizer cycle in this section (Figure 1.7).

The solution proceeds by first specifying the CO₂ temperature and pressure at the inlet to the 1st-stage compressor (T_{E1} and p_{E1}) and the ambient air temperature (T_{air}). The entropy (s_{E1}) and enthalpy (h_{E1}) are found at T_{E1} and p_{E1} using the CO₂ thermodynamic property data [Span and Wagner, 1996]. Identical or different (based on analysis) pressure ratios across the 1st-stage and 2nd-stage compressors are assumed, and then the pressures at the outlets of the compressors, $p_{E1'}$ and p_{E2} , are calculated. The temperature at the outlet of the 1st-stage compressor, $T_{E1'}$, is found based on the assumption of isentropic compression ($s_{E1'} = s_{E1}$) and the known $p_{E1'}$. Then the enthalpy at the outlet of the 1st-stage compressor ($h_{E1'}$) is found at $T_{E1'}$ and $p_{E1'}$.

The enthalpy at the outlet of the gas cooler (h_{E3}) is found at T_{air} and $p_{E3} = p_{E2}$. Then the saturated vapor and liquid enthalpies (h_{E5} and $h_{E3'}$) are found at $p_{E1'} = p_{E3'} = p_{E5}$. The quality of CO₂ in the accumulator becomes

$$x = \frac{h_{E3} - h_{E3'}}{h_{E5} - h_{E3'}}. \quad (2-5)$$

The enthalpy at the outlet of the 2nd expansion valve at p_{E1} , h_{E4} , becomes the same as $h_{E3'}$ based on the assumption of isenthalpic expansion process. The heat capacity of the evaporator is calculated as follows:

$$Q_{e,E} = (h_{E1} - h_{E4}) \times (1 - x). \quad (2-6)$$

The compression work of the 1st-stage compressor is calculated as follows:

$$W_{c1,E} = (h_{E1'} - h_{E1}) \times (1 - x). \quad (2-7)$$

The enthalpy at the inlet to the 2nd-stage compressor ($h_{E1''}$) after the mixing of the saturated vapor CO₂ flowed from the accumulator and the superheated CO₂ at the outlet of the 1st-stage compressor is calculated at the intermediate pressure ($p_{E1'} = p_{E1''}$) as follows:

$$h_{E1''} = h_{E5} \times x + h_{E1'} \times (1 - x). \quad (2-8)$$

Then, the temperature of the CO₂ mixture ($T_{E1''}$) is found with $h_{E1''}$ and $p_{E1''}$ using the thermodynamic property data [Span and Wagner, 1996]. The entropy of the CO₂ mixture ($s_{E1''}$) is found with $T_{E1''}$ and $p_{E1''}$. The temperature of CO₂ at the outlet of the 2nd-stage compressor (T_{E2}) is found with the assumption of isentropic compression process ($s_{E2} = s_{E1''}$) and the known high- side pressure, p_{E2} . Then the enthalpy at the outlet of the

2nd-stage compressor (h_{E2}) is found at T_{E2} and p_{E2} . The compression work of the 2nd-stage compressor is calculated as follows:

$$W_{c2,E} = h_{E2} - h_{E1'} . \quad (2-9)$$

The COP of the Economizer cycle is then calculated as

$$\text{COP}_E = \frac{Q_{e,E}}{W_{c1,E} + W_{c2,E}} . \quad (2-10)$$

2.1.2.1.3 Calculation Method for Intercooler Cycle

The subscript ' I ' is used on all variables to represent the Intercooler cycle in this section (Figure 1.10).

The solution proceeds by first specifying the CO₂ temperature and pressure at the inlet to the 1st-stage compressor (T_{I1} and p_{I1}) and the ambient air temperature (T_{air}). The entropy (s_{I1}) and enthalpy (h_{I1}) are found with the given T_{I1} and p_{I1} using the CO₂ thermodynamic property data [Span and Wagner, 1996]. Identical or different (based on analysis) pressure ratios across the 1st-stage and 2nd-stage compressors are assumed, and then the pressures at the outlets of the compressors, $p_{I1'}$ and p_{I2} , are calculated. The temperature at the outlet of the 1st-stage compressor, $T_{I1'}$, is found based on the assumption of isentropic compression ($s_{I1'} = s_{I1}$) and the known $p_{I1'}$. Then the enthalpy at the outlet of the 1st-stage compressor ($h_{I1'}$) is found at $T_{I1'}$ and $p_{I1'}$. The compression work of the 1st-stage compressor is calculated by subtracting the enthalpy at the inlet to the 1st-stage compressor from the enthalpy at the outlet of the 1st-stage compressor as follows:

$$W_{c1,I} = h_{11'} - h_{11} . \quad (2-11)$$

After heat transfer to the ambient atmosphere through the intercooler, the CO₂ temperature ($T_{12'}$) becomes T_{air} at the outlet of the intercooler. The entropy ($s_{12'}$) and enthalpy ($h_{12'}$) at the inlet to the 2nd-stage compressor are found with $T_{12'}$ and $p_{12'} = p_{11'}$ using the CO₂ thermodynamic property data [Span and Wagner, 1996]. Then, the temperature at the outlet of the 2nd-stage compressor, T_{12} , is found with the assumption of the isentropic compression process ($s_{12} = s_{12'}$) and the known high-side pressure, p_{12} . The enthalpy at the outlet of the 2nd-stage compressor, h_{12} , is found at T_{12} and p_{12} using the CO₂ thermodynamic property data [Span and Wagner, 1996]. The compression work of the 2nd-stage compressor is calculated by subtracting the enthalpy at the inlet to the 2nd-stage compressor from the enthalpy at the outlet of the 2nd-stage compressor as follows:

$$W_{c2,I} = h_{12} - h_{12'} . \quad (2-12)$$

After heat rejection to the ambient atmosphere through the gas cooler, the CO₂ temperature (T_{13}) becomes T_{air} at the outlet of the gas cooler. Then the enthalpy at the inlet to the expansion valve, h_{13} , is found with T_{13} and $p_{13} = p_{12}$ using the thermodynamic property data [Span and Wagner, 1996]. After expansion, the enthalpy, h_{14} , at p_{14} ($= p_{11}$) becomes the same as h_{13} by assuming isenthalpic expansion process. Therefore, the heat removal capacity of the evaporator can be calculated as follows:

$$Q_{e,I} = h_{11} - h_{14} . \quad (2-13)$$

The COP of the Intercooler cycle is then calculated as follows:

$$\text{COP}_I = \frac{Q_{e,I}}{W_{c1,I} + W_{c2,I}} . \quad (2-14)$$

2.1.3 Transcritical CO₂ Cycles with Work Extraction

The transcritical CO₂ cycle with an ED-WOW has been analyzed. The main purpose of this analysis is to examine the effect of the ED-WOW on the system performance. The system efficiencies are calculated for the cycles without the expansion device and the cycles with the ED-WOW. For the cycles with the ED-WOW, two cases have been considered. First, the decrease of the CO₂ enthalpy through the ED-WOW has been considered for the system performance. Then, the work output through the device as well as the decrease of the enthalpy has been considered.

2.1.3.1 Calculation Method

The calculation method for this analysis is the same as that for the cycles without an expansion device producing work in previous sections. The only differences are that the isentropic efficiencies are considered for the compressors and the ED-WOW and the effectiveness of the internal heat exchanger is assumed. The assumed isentropic efficiency of the compressor (η_{comp}) is 0.7. The isentropic efficiency of the ED-WOW (η_{ED-WOW}) is considered to be 0.5 and the effectiveness of the internal heat exchanger (ϵ_{IHX}) is assumed to be 0.7. These component efficiencies are defined as follows:

$$\eta_{comp} = \frac{w_{comp,s}}{w_{comp}} = \frac{h_{comp,out,s} - h_{comp,in}}{h_{comp,out} - h_{comp,in}} = 0.7, \quad (2-15)$$

$$\eta_{ED-WOW} = \frac{w_{ED-WOW}}{w_{ED-WOW,s}} = \frac{h_{ED-WOW,out} - h_{ED-WOW,in}}{h_{ED-WOW,out,s} - h_{ED-WOW,in}} = 0.5, \text{ and} \quad (2-16)$$

$$\epsilon_{IHX} = \frac{q_{IHX}}{q_{IHX,max}} = \frac{T_1' - T_1}{T_3' - T_1} = 0.7. \quad (2-17)$$

Where, the descriptions about the variables are given in the nomenclature section.

The cycles that were analyzed are the Base cycle (Case 1), Base cycle with the ED-WOW (Case 2), internal heat exchanger cycle (IHX cycle, Case 3), IHX cycle with the ED-WOW (Case 4), Intercooler cycle (Case 5), Intercooler cycle with the ED-WOW (Case 6), and Economizer cycle (Case 7). Schematics of these cycles are shown in Figures 2.1 through 2.7.

2.2 Expansion Device

2.2.1 Overview

A literature and technical review has been conducted to determine the suitability of various expansion devices which produce work. Both continuous flow and positive displacement devices were investigated. The operating conditions for a typical expansion device in a prototype transcritical CO₂ cycle are given in Table 2.1. These design operating conditions were determined based on a study of the transcritical CO₂ cycle by Li and Groll [Li and Groll 2001].

Because of their high inherent efficiency, turbomachinery type continuous flow expanders are considered a prime candidate CO₂ cycle application. Several issues must be addressed before their suitability can be properly judged. First, erosion by liquid impingement may be an issue due to the two-phase flow expected in the expansion device. Second, the rotational speed required for efficient performance should be determined to evaluate the required bearing technology.

Thiruvengadam presents a theory for prediction of blade erosion based on the characteristics of the flow and the turbine material [Thiruvengadam, 1966]. This theory assumes erosion damage by repetitive impact by spherical droplets, and expresses the limiting criteria as:

$$\frac{\sigma_e}{\rho_1 C_1 U_1} \cong 2 \quad (2-18)$$

Where:

- σ_e = material limiting stress
- ρ_1 = density of liquid phase
- C_1 = sonic velocity in liquid phase
- U_1 = impact velocity

Alvarez made a preliminary study of the potential for turbo-type expanders for a transcritical CO₂ cycle application and applied this theory to an expander with a nominal inlet CO₂ pressure and temperature of 10 MPa and 40°C [Alvarez, 1999]. With steel as the blade material, velocities of up to 800 m/s were determined to be tolerated without danger of erosion. These values are far in excess of any local velocity to be expected in a machine of this class and type, and thus erosion due to liquid impingement was ruled out as a concern for this device.

Alvarez also applied specific speed and specific diameter correlations [Balje, 1981] to estimate the rotational speed required for a turbine operating between the 10 MPa inlet pressure and 0.4 MPa exit pressure at a flow rate of 0.08 kg/s. For this application, a rotational speed on the order of 500,000 rpm was required to achieve a high efficiency design. Estimations for a partial admission turbine determined that speeds as low as 70,000 rpm could be achieved with a 25 mm diameter radial turbine. However,

this required an extremely low 4% admission resulting in a maximum efficiency of 50%. As correlations in that range are extrapolations of data taken from higher admission device, the actual efficiency may well be lower even if the machine is well designed and manufactured to close tolerances. In addition, the Balje correlations do not include the impact of two-phase flow. Liquid in the turbine flow passages can be expected to migrate due to centrifugal effects and will thus have significant impact on true performance.

Although continuous flow machines have potential for the expander in large scale CO₂ cycles, for the capacity of concern here the small dimensions and high rotational speeds make them a high risk design proposal. Thus, a positive displacement device was chosen as the type of expander to employ in the prototype system. Because of its inherent simplicity and the vast knowledge base available on inherent losses, a piston-cylinder assembly device was chosen as the appropriate expansion device for the prototype application.

The piston device consists of a cylinder, piston and connecting rod as shown in Figure 2.8. The piston is connected to a crank mechanism that drives the shaft. The shaft in turn is connected to a hydraulic pump used as a mechanical loading device. The expansion process is controlled using fast-acting solenoid valves as intake and exhaust valves.

After determination of the appropriate type of device, a representative example was designed and fabricated to form the test subject for the first part of this research effort. Initial testing was performed on this device in isolation, the shaft connected to a torque meter and loading device. Measurements of mass flow rate, expansion ratio, and

work extraction was conducted for the purpose of characterizing component efficiency. This effort is presented in detail in Chapter 3.

2.2.2 Thermodynamic Processes of the Piston Expander

There are three processes that occur within the time period of one revolution: intake, expansion and exhaust. During the intake process, the intake valve opens and the supercritical high pressure CO_2 flows into the cylinder as the piston moves down from Top Dead Center (TDC) to the location of expansion initiation (LOE) as shown in Figure 2.8. When the piston reaches LOE, the intake valve closes and the expansion process begins with the piston moving down further, as the CO_2 expands from high pressure and temperature to low pressure and temperature. When the piston reaches Bottom Dead Center (BDC), the exhaust valve opens. During the second stroke the expanded CO_2 is swept out to the inlet of the evaporator. As the piston reaches TDC, the exhaust valve closes. The next revolution begins by opening the intake valve again. Figure 2.9 shows the p-v diagram of the piston process when the process is ideal.

2.2.3 Theoretical Modeling of the ED-WOW Device

In order to analyze the performance of the prototype expansion device, a theoretical model was developed. This model was used to both verify proper operation of the device in the prototype application, and to identify loss mechanisms in the device so as to guide design improvements. This model should feature sufficient physical detail to model the unique characteristics of the carbon dioxide application. No research has been

published on modeling the expansion device for a transcritical CO₂ cycle. Hence, this is the first model to predict the thermal and mechanical behavior of the expansion device.

2.2.3.1 Basic Loss Mechanisms

The minor losses other than boundary friction have been reviewed for the mass flow into and from the cylinder chamber. The topics for the piston scuffing and lubrication have also been reviewed to predict the piston ring behaviors.

2.2.3.1.1 Minor Flow Losses

In order to simulate the CO₂ flow into and from the cylinder chamber, minor losses due to sudden contractions, sudden enlargements, and bends of flow path must be characterized. Figure 2.10 shows the configuration of the solenoid valve, fittings and the piston-cylinder section. The CO₂ pressure loss from the outlet of the solenoid valve to the cylinder chamber is assumed to consist of losses due to sudden contraction from point 1 to point 2 in the solenoid valve, the bend of flow path in the solenoid valve (from point 2 to point 3), sudden enlargement from solenoid valve to the fitting (from point 3 to point 4), and sudden enlargement from the fitting to the cylinder chamber (from point 4 to point 5). The pressure loss due to the wall friction on few straight sections of the channel is considered much smaller than those associated with the above mentioned sections.

2.2.3.1.1.1 Single-Phase Minor Losses

Most of the analytical and experimental expressions for head losses are based on single-phase phenomena. In this section the minor losses for the single-phase are reviewed. Then two-phase head losses are reviewed in the next section.

The pressure losses due to sudden contraction and enlargement of the flow area are expressed, respectively, as follows [Fox and McDonald, 1992].

$$h_{lm} = K_c \frac{\bar{v}^2}{2} \quad (2-19)$$

$$h_{lm} = K_e \frac{\bar{v}^2}{2} \quad (2-20)$$

where, K_c , K_e , and \bar{v} stand for the minor loss coefficients for the sudden contraction and enlargement, and the flow velocity at the narrow path between upstream and downstream of the flow, respectively.

The minor loss coefficients for sudden expansions and contractions in circular ducts are given in Figure 2.11 [Fox and McDonald, 1992]. Note that both loss coefficients are based on the larger $\frac{\bar{v}^2}{2}$. Thus losses for a sudden expansion are based on

$\frac{\bar{v}_1^2}{2}$, upstream condition, and those for a contraction are based on $\frac{\bar{v}_2^2}{2}$, downstream condition.

There are also head losses due to the flow entrance and exit. The entrance losses occur when a fluid enters a conduit from a large tank or reservoir as shown in Figure 2.12 [Evetts and Liu, 1987]. The amount of head loss is significantly dependent on the shape of the entrance. If the entrance is well-rounded, the entrance loss becomes very small. Entrance loss coefficients can be found in Figure 2.13. Exit losses occur when a liquid

exits a conduit and enters a large tank or reservoir, as shown in Figure 2.14. The exit loss coefficient is 1.0 for all cases (i.e., regardless of the shape of the exit) [Evvett and Liu, 1987].

Gradual expansion losses occur when there is a gradual increase in conduit size, and gradual contraction losses happen when there is a gradual decrease in conduit size. Loss coefficients for gradual expansions can be determined from Figure 2.15 [Evvett and Liu, 1987]. Table 2.2 illustrates loss coefficients for gradual contractions.

The head loss of a bend is larger than for fully developed flow through a straight section of equal length. The additional loss is primarily the result of secondary flow, and is represented most conveniently by an equivalent length of straight pipe. The equivalent length depends on the relative radius of curvature of the bend. Because they are simple and inexpensive to erect in the field, miter bends often are used, especially in large pipe systems [Fox and McDonald, 1992]. Figure 2.16 shows design data for miter bends.

2.2.3.1.1.2 Two-Phase Minor Losses

As the CO_2 expands in the piston-cylinder device, its phase changes from a supercritical state to single-phase state (compressed liquid or superheated vapor) and then to a two-phase state. This means that the CO_2 becomes two-phase at the end of the expansion, leaving the piston device and entering the evaporator as a two-phase fluid. In order to simulate the discharging of CO_2 from the expansion device, literature on head losses in two-phase flow was reviewed. Unfortunately, one of the least-studied aspects of two-phase vapor-liquid flow is that of the change in static pressure and the energy loss with such features as enlargements, contractions, orifices, bends, and valves.

Consider a two-phase flow passing through a sudden enlargement as shown in Figure 2.17. The general method used in single-phase flow is applicable to a one-dimensional separated two-phase flow [Collier, 1972]. Collier discussed that the pressure just downstream of the enlargement (plane 1) is found to be equal to that at the end of the smaller section of pipe and a simplified momentum balance for the combined flow yields:

$$p_1 A_2 - p_2 A_2 = W_g (u_{g2} - u_{g1}) + W_f (u_{f2} - u_{f1}). \quad (2-21)$$

Substituting for W_g , W_f , u_g and u_f in terms of G , x , α , v_f , and v_g using the continuity relationships and defining σ as ratio (A_1/A_2), Equation (2-21) becomes

$$p_2 - p_1 = G^2 \sigma v_f \left[\left\{ \frac{(1-x)^2}{1-\alpha_1} + \left(\frac{v_g}{v_f} \right) \frac{x^2}{\alpha_1} \right\} - \sigma \left\{ \frac{(1-x)^2}{1-\alpha_2} + \left(\frac{v_g}{v_f} \right) \frac{x^2}{\alpha_2} \right\} \right] \quad (2-22)$$

where W and u are the mass flow rate and velocity and subscripts g and f denote the gas phase and liquid phase, respectively. G is mass velocity and is defined as the rate of mass flow divided by the flow area:

$$G = \frac{W}{A} = \rho u = \frac{u}{v}. \quad (2-23)$$

x , α , and v represent the mass quality, void fraction, and specific volume, respectively.

If the void fraction remains unchanged across the feature ($\alpha_1 = \alpha_2 = \alpha$), Equation (2-22) becomes

$$p_2 - p_1 = G^2 \sigma (1 - \sigma) v_f \left[\left\{ \frac{(1-x)^2}{1-\alpha} + \left(\frac{v_g}{v_f} \right) \frac{x^2}{\alpha} \right\} \right]. \quad (2-24)$$

Comparing this result with that for the total flow assumed to be single-phase liquid reveals that the term in the square brackets acts as a two-phase multiplier. For homogeneous flow Equation (2-24) reduces to

$$p_2 - p_1 = G_1^2 \sigma (1 - \sigma) v_f \left[1 + \left(\frac{v_{fg}}{v_f} \right) x \right]. \quad (2-25)$$

Measurements of void fraction made in the vicinity of sudden enlargements by some other authors [Richardson, 1958, for horizontal flow and Petrick and Swanson, 1959, for vertical flow] indicate that the assumption $\alpha_1 = \alpha_2 = \alpha$ is only approximately true.

Figure 2.18 shows a sudden contraction in the cross-sectional area of the pipe two-phase flow. The general approach used for single-phase flow can again be applied to a two-phase separated flow passing through a sudden contraction. As the fluid passes from plane 1 to plane c, at the vena contracta it is accelerated and pressure energy is converted to kinetic energy with little or no friction dissipation [Collier, 1972]. Beyond plane c, however, the conditions are similar to those for a sudden enlargement and frictional dissipation occurs. Collier mentioned that equations derived above could therefore be applied to this 'enlargement' from plane c to plane 2 to obtain an expression for the frictional pressure loss. The coefficient of contraction, C_c , is used to denote the ratio $\frac{A_c}{A_2}$ and replace σ , likewise the mass velocity $G_c \left(= \frac{G_2}{C_c} \right)$ replaces G_1 in Equation (2-22). Rearranging and simplifying the equations yields the following expression for the frictional pressure loss across a sudden contraction.

$$\begin{aligned} \Delta p_f &= \frac{dE}{xv_g + (1-x)v_f} \\ &= \left(\frac{G_2}{C_c} \right)^2 (1 - C_c) \left[\frac{(1 + C_c) \left\{ \frac{x^3 v_g^2}{\alpha^2} + \frac{(1-x)^3 v_f^2}{(1-\alpha)^2} \right\}}{2 \{ xv_g + (1-x)v_f \}} - C_c \left\{ \frac{x^2 v_g}{\alpha} + \frac{(1-x)^2 v_f}{1-\alpha} \right\} \right] \quad (2-26) \end{aligned}$$

Then the change in static pressure at a sudden contraction can be given by the sum of the frictional dissipation and the theoretical kinetic energy change. For a homogeneous model [Collier, 1972]

$$p_1 - p_2 = \frac{G^2 v_f}{2} \left[\left(\frac{1}{C_c} - 1 \right)^2 + \left(1 - \frac{1}{\sigma^2} \right) \right] \left[1 + \left(\frac{v_{fg}}{v_f} \right) x \right] \quad (2-27)$$

where, v_f , v_{fg} , and x represent the specific volume of liquid phase, specific volume difference between vapor and liquid phases, and vapor quality, respectively. In the above equation, the coefficient of contraction, C_c , is a function of $\sigma \left(= \frac{A_1}{A_2} \right)$. Table 2.3 shows the relation between C_c and σ for turbulent single-phase flow.

Collier said that Ferrel and McGee [Ferrel and McGee, 1966] and Geiger and Rohrer [Geiger and Rohrer, 1966] found that the homogeneous model (Equation (2-27)) satisfactorily represented their experimental data for steam-water through sudden contractions [Collier, 1972]. Again measurements of void fraction made by some other authors [Richardson, 1958, for horizontal flow and Petrick and Swanson, 1959, for vertical flow] in the vicinity of sudden contractions indicate that the assumption implicit in Equation (2-27), $\alpha_1 = \alpha_2 = \alpha$, is only approximately true [Collier, 1972].

2.2.3.1.2 Piston Ring Scuffing and Lubrication

Piston ring behavior must be characterized to properly model the expansion device producing work. If there is a separating oil film between the rubbing surfaces, there is no piston ring contact with the wall, or "scuffing". Scuffing is a consequence of

the contact pressure exceeding the pressure the momentary local lubricating conditions can bear [Aue, 1975].

2.2.3.1.2.1 Piston Ring Scuffing

Aue investigated the piston ring behavior experimentally for internal combustion engine applications [Aue, 1953]. He developed a test facility to perform investigations of piston rings when running under various pressures and lubricating conditions. In the first test, lubrication was adjusted to correspond to normal combustion engine conditions. The conclusion of the test was that even an extremely thin lubricating film, so long as it was still present, would prevent metal-to-metal contact and the resulting scuffing. Other testing focused on a complete stationary set of five piston rings on a piston with constant and pulsating pressure loading. The result of the test was that the last piston ring alone took most of the pressure drop across the piston with both of well-fitting rings and poor-fitting rings.

Aue also examined the behavior of a piston ring theoretically [Aue, 1974]. He mentioned that wear would correct minor imperfections and a little wear in service would stabilize operation. He suggested rotation of the piston about its axis to improve the running condition.

Wakuri and Ono carried out experimental studies on the abnormal wear of cylinder liners and piston rings in large-sized marine Diesel engines [Wakuri and Ono, 1973]. The authors investigated the mechanism of abnormal wear, detecting procedures, and the effect of some factors on the occurrence of abnormal wear. Some results of their studies were similar to those of work done by Aue. Abnormal wear is initiated by the

scuffing caused by serious edge-loading of piston rings and is accelerated by the abrasive wear due to very large-sized worn particles scraped off from the cylinder liner. They discussed that a roughened surface had much more resistance to scuffing than a smooth surface and that rotation of a piston was more effective to increase the resistance to scuffing.

2.2.3.1.2.2 Piston Ring Lubrication

If there is a separating oil or fluid film between the rubbing surfaces, it prevents scuffing. In general, the starting point for analysis of the piston ring lubrication is the Reynolds equation. The derivation of Reynolds equation is given in Appendix A.

Baker et al. developed a computer program to predict lubricant film thickness, friction for a piston ring and pressure differences across a piston ring face over the crank angle [Baker et al., 1973]. The authors discussed that serious reduction in film thickness may be expected if the radius of curvature of the piston ring falls much below 10^{-2} inches.

Rohde and Whitaker presented a mathematical model of the hydrodynamic lubrication of piston rings [Rohde and Whitaker, 1979]. The authors examined the effects of engine speed, engine geometry, lubricant viscosity, piston ring face profile, tension, and thickness. They calculated the power loss by multiplying friction force by piston velocity. They did not consider the term of film squeeze in the power loss calculation.

Sun developed a subroutine package to solve the inverse problem of slider lubrication, i.e., load being given and the minimum film thickness being sought [Sun, 1990]. The author mentioned that the problem might also contain all or any combination

of finite-width, squeeze action, and oil starvation. The author calculated the power loss by considering both the friction obtained by integrating the shear stress and squeeze of film.

Jeng performed theoretical analysis for piston ring lubrication by considering fully flooded lubrication and starved lubrication [Jeng, 1992]. He developed a system of nonlinear equations formulated based on the hydrodynamic lubrication theory. He solved the system of equations using a modified Newton's method. He demonstrated the capability of his computer model by investigating the effect of operating conditions, ring tensions, and ring face profile for the fully flooded and starved inlet conditions. He showed that the starved lubrication occurred when the lubricant supply was not adequate for fully flooded lubrication.

Radakovic and Khonsari investigated the effects of viscosity variations with temperature, in conjunction with the non-Newtonian shear thinning behavior of multigrade oils on the hydrodynamic lubrication of the piston ring [Radakovic and Khonsari, 1997]. Their simulation results showed that shear thinning could have a significant effect on parameters such as film thickness, viscous drag force, and power loss. The thermal effects from viscous dissipation in the clearance space along the piston ring also influenced these parameters, but to a lesser degree.

2.2.3.2 Fluid Mechanic Model for the ED-WOW Device

A theoretical model was developed to predict the efficiency of the ED-WOW based on a piston-cylinder type device. The overall model is composed of several sub-models. The main modeling effort focused on frictional losses between the piston rings

and cylinder walls and on loss due to squeeze of film. The model is based on the lubrication theory and assumes that the piston ring in the device is a slipper-pad bearing. The model predicts the film thickness of the lubricant, in this case either CO₂ or CO₂ and oil. The pressure distribution under the piston ring, power loss, and work done by the CO₂ are also calculated.

Figure 2.19 shows the flow diagram of the model. As the first step, the displacement and velocity of the piston, crank angle, and the work done by the CO₂ are calculated for a given time step. The power loss and frictional force are calculated based on lubrication theory. In addition, the CO₂ mass flow into or out of the device (based on the process) is predicted. Finally, the program calculates the pressure and temperature of the CO₂ and stores the results for the given time step. The same calculations are repeated for the next time step and so on until the device goes through two full revolutions (720°). Once the program concludes the calculations for the two revolutions, global parameters, such as total power output, power loss, and efficiency are calculated. This model is referred to as 'ED-WOW' (Expansion Device With Output Work for CO₂ cycle).

2.2.3.2.1 Modeling for Mass Flow into Chamber

The theoretical considerations of the various minor losses are quite complicated; therefore, minor losses are usually evaluated by empirical methods. Figure 2.10 shows configuration of the connection of a solenoid valve to fittings and chamber of cylinder. The mass flow into the chamber of the cylinder is calculated based on the configuration of Figure 2.10. Figure 2.20 shows geometries causing minor losses. The assumptions for this model are as follows.

- Pressure losses due to friction (other than minor losses) are negligible.
- Potential energy change is negligible.
- If two-phase flow occurs, it is assumed to be homogeneous flow. Therefore, the single-phase formula can be applied with the averaged properties.
- The chamber is large compared to the flow path dimension so that it is considered as a reservoir.
- The flow is isothermal.

Four major contributions for the pressure losses are considered. They are pressure losses due to sudden contraction, sudden enlargement, miter bend, and pressure loss at exit.

2.2.3.2.1.1 Pressure Loss due to Sudden Contraction

The pressure loss due to sudden contraction of flow area is given as [White, 1986]

$$\Delta p_{1 \rightarrow 2} = K_c \frac{\rho v^2}{2}. \quad (2-28)$$

The equation above can be expressed as

$$p_1 - p_2 = C_D \left(1 - \frac{A_2}{A_1} \right) \frac{\rho_2 v_2^2}{2}. \quad (2-29)$$

C_D is a discharge coefficient and is determined experimentally by comparing the filling behavior predicted by computer model to the experimental data. It is discussed in Section 2.2.3.2.3.

2.2.3.2.1.2 Pressure Loss due to Miter Bend

It is assumed that the flow path is bent by 90° without change of flow area as shown in Figure 2.20. This type of bend is known as 'miter bend'. Pressure loss due to bending is described in terms of friction loss as follow [Fox and McDonald, 1992]:

$$\Delta p_{bend} = f \frac{D_e}{L} \frac{\rho_2 v_2^2}{2} = p_2 - p_3 \quad (2-30)$$

The value of $\frac{D_e}{L}$ is 60 for 90° miter bends as shown in Figure 2.16. The friction loss coefficient is determined by assuming single-phase flow. $\frac{e}{D}$ is about 0.0032 for commercial steel for $D = \frac{3}{64}$. The Reynolds number is given as

$$Re = \frac{\rho v D}{\mu} \quad (2-31)$$

where D is diameter of flow channel and ρ , v , and μ represent the density, velocity, and viscosity of the fluid in the flow channel, respectively. In the case of CO_2 between $0^\circ C$ and $100^\circ C$, the value of the viscosity is about $1.5 \times 10^{-5} \frac{N \cdot s}{m^2}$ [Fox and McDonald, 1992].

When the flow is laminar ($Re \leq 2000$), the friction coefficient is calculated as

$$f = \frac{64}{Re}. \quad (2-32)$$

If the flow is turbulent ($Re > 2000$), it is determined from Moody diagram and is about 0.025.

2.2.3.2.1.3 Pressure Loss due to Sudden Enlargement

The pressure loss due to sudden enlargement of flow area is given as [White, 1986]

$$\Delta p_{3 \rightarrow 4} = K_e \frac{\rho v^2}{2}. \quad (2-33)$$

The equation above can be expressed as

$$p_3 - p_4 = C_{D,e} \left(1 - \frac{A_3}{A_4}\right)^2 \frac{\rho_3 v_3^2}{2}. \quad (2-34)$$

$C_{D,e}$ is a discharge coefficient for sudden enlargement and is generally given as 1.0.

Therefore, the pressure loss due to sudden expansion is

$$p_3 - p_4 = \left(1 - \frac{A_3}{A_4}\right)^2 \frac{\rho_3 v_3^2}{2}. \quad (2-35)$$

2.2.3.2.1.4 Pressure Loss due to Exit

Pressure loss at exit to a reservoir is expressed as

$$\Delta p_{4 \rightarrow 5} = K_{exit} \frac{\rho_4 v_4^2}{2} \quad (2-36)$$

where, the loss coefficient, K_{exit} , is given as 1.0 for all shape of exit [Evet and Liu, 1987].

2.2.3.2.2 Calculation Method for Mass Flow into Chamber

Total pressure loss from the outlet of the solenoid valve to the chamber consists of all of the losses given above. It means that total pressure loss is given as

$$\Delta p_{tot} = \Delta p_{1 \rightarrow 2} + \Delta p_{bend} + \Delta p_{3 \rightarrow 4} + \Delta p_{4 \rightarrow 5}. \quad (2-37)$$

If the total pressure loss is known, the mass flow rate can be calculated using Equation

(2-37). When p_1 and p_5 are given, the calculation procedure is as follows:

- Estimate $p_2^1 = \frac{p_1^1 + p_5^1}{2}$.
- Find ρ_2 with assumption of isothermal process ($T_2 = T_1$).
- Calculate v_2 by using Equation (2-29). C_D will be determined later based on experiment.
- Calculate p_3 by using Equation (2-30).
- Calculate p_4 by using Equation (2-35).
- Calculate ρ_4 and v_4 by assuming isothermal process ($T_4 = T_1$).

Check if Equation (2-37) is satisfied with the given and predicted values. If it is not satisfied, p_2^2 (or p_2^{n+1}) for the next trial is determined by using 'Bisection method' [Hoffman, 1992] as follows:

$$p_2^{n+1} = \frac{p_2^n + p_2^{n-1}}{2} \quad (2-38)$$

Repeat the calculation until Equations (2-29), (2-30), (2-34), (2-35) and (2-36) are all satisfied.

Mass flow rate can be calculated by using mass conservation as follow:

$$\dot{m}_{in} = \rho_2 v_2 A_2 \text{ or } \dot{m}_{in} = \rho_3 v_3 A_3 = \dots \quad (2-39)$$

Figure 2.21 shows the flow diagram for the mass calculation.

2.2.3.2.3 Determination of Discharge Coefficient of Sudden Contraction

As mentioned before, the discharge coefficient for sudden contraction is determined experimentally. Experiments were performed to investigate the characteristics of the solenoid valve as mentioned in Chapter 3. The results of the experiments were used to determine the coefficient. The discharge coefficient is obtained based on Equation (2-37) but not determined exactly and directly from a separate experiment because no experiment was conducted for that.

Figure 2.22 shows the comparison of predicted filling behaviors of CO₂ to the experimental data. The y-axis represents dimensionless pressure. The measured pressure is dynamic pressure but the predicted pressure is absolute pressure. The experimental curve shows the decrease of pressure after a peak of pressure because of its dynamic pressure. It is considered that there is pressure equilibrium in the chamber at the peak pressure point. When C_D is 1.0, the time at which the predicted pressure reaches a peak is far away from the experimental data. Trial-error method was used to obtain C_D of 6.5 to give the same time for pressure equilibrium in the chamber, as shown in Figure 2.22.

2.2.3.2.4 Modeling for Mass Flow Out from Chamber

At the end of the expansion process the CO₂ pressure is expected to be about 3.4MPa (500 psig) and the state will be two-phase. In order to predict the mass flow out from the chamber, a two-phase flow model is required for sudden contraction. Flow area is assumed to decrease suddenly when CO₂ is discharged from the chamber to the inlet of the evaporator. Figure 2.18 shows the sudden contraction in cross-sectional area of the pipe with two-phase flow. A homogeneous two-phase flow model for sudden contraction is expressed [Collier, 1972] as follows:

$$p_1 - p_2 = \frac{G_2^2 v_{2,f}}{2} \left[\left(\frac{1}{C_c} - 1 \right)^2 + \left(1 - \frac{1}{\sigma^2} \right) \right] \left[1 + \left(\frac{v_{2,fg}}{v_{2,f}} \right) x \right]. \quad (2-40)$$

A detailed explanation of the above equation is given in Section 2.2.3.1.1.2.

If the pressures in and downstream of the chamber are known, the mass velocity, G_2 , can be calculated. As shown in Equation (2-23), the mass velocity is expressed as

$$G_2 = \frac{W}{A_2} = \rho_2 u_2 = \frac{u_2}{v_2}. \quad (2-41)$$

Therefore, the mass flow rate from the chamber is calculated as

$$\dot{m}_{out} = \rho_2 u_2 A_2 = G_2 A_2. \quad (2-42)$$

Subscript '2' represents the downstream of the chamber shown in Figure 2.18.

2.2.3.3 Modeling for Piston Ring Lubrication

As a piston moves up and down, there is loss of energy due to the friction, squeeze of the piston ring, heat transfer, blowby, etc. In this section the losses due to the friction and squeeze motion of the piston ring are modeled. Figure 2.23 shows a schematic of the piston ring and cylinder wall conjunction.

2.2.3.3.1 Theoretical Model

2.2.3.3.1.1 Governing Equation

The piston ring can be treated as a reciprocating, dynamically loaded bearing with a combined sliding and squeeze motion [Jeng, 1992]. As discussed in Appendix A, the Reynolds equation for an incompressible lubricant can be written as:

$$\frac{1}{\mu} \frac{\partial}{\partial x} \left(h^3 \frac{\partial p}{\partial x} \right) = 6U \frac{\partial h}{\partial x} + 12V(t) \quad (2-43)$$

where μ , h , and U stand for the viscosity, film thickness of the lubricant, and the piston speed, respectively, and $V(t)$ represents the velocity of piston ring in the y-coordinate (h-coordinate in this case) and can be expressed as:

$$V(t) = \frac{dh}{dt}. \quad (2-44)$$

2.2.3.3.2 Geometry of Piston Ring

The film thickness can be expressed as:

$$h(x, t) = h_m(t) + h_s(x) \quad (2-45)$$

where h_m is the time varying minimum film thickness and h_s is the ring face profile. A parabolic form for the ring face profile is sufficiently accurate [Jeng, 1992]. Therefore, the ring face profile can be written with the assumption of no offset of the piston ring as:

$$h_s(x) = \frac{4C_R}{b^2} x^2 \quad (2-46)$$

where C_R is the crown height and b is the width of the ring as shown in Figure 2.23.

2.2.3.3.3 Boundary Conditions

A fully flooded inlet condition is assumed, that is, the lubricant supply is always adequate at the inlet. The inlet and exit boundary conditions are expressed as:

$$p\left(-\frac{b}{2}, t\right) = p_{bot}(t) \quad (2-47)$$

$$p\left(\frac{b}{2}, t\right) = p_{top}(t) \quad (2-48)$$

where p_{bot} and p_{top} stand for the pressure at the trailing and leading edges of the ring, respectively. The values of p_{bot} and p_{top} depend on the direction of motion and piston position. For example, when the piston moves to the direction of the right hand side in Figure 2.23 (during the down stroke, intake and expansion stroke), p_{bot} is the CO₂ pressure in the cylinder chamber and p_{top} the pressure between the first and second compression rings.

2.2.3.3.4 Initial Condition

An initial condition is needed to solve the problem of dynamically loaded bearings. It is obtained arbitrarily by assuming that

$$V(t_0) = \left. \frac{dh}{dt} \right|_{t_0} = 0. \quad (2-49)$$

2.2.3.3.5 Piston Ring Elastic Characteristics

The piston ring is assumed to be ideal, that is, the ring is truly circular and exerts uniform pressure all around the cylinder wall. It is also assumed that the ring only moves

radially as a unit under loading. Therefore, the piston ring can be treated as a thin walled cylinder. Then, the radial deflection of the ring is

$$C = \frac{(p_M - p')r^2}{E \cdot t_r} \quad (2-50)$$

where p_M is the external mean hydrodynamic pressure, p' is the uniform internal gas pressure, E is the Young's modulus of the ring, r is radius of the ring, and t_r is the ring thickness. The radius of the ring is assumed to be half of the diameter of the cylinder wall $\left(\approx \frac{B}{2}\right)$. The radial deflection of the ring is equivalent to the minimum film

thickness, h_m , and the minimum film thickness is written as:

$$h_m = \frac{(p_M - p')r^2}{E \cdot t_r} \quad (2-51)$$

Equation (2-50) can be expressed differently after mathematical manipulation with some definitions as follows:

$$p_{el} = \frac{2T}{bB} \quad (2-52)$$

where p_{el} is the ring elastic pressure, T is the tangential ring tension and B is the cylinder bore diameter.

2.2.3.3.6 Method of Solution

2.2.3.3.6.1 Pressure Distribution

Integration of Equation (2-43) with respect to x gives

$$h^3(x, t) \frac{\partial p}{\partial x} = 6\mu U(t)h(x, t) + 12\mu \frac{dh(x, t)}{dt} x + C_1. \quad (2-53)$$

where C_1 is a constant. The time derivative of h can be expressed as:

$$\frac{dh(x, t)}{dt} = \frac{d[h_m(t) + h_s(x)]}{dt} = \frac{dh_m}{dt}. \quad (2-54)$$

Integration of Equation (2-53) with respect to x gives

$$p(x, t) = 12\mu \int_{-\frac{b}{2}}^x \frac{1}{h^3(s, t)} \left[\frac{U(t)h(s, t)}{2} + \frac{dh_m}{dt} s + C_2 \right] ds + C_3 \quad (2-55)$$

where C_2 is a constant. By applying the boundary conditions the pressure distribution is obtained as:

$$p(x, t) = 12\mu \int_{-\frac{b}{2}}^x \frac{1}{h^3(s, t)} \left[\frac{U(t)h(s, t)}{2} + \frac{dh_m}{dt} s + C_2 \right] ds + p_{bot} \quad (2-56)$$

and the integral constant C_2 is

$$C_2 = \frac{\frac{p_{top} - p_{bot}}{12\mu} - \int_{-\frac{b}{2}}^{\frac{b}{2}} \frac{1}{h^3(s, t)} \left[\frac{U(t)h(s, t)}{2} + \frac{dh_m}{dt} s \right] ds}{\int_{-\frac{b}{2}}^{\frac{b}{2}} \frac{1}{h^3(s, t)} ds}. \quad (2-57)$$

As shown in Figure 2.23, the profile of the ring face is assumed to be parabolic and there are convergent and divergent portions of the gap. Cavitation may occur in the divergent portion. Therefore, the pressure is assumed to be constant in the lubricant in the divergent portion of the gap if a cavitation occurs there. Figure 2.24 shows the pressure distribution under the piston ring with this assumption. The pressure in the divergent portion is cut-off and assumed to be p_{bot} during the intake and expansion stroke.

The x-coordinate was normalized by dividing the distance, x , by the half thickness of the piston ring, $b/2$, as shown in Figure 2.23.

2.2.3.3.6.2 Friction Force

Velocity profile in the y-coordinate is given by Equation (A-15) in Appendix A

$$u(y) = \frac{1}{2\mu} \frac{\partial p}{\partial x} (y^2 - yh) + U \left(1 - \frac{y}{h} \right). \quad (\text{A-15})$$

The shear stress acting on the piston ring is derived using the above velocity profile as:

$$\tau = \mu \left. \frac{\partial u}{\partial y} \right|_{y=h} = \frac{h}{2} \frac{\partial p}{\partial x} - \frac{\mu U}{h}. \quad (2-58)$$

The friction force for hydrodynamic lubrication can be written as:

$$F = \int_A \tau \cdot dA = \int_A \left(\frac{h}{2} \frac{\partial p}{\partial x} - \frac{\mu U}{h} \right) dA \quad (2-59)$$

where A represents the area of the lubricant region.

In the case of boundary lubrication, the friction force on the ring is calculated by:

$$F = \mu_c (\pi BW) \text{sign}(U) \quad (2-60)$$

where μ_c , B and W are the coefficient of friction, the cylinder bore, and the load imposed on the ring, respectively. W is expressed as:

$$W = b[p_{el} + p_{bk}] \quad (2-61)$$

where p_{el} and p_{bk} are the ring elastic pressure of Equation (2-52) and the pressure at the back side of the ring, respectively.

2.2.3.3.6.3 Power Loss

When hydrodynamic lubrication is present between the piston ring and cylinder wall, the power loss is [Jeng, 1992]

$$P = \int_A \frac{\mu}{h} U^2 dA + \int_A \frac{h^3}{12\mu} \left(\frac{\partial p}{\partial x} \right)^2 dA. \quad (2-62)$$

This equation automatically includes the power loss due to squeeze motion.

In the case of boundary lubrication, the power loss is calculated by:

$$P = \mu_c (\pi BW) |U|. \quad (2-63)$$

2.2.3.3.7 Numerical Scheme

Equations (2-51) and (2-56), the film thickness and pressure distribution in the lubricant, are coupled to each other and are a system of nonlinear equations. The system is solved iteratively by using the internal halving method [Hoffman, 1992]. First, the minimum film thickness, h_m , is determined by using the internal halving method. Let this minimum film thickness be h_{m1} . Then, the time derivative of h_m , the squeeze velocity, is calculated by using the values of the current and previous steps as:

$$\frac{dh_m^n}{dt} = \frac{h_m^n - h_m^{n-1}}{\Delta t} \quad (2-64)$$

where superscripts n and $n-1$ represent current and previous time steps, respectively, and Δt stands for the time interval. Now Equation (2-56) can be solved because there are no unknown variables in that equation. The pressure in the lubricant can be determined after double integrations as shown in Equations (2-56) and (2-57). Analytical expression for each term of the integrations in Equations (2-56) and (2-57) have been developed and

shown in Appendix B. The external mean hydrodynamic pressure, p_M , is calculated numerically by using Simpson's 1/3 rule [Hoffman, 1992] as:

$$p_M = \frac{1}{b} \int_{-\frac{b}{2}}^{\frac{b}{2}} p dx = \frac{1}{b} \left[\frac{1}{3} \Delta x (p_0 + 4p_1 + 2p_2 + 4p_3 + \dots + 4p_{n-1} + p_n) \right]. \quad (2-65)$$

where Δx and subscript n stand for the mesh size and the number of meshes, respectively. Then h_m is calculated again using Equation (2-51) and let this be h_{m2} . The two minimum film thicknesses, h_{m1} and h_{m2} , are compared to check if the Equations (2-51) and (2-56) are related correctly. This procedure is terminated when the periodic condition is satisfied, i.e., when:

$$|h_{m1} - h_{m2}| < \varepsilon \quad (2-66)$$

where ε is the convergence tolerance. If the solved h_m is less than the composite rms roughness, σ , it is assumed that the lubrication mode is boundary lubrication and h_m is equal to the composite rms roughness. In the case of hydrodynamic lubrication, friction force and power loss are calculated numerically by using Simpson's 1/3 rule.

2.2.3.3.8 Validation of the Model for the Piston Ring Lubrication

This model for the piston ring lubrication has been tested by simulating an internal combustion engine of 2000 rpm revolutionary speed. Its results have been compared to the results of [Jeng, 1992] and [Radakovic and Khonsari, 1997] who performed lubrication analysis for the same engine. Table 2.4 shows the values of the parameters of the piston ring and operating conditions for the simulated engine. Figures

2.25 and 2.26 illustrate the piston speed of the engine as a function of crank angle and the combustion pressure of the engine versus crank angle, respectively.

Figure 2.27 shows the minimum film thickness predicted by the models of Jeng and Radakovic and Khonsari. In the legend of the figure, 'current analysis' notation stands for the prediction by Radakovic and Khonsari and 'Y. R. Jeng' indicates the prediction by the model of Jeng. Figure 2.28 illustrates the power losses predicted by the model of Radakovic and Khonsari. They considered four kinds of lubricants in their analysis as shown in the legend of the figure. Among them 'Newtonian/Isothermal' curve is compared to the power loss predicted by this model because of the same characteristics of the lubricant simulated in this analysis.

Figures 2.29 and 2.30 show the predicted minimum film thickness and power loss by this model, respectively. As shown in the figures, in general, the trends and magnitude are very similar to those of Jeng, and Radakovic and Khonsari. The differences between exact magnitudes of the minimum film thickness and power loss seem to be due to the difference in the treatment of the piston ring and handling some parameters such as the pressure distribution under the piston ring. Jeng used a value for tangential ring tension to define the elastic deflection of the ring but the present analysis treats the piston ring as a thin ring subject to internal and external pressure which will deflect according to its elastic modulus. The present analysis assumes that the pressure in the divergence section of the gap is the same as the p_{bot} , pressure at the trailing edge of the ring. Jeng considered no pressure at all if a cavitation occurred under ring and Radakovic and Khonsari assumed that the pressure in the divergence section of the gap

was the same as the pressure at the throat (the minimum flow area). As mentioned before, however, the overall trends are in a good agreement.

2.2.3.4 Modeling for Thermodynamic Processes

There are three processes within one revolution of crankshaft: intake, expansion, and exhaust. As discussed in Chapter 3, the intake valve opens and the supercritical high pressure CO₂ flows into the cylinder and pushes the piston down from the Top Dead Center (TDC) to the location of expansion initiation (LOE) during the intake process. All valves close as the piston reaches the LOE and the expansion process starts with constant CO₂ mass. When the piston reaches the Bottom Dead Center (BDC), the exhaust valve opens and CO₂ is swept out as the piston moves up during the exhaust stroke. This exhaust process continues until the piston reaches TDC. The same processes are repeated during the next revolution of the crankshaft of the device. This calculation continues until the crank angle becomes 720° (two revolutions of the crankshaft).

2.2.3.4.1 Intake Process

The intake valve opens during the intake process and CO₂ flows into the chamber as shown in Figure 2.31. In the modeling of the intake process, the kinetic and potential energies are neglected and the thermodynamic properties are assumed to be uniform in the chamber. No heat transfer is assumed (adiabatic flow) but the power loss due to the friction and squeeze motion of the piston ring is considered as heat loss. The last

assumption in the intake model is that the pressure in the chamber is constant at each time step so that the work done by CO₂ [Wark, 1995] can be calculated as

$$W = - \int_{V_1}^{V_2} p dv = -p_1(V_2 - V_1) = -p_1 \Delta V. \quad (2-67)$$

2.2.3.4.2 Calculation Procedure

There are two steps for the calculation of mass flow rate and thermodynamic properties at each time step in this process. First, the mass flow rate is calculated by using the method in Section 2.2.3.2.1 with the pressure difference between upstream of the intake valve and chamber. In this calculation the piston does not move i.e., $V_1 = \text{constant}$. The amount of CO₂ flowing into the chamber becomes

$$m_{in} = \dot{m}_{in} \cdot \Delta t. \quad (2-68)$$

In the second step, the piston moves down with the new mass in the chamber ($m = \text{constant}$) for the given Δt and V_2 is determined. Then, after calculating the work done by the carbon dioxide by using Equation (2-67) and power loss by using Equation (2-62) or (2-63), the thermodynamic properties are determined. If the predicted pressure is higher than or equal to that upstream of the valve ($p_2 \geq p_{in}$), the pressure in the chamber is assumed to be the same as the inlet pressure and constant during the rest of intake process.

2.2.3.4.3 Determination of Thermodynamic Properties

When the pressure in the chamber is lower than the inlet pressure, the 1st law of thermodynamics is expressed as:

$$\frac{dE_{cv}}{dt} = \dot{Q} + \dot{W} + \dot{m}_{in}h_{in}. \quad (2-69)$$

The above equation can be written by multiplying both of the left hand side (LHS) and right hand side (RHS) of the equation by dt as:

$$\Delta E = \Delta U = m_2u_2 - m_1u_1 = -P + W + m_{in}h_{in} \quad (2-70)$$

where the subscripts '1', '2', and 'in' represent the states before and after the piston movement, and inlet state, respectively. m_{in} , P , and W stand for the mass flowed into the chamber, power loss, and work done by CO₂, respectively. The specific internal energy and density of CO₂ at state '2' can be obtained as:

$$u_2 = \frac{1}{m_2} [m_1u_1 - P + W + m_{in}h_{in}] \text{ and} \quad (2-71)$$

$$\rho_2 = \frac{m_2}{V_2}. \quad (2-72)$$

The pressure and temperature in the case of single-phase or the pressure and quality in the case of two-phase are determined by using the thermodynamic property data [Span and Wagner, 1996] for CO₂ with Equations (2-71) and (2-72).

When the pressure in the chamber becomes equal to the inlet pressure, the method in Section 2.2.3.2.1 can't be applied to predict the amount of mass flowed into the chamber because the pressure in the chamber is assumed to be constant and there is no pressure difference between the upstream of the intake valve and the chamber during the rest of the intake process. The 1st law of thermodynamics in this case is

$$\Delta U = m_2 u_2 - m_1 u_1 = -P + W + (m_2 - m_1) h_{in}. \quad (2-73)$$

Unknowns are m_2 and u_2 in Equation (2-73) but m_2 can be expressed as:

$$m_2 = V_2 \rho_2. \quad (2-74)$$

The Secant method is used to find the temperature that is satisfied with u_2 and ρ_2 for the given constant pressure ($p_2 = p_{in} = \text{constant}$). Let's define a function $F(T)$ from Equation (2-73) as follows:

$$F(T) = V_2 \rho_2(T) [u_2(T) - h_{in}] - [m_1 (u_1 - h_{in}) - P + W] = 0 \quad (2-75)$$

where T stands for temperature and the unknown variable is temperature. The slope of the secant passing through two points is

$$F'(T_n) = \frac{F(T_n) - F(T_{n-1})}{T_n - T_{n-1}} = \frac{F(T_{n+1}) - F(T_n)}{T_{n+1} - T_n} = \frac{-F(T_n)}{T_{n+1} - T_n} \quad (2-76)$$

where subscripts n and $n+1$ represent the iteration steps and $F(T_{n+1})$ is the same as $F(\alpha)$. α is the solution of the above equation and $F(T_{n+1})$ becomes zero by the definition of the function. Hence, the temperature at $n+1$ iteration step is

$$T_{n+1} = T_n - \frac{F(T_n)}{F'(T_n)}. \quad (2-77)$$

This calculation procedure is repeated until the convergence tolerance is satisfied as follows:

$$|T_{n+1} - T_n| < \varepsilon. \quad (2-78)$$

2.2.3.4.4 Expansion Process

All the solenoid valves close during the expansion process so that mass is constant but volume increases in the chamber as shown in Figure 2.32. The pressure and temperature are changed due to the volume increase and some energy losses. As done in the intake process, the thermodynamic properties are predicted by considering power loss as well as volume increase. No heat transfer is assumed (adiabatic flow) but the power loss is considered as heat loss. The pressure is assumed to be constant in the chamber at each time step so that the work done by CO₂ can be calculated by using Equation (2-67).

The 1st law of thermodynamics in this case is

$$\frac{dE_{cv}}{dt} = \dot{Q} + \dot{W} . \quad (2-79)$$

By multiplying both of the LHS and RHS of the equation by dt , the above equation can be written as:

$$m(u_2 - u_1) = -P + W \quad (2-80)$$

where m is the CO₂ mass in the chamber. Unknown variable is only u_2 and it can be expressed as:

$$u_2 = u_1 + \frac{-P + W}{m} . \quad (2-81)$$

The density of CO₂ at state '2' becomes

$$\rho_2 = \frac{m}{V_2} . \quad (2-82)$$

The pressure and temperature (in the case of single-phase) or pressure and quality (in the case of two-phase) at state '2' are determined with the specific internal energy and density. The bisection method is used to find them.

2.2.3.4.5 Exhaust Process

The exhaust valve opens during the exhaust period and mass of CO₂ is discharged to the inlet to the evaporator as shown in Figure 2.33. The state of CO₂ is two-phase in this process and the mass flow rate is calculated by using the method in Section 2.2.3.2.4. The assumptions are the same as in the intake process. The kinetic and potential energies are neglected. Even though the process is an adiabatic flow, the power loss is considered as heat loss. The pressure is assumed to be constant at each time step so that the work done by CO₂ is calculated by Equation (2-67). Additional assumptions are that the flow is quasi-steady-state and homogeneous.

There are two steps for the calculation of mass flow rate and thermodynamic properties at each time step like in the intake process. In the first step, the mass amount flowed out from the chamber is calculated with the pressure difference between the chamber and downstream of the exhaust valve. There is no piston movement at this time, i.e., $V_1 = \text{constant}$. The amount of CO₂ flowed out from the chamber becomes

$$m_{out} = \dot{m}_{out} \cdot \Delta t. \quad (2-83)$$

Then, the piston moves up and the volume of the chamber decreases with the new mass of CO₂ in the second step.

The thermodynamic properties are calculated with new specific internal energy and density by using the bisection method. The 1st law of thermodynamics in this case is

$$\frac{dE_{cv}}{dt} = \dot{Q} + \dot{W} - \dot{m}_{out} h_{out}. \quad (2-84)$$

After some mathematical manipulations with thermodynamic definitions, the above equation can be written as:

$$u_2 = \frac{1}{m_2} (m_1 u_1 - P + W - m_{out} h_{out}) \quad (2-85)$$

and the density becomes $\rho_2 = \frac{m_2}{V_2}$. Then the pressure and quality of the CO₂ are found by using the bisection method.

2.2.3.4.6 Total Power Loss and Net Work Output

Total power loss for one revolution or during unit time scale can be obtained by summing the power loss at each time step as follow:

$$P_{tot} = \sum P. \quad (2-86)$$

Net work output is also obtained by adding the work at each time step as:

$$W_{net} = \sum_{intake} W + \sum_{expansion} W + \sum_{exhaust} W. \quad (2-87)$$

During the intake and expansion processes, the work is generated by CO₂ but during the exhaust process, the work is needed to sweep out the CO₂ from the chamber to the inlet to the evaporator.

2.3 Experiments for Cycle with ED-WOW Device

To evaluate the effects on system performance the prototype expansion device was installed in a working transcritical CO₂ refrigeration cycle. Figure 2.34 shows a schematic of the CO₂ based environment control unit (ECU) of a unit designed for the United States Army [Li and Groll, 2001]. This system was built to test a carbon dioxide based air-to-air breadboard system. The ED-WOW will be incorporated into this

experimental setup after modification. Figure 2.35 illustrates the schematic of the test setup with the expansion device. As shown in this figure, the ED-WOW does not replace the expansion valve entirely. Depending on the final capacity of the prototype expander, a portion of total working fluid may be bypassed through a normal expansion valve.

2.3.1 Description of Testing Procedure

Carbon dioxide is pressurized by a compressor, achieving a supercritical state at the outlet of the compressor. Heat is removed through the gas cooler to the atmosphere and the thermodynamic properties of carbon dioxide change from 'vapor like' to 'liquid like' fluid. Then, CO_2 expands through the ED-WOW from high pressure to low pressure and work is produced during this process. The bypass valve allows a portion of the flow to pass through an ordinary expansion valve. The carbon dioxide becomes two-phase at the outlet of the ED-WOW. Heat is then transferred to the CO_2 through the evaporator and it becomes saturated or superheated vapor at the outlet of the evaporator.

The system of Figure 2.35 is installed in two temperature and humidity controlled psychrometric rooms so that independent control of the indoor and outdoor environment can be achieved. The gas cooler is located in the outdoor psychrometric room and the other parts of the system in the indoor psychrometric room.

To provide a load to absorb extracted work, a hydraulic pump with water as the working fluid is connected to the output shaft of the ED-WOW device. The revolutionary speed of the ED-WOW is controlled by increasing or decreasing the load of the hydraulic pump, and the work produced by the ED-WOW is measured indirectly by measuring the performance of the hydraulic pump. Figure 2.36 shows the schematic of

the connection of the hydraulic pump system to the ED-WOW. Static pressures are measured before and after the pump, and the volumetric flow rate of the water (the working fluid) is measured using a rotameter. The ideal pump work is then calculated using the pressure difference across the pump and the water flow rate, as well as the pump efficiency. As discussed above, this hydraulic pump work will be used to measure the work produced through the ED-WOW with the efficiency of the pump.

Table 2.1: Operating conditions for a typical expansion device in the transcritical CO₂ cycle.

Parameter	Operating value
High-side pressure, p_{high}	10.2MPa
High-side temperature, T_{high}	49°C
Low-side pressure, p_{low}	3.4MPa
Low-side temperature, T_{low}	Saturation temperature at 3.4MPa.
CO ₂ flow rate	0.04kg/s

Table 2.2: Loss coefficients for gradual contractions: Round and rectangular ducts
[Fox and McDonald, 1992].

$\frac{A_2}{A_1}$	Included angle, θ , degree						
	10	15-40	50-60	90	120	150	180
0.50	0.05	0.05	0.06	0.12	0.18	0.24	0.26
0.25	0.05	0.04	0.07	0.17	0.27	0.35	0.41
0.10	0.05	0.05	0.08	0.19	0.29	0.37	0.43

Note: Coefficients are based on $h_{lm} = K \frac{\bar{v}_2^2}{2}$. Subscript 2 stands for small pipe.

Table 2.3: Relation between the coefficient of contraction C_c and area ratio σ [Collier, 1972].

$\frac{1}{\sigma}$	0	0.2	0.4	0.6	0.8	1.0
C_c	0.586	0.598	0.625	0.686	0.790	1.0
$\left(\frac{1}{C_c} - 1\right)^2$	0.5	0.45	0.36	0.21	0.07	0

Table 2.4: Relevant engine parameters.

Parameters used by Jeng, and Radakovic and Khonsari	Values	Unit
Engine speed	$S = 2000$	rpm
Cylinder bore	$B = 88.9$	mm
Bore radius	$r = 44.45$	mm
Crank radius	$R = 40.0$	mm
Connecting rod length	$L = 141.9$	mm
Composite roughness	$\sigma = 0.5$	μm
Piston ring width	$b = 1.475$	mm
Ring thickness	$t_r = 3.8$	mm
Ring modulus	$E = 70.0$	GN/m^2
Ring crown height	$C_R = 14.9$	μm
Friction coefficient	$f = 0.08$	-
Lubricant viscosity	$\mu = 0.00689$	$\text{Pa} \cdot \text{s}$
Tangential ring tension	$T = 22.38$	N

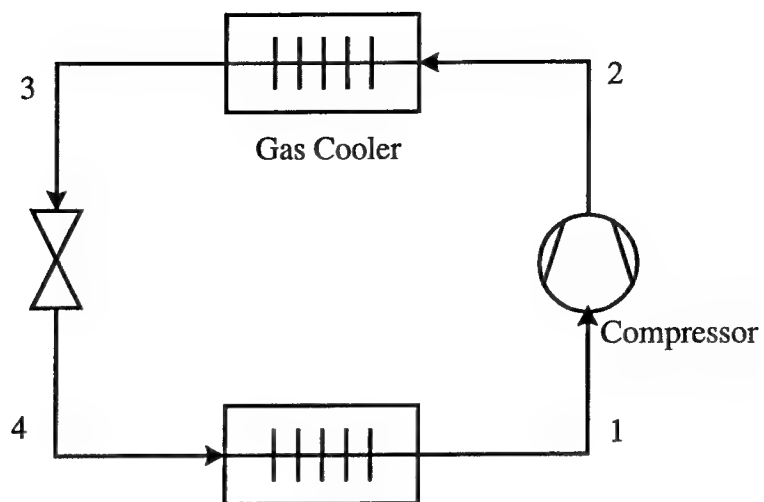


Figure 2.1: Basic transcritical CO₂ cycle (Base cycle) – Case 1.

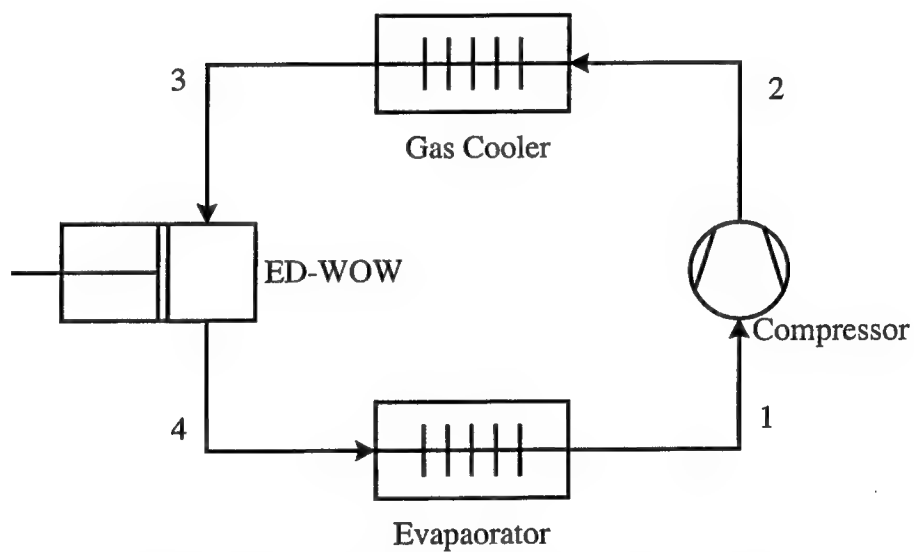


Figure 2.2: Base cycle with ED-WOW – Case 2.

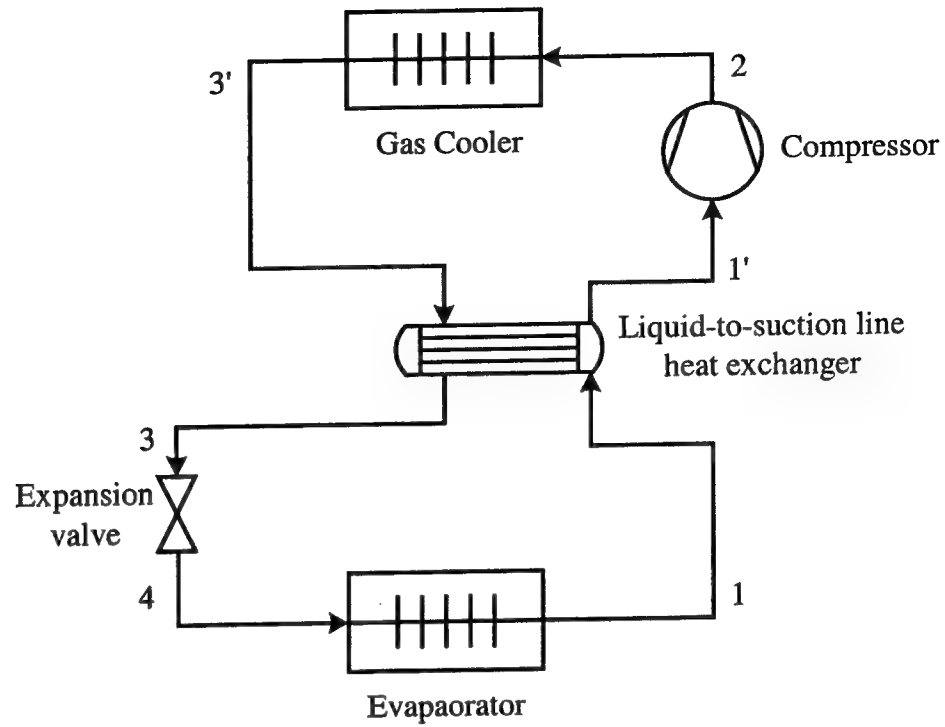


Figure 2.3: Base cycle with internal heat exchanger (IHX cycle) – Case 3.

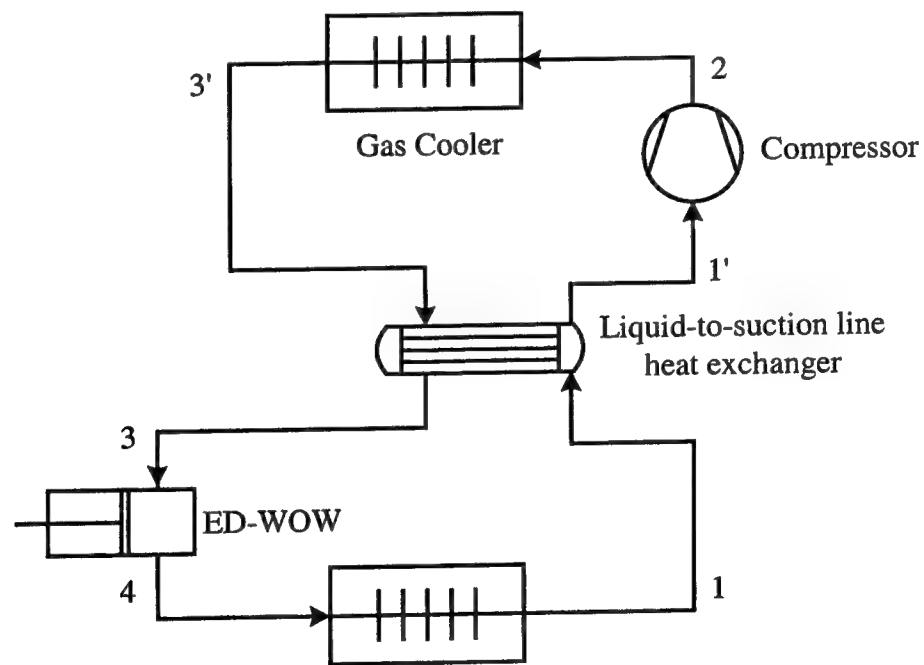


Figure 2.4: IHX cycle with ED-WOW – Case 4.

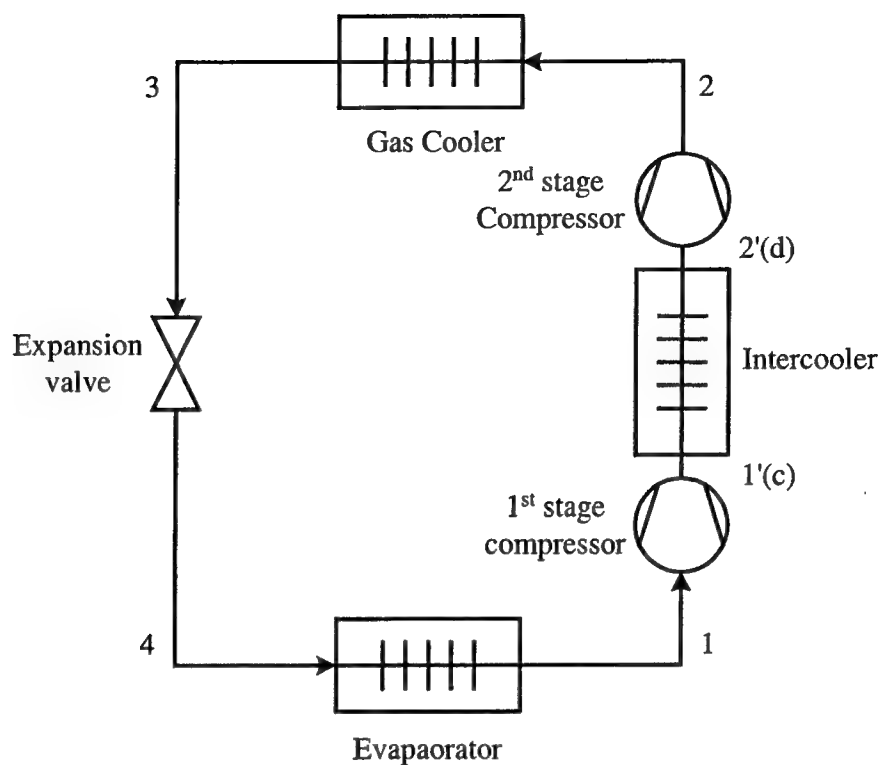


Figure 2.5: Intercooler cycle – Case 5 and Case 8.

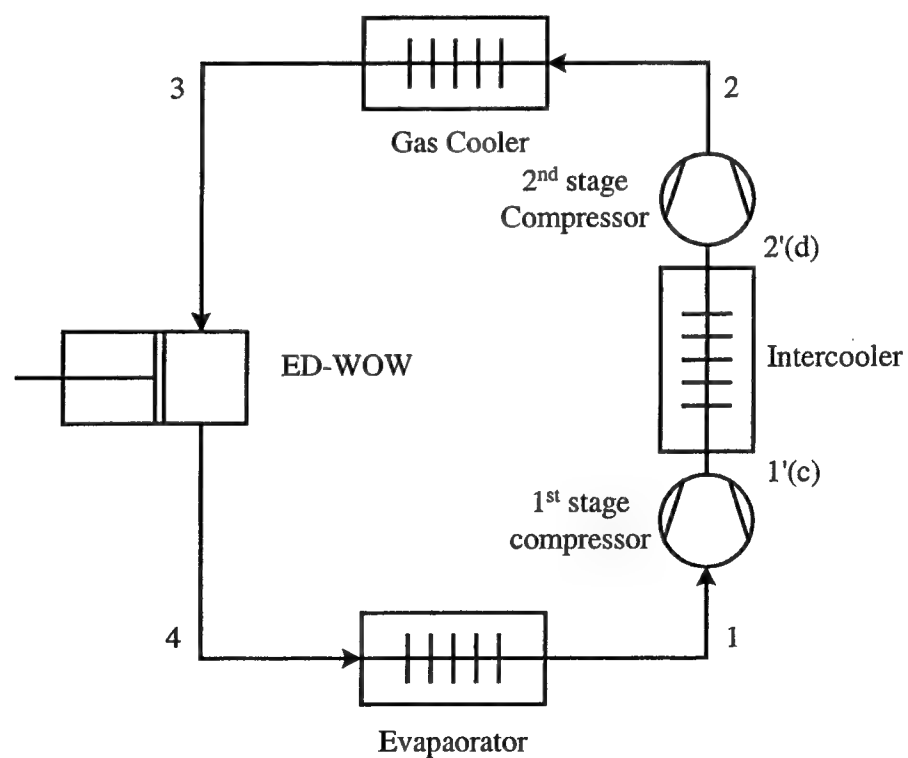


Figure 2.6: Intercooler cycle with ED-WOW – Case 6 and Case 9.

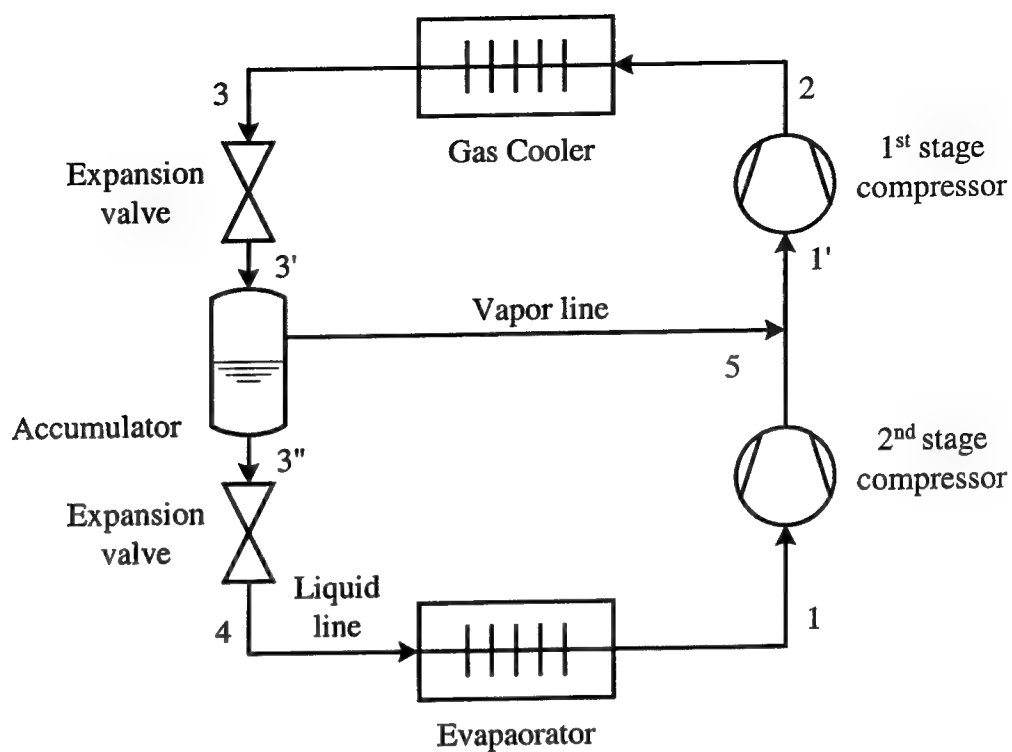


Figure 2.7: Economizer cycle – Case 7 and Case 10.

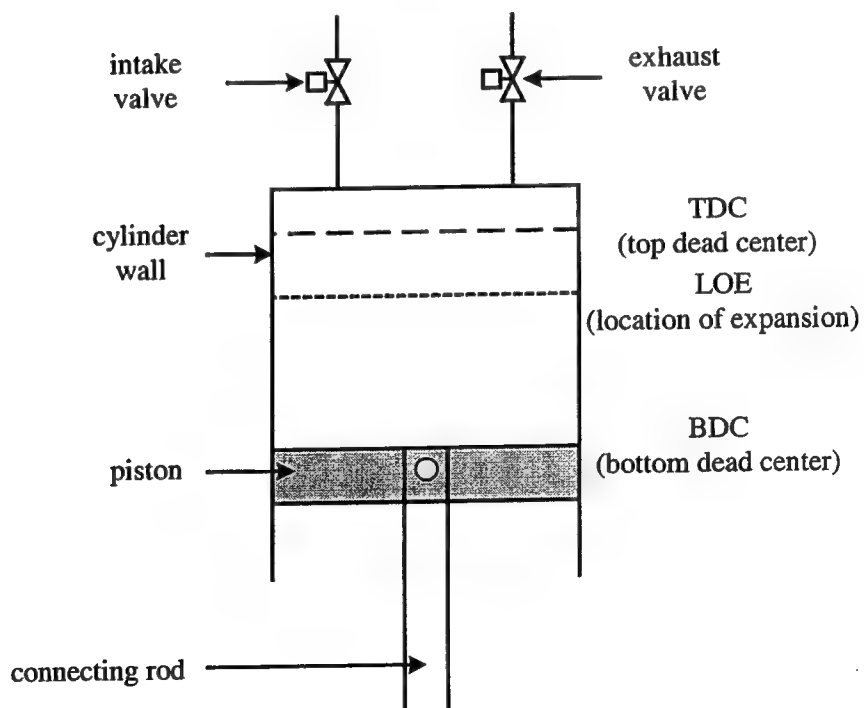


Figure 2.8: Piston-cylinder device with the related components and piston positions.

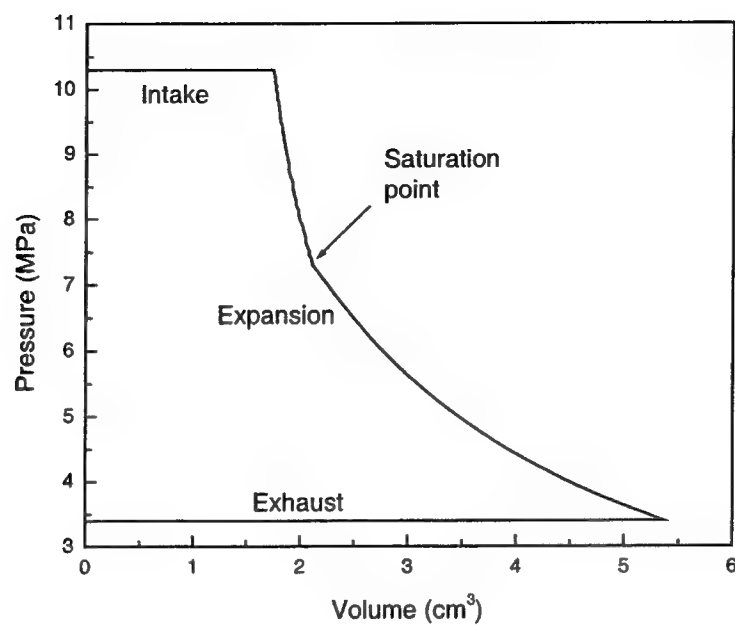


Figure 2.9: Piston processes with assumption of ideal process.

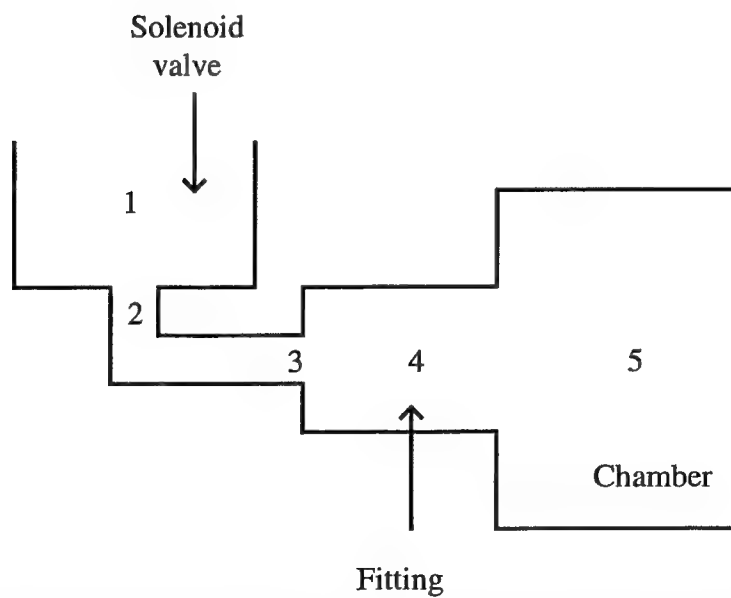


Figure 2.10: Schematic of connection of the solenoid valve to the fitting and cylinder chamber.

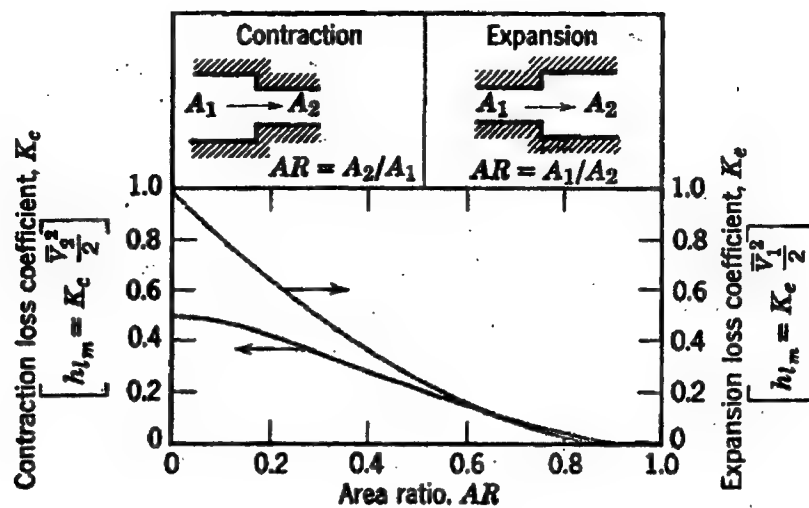


Figure 2.11: Loss coefficients for flow through sudden area changes [Fox and McDonald, 1992].

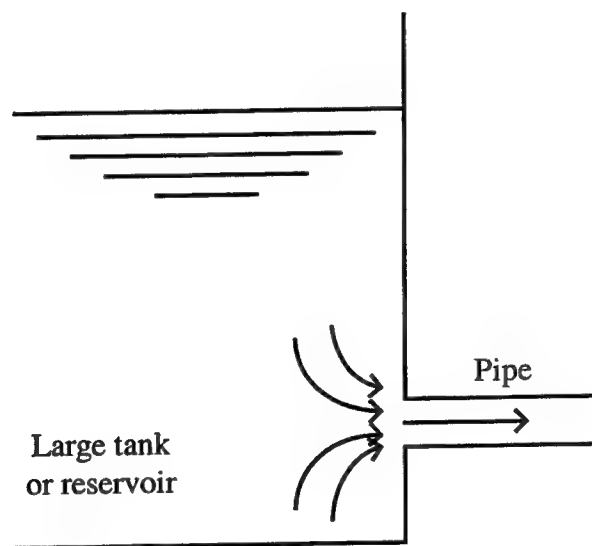


Figure 2.12: Entrance loss.

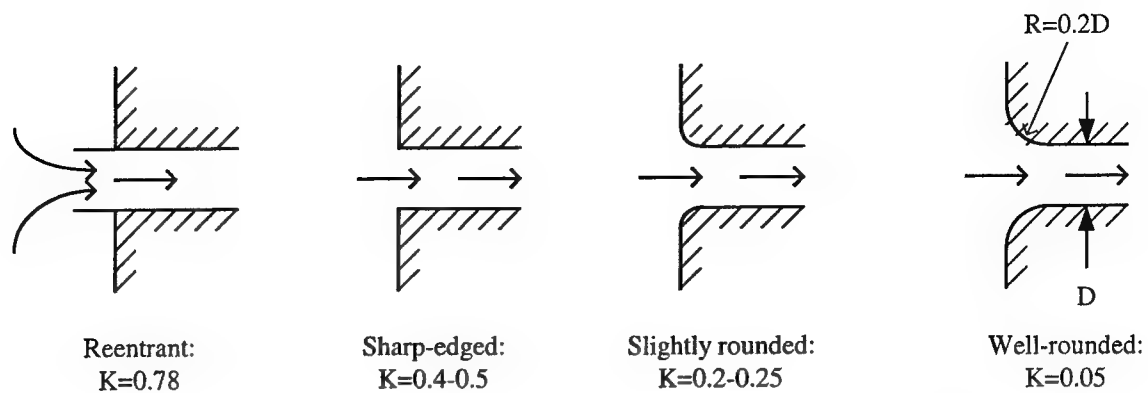


Figure 2.13: Entrance loss coefficients [Evvett and Liu, 1987].

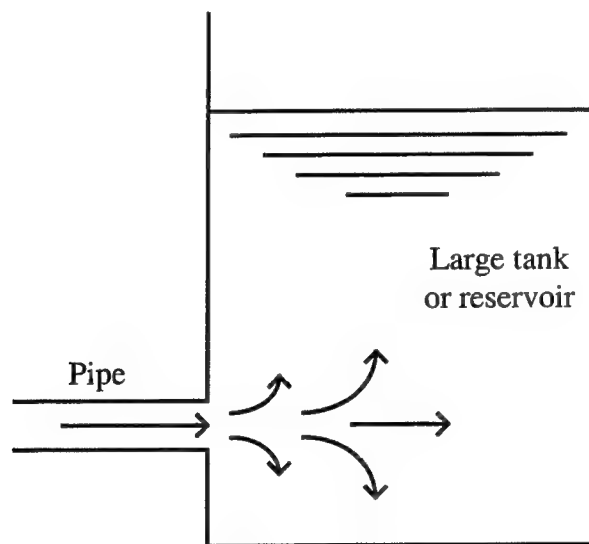


Figure 2.14: Exit loss.

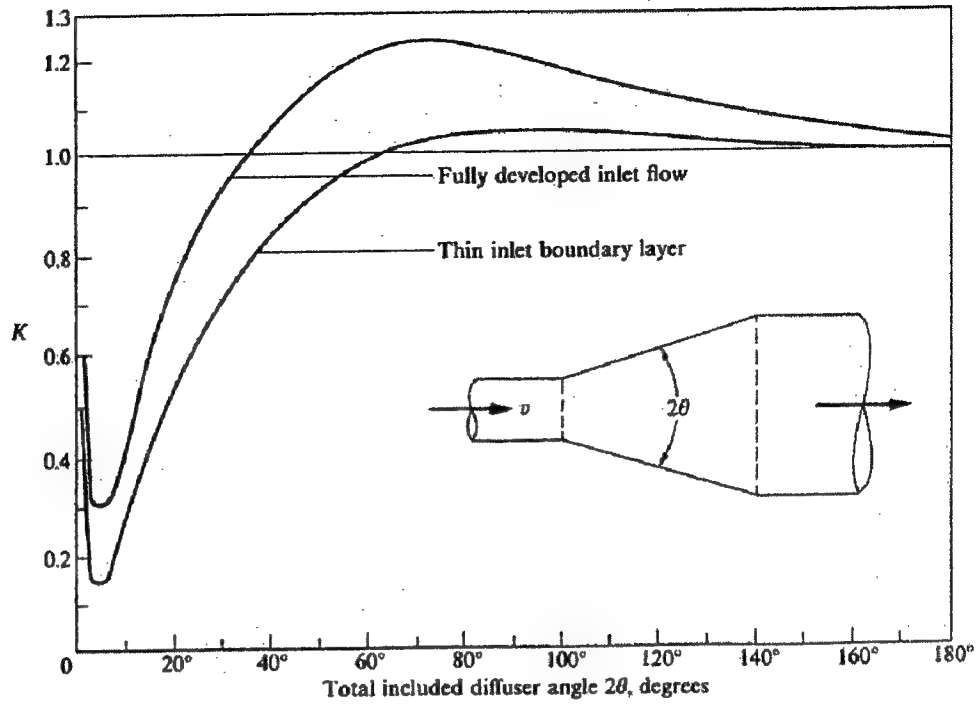


Figure 2.15: Flow losses in a gradual conical expansion region [Evetts and Liu, 1987]. Note that the loss is based on velocity head in the small pipe.

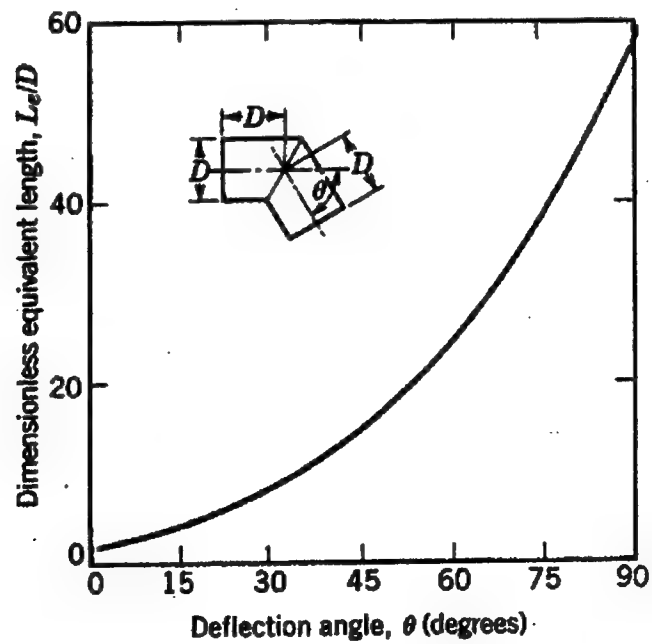


Figure 2.16: Representative total resistance (L_e/D) for miter bends [Fox and McDonald, 1992].

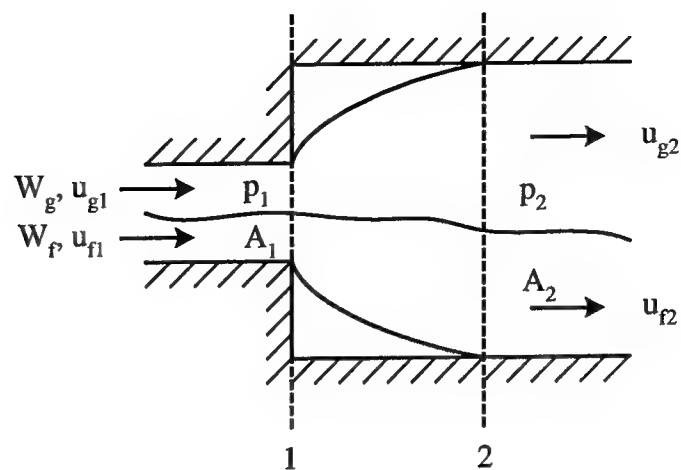


Figure 2.17: Sudden enlargement in two-phase flow.

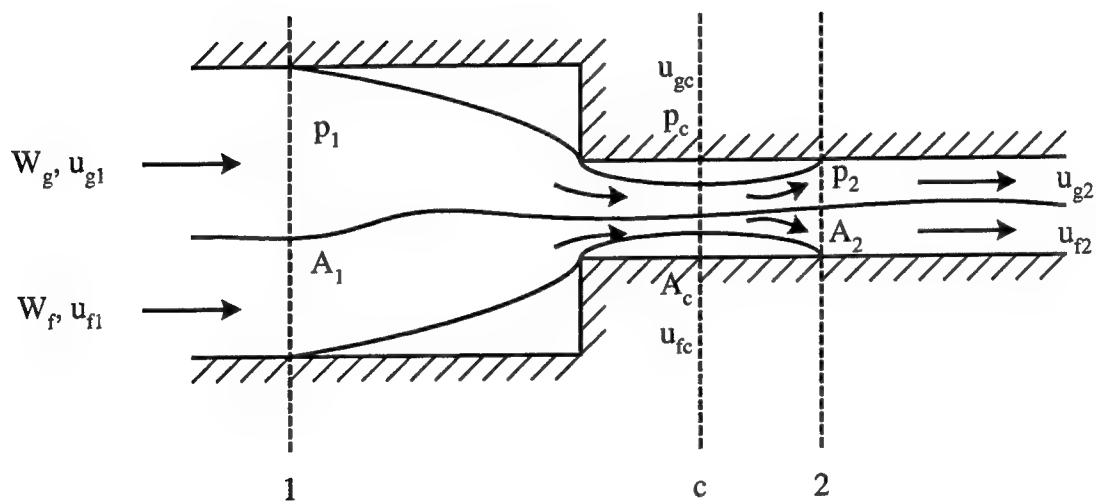


Figure 2.18: Sudden contraction in two-phase flow.

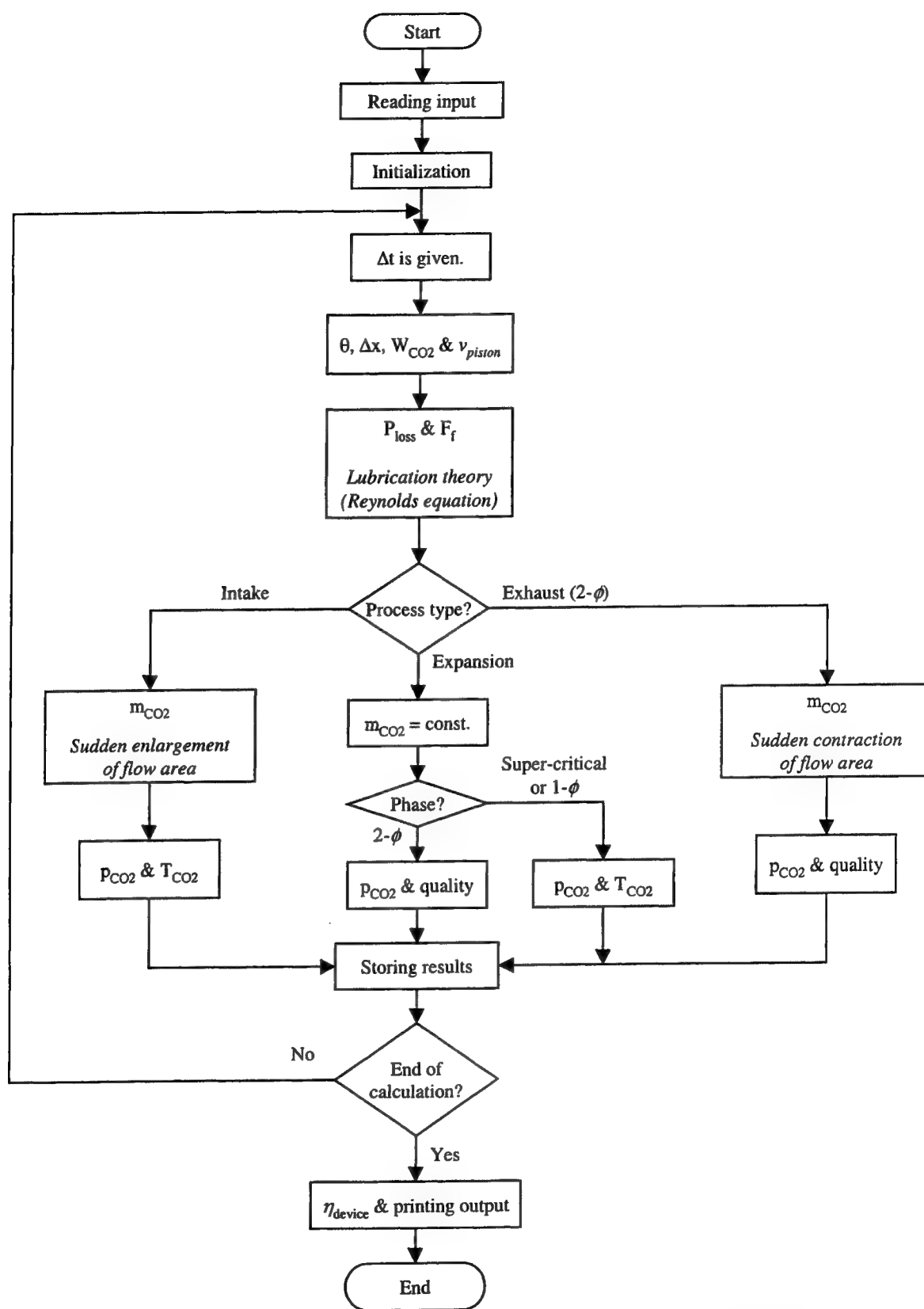
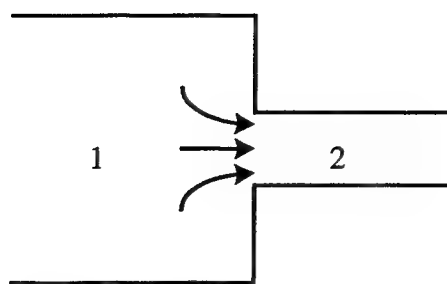
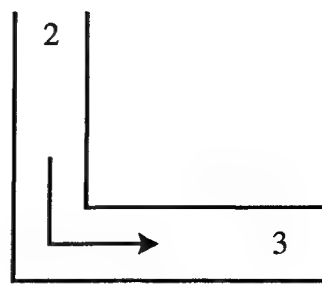


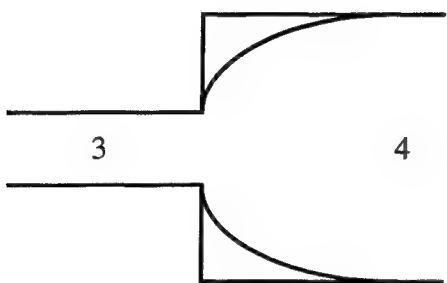
Figure 2.19: Flow diameter of the computer program modeling.



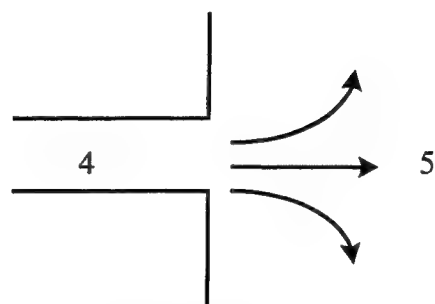
(a) Sudden contraction



(b) Miter bend



(c) Sudden enlargement



(d) Exit loss

Figure 2.20: Pressure losses.

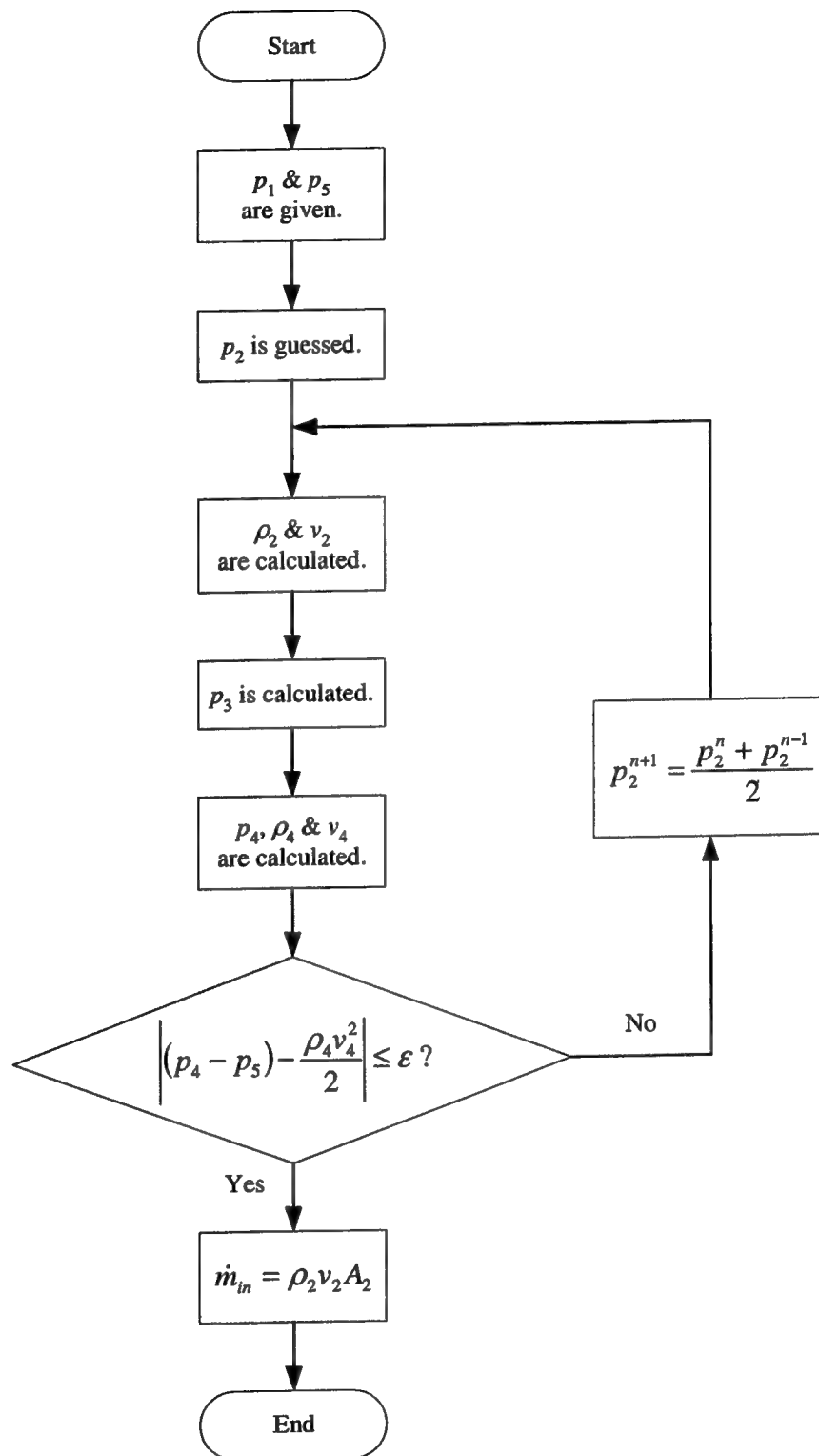


Figure 2.21: Flow diagram for calculation of mass flow into the chamber.

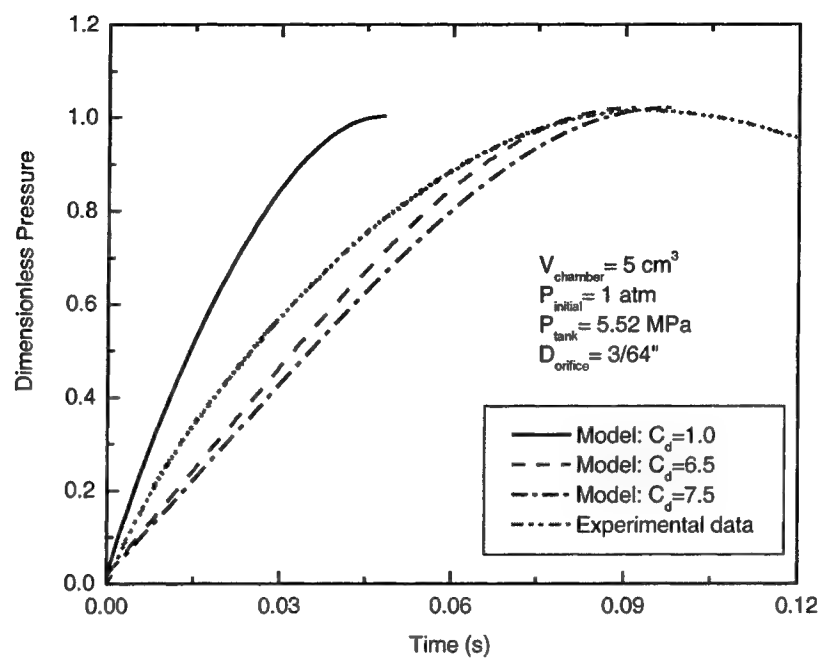


Figure 2.22: Determination of discharge coefficient for sudden contraction.

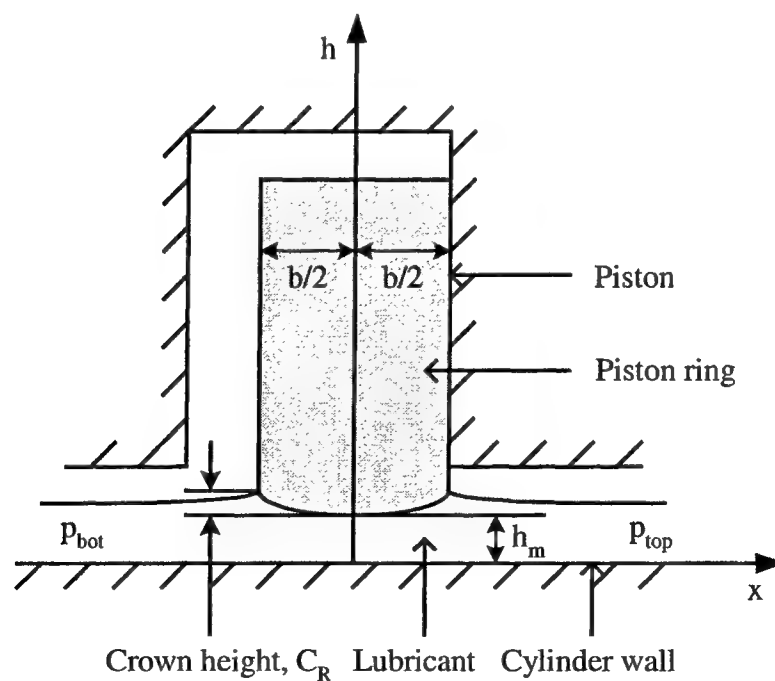


Figure 2.23: Piston ring geometry.

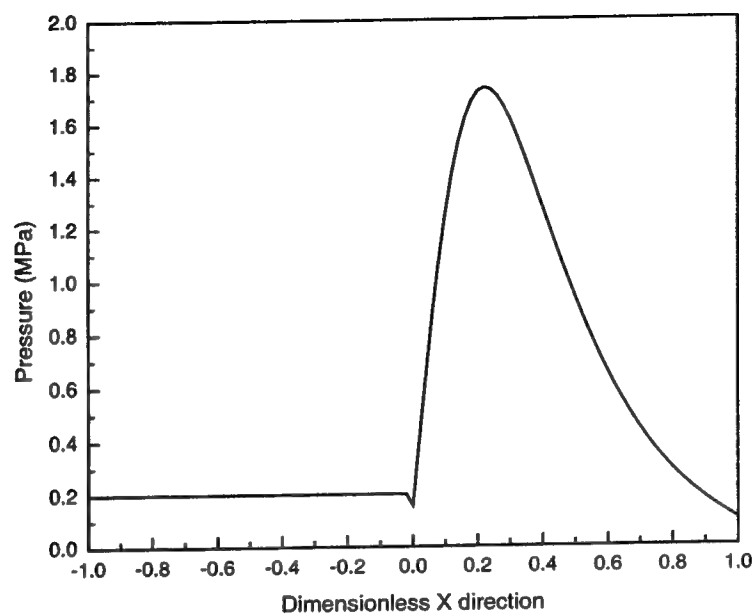


Figure 2.24: Pressure distribution under the piston ring during the intake and expansion stroke.

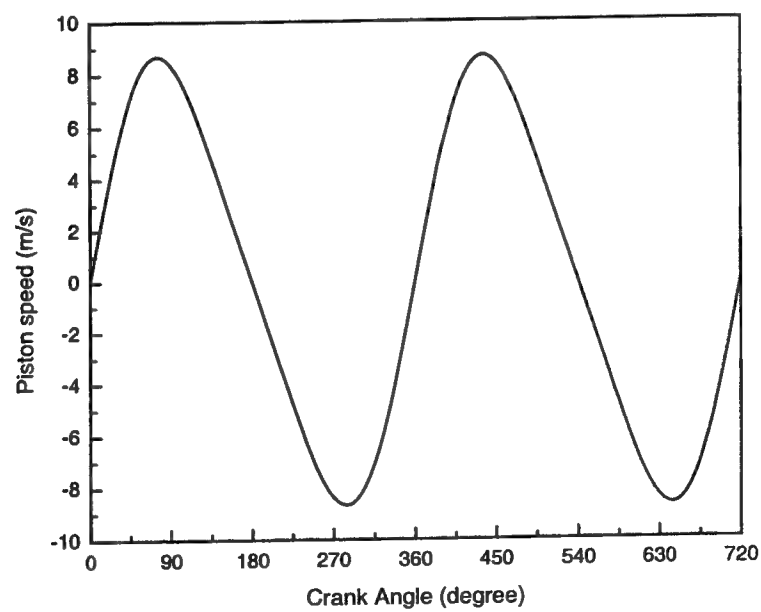


Figure 2.25: Piston speed versus crank angle for 2000 rpm engine speed.

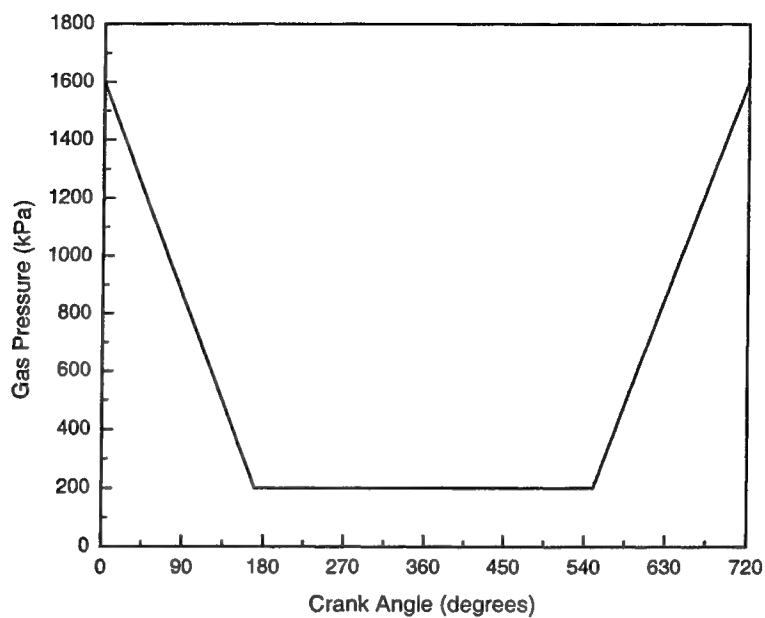


Figure 2.26: Combustion chamber pressure versus crank angle.

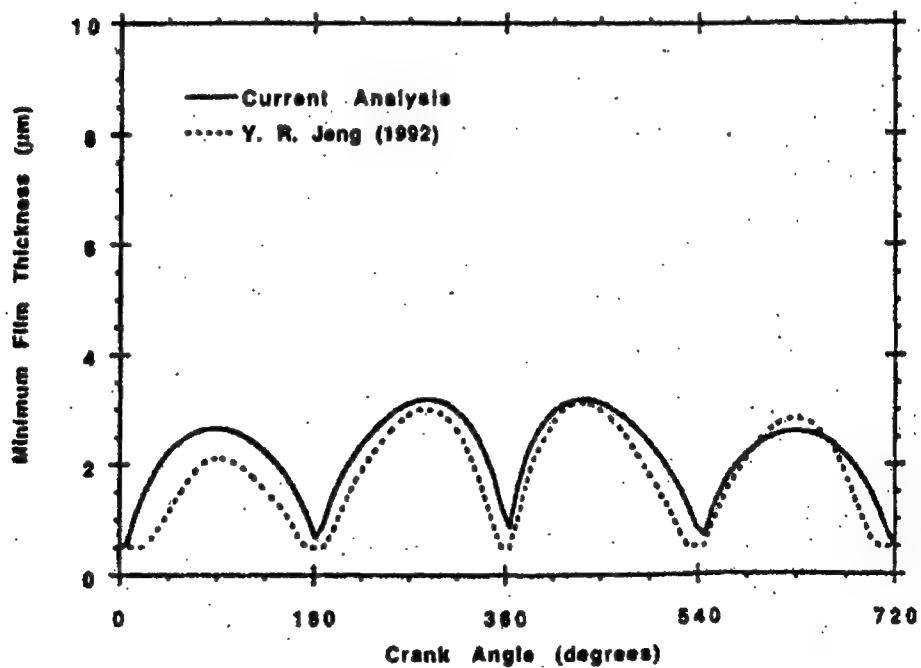


Figure 2.27: Minimum film thickness predicted by models of Jeng and Radkovic and Khonsari [Radkovic and Khonsari, 1997].

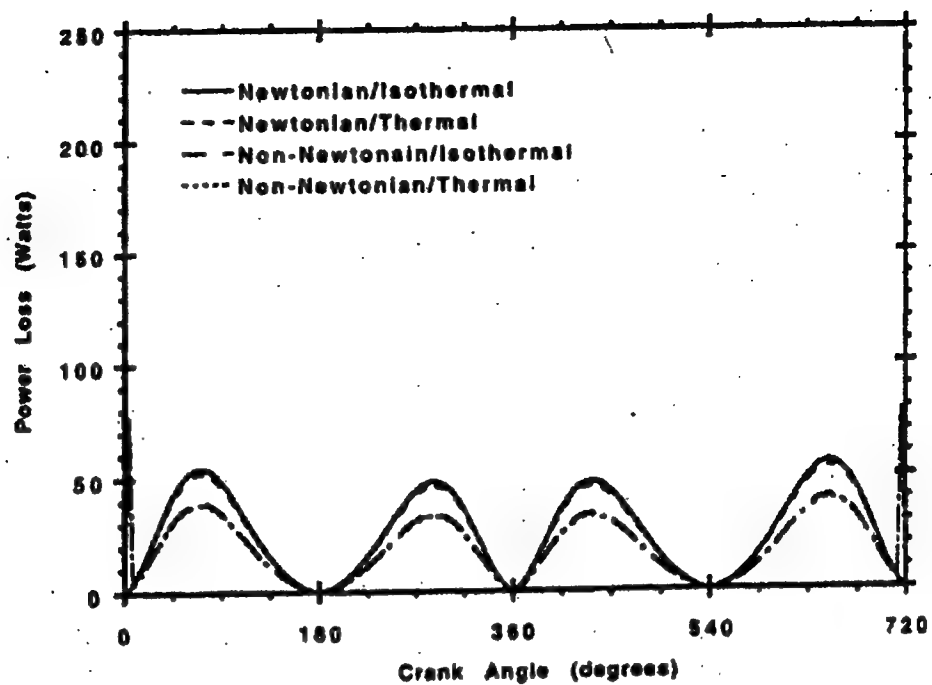


Figure 2.28: Power losses predicted by model of Radkovic and Khonsari [Radkovic and Khonsari, 1997].

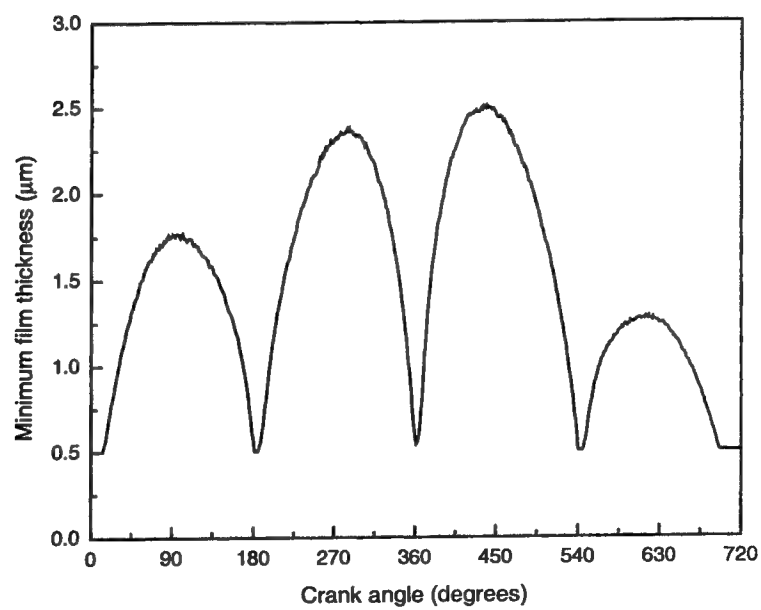


Figure 2.29: Minimum film thickness versus crank angle.

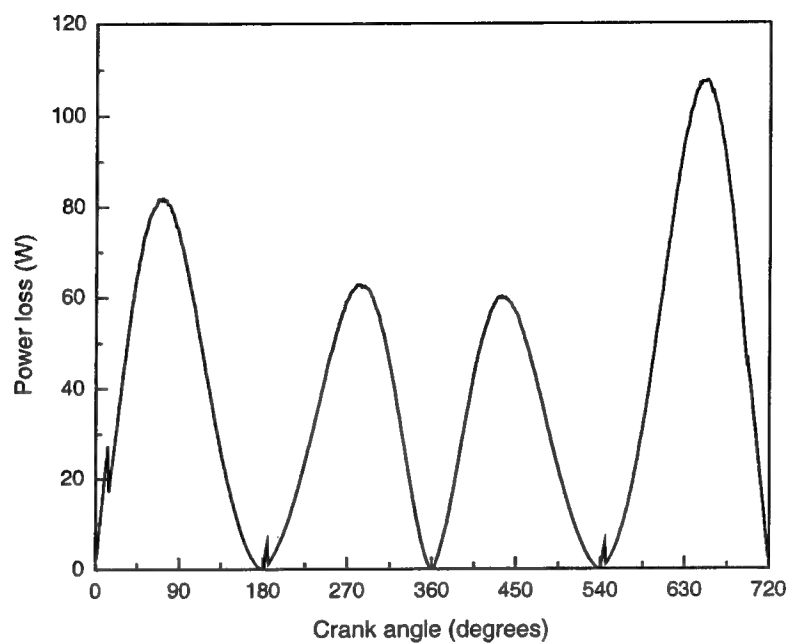


Figure 2.30: Power loss versus crank angle.

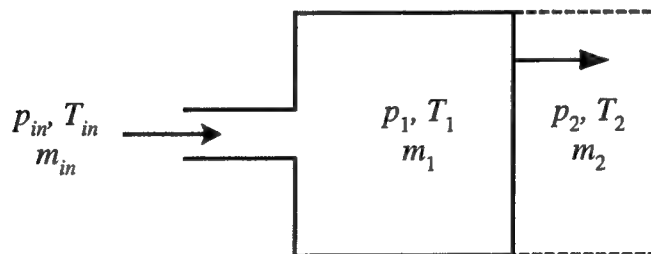


Figure 2.31: Intake process.

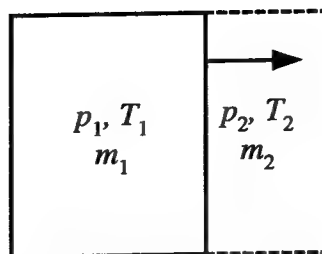


Figure 2.32: Expansion process.

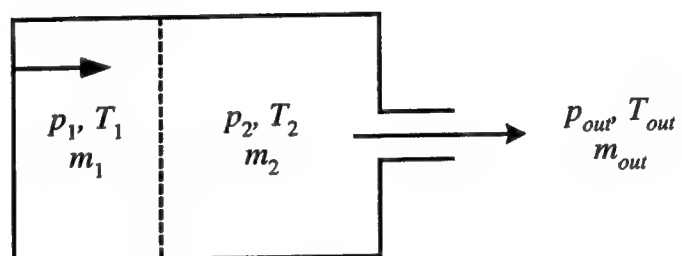
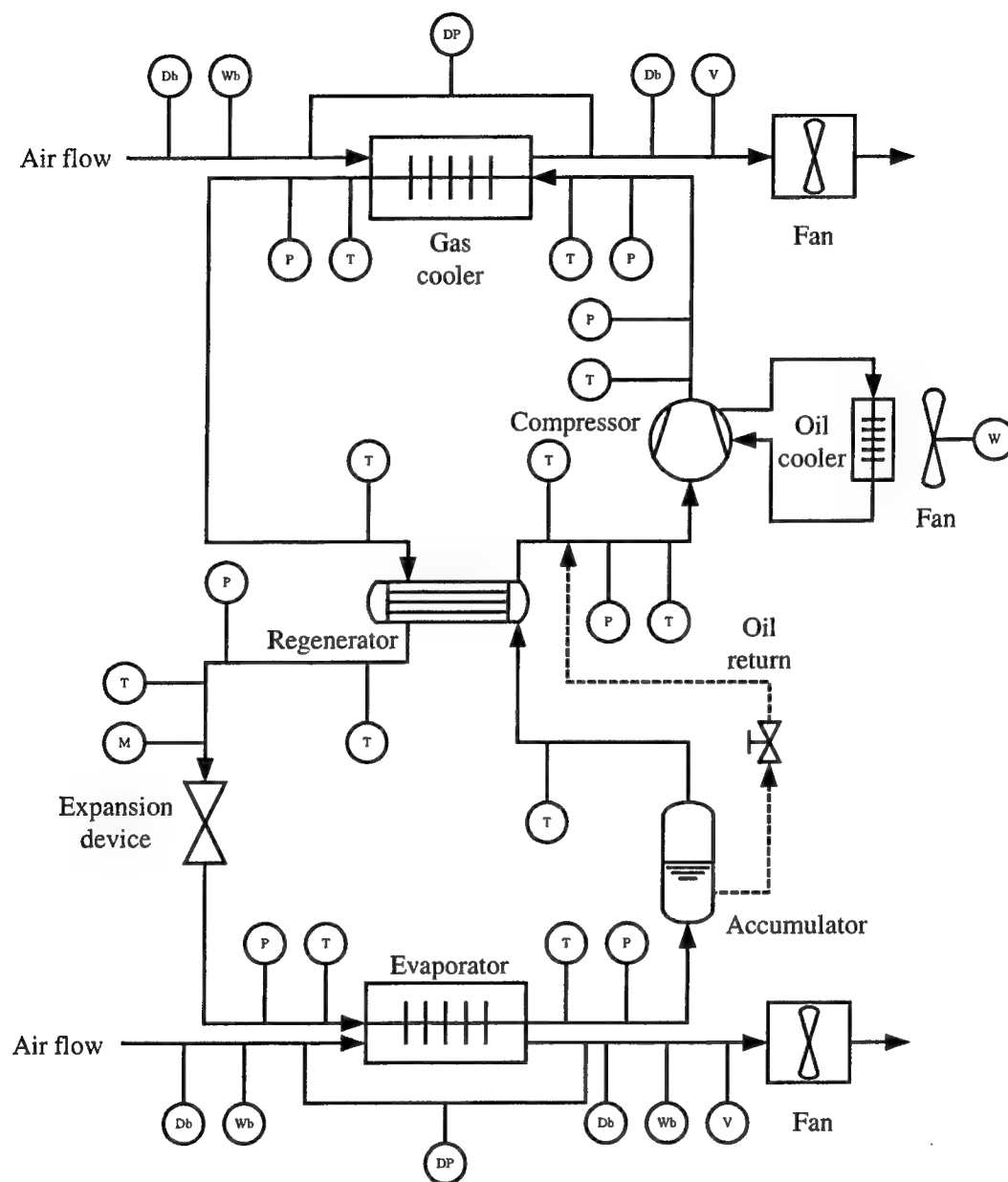
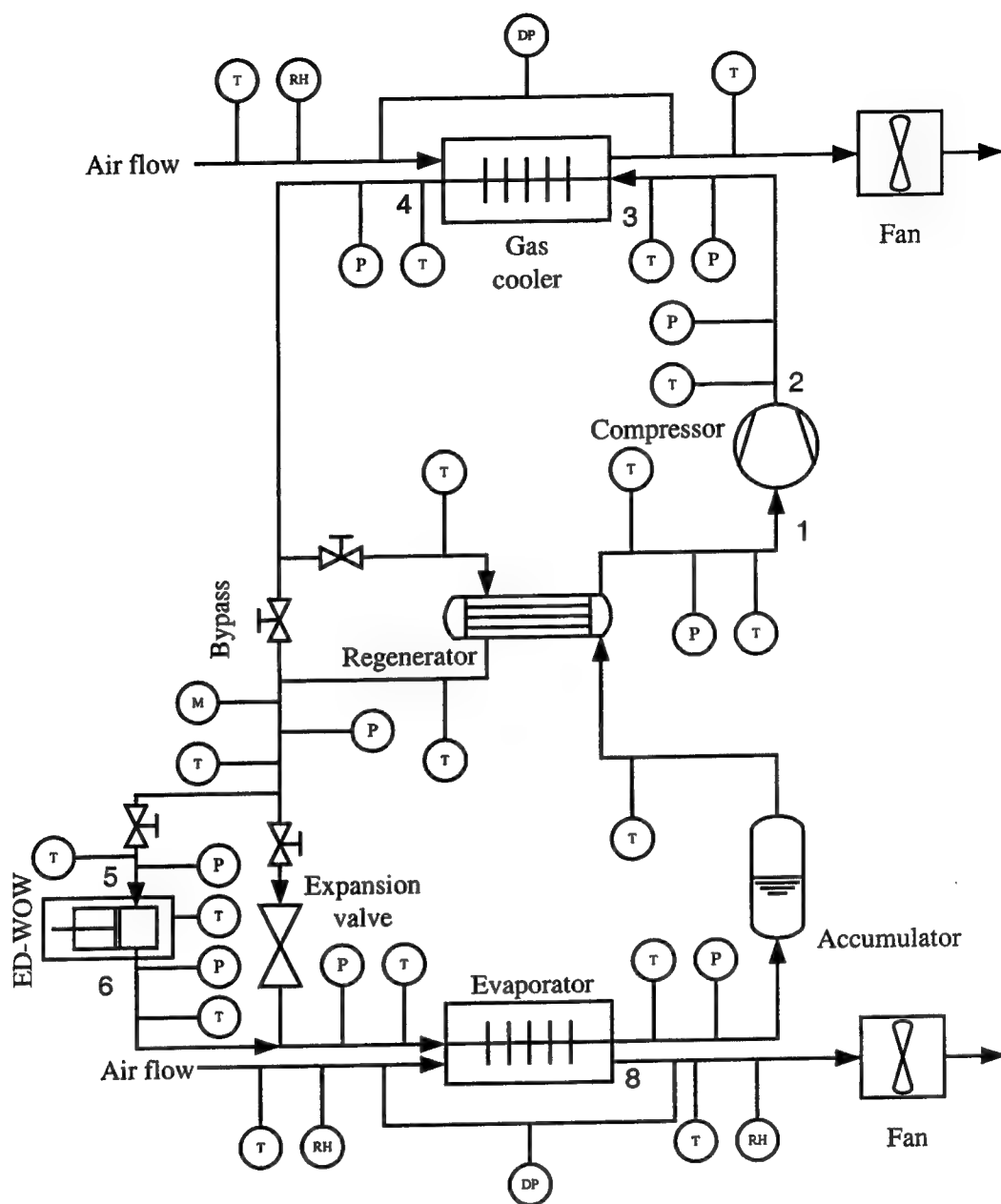


Figure 2.33: Exhaust process.



Legend of sensors : T-temperature, P-pressure, V-volumetric flow rate, M-mass flow rate, Db-dry bulb temperature, Wb-wet bulb temperature, W-power, DP-differential pressure.

Figure 2.34: Schematic of CO₂ based ECU test setup.



Legend of sensors : T-temperature, P-pressure, M-mass flow rate, W-power, DP-differential pressure.

Figure 2.35: Schematic of experimental setup for transcritical CO₂ cycle with ED-WOW.

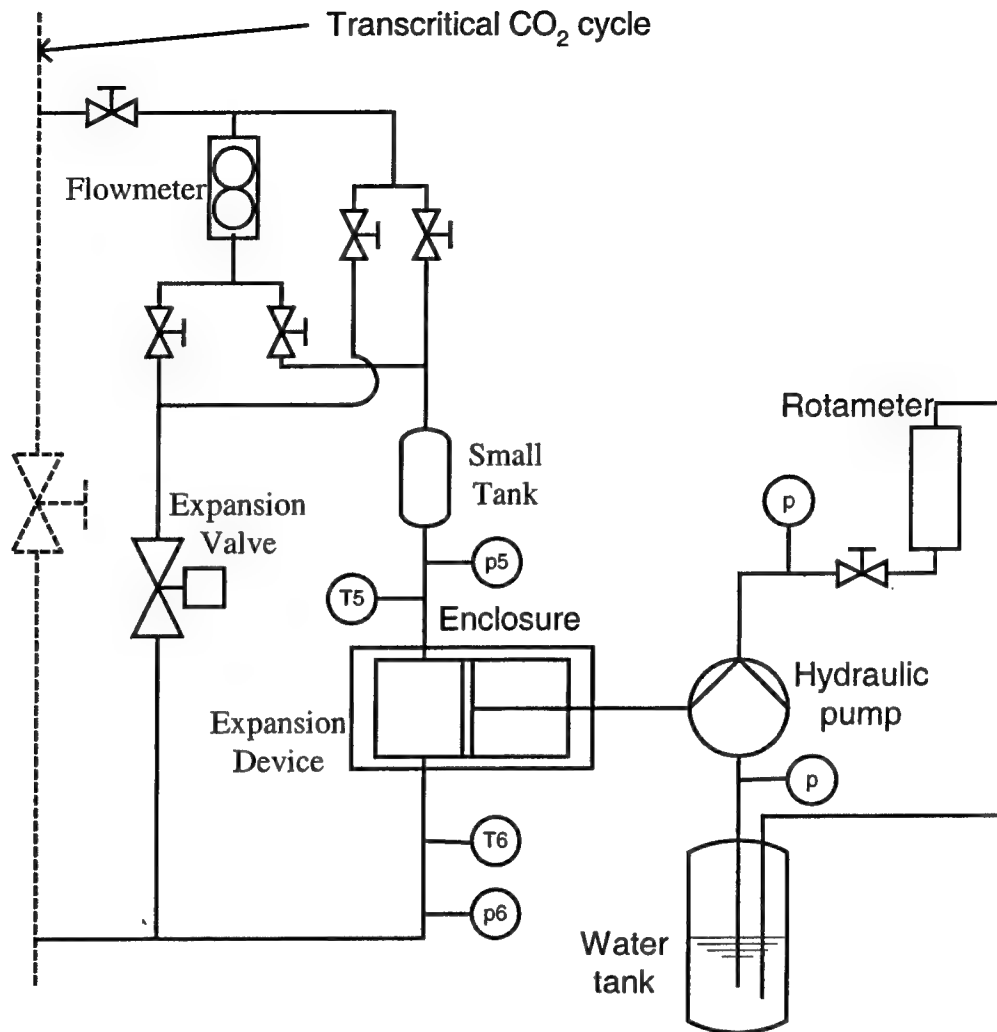


Figure 2.36: Schematic of the connection of the hydraulic pump system to the expansion device producing work.

3 DESIGN OF ED-WOW EXPANSION DEVICE

As discussed in Chapter 2, a piston-cylinder assembly device was chosen as the appropriate expansion device for the prototype application. A representative expansion device was designed and fabricated. The parameters for a typical expansion device for prototype transcritical CO₂ cycle are given in Table 2.1.

The details of the design of the expansion device with output of work (ED-WOW) are given in this chapter. The basic design is based on a piston expander controlled by electrically actuated valves. The crankshaft of the piston expander is connected to a mechanical loading device, a hydraulic pump, which absorbs the work produced during the expansion of CO₂.

3.1 Design of Control Valves

The expansion process is controlled using fast-acting solenoid valves as intake and exhaust valves. As smaller valves exhibit more rapid cycling response, the valves must be sized for the specific application. Two valve sizes, indicated by orifice diameter, are used for the solenoid valves. Solenoid valves with 3/64 in orifice diameter are used as the intake valve. Solenoid valves with 1/16 in orifice diameter are the exhaust valves. There is some time lag for the solenoid valves to response to an input signal. In order to

control the expansion process as desired, the characteristics of the valve should be known.

3.1.1 Experiments for the Characteristics of the Solenoid Valve

Experiments have been performed to characterize the filling behavior of CO₂ into the ED-WOW. For this purpose, a fixed-volume chamber was designed that represents the volume of the ED-WOW at the instant of time on the expansion stroke when the intake valve is required to close. In order to guarantee minimum throttling in the expansion device, the time that it takes for the CO₂ to fill the chamber volume and to pressurize the chamber up to the pressure upstream of the intake valve needs to be known. Figure 3.1 shows the schematic of the experimental test stand. The electric heater is used to increase the CO₂ pressure inside the small tank up to the desired conditions.

The solenoid valve with 3/64 in orifice diameter was tested. The pressure transducer installed in the chamber is used to measure the dynamic pressure inside the chamber after energizing the solenoid valve (opening of the valve). This transducer is AC coupled, and thus only provides the unsteady portion of the pressure signal. Thus, the peak of the unsteady signal indicates when the volume can be considered 'filled'. Figures 3.2 and 3.3 show the pressure signal (in Volts) as CO₂ fills the chamber. In the legend of the figures, p_1 and p_2 stand for the initial pressures upstream of the valve and in the chamber, respectively. As shown in these figures, the pressure starts to increase approximately 0.01 seconds after opening of the valve. This time is the time lag when

the intake valve opens. This time will be taken as that representative of the time required to open the intake valves.

It can be seen from Figure 3.2 that the time that it takes to reach the maximum pressure increases slightly as the inlet pressure increases. Figure 3.3 shows the comparison of the pressure increase for similar absolute pressure differences across the solenoid valve, but with different inlet pressures. From Figure 3.3 it can be seen that the time that it takes to reach the maximum pressure decreases as the inlet pressure increases. As shown in Figures 3.2 and 3.3, it takes more than 0.075 seconds for the pressures to reach maximum values. The design calculation shows that the possible valve opening time is approximately 0.072 seconds for the revolution speed of the expansion device of 120 rpm (See Section 3.7). Therefore, it was determined that two intake valves and one exhaust valve must be used in order to give large enough flow area into the piston-cylinder chamber.

Other experiments have been conducted without CO₂ flow, i.e., no pressure difference across the valve to measure the valve closing time. Table 3.1 shows the response time to the signal to close the solenoid valve with 3/64 in orifice diameter. The average time is 0.05323 s and its 95% confidence interval is 0.05253-0.05393. The average time will be taken as that representative of the time required to close the intake and exhaust valves.

Table 3.1 also shows the response time to the signal to open the valve when there is no pressure difference across the valve. Its average time and 95% confidence interval are 0.0104 s and 0.009994-0.010806 s, respectively. This average time will be taken as that representative of the time required to open the exhaust valve.

3.1.2 Example of Valve Control

Figure 3.4 shows the desired piston displacement from the top ceiling of the piston-cylinder device over time as determined from the expansion device producing work design. The assumed revolutionary speed is 120 rpm and the lengths of the connecting rod and crank are 38.8 mm and 11.0 mm. The detailed description about the ED-WOW is given in the next sections. Also indicated in Figure 3.4 are the timings for the intake and exhaust valves. As discussed before, the design calculation indicates that the intake valve should open at the TDC at time zero and close when the piston reaches 5.21 mm from TDC (at the displacement of 8.01 mm) at 0.072 seconds. The exhaust valve should open at the displacement of 24.80 mm (Bottom Dead Center, BDC) at 0.25 seconds and close when the piston reaches the TDC again. The lead times for the control signals required for the valves to open and close fully are indicated in the figure. The circle and square stand for the timings of input signal to open and close the intake and exhaust valves in Figure 3.4, respectively.

An encoder is attached to the ED-WOW to read the exact angle of the crankshaft of the device. The encoder generates a gate signal (Z signal) and an A signal of 2048 pulses per revolution. This encoder is connected to a data acquisition system and a program was written to control the solenoid valves based on the reading of the angle of the crankshaft.

3.2 Design of Expander Cylinder, Piston, and Crank

The prototype piston type ED-WOW is based on a highly modified small four-cycle, two-piston engine of displacement $13.26 \text{ cc} \times 2$ that is commercially available. In

the original design, both pistons are on the same firing order, meaning that both pistons achieve TDC at the same instant. In the CO₂ expander application, the goal is to reduce the need for mechanical inertia (e.g. a flywheel) by using an out-of-phase firing order, with the piston on the expansion stroke providing the force required to drive the opposing piston through the evacuation stroke. To achieve this, the crankshaft of the original device was modified, and is shown in Figure 3.5.

An assembly of the piston, piston ring, and connecting rod is used for the expansion device. Figure 3.6 shows the assembly that is commercially available. The assembly is used to deliver the force of CO₂ inside the cylinder chamber and rotate the crank of the device described above. Table 3.2 shows the dimensions of the cylinder, connecting rod, crank, etc.

3.3 Design of Top of Expander Cylinder

The cylinder head connects the dual intake and single exhaust solenoid valves to the cylinder. The major design constraint for the device was achieving the absolute minimum dead volume in the system (i.e. the volume downstream of the intake valve at piston top dead center). This minimal dead volume is critical to achieving an efficient expansion process, as it is directly proportional to the throttling losses at the beginning of the expansion stroke. Figure 3.7 presents several views of the cylinder head design, showing the three ports that allow for connection of the valves. Each of the two cylinder heads is bolted to the crank housing with four machine screws. The three valves for each head connect via 1/8 in NPT fittings, and in turn are attached to a retention plate (not shown) with machine screws. Tie rods span between the cylinder head retention plates

on each of the two opposed cylinders, allowing for a rigid structure resistant to vibration-induced leakage in the head gasket. Figures 3.8 and 3.9 illustrate the dimensions of the head (in inches).

3.4 Design of Enclosure

The prototype ED-WOW has been designed to operate at an inlet pressure of 1500 psig and an outlet pressure of 500 psig. Due to these high pressures, it is anticipated that some CO₂ will leak from the expansion volume to the crank housing along the piston rings, and from the crank housing to the surrounding environment through bearings and seals. Therefore, the whole ED-WOW is placed in an enclosure to prevent the refrigerant from leaking out of the system. The enclosure is under discharge pressure as it is intended that the CO₂ exiting the discharge valve enters the enclosure. Thus, the enclosure needs to be strong enough to withstand the discharge pressure of about 500 psig during normal operation.

Based on current design of the ED-WOW, the inner diameter of the enclosure needed to be at least 16 inches to fit all valves and mountings into the enclosure. Figure 3.10 shows a cut view of the enclosure with the expansion device drawn to scale. As shown in this figure, the expansion device can be located in two domed pipe end caps with an 18 inch outer diameter. Flanges are welded to each domed end cap to allow the opening and closing of the enclosure using bolted joints. The material of the domed end caps is schedule 10, 304-stainless steel, the inner diameter is 17.25 inch, and the wall thickness is 3/8 inch. Figure 3.11 shows several views of the enclosure. The flanges of the enclosure were sealed using an O-ring.

The crankshaft of the ED-WOW must penetrate through the enclosure so that it can be connected to the loading device which absorbs the extracted energy when the CO₂ expands from high to low pressure. A penetration is made at the center of one of the domed end caps for the crankshaft. In order to prevent CO₂ leakage through the shaft penetration, a high-pressure rotary shaft seal was installed in the penetration.

The enclosure has two additional penetrations: one for the high-pressure inlet piping to the expansion device and the other one for the extraction of the expanded CO₂ at the bottom of the enclosure which is fed to the inlet of the evaporator. In addition, a safety relief valve was installed at the top of the enclosure.

Several wires needed to be connected to the encoder and the solenoid valves inside the enclosure in order to read the angle of the crankshaft and to open and close the valves to control the CO₂ expansion process. A commercially available "electrical feedthrough" was plugged into the wall of one of the domed end caps. Since the electrical feedthrough is designed for high pressure operation, no CO₂ leakage is expected. The outside and inside wires are connected on both sides of the electrical feedthrough.

A flat plate is welded to the inside of the enclosure to provide the base for the expansion device. Figure 3.12 shows the fabricated enclosure. Figures 3.12 (a) and (b) illustrate the front half of the enclosure with the ED-WOW mounted on the plate and the rear half of the enclosure, respectively. Table 3.3 shows the summary of the design of the enclosure.

3.5 Design of Loading Device

A mechanical loading device is connected to the ED-WOW. A hydraulic pump is used as the mechanical loading device. Figure 3.13 shows the ED-WOW with the hydraulic pump before the expansion device is placed inside the enclosure. The load is increased by closing the hand valves at the inlet to the hydraulic pump and thus, increasing the flow resistance to the fluid in the hydraulic pump system. There are two kinds of valves, a ball valve and a needle valve. The ball valve is used to adjust the coarse load amount and the needle valve is for the fine adjustment.

3.5.1 Calibration of Hydraulic Pump

The hydraulic pump has been calibrated to calculate its efficiency. This pump efficiency is used to measure the work output through the expansion device. During normal operation of the transcritical CO₂ system, the power is measured with the hydraulic pump. Then, the extracted work through the ED-WOW is calculated using the measured power and pump efficiency.

Figure 3.14 shows the schematic of the set-up for the measurement of torque using a spring scale and string. A string is tied up to a spring scale, wound on the large rod several times and a mass is given at the end of the other side of the string, as shown in Figure 3.14. As the crankshaft of the expansion device rotates, the string becomes taut due to the friction between the surface of the rod and the string. At a certain point the system reaches an equilibrium state owing to the torque balance between the ED-WOW and the system of the spring scale, string, and mass. At that point the rotational speed of the expansion device becomes constant and the string delivers forces to the spring scale

and mass. The spring force and rotation speed of the ED-WOW are measured. The radius of the large rod is 4.37 cm. The torque is calculated as:

$$T_q = (F_{scale} + F_{mass}) \times r \quad (3-1)$$

where T_q , F_{scale} , F_{mass} , and r are the torque, the force measured by spring scale, the force due to the mass, and radius of the rod. Then, the power becomes

$$P_{ss} = T_q \times \omega \quad (3-2)$$

P_{ss} and ω stands for the power calculated using the torque of the ED-WOW and the rotational speed of the expansion device in radian/s, respectively.

Then, the pump power is calculated. The pump connection to the ED-WOW is shown in Figure 3.15. The pressures are measured before and after the hydraulic pump and volumetric water flow rate is also measured using a rotameter. The power of the hydraulic pump is calculated as follows.

$$P_{pp} = \Delta p \times \dot{Q} \quad (3-3)$$

where P_{pp} , Δp , and \dot{Q} are the power of the hydraulic pump, pressure difference across the hydraulic pump, and the volumetric water flow rate, respectively.

The hydraulic pump efficiency can be calculated by comparing P_{ss} and P_{pp} for the similar test conditions. Table 3.4 and Table 3.5 show the measured values of the forces and pressures, the calculated torque and powers, and the pump efficiencies. The description for the parameters is given in the tables. As shown in the tables, the pump efficiency becomes 68.14% when p_{in} , the inlet pressure of the ED-WOW, is about 4.3 MPa and the rotational speed is about 300 RPM. It also becomes 47.48% when p_{in} and ω

are about 3.0 MPa and 294 RPM. As discussed before, this efficiency of the hydraulic pump is used to measure the work produced through the ED-WOW.

The pump was calibrated at two points only due to the difficulty of the experiment. The initial desire of this calibration was to obtain enough data and to make a calibration curve for the pump efficiency. However, the system was too sensitive to the friction of the string. The ED-WOW did not work once the friction was further increased to decrease the rotational speed of the ED-WOW.

3.6 Establishment of Input Timings for the Intake and Exhaust Valves

Another experiment has been performed to establish correct input timings for the solenoid valves to control the expansion process of CO₂ through the expansion device producing work. Figure 3.16 shows the schematic of the test stand.

As mentioned in the previous sections, the input signals should be given prior to certain locations of the crankshaft due to the time lags of the solenoid valves. However, the expansion device was not working when the originally predicted time lags were considered. It seemed that immediately after the signal to open the intake valve #1 is given, high-pressure gas flows into cylinder #1 even though piston #1 has not reached Top Dead Center (TDC). At the same time, the high-pressure gas inside cylinder #2 pushes piston #2 as it expands from the high pressure to the low pressure. Number 1 (#1) and number 2 (#2) illustrate the one side of two piston-cylinders and the other side, respectively. If the pressure in cylinder #1 increases rapidly and the device has not enough momentum to move piston #1 through the TDC position (against the force of the

incoming high-pressure gas, since the intake valve opened too early), piston #1 will move backwards until the pressures in both cylinders have equalized and the device is stuck.

Thus, the timing table shown in Figure 3.4 has been modified. The signal to open the intake solenoid valve was delayed until just after the piston reached TDC. However, the signal to close the intake valve remained the same in order to achieve the desired volume expansion ratio. Figures 3.17 and 3.18 show the new timing tables for the intake valves #1 and the exhaust valve #2, and for the intake valves #2 and the exhaust valve #1, respectively. Figure 3.19 shows the timing table for all solenoid valves. The x-axis stands for the number of pulses of the encoder connected to the expansion device for one revolution of the crankshaft (2048 pulses/revolution), and the y-axis stands for on (=1, open) and off (=0, closed) of the valve actuation. As shown in the figures, the signal to open the intake valves is given 10 pulses after Top Dead Center (TDC) and the valves remain open for 70 pulses. The signal to open the exhaust valve is given 10 pulses before BDC and the signal to close the exhaust valve is given 10 pulses after TDC. This timing table is based on a crankshaft speed of 120 rpm.

Appendix C shows the program written in 'Visual C++' to control the solenoid valves. As mentioned above, this program is written based on the rotational speed of 120 RPM.

3.7 Determination of Revolution Speed of the Expansion Device

As mentioned above, the revolution speed of the ED-WOW is determined as 120 RPM. Based on the desired operating condition shown in Table 2.1 and the dimensions of the ED-WOW shown in Table 3.2, the LOE (location of expansion initiation) must be

5.21 mm from the location of the TDC. Table 3.6 shows the revolution speed of the expansion device versus the time that it takes for the piston to reach 5.21 mm from the TDC during the down stroke (intake stroke).

As mentioned above, the time lag of the intake valve to the input signal for closing is 0.053s. The input signal must be given 0.053s prior to the piston reaching the LOE. The time to reach the LOE should be larger than 0.053s. As shown in Table 3.6, when the revolution speed is equal to or larger than 180 rpm, the intake valve can't be closed at the exact position of the piston of the LOE because of the short time duration of the intake process from the TDC to the LOE. The intake valve will be closed after the LOE. In this case, CO₂ will be under-expanded due to the larger amount of mass at the initiation of the expansion. Therefore, the revolution speed should be slower than 180 rpm.

When the speed of the device is too low, the momentum becomes too low to keep running the device during normal operation. Therefore, the speed of 120 rpm is determined rather than 60 rpm as the operating speed of the expansion. In this case, there is enough time to close the intake valve at the LOE to get the desired low-side pressure and there is also comparatively large momentum to run the ED-WOW continuously.

Table 3.1: Valve fully opening and closing timings for the solenoid valve with 3/64 in orifice.

Case	Time (s)	Average time (s)	Standard deviation (s)	95% confidence interval (s)
Measurement of closing time	0.0525	0.05323	0.000667	0.05253 - 0.05393
	0.0525			
	0.0537			
	0.0531			
	0.0532			
	0.0544			
Measurement of opening time	0.0106	0.0104	0.000387	0.009994 - 0.010806
	0.0105			
	0.0106			
	0.0096			
	0.0108			
	0.0103			

Table 3.2: Dimensions of the expansion device producing work.

Diameter of cylinder	27.7 mm
Displacement	13.26 cc
Stroke	22.0 mm
Length of crank	11.0 mm
Length of connecting rod	38.75 mm
Length from the top of the cylinder to the head of the piston at TDC	2.8 mm
Volume of cylinder at TDC	1.685 cm ³
Volume of cylinder at BTC	14.95 cm ³
Volume of fittings connected to the device	0.813 cm ³

Table 3.3: Summary of the design of the enclosure.

Dimension	<ol style="list-style-type: none"> 1. Outer diameter: 18" 2. Inner diameter: 17.624" 3. Wall thickness: 3/16" 4. Total length: 16" 5. Length of straight section: about 6.6"
Material	1. Schedule 10 304-stainless steel
Penetrations	<ol style="list-style-type: none"> 1. One at the top for the crankshaft that will be connected to the loading device. 2. One for high-pressure inlet piping to the expansion device. 3. One at the top for a safety relief valve (1/4" male NPT). 4. One at the top for a pressure gage. 5. One at the top for temperature measurement. 6. One at the bottom of the enclosure to extract the expanded CO₂ to an evaporator. 7. One at the bottom to release the leaked CO₂ to the inlet of the evaporator through a check valve. 8. Two at the top for the electrical feedthroughs to connect the inside and outside wires
Welding	<ol style="list-style-type: none"> 1. One flat plate to support the expansion device inside the enclosure. 2. Two flanges to fasten the domed caps with some bolts.
Total weight	1. About 235 lb.

Table 3.4: Power measurement using torque of the expansion device producing work.

Test no.	1	2	3	4
P _{in} (kPa), STD	4323.9, 48.4	2974.6, 46.0	2990.1, 38.9	3038.5, 60.1
P _{out} (kPa), STD	161.9, 83.2	137.6, 43.6	N/A	N/A
T _{in} (°C), STD	16.38, 0.33	16.78, 0.42	18.01, 0.29	17.43, 0.39
T _{out} (°C), STD	3.40, 0.72	3.64, 0.84	12.27, 0.72	10.73, 0.40
F-scale (kgf)	6.03 ± 0.23	4.90 ± 0.23	4.90 ± 0.23	4.90 ± 0.23
F-mass (kgf)	0.05	0.15	0.055	0.055
Total F (N)	6.08 ± 0.23	5.05 ± 0.23	4.96 ± 0.23	4.96 ± 0.23
ω (RPM)	300 ± 12	282 ± 12	288 ± 12	294 ± 12
Torque (N-m)	2.61	2.16	2.12	2.12
Power (W) P _{ss}	85.19	66.63	64.0	64.71

Table 3.5: Power measurement of the hydraulic pump and its efficiency.

Test no.	5	6	7	8	9
P_{in} (kPa), STD	4436.4, 36.7	2980.4, 26.6	3055.1, 64.0	3065.5, 55.7	N/A
P_{out} (kPa), STD	139.4, 48.2	130.1, 34.2	133.2, 36.1	125.4, 38.9	N/A
T_{in} (°C), STD	20.37, 0.27	16.54, 0.22	16.30, 0.16	16.42, 0.15	N/A
T_{out} (°C), STD	15.08, 0.98	8.21, 0.20	7.75, 0.21	7.80, 0.21	N/A
$P_{p,in}$ (psig)	-2.5 ± 0.1	-2.1 ± 0.1	-2.1 ± 0.1	-2.1 ± 0.1	-2.1 ± 0.1
$P_{p,out}$ (psig)	23.0 ± 0.2	12.0 ± 0.2	11.0 ± 0.2	10.0 ± 0.2	12.0 ± 0.2
\dot{Q} (GPM)	3.3 ± 0.1	3.3 ± 0.1	3.3 ± 0.1	3.3 ± 0.1	3.3 ± 0.1
ω (RPM)	294 ± 12	294 ± 12	294 ± 12	294 ± 12	294 ± 12
Power (W) P_{pp}	58.04	32.10	29.82	27.54	32.10
Pump Eff. (%)	68.14	50.15	46.59	43.04	50.15

Descriptions of parameters: STD: standard deviation, P_{in} : inlet pressure of the ED-WOW, P_{out} : outlet pressure of the ED-WOW, T_{in} : inlet temperature of the ED-WOW, T_{out} : outlet temperature of the ED-WOW, F-scale: force measured by the scale, F-mass: force due to the mass, $P_{p,in}$: inlet pressure of the hydraulic pump, $P_{p,out}$: inlet pressure of the hydraulic pump, \dot{Q} : volumetric flow rate of water.

Table 3.6: Revolution speed of the expansion device versus the time to reach LOE.

Speed (rpm)	Angular velocity (rad/s)	Time (s)
60	6.28	0.1442
120	12.57	0.0721
180	18.85	0.0481
240	25.13	0.0360

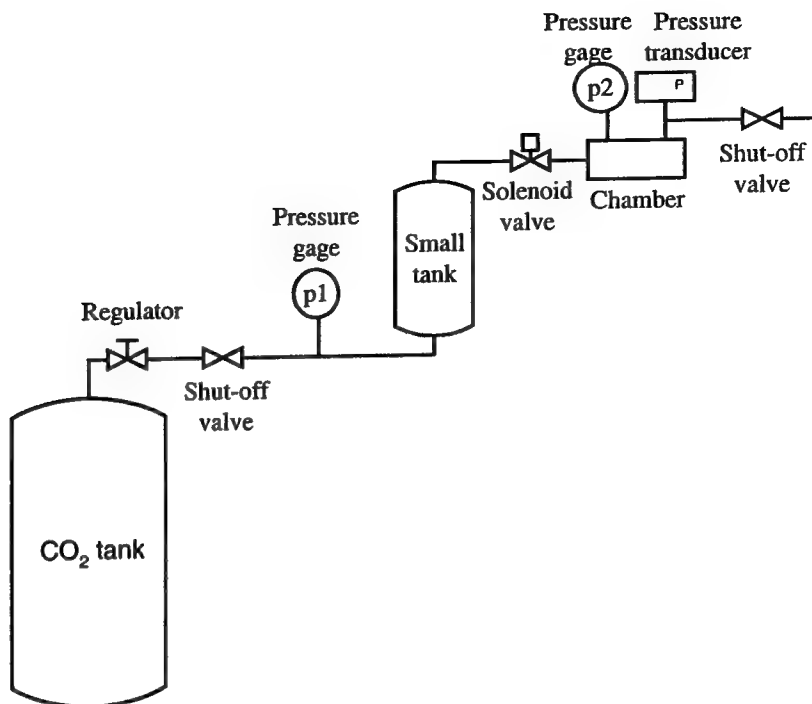


Figure 3.1: Schematic of test stand to determine the characteristics of the solenoid valve.

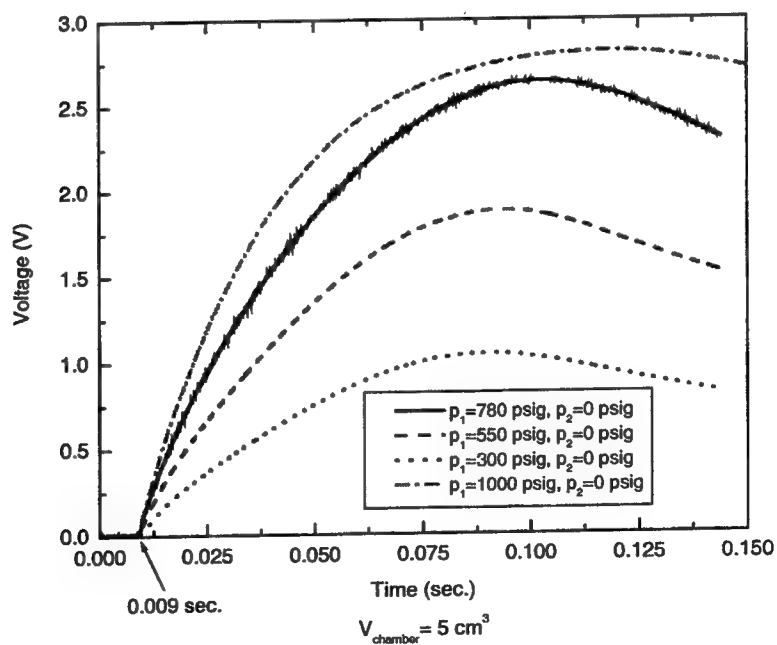


Figure 3.2: Filling behaviors of CO₂ in the chamber with the intake valve ($D_{\text{orifice}} = 3/64$ in.).

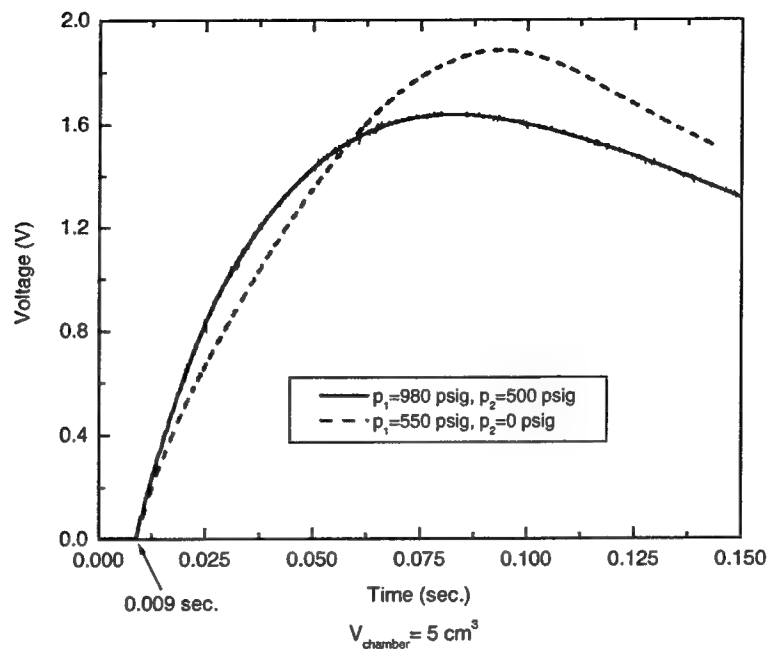


Figure 3.3: Comparison of filling behaviors for similar pressure differences, but with different p_1 s.

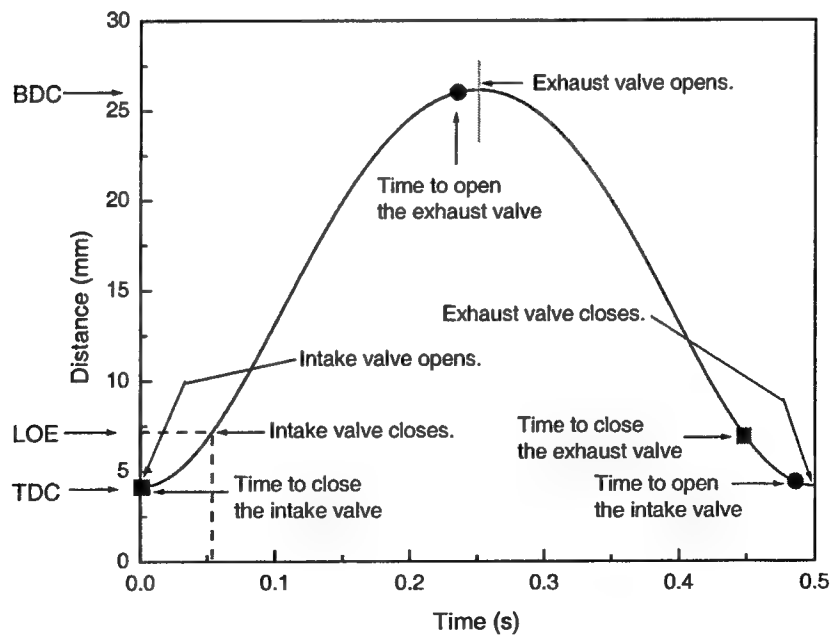


Figure 3.4: Timings for input signals to the solenoid valves.

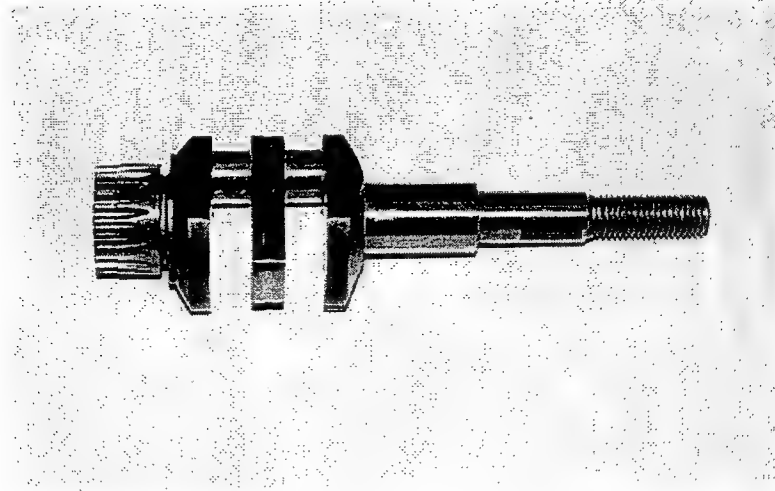


Figure 3.5: Crankshaft of the expansion device producing work.



Figure 3.6: Assembly of a piston, piston ring and connecting rod.

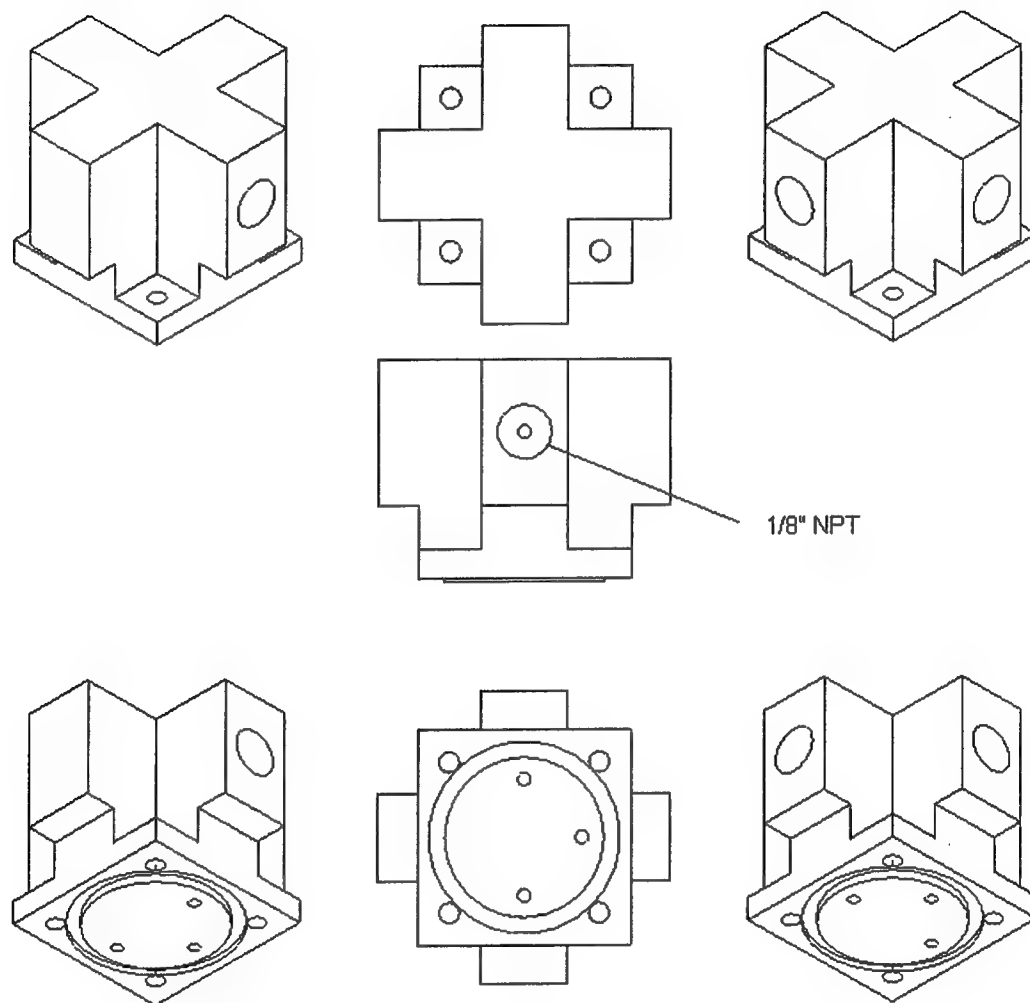


Figure 3.7: Several views of the head of the piston-cylinder device.

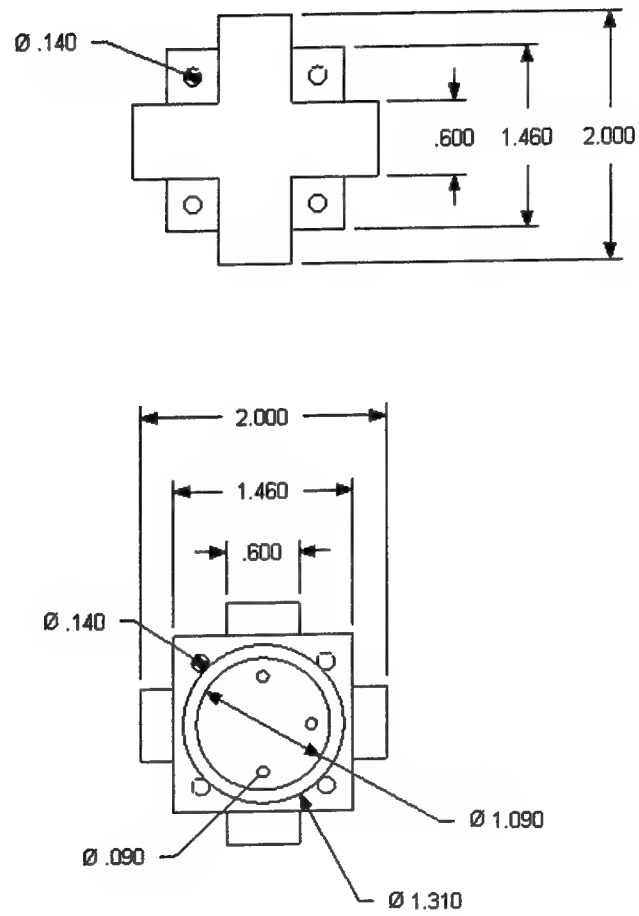


Figure 3.8: Top and bottom views of the cylinder head.

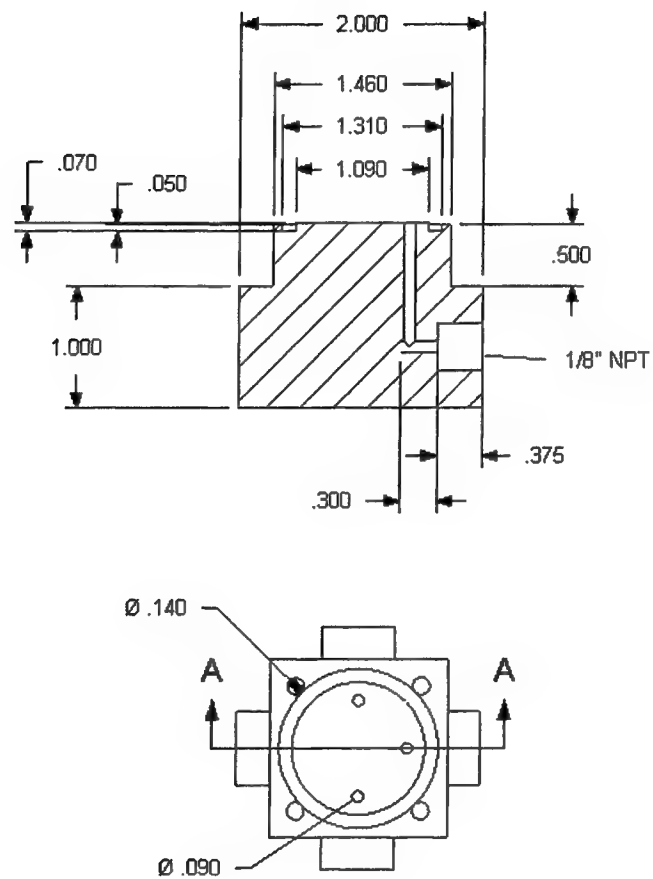


Figure 3.9: Bottom and cut-way views of the cylinder head.

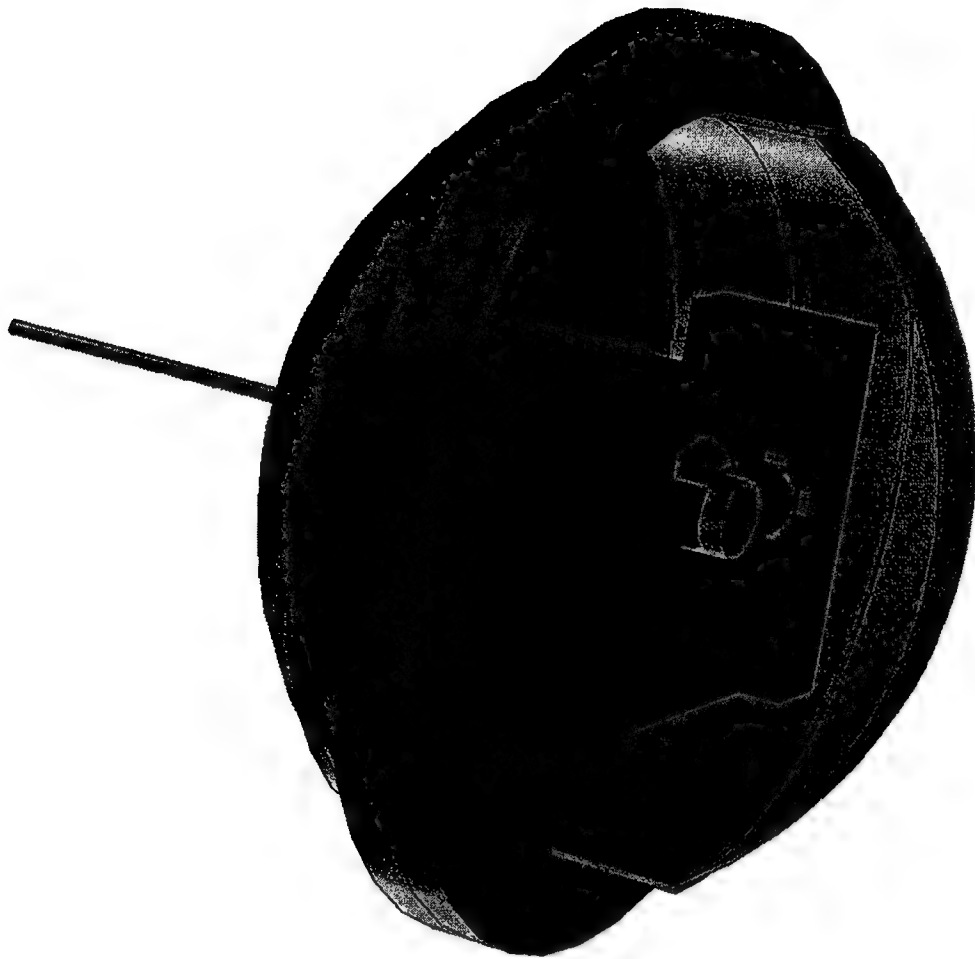


Figure 3.10: Cut view of the designed enclosure with expansion device in scale.

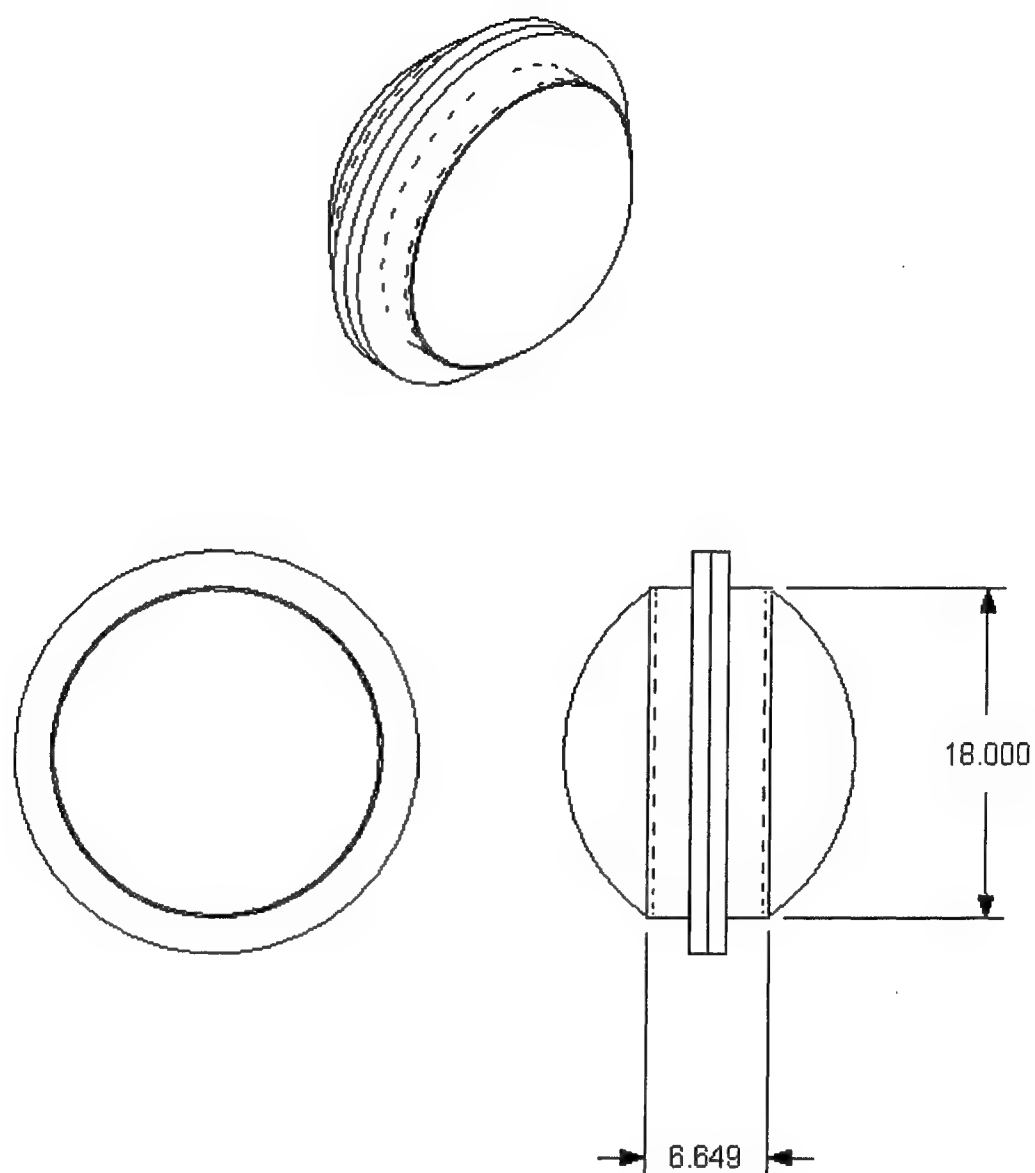
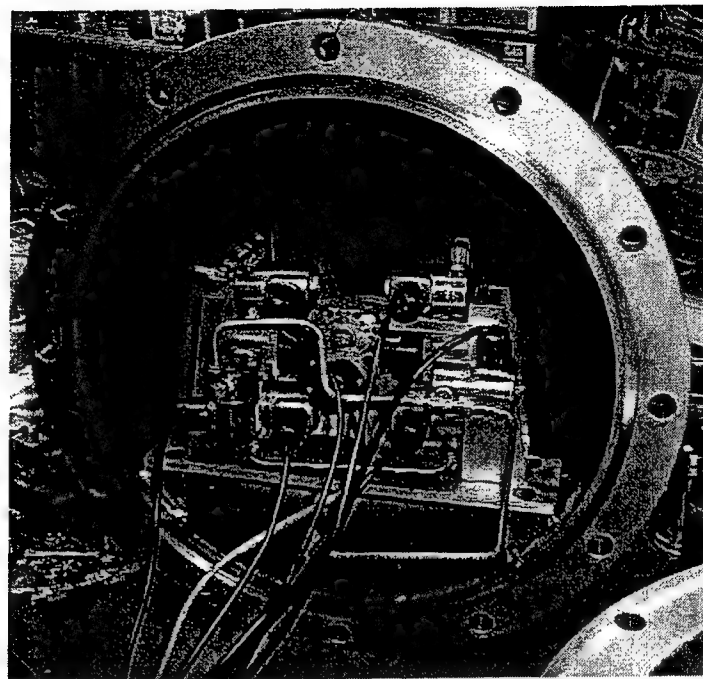
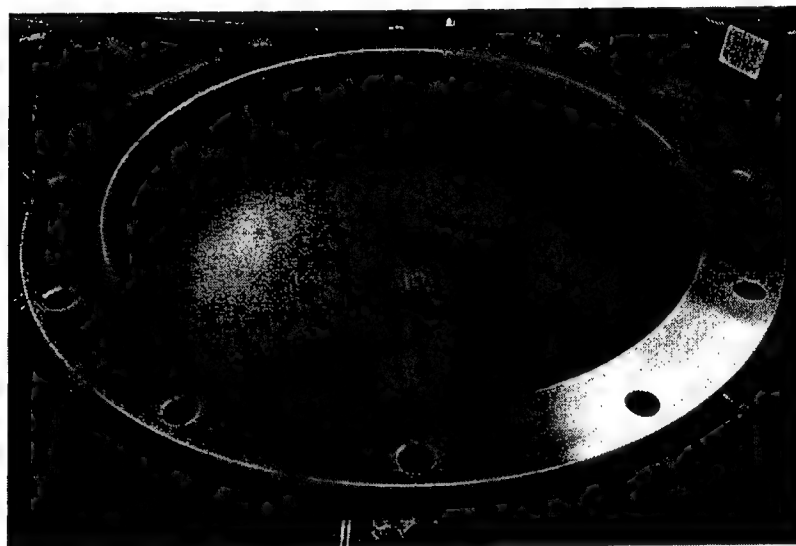


Figure 3.11: Several view of the enclosure.



(a)



(b)

Figure 3.12: Fabricated enclosure.
(a): Front half of the enclosure with the ED-WOW.
(b): Rear half of the enclosure.

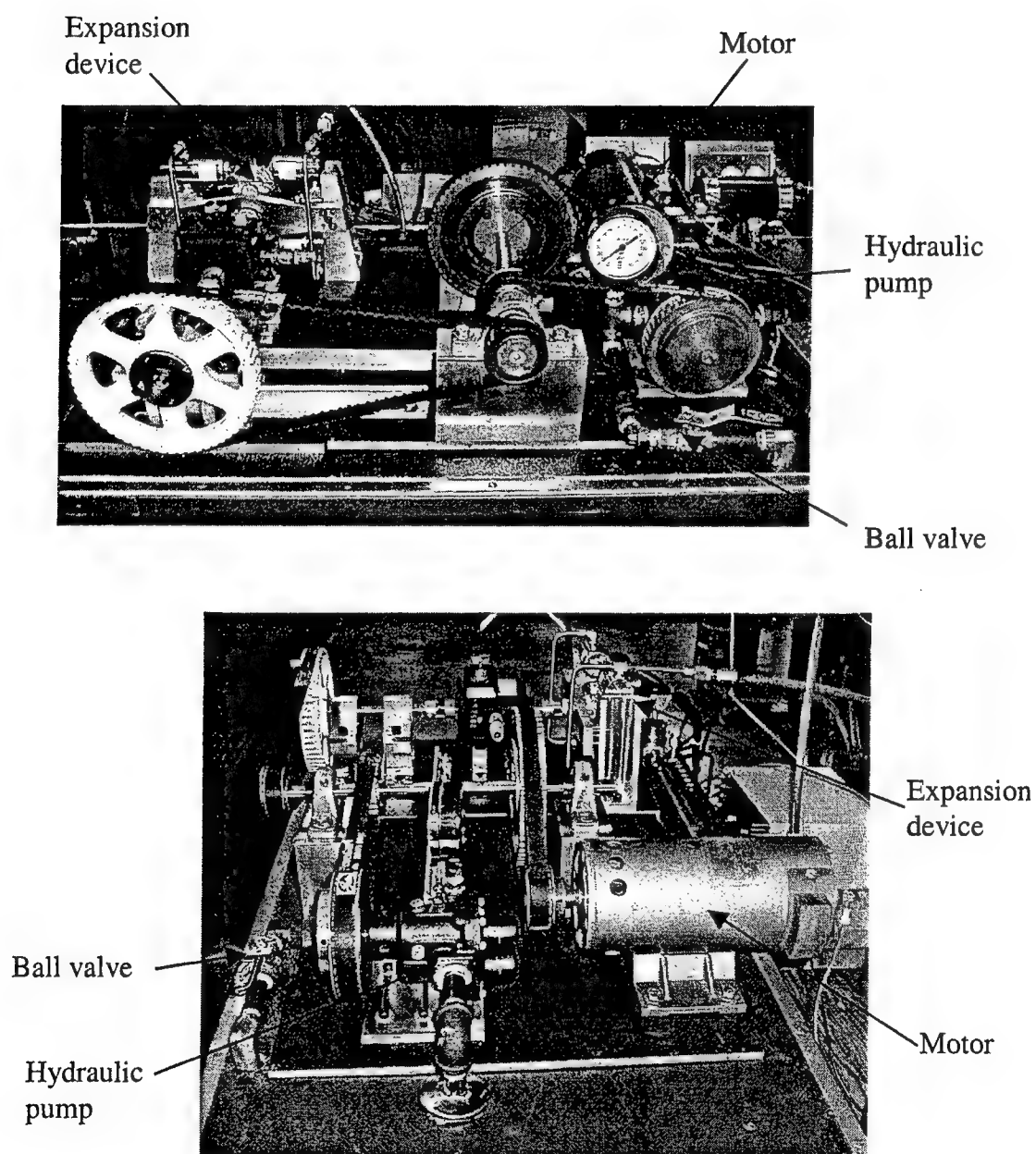


Figure 3.13: Front and side views of the expansion device and hydraulic pump.

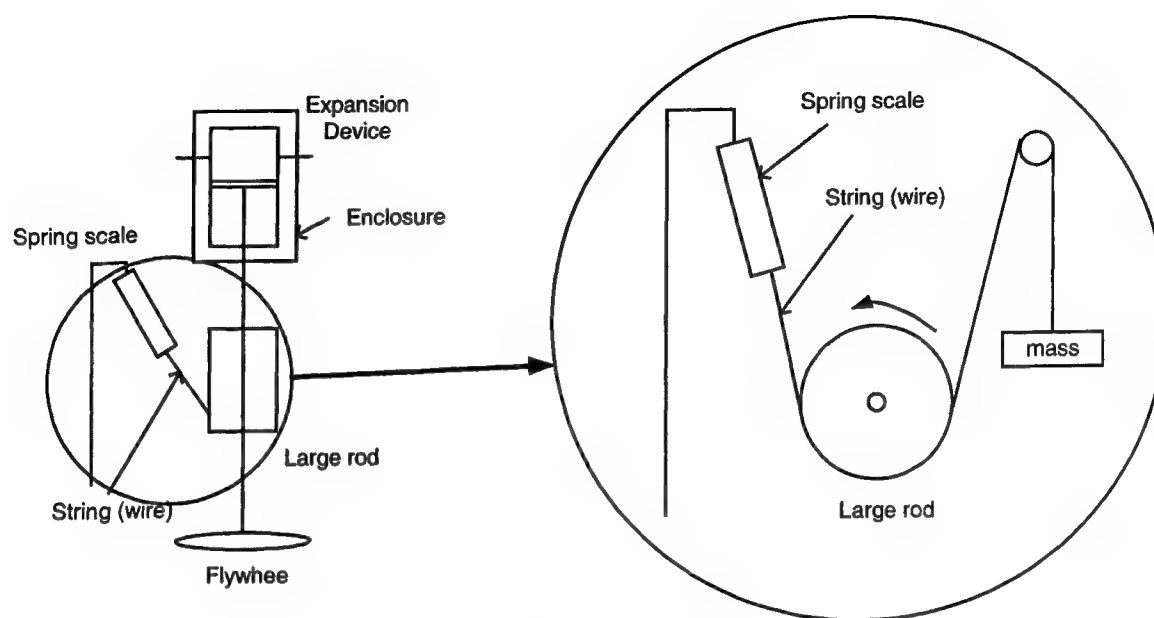


Figure 3.14: Schematic of set-up for torque measurement using spring scale and string.

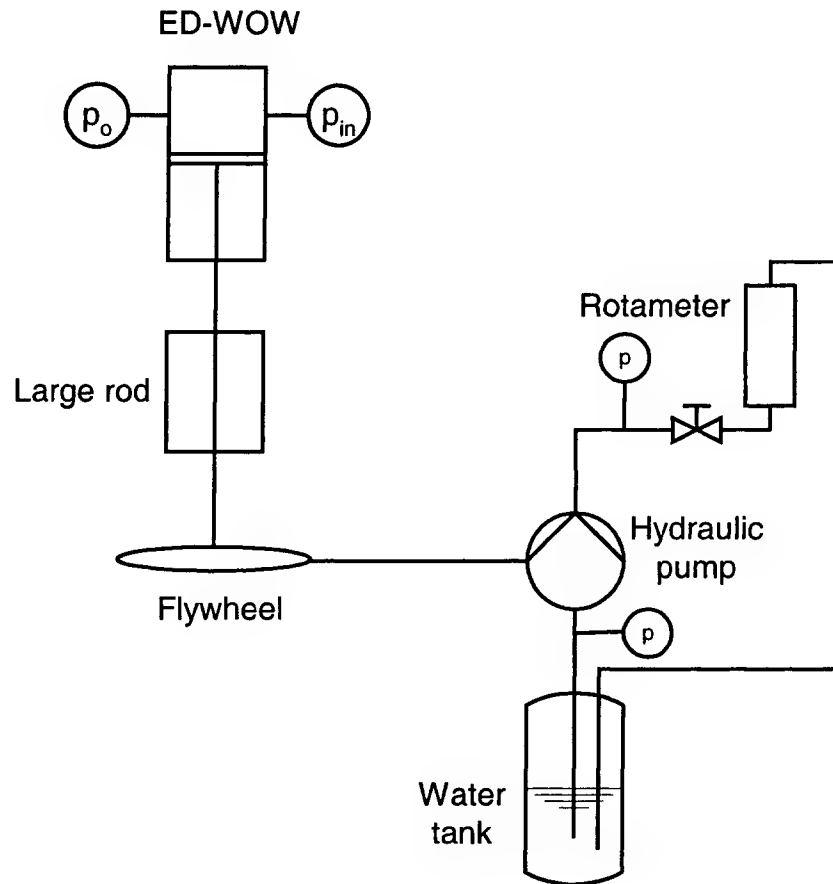


Figure 3.15: Connection of hydraulic pump to expansion device producing work.

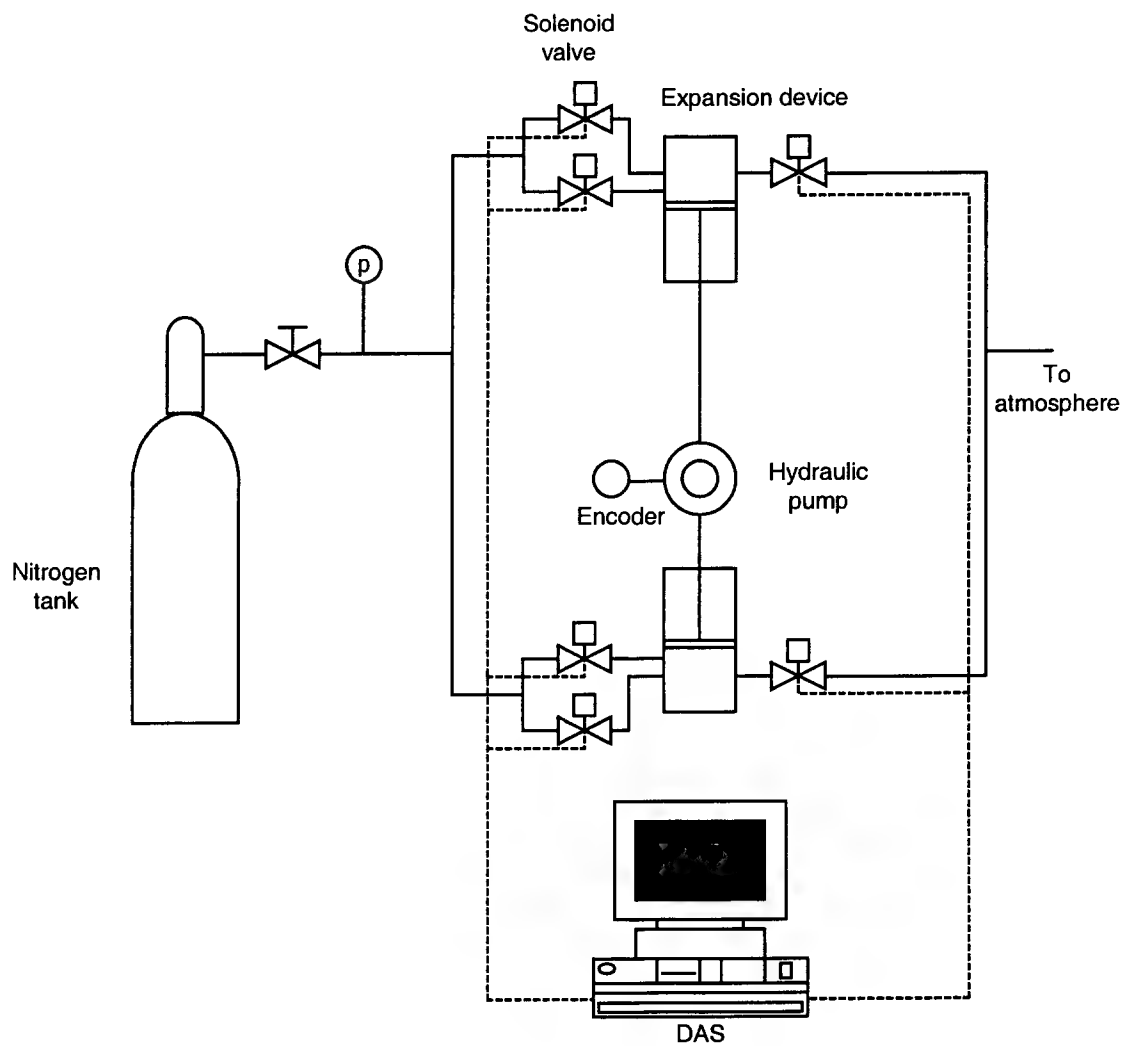


Figure 3.16: Schematic of the test stand for the establishment of the input timings for the intake and exhaust valves.

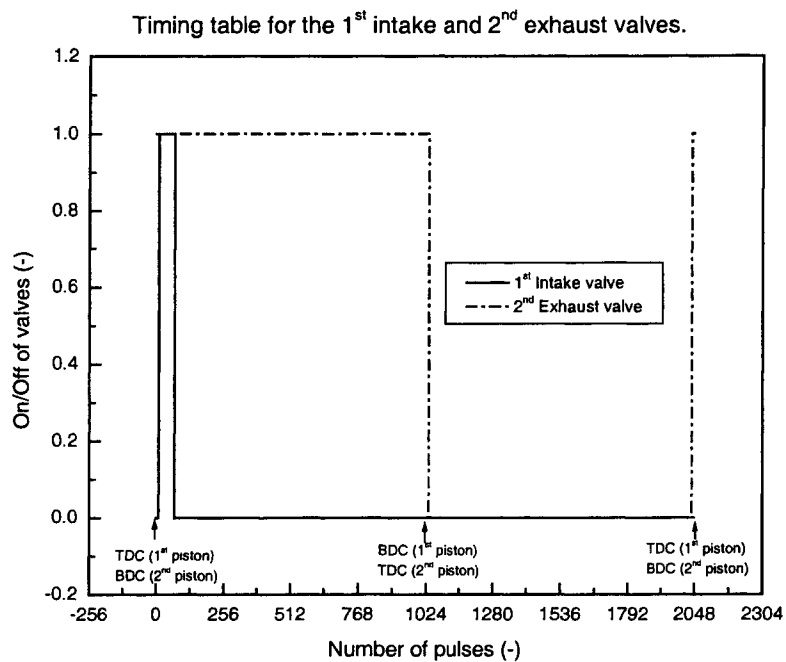


Figure 3.17: Valve on/off timing of 1st intake and 2nd exhaust valves.

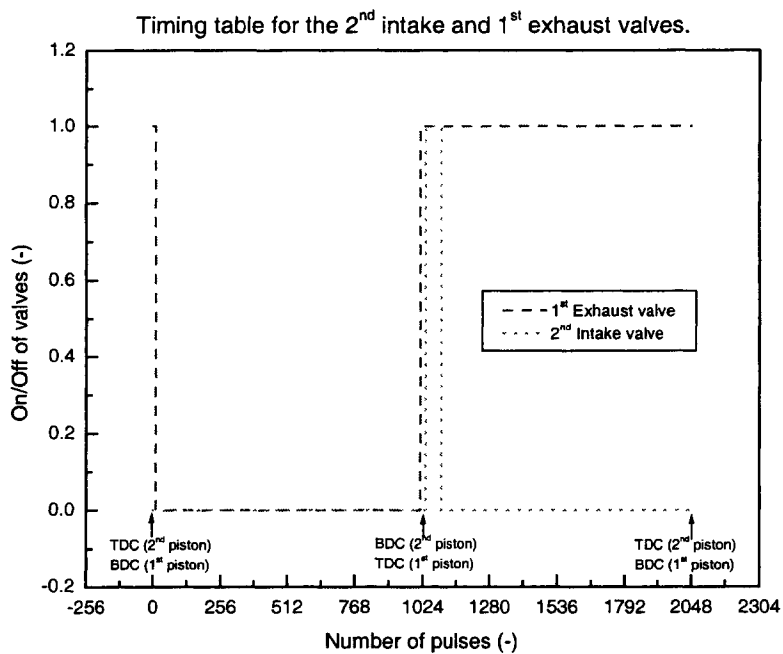


Figure 3.18: Valve on/off timing of 2nd intake and 1st exhaust valves.

Timing table for the solenoid valves to control the expansion process.

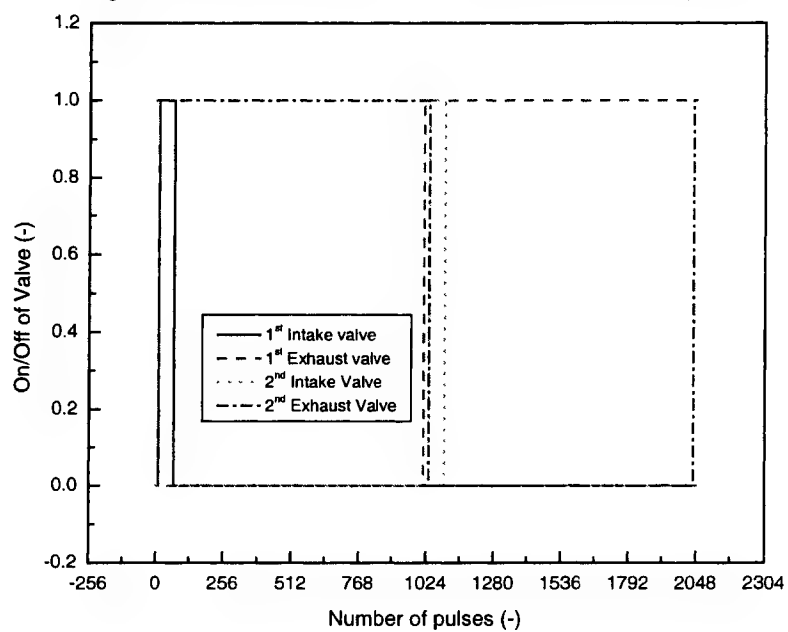


Figure 3.19: Desired timing table to control all solenoid valves.

4 RESULTS

4.1 Results of Analysis for Cycles with an Economizer or Intercooler

The transcritical CO₂ cycle was analyzed with the effect of an intercooler or economizer incorporated into the base cycle.

4.1.1 Comparison of COPs of Base, Economizer, and Intercooler Cycles

4.1.1.1 Economizer and Base Cycles

Figure 4.1 shows the comparison of COPs of Economizer cycle (Figure 1.7) and Base cycle (Figure 1.1). For this analysis, the temperature and pressure at the inlet of the 1st-stage compressor, T_{E1} and p_{E1} , and the air temperature, T_{air} , are assumed to be 25°C, 3MPa and 35°C, respectively. The same conditions are assumed for the Base cycle. As shown in this figure, the Economizer cycle has larger COPs than Base cycle for the pressure ratio larger than 1.6. The maximum COPs of Economizer and Base cycles are 3.564 and 3.043, respectively. The maximum COP increases by 17.1% by using the Economizer cycle.

The same trend has been observed when the pressure at the inlet to the 1st-stage compressor, p_{E1} , is changed but the other input variables are fixed. It can be seen in

Figure 4.1 that the COP of the Economizer cycle is zero from values of pressure ratio from 1.0 to 1.5. This means that the COP was not calculated for that pressure ratio range. When the pressure ratio is small and the air temperature (heat sink in the gas cooler) is high, the enthalpy at the outlet of the gas cooler is higher than that of the vapor phase at the intermediate pressure. Therefore, the CO₂ becomes the superheated vapor and there is no phase separation in the accumulator after the 1st expansion. From this figure it can be seen that the CO₂ becomes two-phase in the accumulator for the pressure ratios larger than 1.5.

It can also be seen from Figure 4.1 that the COP of the Base cycle is zero for pressure ratios from 1.0 to 1.5. This means that the COP of the Base cycle was not calculated because the Economizer cycle is not applicable at this range of the pressure ratios.

4.1.1.2 Intercooler and Base Cycles

Figure 4.2 shows the comparison of the COP of the Intercooler cycle (Figure 1.10) with that of the Base cycle. It is assumed that the temperature and pressure at the inlet of the 1st-stage compressor, T_{11} , p_{11} , and the air temperature, T_{air} , are constant and those values are 25°C, 3.5MPa and 35°C, respectively. Again, the same conditions are given for the Base cycle. Identical pressure ratios are used for both of the compressors and varied from 1.0 to 2.4 to calculate the COP. The solid line in the legend stands for the Base cycle and the dashed line the Intercooler cycle in the figure. It is observed that the COP of the Intercooler cycle is higher than that of the Base cycle and the maximum

COP of 4.018 occurs at the pressure ratio of 1.58 in the case of the Intercooler cycle. The maximum COP of Base cycle is 3.618 at a pressure ratio of 1.56. The maximum COP increases by 11.1% by using Intercooler cycle.

As shown in the figure, the COP of the Intercooler cycle is zero from values of pressure ratio from 1.0 to 1.12. This is due to the fact that when the intermediate temperature, T_{I2} , of the CO_2 after the 1st-stage compressor is lower than T_{air} , there will be no heat transfer through the intercooler and no calculation of the COP has been performed. From this figure it can be seen that T_{I2} begins to exceed T_{air} for pressure ratios larger than 1.14.

In addition, the COP of the Base cycle is zero for pressure ratios from 1.0 to 1.12. This means that the COP of the Base cycle was not calculated because the intercooler cycle is not applicable at this range of the pressure ratios.

It can also be observed in Figure 4.2 that the COP of the Intercooler cycle increases again at a pressure ratio of approximately 2.2, then decreases. That means there is the 2nd peak of COP in the Intercooler cycle. This is caused by the decrease of the total combined work of the 1st- and 2nd-stage compressors. Figure 4.3 shows the comparison of the COP and the compression work. From the pressure ratio of 2.2 the total combined work of the 1st- and 2nd-stage compressors becomes less and this results in increase of COP as shown in Figure 4.3. Starting at a pressure ratio of 2.36, the COP decreases again as the compression work increases.

As discussed above, the system performance can be improved by modifying the Base cycle into the Economizer cycle or the Intercooler cycle. In addition, the system efficiencies of the Economizer and Intercooler cycles can be increased much further if the

optimum operating condition is selected. In the next sections, the analyses are discussed in detail about the effects of some important parameters on COPs of Economizer and Intercooler cycles for the optimum operating condition.

4.1.2 Effects of Pressure Ratios on COP

In order to give the minimum compression work in the Intercooler cycle, it is common to give the same pressure ratio across the two compressors [Wark, 1988]. In addition, the temperature of the CO₂ at the outlet of the 1st-stage compressor (T_{H1}) is cooled down through the intercooler to the temperature of CO₂ at the inlet to the 1st-stage compressor (T_{H1}). During warm weather periods, however, the intercooler may not be able to reject enough heat for the CO₂ temperature to be reduced to T_{H1} . In this case, different pressure ratios for each of the two compressors will be required to give the minimum compression work. Therefore, it is necessary to evaluate what combination of pressure ratios across the compressors give the maximum COP for a given operating condition.

Figure 4.4 shows the behavior of the COP for the Intercooler cycle. The CO₂ pressure, p_{H1} , and temperature, T_{H1} , at the inlet to the 1st-stage compressor are assumed to be 3.5MPa and 25°C, respectively. The air temperature, T_{air} , is a heat sink temperature and assumed to be 35°C. The pressure, p_{H2} , at the outlet of the 2nd-stage compressor, is taken to be 10MPa. If the same pressure ratio is assumed across the compressors, the maximum COP of 3.842 occurs at pressure ratio of 1.69 and intermediate pressure of 5.92MPa. The COP of the Base cycle for this condition becomes 3.361. As shown in

Figure 4.4, however, the COP continues to increase if the intermediate pressure is increased with an optimum COP of 3.956 occurring at intermediate pressure of 8.12MPa. In this case, the pressure ratios across the 1st-stage compressor and 2nd-stage compressor are 2.32 and 1.23, respectively. From this result it could be deduced that improvements of COP could be obtained if the pressure ratios are chosen appropriately.

As shown in Figure 4.4, there is sudden increase of COP at around the pressure ratio of 2.25 and the COP reaches its maximum point at the pressure ratio of 2.32. This behavior of COP is due to the sudden decrease of total compression work. Figure 4.5 shows the comparison of the compression works for this case. In the legend of the figure, '1st-stage compression work', '2nd-stage compression work', and 'Total compression work' stand for the compression work of the 1st-stage compressor, the compression work of the 2nd-stage compressor, and the summation of the 1st- and 2nd-stage compression works, respectively. As shown in this figure, the compression work of the 2nd-stage compressor decreases much at around the pressure ratio of 2.25 and the total compression work becomes the minimum at the pressure ratio of 2.32 at which the maximum COP occurs. At this point, the pressure ratio across the 2nd-stage compressor is 1.23.

The behavior of the compression work over the pressure ratio across the compressors is due to the thermodynamic characteristics of the carbon dioxide. Figure 4.6 shows the processes of the Intercooler cycle with the fixed pressure ratios and the different pressure ratios on the pressure-enthalpy diagram. When the fixed pressure ratios of 1.69 are applied, the intermediate pressure at the intercooler becomes 5.92MPa. In this case, the paths of the refrigeration processes are $11-11'-12'-12-13-14-11$. The subscript 'f' represents the case of the fixed pressure ratio. If the different pressure

ratios, 2.32 for the 1st-stage compressor and 1.23 for the 2nd-stage compressor, are considered, the intermediate pressure becomes 8.12MPa. Hence the paths of the processes become $11-11'_d-12'_d-12_d-13-14-11$. The subscript 'd' represents the case of the different pressure ratios. The total compression works for both cases are as follows:

$$w_f = (h_{11'} - h_{11}) + (h_{12_s} - h_{12_s'}) \quad (4-1)$$

and

$$w_d = (h_{11'_d} - h_{11}) + (h_{12_d} - h_{12'_d}). \quad (4-2)$$

Equations (4-1) and (4-2) represent the total compression work of the cases of the fixed pressure ratio and different pressure ratio, respectively. The first and second terms in the right hand sides of Equations (4-1) and (4-2) stand for the compression works of the 1st-stage and 2nd-stage compressors, respectively. As discussed above, the 2nd-stage compression work decreases suddenly at the pressure ratio of 2.32 across the 1st-stage compressor. As shown in Figure 4.6, the enthalpy increase through the 2nd-stage compressor becomes very small at that point. It results in the minimum total compression work. Therefore, the COP of the Intercooler cycle becomes the maximum with the constant capacity of the evaporator. It can be also seen in Figure 4.6 that there is a large enthalpy decrease through the intercooler at the intermediate pressure of 8.12MPa due to the almost zero slope of the temperature curve of carbon dioxide with temperature of 35°C at that pressure, even though the figure does not show it clearly because of the

coarse picture. Therefore, in this case, most of the heat of CO_2 in the system is removed through the intercooler cycle and a small portion of the heat through the gas cooler.

4.1.3 Effect of Low-Side Pressure on COP

In the previous section, the pressure ratio effect on the COP was investigated. In this section, identical pressure ratios across both of the two compressors are assumed to illuminate the specific thermodynamic performance difference between the proposed transcritical CO_2 cycles. For the Base cycle, the pressure ratio across the compressor is square of the pressure ratio of the modified cycles to give the same high-side pressure (p_{E2} or p_{I2}).

4.1.3.1 Economizer Cycle

Figure 4.7 shows the effects of the CO_2 pressure at the inlet to the 1st-stage compressor (low-side pressure), p_{E1} , on the COP of the Economizer cycle. It can be observed from this figure that as the p_{E1} increases, the COP increases and the pressure ratio across the 1st-stage compressor at which the maximum COP occurs decreases. When p_{E1} is 4.5MPa, the maximum COP of 5.835 occurs at the pressure ratio of 1.36. When p_{E1} is 2.5MPa, the maximum COP becomes 3.017 at the pressure ratio of 1.84. The COP can increase by 93.4% by increasing the CO_2 pressure at the inlet to the 1st-stage compressor from 2.5MPa to 4.5MPa.

Actually, the control of the low-side pressure as a function of operating conditions is a difficult task to achieve because the low-side pressure strongly depends on

the capacity, heat source temperature, and geometry of the evaporator. However, this is a parametric study, in which it is assumed that depending on the evaporator design, a higher the low-side pressure may be achievable.

Figure 4.8 shows a comparison of the heat removal capacity of the evaporator in the Economizer cycle. The capacity is 118.08kJ/kg at the pressure ratio of 1.36 when p_{E1} is 4.5MPa. When p_{E1} is 2.5MPa, it becomes 145.98kJ/kg at a pressure ratio of 1.84. The evaporator heat removal capacity is decreased by 19.1% by increasing the pressure at the inlet to the 1st-stage compressor from 2.5MPa to 4.5MPa. Table 4.1 shows the compression work at the pressure ratio of each low-side pressure at which the maximum COP occurs. As shown in the table, the compression work decreases considerably, by 53.3%, when the low-side pressure increases from 2.5Mpa to 4.5MPa. Therefore, the effect of increasing the pressure at the inlet to the evaporator is a net increase in the COP, due to a larger decrease of the compression work and a smaller decrease of the heat removal capacity of the evaporator.

4.1.3.2 Intercooler Cycle

Figure 4.9 shows the effect of the pressure at the inlet to the 1st-stage compressor, p_{I1} , on the COP of the Intercooler cycle. The effect of the pressure is the same as in the case of Economizer cycle. As shown in the figure, the maximum COP increases as p_{I1} increases. Also the pressure ratio at which this maximum COP occurs decreases as the p_{I1} increases. When p_{I1} is 4.5MPa, the maximum COP of 5.612 occurs at a pressure ratio of 1.38. When p_{I1} is 2.5MPa, the maximum COP becomes 2.872 at the pressure ratio of 1.88. The COP is thus increased by 100.7% by increasing the CO₂ pressure at the inlet to

the 1st-stage compressor from 2.5MPa to 4.5MPa. The reason for the increase of COP with increase of P_{H1} is the same as in the case of the Economizer cycle. It is due to a larger decrease of the compression work and a smaller decrease of the heat removal capacity of the evaporator.

4.1.4 Effect of High-Side Pressure on COP

As mentioned above, the COP of the transcritical CO₂ cycle depends strongly on the low-side pressure if the evaporator is selected correctly. In addition, the COP is dependent on pressure ratio split between the two compressors in case of the two-stage compression cycles. In this section, the optimum condition for pressure at the gas cooler is investigated for the Intercooler cycle at a given air temperature and CO₂ pressure at the evaporator.

The COP of the Intercooler cycle has been calculated by changing the high-side pressure for given CO₂ temperature, T_{H1} , and pressure, p_{H1} , at the inlet to the 1st-stage compressor with several air temperature, T_{air} . The values of T_{H1} and p_{H1} are 26.7°C and 3.5Mpa, respectively. Figures 4.10 through 4.14 show the change of the maximum COPs over high-side pressure for the given air temperatures of 27.8°C, 35°C, 40.6°C, 46.1°C and 51.7°C, respectively. In the legend of the figures, 'Intercooler-1' and 'Intercooler-2' stand for the Intercooler cycle with identical pressure ratios for both compressors and different pressure ratios, respectively. The calculation has been performed at the high-side pressures (P_{H2}) of 8MPa, 10MPa and 12MPa. It can be observed from these figures that the maximum COP does not occur at the same high-side pressure. In other words,

there is a specific high-side pressure at which the maximum COP occurs for a given air temperature. When the air temperature is low, $T_{air}=27.8^{\circ}\text{C}$, the maximum COP occurs at the high-side pressure of 8MPa. At an intermediate air temperature, $35^{\circ}\text{C} \leq T_{air} \leq 40.6^{\circ}\text{C}$, the maximum COP occurs at 10.0MPa. When the air temperature is high, it occurs at 12MPa.

This phenomenon happens due to the significant change of the enthalpy of the CO_2 over temperature drop at a specific pressure after the critical point as shown in Figure 4.15. Figure 4.15 shows the thermodynamic characteristics of the CO_2 on the p-h diagram. One of the assumptions is that the CO_2 temperature drops down to the air temperature due to the heat rejection in the gas cooler. When the air temperature is 27.8°C , the ratio of the decrease of the CO_2 enthalpy through the gas cooler to the compression work becomes larger at the high pressure of 8.0MPa than at 10.0MPa or at 12.0MPa. Therefore, when the air temperature is 27.8°C , the COP becomes the largest at the high-side pressure of 8MPa by assuming the isenthalpic expansion. However, when T_{air} is 35°C or 40.6°C , the largest ratio of the CO_2 enthalpy change to the compression work occurs at 10.0MPa. When the air temperature is very high, 46.1°C or 51.7°C , it occurs at 12.0MPa of the high-side pressure.

Some other cases are analyzed under similar conditions to the previous cases, except for the CO_2 temperature (T_{11}) of 32.2°C at the inlet to the 1st-stage compressor. The values of T_{11} and p_{11} are 32.2°C and 3.5Mpa, respectively. Figures 4.16 through 4.19 show the change of the maximum COPs over high-side pressure for the given air temperatures of 35°C , 40.6°C , 46.1°C and 51.7°C , respectively. As shown in these

figures, the results of these cases demonstrate similar behavior of the COP to the previous cases.

In order to obtain the high-side pressure at which the maximum COP occurs at a given air temperature, the calculation of the COP has been performed again by increasing the high-side pressure from 8MPa to 12MPa in 0.2MPa increments. The different pressure ratios for the compressors are considered by variation of the pressure ratio across the 1st-stage compressor from 1.0 to 3.5 by 0.02. Figures 4.20 through 4.24 show the behavior of the COP in the three-dimensional axes. The x-axis, y-axis and z-axis represent the high-side pressure, pressure ratio, and COP, respectively. From these figures, it can be seen that there is a specific high-side pressure at which the maximum COP of the cycle occurs. It can also be observed that there is a pressure ratio across the 1st-stage compressor at which the COP becomes the maximum. Table 4.2 shows the maximum COP values for a given condition, the high-side pressure and pressure ratio across the 1st-stage compressor at which the maximum COP occurs.

It can be deduced from these results that if the pressure at the gas cooler is chosen carefully for a given CO₂ temperature at the outlet of the gas cooler, high thermodynamic performance of the cycle can be obtained. In addition, the different pressure ratio across the 1st-stage compressor should be also decided for optimum thermodynamic performance.

4.1.5 Summary for Cycles with an Economizer or Intercooler

The transcritical CO₂ cycles with an economizer or an intercooler (Economizer cycle and Intercooler cycle) have been considered for analysis of their thermodynamic

performances. The results show that there is significant improvement of the COP in the Economizer cycle and Intercooler cycle. It is also observed that the higher the low-side pressure is, the higher the COP of the CO₂ cycle. The effect of the pressure ratios for the compressors has also been investigated. When the cycles are optimized, different pressure ratios for each compressor give better performance than using identical pressure ratios across the both compressors during warm weather period. The coefficient of performance of the transcritical CO₂ cycle with two compressors including intercooling (Intercooler cycle) depends on the high-side pressure for a given air temperature as a heat sink. It is also dependent of the pressure ratio across the 1st-stage compressor for a given pressure difference between the low-side pressure and the high-side pressure.

4.2 Results of Analysis for Cycles with Work Extraction

4.2.1 Constant Pressure Ratios across Compressors

Table 4.3 shows the results of the analysis for various CO₂ cycles with and without the ED-WOW. In the analysis shown in Table 4.3, constant pressure ratios across the compressors were considered for the Intercooler cycle (Case 5 and 6) and the Economizer cycle (Case 7). The percentage of the pressure increase across the 1st- and 2nd-stage compressors of the Intercooler cycle were 85.22% and 14.78%, respectively, which equals to pressure ratios of 1.88 (1st-stage) and 1.08 (2nd-stage) at an evaporator pressure of 5.087 MPa and a CO₂ gas cooler pressure of 10.34 MPa. These pressure ratios were chosen because they gave maximum COP at upper limit design point

conditions of an evaporator pressure of 5.087 MPa (equal to an evaporation temperature of 15°C), a CO₂ gas cooler outlet temperature of 55°C, and a CO₂ gas cooler pressure of 10.34 MPa.

For the Economizer cycle, equal pressure ratios across each compressor stage were used. This is due to the fact that if the pressure ratios of 1.88 and 1.08 (as used in the Intercooler cycle) are used, the intermediate pressure becomes higher than the critical pressure at the design point conditions. Therefore, a single-phase fluid will enter the accumulator, which is at the intermediate pressure, and no phase separation will occur. Thus, the cycle is not applicable (N/A). Even by assuming equal pressure ratios across the first and second stage compressors, for some operating conditions the state of carbon dioxide at the accumulator inlet is compressed liquid ("Comp. Liq.") or superheated vapor ("Sup. Vapor"), which makes the cycle not applicable, as shown in Table 4.3. In these cases, an analysis of the compression work, heat removal capacity of the evaporator, and COP was omitted and labeled "N/A".

There are eight kinds of operating condition labeled "OC-1" through "OC-8" for each CO₂ cycle. "OC" stands for the operating condition. The operating condition OC-8 is the upper limit design point condition (CO₂ evaporation temperature (T_{evap}) = 15°C, CO₂ temperature at the gas cooler outlet ($T_{\text{gas-out}}$) = 55°C, and high-side pressure (p_{high}) = 10.34 MPa). For the first four operating conditions, OC-1 through OC-4, the evaporator temperature is changed while the other parameters are fixed. As shown in the table, the COP of the Base cycle (Case 1) increases with an increase in evaporation temperature (or pressure). This is due to the small decrease of the heat removal capacity of the evaporator compared to the large decrease of the compression work as T_{evap} increases.

For the next five conditions (OC-4 through OC-8), $T_{\text{gas-out}}$ is changed while the other parameters are fixed. As shown in Table 4.3, the COP of the Base cycle decreases with the increase of $T_{\text{gas-out}}$. The COP becomes 0.49 at the upper limit design point condition, OC-8. This is caused by the significant decrease of the heat removal capacity of the evaporator.

The same trend is observed in the other CO₂ cycles (Case 2 through Case 7). When the COPs of the CO₂ cycles are compared at the operating condition OC-8, the IHX cycle with the ED-WOW (Case 4) gives the highest COP, 1.798, by using the work output of the ED-WOW to assist the compression work. This is due to the relatively large heat removal capacity of the evaporator caused by the heat transfer from hot CO₂ to cold CO₂ through the internal heat exchanger. As shown in Table 4.3, Case 4 gives the highest COP when $T_{\text{gas-out}}$ is very high (50°C and 55°C). However, when $T_{\text{gas-out}}$ is not as high (less than or equal to 45°C), the Intercooler cycle with the ED-WOW (Case 6) gives the highest COP. This is due to relatively small compression work compared to that of Case 4.

Two cases are considered for the ED-WOW. The first case is that only the lower enthalpy effect of the ED-WOW at the inlet to the evaporator is considered. Then, the work extraction effect as well as the lower enthalpy effect has been considered and the extracted work has been assumed to be used to run the compressor. As shown in Table 4.3, the COPs of the CO₂ cycle are increased a little in the first case. However, the system performance is improved significantly when both effects of the expansion device are considered as shown in the table.

Based on this analysis, it can be concluded that at high $T_{\text{gas-out}}$, the IHX cycle with the ED-WOW gives the highest system performance, and at intermediate $T_{\text{gas-out}}$, the intercooler cycle with the ED-WOW shows the best system performance. It can also be concluded that when the ED-WOW is used instead of a throttling expansion valve, the system performances of the CO_2 cycles increase significantly. For instance, the COP of the Base cycle is increased by up to 112% with the ED-WOW.

4.2.2 Different Pressure Ratios across Compressors

Table 4.4 shows the results of the analysis for the Intercooler cycle (Case 8), Intercooler cycle with the ED-WOW (Case 9), and Economizer cycle (Case 10) with varying pressure ratios across the first and second stage compressors. For each operating condition, the pressure ratios across the first and second stage compressors were adjusted to give the maximum system COP. Table 4.4 indicates the optimum pressure ratios and the maximum COPs for the cycles.

By comparing the COPs in Table 4.3 and Table 4.4, it can be observed that the COPs of the Intercooler and Economizer cycles can be significantly increased by selecting the optimum pressure ratios for the given operating conditions. However, to independently control the intermediate pressure in two-stage compression systems as a function of operating conditions may be a difficult task to achieve in actual equipment.

As discussed in the previous section, the system performances of the transcritical CO_2 cycles are increased considerably with the ED-WOW as shown in Table 4.4.

4.3 Results of Theoretical Model for ED-WOW Device

Analysis of the ED-WOW has been performed using the developed simulation model. As discussed before, the ED-WOW consists of flat twin-cylinder in which the pistons are on out-of-phase firing order. In the analysis it is assumed that there is no time-delay of the valves to respond to input signals. This assumption gives conservatism in terms of the CO₂ mass flow into the cylinder of the ED-WOW.

Four revolution speeds of crankshaft are considered. Those are 120 rpm, 240 rpm, 360 rpm, and 600 rpm. The one revolution of the crankshaft takes 0.5 s for 120 rpm, 0.25 s for 240 rpm, 0.167 s for 360 rpm, and 0.1 s for 600 rpm, respectively. The input values for the parameters are shown in Table 4.5. Among the input values, the crown height of the piston ring and friction coefficient of the cylinder are assumed to be 14.9 μm and 0.08. As discussed before, it is considered that the valves open and close instantaneously and the LOE is fixed in this analysis. Figure 4.25 shows the piston speeds of the ED-WOW over its crank angle. As expected, the piston speed becomes faster as the revolution speed increases.

The analysis has been done for several revolutions of the crankshaft to remove any uncertainties which may exist in the input values. As shown in figure 4.26, the same trends of the pressure behavior are repeated for 120 RPM and 240 RPM during the 2nd, 3rd, 4th, and 5th revolutions. Therefore, the second revolution (360° ~720°) of the crankshaft is the focused of the current analysis.

4.3.1 Chamber Pressure

Figure 4.27 shows the behavior of the CO₂ pressure in the chamber over the crank angle. It can be seen in this figure that the low revolution speeds of this expansion device, 120 rpm and 240 rpm, are better than other faster speeds to get the inlet high pressure inside the cylinder. When the speed becomes equal to or faster than 360 rpm, the valve opening time is too short for the carbon dioxide to fill the chamber and to reach the pressure upstream of the inlet valve because of the characteristics of the valves as described in Chapter 3. In addition, the power loss becomes larger due to the increase of friction force with the faster speed and it reduces the pressure and temperature inside the chamber of the ED-WOW.

When the speed of device is 240 rpm, there is an increase of pressure in the cylinder during the exhaust process as shown in Figure 4.27. This is because of small orifice diameter of the exhaust valve and relatively short time period to sweep out the expanded CO₂ from the cylinder compared to the case of 120 rpm. Therefore, the revolution speed of the device of 120 rpm is considered as the optimum operating speed for our application. As discussed in Chapter 3, the speed of 120 rpm was also considered as the optimum operating speed based on the experiments. Only the case of 120 rpm is analyzed and discussed in detail in the rest of this section.

In the case of 120 rpm the pressure in the cylinder reaches the intake pressure very quickly and remains constant during the rest of the intake period as shown in Figure 4.27. Then, it decreases suddenly as CO₂ expands in the expansion process. At the end of the expansion, the CO₂ pressure becomes about 3.4MPa that is the desired operating

low-side pressure. This means that the location of the expansion initiation of 8.01 mm from the top of the chamber (5.21 mm from TDC) was determined reasonably well.

The pressure oscillates at the end of the exhaust period. This is due to the dynamic behavior of the CO₂ flow. The pressure in the chamber reaches the pressure at the inlet of the evaporator (or in the crank housing) at the angle of the crankshaft of around 680 degree. At the next time step, the chamber pressure becomes less than that of crank housing due to the CO₂ discharge so that there is no mass discharge because there is no driving force to sweep out the expanded CO₂ from the cylinder. As the piston moves up further, however, the chamber volume decreases and it leads to increase of the chamber pressure and CO₂ mass is discharged. This behavior continues until the end of the exhaust process.

4.3.2 Work Done by CO₂

This simulation model predicts the work done by CO₂ as shown in Figure 4.28. Positive work stands for the work done into the CO₂ and negative work means the work done by CO₂. It can be seen in this figure that the work is produced during the intake and expansion processes but work is required to push the piston up and to sweep out CO₂ from the device to the inlet of the evaporator through the exhaust valve during the exhaust period, as expected. However, the work output is much larger than the work required so that work is generated through the device. The work generated is 40.6 J/piston-revolution when the device is being operated at 120 rpm with the high-side pressure of 10.3 MPa and the low-side pressure of 3.4 MPa.

4.3.3 Minimum Film Thickness Under the Piston Ring

Figure 4.29 shows the minimum film thickness under the piston ring. As shown in the figure, the film thickness is constant over the whole processes. Its value is too small and the same as the composite roughness of the cylinder. This means that there is always the boundary lubrication but no hydrodynamic lubrication. There is always the piston scuffing. This boundary lubrication occurs due to the very low piston speed in this case, as shown in Figure 4.25. The low piston speed leads to low pressure under the piston ring so that the internal gas pressure is always high enough to push the piston ring radially and outwardly and the ring touches the surface of the cylinder wall always.

4.3.4 Power Loss

As discussed in the previous section, the piston ring scuffing occurs during the whole processes. Therefore, the power loss is due to only the friction of the piston ring as shown in Equation (2-63). There is no power loss due to the squeeze motion of the piston ring because the ring always touches the surface of the cylinder wall. The power loss becomes small as shown in Figure 4.30. The total power loss is about 2.1 J/piston-revolution in this case.

There is a sharp decrease of the power loss as the expansion process begins. This is due to the sudden decrease of the pressure inside the device at that point as shown in Figure 4.27. The power loss depends on the pressure inside the expansion device as described in Equations (2-61) through (2-63).

4.4 Experimental Results for Cycle with ED-WOW Device

The ED-WOW has been implemented into a prototype transcritical CO₂ cycle as shown in Figure 2.35. As shown in the figure, the system consists of an evaporator, a compressor, a gas cooler, an internal heat exchanger, and an ED-WOW. In addition, there is an ordinary expansion valve. Experiments have been performed to investigate the system performance and the concept of the ED-WOW has been proved by the improvement of the system efficiency.

4.4.1 Experimental Test Conditions

Experiments have been performed for three different operating conditions. Table 4.6 shows the experimental conditions for the cases. In the table, T_{indoor} and T_{outdoor} stand for the indoor temperature and outdoor temperature, respectively. The same indoor and outdoor temperatures have been considered for all cases and they are 20°C and 35°C, respectively. $P_{\text{c,out}}$, $P_{\text{c,in}}$, $T_{\text{c,out}}$, and $T_{\text{c,in}}$ indicate the compressor discharge pressure, compressor suction pressure, compressor discharge temperature, and compressor suction temperature, respectively. The compressor discharge pressure considered is 6620 kPa to 7971 kPa and the compressor suction pressure changes from 2528 kPa to 2771 kPa. The compressor discharge temperatures considered are from 88°C to 118°C and the compressor suction temperature is approximately 20°C for all cases. \dot{m}_{CO_2} represents the CO₂ mass flow rate in the system and the range of 9.7 kg/s to 13.5 g/s has been determined based on the compressor capacity. ω_{ED} and Δt_{intake} are the rotational speed and the intake valve opening time of the ED-WOW.

$P_{gc,in}$, $P_{gc,out}$, $P_{ED,in}$, $P_{ED,out}$, and $P_{evap,out}$ are the pressures at the inlet and outlet of the gas cooler, at the inlet and outlet of the ED-WOW, and at the outlet of the evaporator, respectively. $T_{gc,in}$, $T_{gc,out}$, $T_{ED,in}$, and $T_{evap,out}$ are the temperature at the inlet and outlet of the gas cooler, at the inlet of the ED-WOW, and at the outlet of the evaporator, respectively.

4.4.2 Cycle Performance

Figure 4.31 shows the p-h diagram of the processes of the system for all cases. The numbers in the figure show the state at each point. Those states are also shown in Figure 2.35. As shown in Table 4.6 and Figure 4.31, the pressure at the outlet of the compressor, 7971 kPa, is higher than the critical pressure of CO₂ (7377 kPa) in Case 3.

There is a relatively large pressure drop from state 4, the outlet of the gas cooler, to state 5, the inlet of the ED-WOW. This is due to the many valves and fittings and the internal heat exchanger (IHX) between these stations as shown in Figures 2.35 and 2.36. These valves have been arranged to measure the mass flow rate of CO₂ during the experiment. It can also be seen in the figure that pressure decreases relatively much from the outlet of the evaporator to the inlet of the compressor. This is caused by the internal heat exchanger and the accumulator between the evaporator and compressor.

The process from state 5 to state 7 stands for the case of the isenthalpic expansion process (assuming the expansion through the ordinary expansion valve) in Figure 4.31. As expected, the enthalpy decreases at the inlet of the evaporator when CO₂ expands through the ED-WOW even though the amount of the enthalpy decrease does not seem great

As previously mentioned, the work generated through the ED-WOW has been measured indirectly by measuring the power of the hydraulic pump. The efficiency of the pump was measured at approximately 50% at an ED-WOW speed of 300 RPM. As the design speed of the ED-WOW in the current tests is 120 RPM, the pump efficiency can be expected to be less than this value. As the actual pump efficiency could not be measured at this low speed, the current assumption of the pump efficiency will be taken at 50% which will thus provide a conservative estimate of the work extracted from the ED-WOW.

The measured works produced by the ED-WOW are 23.2 W, 28.7 W, and 34.8 W for Cases 1, 2, and 3, respectively. As pressure difference increases across the ED-WOW, the work produced increases. The measured isentropic efficiency of the ED-WOW ($\epsilon_{s,ED}$) is about 10% as shown in Table 4.7.

Table 4.7 and Table 4.8 show the results of the experiments. $P_{ED,in}$, $P_{ED,out}$, and $T_{ED,in}$ stand for the pressures at the inlet and outlet of the ED-WOW and the temperature at the inlet of the ED-WOW, respectively. \dot{Q}_{isenth} and \dot{Q}_{ED} represent the evaporator capacity when CO₂ expands through the ordinary expansion valve and the ED-WOW, respectively. As discussed above, the evaporator capacity increases with the CO₂ expansion through the ED-WOW. \dot{W}_{comp} and \dot{W}_{ED} illustrate the compressor work and the work produced through the ED-WOW, respectively. COP_{EXV} is the COP based on the isenthalpic expansion. COP_{ED-1} and COP_{ED-2} are the COPs based on the expansion through the ED-WOW. COP_{ED-1} is the COP of the system when only the lower enthalpy effect is considered. When not only the lower enthalpy effect but also work output effect

is considered, COP_{ED-2} is calculated by reducing the compressor work input. This means that the work produced through the ED-WOW is considered to use to run the compressor, some part of the compression work. So, it saves some compression work. Those COPs are calculated as follows:

$$COP_{EXV} = \frac{\dot{Q}_{isenth}}{\dot{W}_{comp}} \quad (4-3)$$

$$COP_{ED-1} = \frac{\dot{Q}_{ED}}{\dot{W}_{comp}} \quad (4-4)$$

$$COP_{ED-2} = \frac{\dot{Q}_{ED}}{\dot{W}_{comp} - \dot{W}_{ED}} \quad (4-5)$$

The concept of the ED-WOW to improve system performance has been proven experimentally. As shown in Tables 4.7 and 4.8, the COP increases with the ED-WOW. When only the effect of lower enthalpy is considered, the COP increases by 3.3% to 5.4% compared to the COP based on the isenthalpic expansion. If both of the lower enthalpy and work producing effects are considered, COP are increased much by 6.7% to 9.9%. Again, as mentioned previously, the hydraulic pump efficiency that is used to calculate the work output of the ED-WOW is a conservative estimate. If a more accurate efficiency at the given condition is used, it is likely the work output through the ED-WOW will be larger than the value resulting in more improvement in the system performance.

As shown in Table 4.7, the capacity of the evaporator increases with increase of the high-side pressure (compressor discharge pressure). In addition, the work produced through the ED-WOW is increased when $P_{c,out}$ increases. However, the percentage of the

increase of the evaporator and COP_{ED-1} decreases with the increase of the $P_{c,out}$. The largest percentage for the increase of \dot{Q}_{ED} occurs in Case 1 and for the increase of COP_{ED-1} also in Case 1. When both of the lower enthalpy and work output effects are considered, there is the same tendency that the system performance improvement decreases with the increase of $P_{c,out}$. The largest improvement of the system performance occurs in Case 1 (lowest compressor discharge pressure, 6621 kPa) and it is 9.9%. When the compressor discharge pressure is highest (7971 kPa, Case 3), the system efficiency improvement becomes the smallest and it is 6.7% even though the absolute amounts of enthalpy decrease at the inlet of the evaporator and work output through the ED-WOW are the largest.

4.4.3 Uncertainty Analysis

An uncertainty analysis was conducted for the results of the experiments. The Kline and McClintock method [Kline and McClintock, 1953] was used which sums the square of errors:

$$w_A = \left[\sum_{i=1}^j \left(\frac{\partial A}{\partial z_i} w_z \right)^2 \right]^{\frac{1}{2}} \quad (4-6)$$

where w_A , z_i , and w_z are the total uncertainty associated with the dependent variable A, the independent variable which affects the dependent variable A, and the uncertainty of the variable z_i , respectively. Equation (4-6) is referred to as the second-power equation. The uncertainties of the measurements are given in Table 4.9.

The work generated through the ED-WOW is calculated as:

$$\dot{W}_{ED} = \frac{\dot{V} \Delta p_{pump}}{\eta_{pump}} = \frac{\dot{V} (p_{pump,o} - p_{pump,i})}{\eta_{pump}} \quad (4-7)$$

where \dot{V} , Δp_{pump} , η_{pump} , $p_{pump,o}$, and $p_{pump,i}$ are volumetric flow rate of water, pressure difference across the hydraulic pump, the efficiency of the pump, the static pressure at the outlet of the pump, and the static pressure at the inlet of the pump, respectively. Actually, there is a large uncertainty in the efficiency of the pump. However, the uncertainty analysis has been conducted for the given pump efficiency (fixed pump efficiency).

The total uncertainty for the generated work becomes:

$$\frac{w_{\dot{W}_{ED}}}{\dot{W}_{ED}} = \left[\left(\frac{w_{\dot{V}}}{\dot{V}} \right)^2 + \left(\frac{w_{p_{pump,o}}}{\Delta p_{pump}} \right)^2 + \left(\frac{w_{p_{pump,i}}}{\Delta p_{pump}} \right)^2 \right]^{\frac{1}{2}} \quad (4-8)$$

where $w_{\dot{W}_{ED}}$, $w_{\dot{V}}$, $w_{p_{pump,o}}$, and $w_{p_{pump,i}}$ represent the uncertainties for the work produced through the ED-WOW, volumetric water flow rate, pressure at the outlet of the pump, and pressure at the inlet of the pump, respectively.

The ideal work output in an isentropic expansion process is:

$$\dot{W}_{s,ED} = \dot{m} (h_{ED,i} - h_{s,ED,o}) \quad (4-9)$$

where \dot{m} , $h_{ED,i}$, and $h_{s,ED,o}$ stand for CO₂ mass flow rate, enthalpy at the inlet of the ED-WOW, and enthalpy at the outlet of the ED-WOW for the isentropic expansion process, respectively. The enthalpy at the outlet of the ED-WOW is a function of the pressure at the outlet of the ED-WOW and the entropy at the inlet of the ED-WOW:

$$h_{s,ED,o} = f(p_{ED,o}, s_{ED,i}) \quad (4-10)$$

where $p_{ED,o}$ and $s_{ED,i}$ are the pressure at the outlet of the ED-WOW and the entropy at the inlet of the ED-WOW, respectively. The entropy at the inlet of the ED-WOW is given by:

$$s_{ED,i} = f(p_{ED,i}, T_{ED,i}) \quad (4-11)$$

where $p_{ED,i}$, and $T_{ED,i}$ are the pressure and temperature at the inlet of the ED-WOW, respectively. Also, the enthalpy at the inlet of the ED-WOW is a function of pressure and temperature is given by:

$$h_{ED,i} = f(p_{ED,i}, T_{ED,i}). \quad (4-12)$$

The uncertainty of the ideal work output through the ED-WOW becomes:

$$\frac{w_{\dot{W}_{s,ED}}}{\dot{W}_{s,ED}} = \left[\left(\frac{w_{\dot{m}}}{\dot{m}} \right)^2 + \left(\frac{w_{h_{ED,i}}}{h_{ED,i} - h_{s,ED,o}} \right)^2 + \left(\frac{w_{s,h_{ED,o}}}{h_{ED,i} - h_{s,ED,o}} \right)^2 \right]^{\frac{1}{2}} \quad (4-13)$$

where $w_{\dot{W}_{s,ED}}$, $w_{\dot{m}}$, $w_{h_{ED,i}}$, and $w_{s,h_{ED,o}}$ are the uncertainties of the ideal work produced through the ED-WOW, CO₂ mass flow rate, enthalpy at the inlet of the ED-WOW, and enthalpy at the outlet of the ED-WOW for the isentropic expansion process, respectively. The uncertainty for the enthalpy at the inlet of the ED-WOW is calculated as follows:

$$\frac{w_{h_{ED,i}}}{h_{ED,i}} = \left[\left(\frac{w_{p_{ED,i}}}{p_{ED,i}} \right)^2 + \left(\frac{w_{T_{ED,i}}}{T_{ED,i}} \right)^2 \right]^{\frac{1}{2}} \quad (4-14)$$

where $w_{p_{ED,i}}$, and $w_{T_{ED,i}}$ are the uncertainties for the pressure and temperature at the inlet of the ED-WOW, respectively. The enthalpy, $h_{ED,i}$, is a relative value to a reference

point. For conservatism and convenience, the enthalpy difference of $h_{ED,i} - h_{s,ED,o}$ is used instead of $h_{ED,i}$. Hence, the uncertainty becomes:

$$\frac{w_{h_{ED,i}}}{h_{ED,i} - h_{s,ED,o}} = \left[\left(\frac{w_{p_{ED,i}}}{p_{ED,i}} \right)^2 + \left(\frac{w_{T_{ED,i}}}{T_{ED,i}} \right)^2 \right]^{\frac{1}{2}}. \quad (4-15)$$

The uncertainty for the enthalpy at the outlet of the ED-WOW is:

$$\frac{w_{s,h_{ED,o}}}{h_{s,ED,o}} = \left[\left(\frac{w_{p_{ED,o}}}{p_{ED,o}} \right)^2 + \left(\frac{w_{s_{ED,i}}}{s_{ED,i}} \right)^2 \right]^{\frac{1}{2}} \quad (4-16)$$

where $w_{p_{ED,o}}$, and $w_{s_{ED,i}}$ are the uncertainties for the pressure at the outlet of the ED-WOW and entropy at the inlet of the ED-WOW, respectively. Again, the enthalpy difference of $h_{ED,i} - h_{s,ED,o}$ is used instead of $h_{s,ED,o}$. The uncertainty is written as:

$$\frac{w_{s,h_{ED,o}}}{h_{ED,i} - h_{s,ED,o}} = \left[\left(\frac{w_{p_{ED,o}}}{p_{ED,o}} \right)^2 + \left(\frac{w_{s_{ED,i}}}{s_{ED,i}} \right)^2 \right]^{\frac{1}{2}}. \quad (4-17)$$

The uncertainty at the inlet of the ED-WOW becomes:

$$\frac{w_{h_{ED,i}}}{s_{ED,i}} = \left[\left(\frac{w_{p_{ED,i}}}{p_{ED,i}} \right)^2 + \left(\frac{w_{T_{ED,i}}}{T_{ED,i}} \right)^2 \right]^{\frac{1}{2}}. \quad (4-18)$$

The total uncertainty for the ideal work produced through the ED-OW can be obtained by substituting the uncertainties of Equations (4-15), (4-17) and (4-18) in Equation (4-13).

The isentropic efficiency of the ED-WOW is calculated as follows:

$$\eta_{ED} = \frac{\dot{W}_{ED}}{\dot{W}_{s,ED}}. \quad (4-19)$$

The uncertainty of the isentropic efficiency becomes:

$$\frac{w_{\eta_{ED}}}{\eta_{ED}} = \left[\left(\frac{w_{\dot{W}_{s,ED}}}{\dot{W}_{s,ED}} \right)^2 + \left(\frac{w_{\dot{W}_{ED}}}{\dot{W}_{ED}} \right)^2 \right]^{\frac{1}{2}}. \quad (4-20)$$

The heat removal capacity of the evaporator is expressed as:

$$\dot{Q}_{ED} = \dot{m}(h_{evap,o} - h_{evap,i}) \quad (4-21)$$

where \dot{Q}_{ED} , $h_{evap,o}$, and $h_{evap,i}$ are the heat capacity of the evaporator, enthalpy at the outlet of the evaporator, and enthalpy at the inlet of the evaporator, respectively. The enthalpy at the inlet of the evaporator is given by:

$$\dot{m}h_{evap,i} = \dot{m}h_{ED,i} - \dot{W}_{ED} \quad (4-22)$$

Hence, Equation (4-22) can be written as:

$$\dot{Q}_{ED} = \dot{m}(h_{evap,o} - h_{ED,i}) + \dot{W}_{ED}. \quad (4-23)$$

The uncertainty of the heat capacity of the evaporator becomes:

$$w_{\dot{Q}_{ED}} = \left[\left((h_{evap,o} - h_{ED,i})w_{\dot{m}} \right)^2 + \left(\dot{m}w_{h_{evap,o}} \right)^2 + \left(\dot{m}w_{h_{ED,i}} \right)^2 + \left(w_{\dot{W}_{ED}} \right)^2 \right]^{\frac{1}{2}} \quad (4-24)$$

where $w_{\dot{Q}_{ED}}$ and $w_{h_{evap,o}}$ are the uncertainties of the heat capacity of the evaporator and the enthalpy at the outlet of the evaporator, respectively. The enthalpy at the outlet of the evaporator is a function of pressure and temperature at the outlet of the evaporator as follows:

$$h_{evap,o} = f(p_{evap,o}, T_{evap,o}) \quad (4-25)$$

where $p_{evap,o}$ and $T_{evap,o}$ are the pressure and temperature at the outlet of the evaporator, respectively. Therefore, the uncertainty of the enthalpy at the outlet of the evaporator can be obtained as follows:

$$\frac{w_{h_{evap,o}}}{h_{evap,o}} = \left[\left(\frac{w_{p_{evap,o}}}{p_{evap,o}} \right)^2 + \left(\frac{w_{T_{evap,o}}}{T_{evap,o}} \right)^2 \right]^{\frac{1}{2}} \quad (4-26)$$

where $w_{h_{evap,o}}$, $w_{p_{evap,o}}$, and $w_{T_{evap,o}}$ are the uncertainty of the enthalpy, pressure, and temperature at the outlet of the evaporator, respectively. Again, for conservatism and convenience, the enthalpy difference of $h_{evap,o} - h_{ED,i}$ is used instead of $h_{evap,o}$. Hence, the uncertainty becomes:

$$\frac{w_{h_{evap,o}}}{h_{evap,o} - h_{ED,i}} = \left[\left(\frac{w_{p_{evap,o}}}{p_{evap,o}} \right)^2 + \left(\frac{w_{T_{evap,o}}}{T_{evap,o}} \right)^2 \right]^{\frac{1}{2}}. \quad (4-27)$$

The uncertainty of the heat capacity of the evaporator can be obtained by substituting the correct uncertainty values into Equation (4-24).

The compression work is expressed as follows:

$$\dot{W}_{comp} = \tau \omega \quad (4-28)$$

where \dot{W}_{comp} , τ , and ω are the compression work rate, torque of the compressor, and rotational speed of the compressor, respectively. The uncertainty of the compression work becomes:

$$\frac{w_{\dot{W}_{comp}}}{\dot{W}_{comp}} = \left[\left(\frac{w_{\tau}}{\tau} \right)^2 + \left(\frac{w_{\omega}}{\omega} \right)^2 \right]^{\frac{1}{2}} \quad (4-29)$$

where $w_{\dot{W}_{comp}}$, w_{τ} , and w_{ω} stand for the uncertainties of the torque and rotational speed of the compressor, respectively.

The COP is calculated by dividing the heat capacity of the evaporator by the compression work as follows:

$$COP = \frac{\dot{Q}_{ED}}{\dot{W}_{comp} - \dot{W}_{ED}} \quad (4-30)$$

The uncertainty of the COP is obtained as:

$$\frac{w_{COP}}{COP} = \left[\left(\frac{w_{\dot{Q}_{evap}}}{\dot{Q}_{evap}} \right)^2 + \left(\frac{w_{\dot{W}_{comp}}}{\dot{W}_{comp} - \dot{W}_{ED}} \right)^2 + \left(\frac{w_{\dot{W}_{ED}}}{\dot{W}_{comp} - \dot{W}_{ED}} \right)^2 \right]^{\frac{1}{2}} \quad (4-31)$$

where w_{COP} is the uncertainty of the COP.

Table 4.10 shows the calculated uncertainties for Case 3. As shown in the table, the uncertainty of the work generated through the ED-WOW is relatively large. This is due to the fact that the instrumentations that were used to measure the pressures and water flow rate were oversized for the recorded measurements. In order to reduce the uncertainties, instrumentations with appropriate measurements ranges need to be used. The large uncertainty value of the isentropic efficiency of the ED-WOW is caused by the large uncertainty of the work produced through the ED-WOW.

4.5 Analysis of the ED-WOW as Installed in Cycle

The ED-WOW has been analyzed with the theoretical model for the experiments (Case 1 through Case 3). For more realistic simulation the time-delay of 0.053 s is assumed for the intake valve to respond to the input signal for closing in this analysis. As discussed in Chapter 3, the time-delays of the valves were measured experimentally.

Figure 4.32 shows the results of the simulation for the pressure behavior inside the cylinder of the ED-WOW. Table 4.11 also indicates some results of the simulation. In Table 4.11 the first row represents the case number and the next four rows stand for the ED-WOW inlet pressure, ED-WOW outlet pressure, CO₂ mass flow rate, work produced through the ED-WOW in the experiments. The rest of the rows in Table 4.11 indicate the predicted values.

As shown in Figure 4.32, the predicted pressures at the end of the expansion are higher than the experiments for all cases. This means that the predicted density inside the cylinder at that point is higher than the experiment. The predicted density should be reduced to decrease the pressure at the end of the expansion. This means that there is some leakage of CO₂ from the cylinder to the crank housing through the piston ring during the experiments. This fact can be ascertained by comparing the CO₂ mass flow rates of the experiments and simulations shown in the 4th and 7th rows in Table 4.11. The value of mass flow rate in the 7th row has been predicted by considering zero leakage of CO₂ through the piston ring. As shown in the table, the measured mass flow rates are larger than the predicted ones.

The simulations have been repeated by considering some leakage of CO₂ through the piston ring during the intake and expansion processes as shown in Table 4.11. The values of the 10th row through 15th row are predicted with the assumption of the leakage of CO₂. The rates of the leakage have been determined by the trial and error method in order to make the similar mass flow rates with the experiments as shown in the 4th and 11th rows. With some leakage of CO₂, the predicted pressures at the end of expansion are decreased much compared to the values of the zero leakage assumption and those values

are very similar to the measured ones especially for Case 1 and Case 2 as shown in the 3rd and 10th rows in Table 4.11. The predicted pressure is still a bit higher than the measured one for Case 3. The general results and trends of the simulation with the assumption of the leakage are in a good agreement with the experiments. Therefore, it can be deduced that there is a leakage of CO₂ from the cylinder of the ED-WOW to the crank housing through the piston ring during the intake and expansion processes. The predicted CO₂ leakage rate and its percentage to the total CO₂ flow rate are shown in the 13th and 14th rows in Table 4.11. The range of the leakage rate is about 31.3% to 39.6% of the CO₂ mass flow rate. Figure 4.33 shows the pressure behavior inside the cylinder with the assumption of some leakage of CO₂.

The leakage rate is 4.21 g/s and its percentage is 31.3% of the CO₂ flow rate for Case 3. The percentage seems to be high and thus, it was checked if the predicted leakage rate is reasonable by examining the leakage area. The leakage area is calculated based on the leakage flow rate.

A two-phase state is assumed in the cylinder of the ED-WOW and two-phase flow is considered for the leakage through the piston ring to the crank-housing. Equation (2-40) is used for the leakage calculation. The pressure of the crank-housing is assumed to be 3.4 MPa. Two cylinder pressures are considered. They are 7 MPa and 4 MPa. In addition, two vapor qualities, $x = 0.9$ and $x = 0.5$, are examined. These conditions will confine the possible operating condition of the ED-WOW during the experiments. Table 4.12 shows the calculation conditions and the results for Case 3.

The mass velocities are calculated by using Equation (2-40) as mentioned. Then, the flow area for the mass flow rate of 4.21 g/s is calculated and is given in the 3rd row of

Table 4.12. The ED-WOW consists of two cylinders and its rotational speed was about 120 RPM (2 Hz) during the experiments. In addition, it is assumed that the CO₂ leakage occurred only during the intake and expansion processes because the cylinder pressure needs to be higher than the pressure in the crank-housing. Therefore, the leakage area becomes half of the calculated flow rate as shown in the 4th row of Table 4.12.

If it is assumed that the end tips of the piston ring does not touch and there is a gap between the ends of piston ring, the size of the gap becomes 0.0685 mm when p_1 is 7 MPa and vapor quality is 0.9. The measured width of the piston ring is 1.067 mm as shown in Table 4.5. The calculated sizes of the leakage gap are shown in the 5th row of Table 4.12. As shown in the table, the range of the size of the leakage gap is 0.0685 mm to 0.2158 mm.

In addition, another situation is considered. If the piston ring does not touch the cylinder wall, there is a gap between the cylinder wall and the piston ring. This assumption is the opposite of the results of the simulation because the piston ring was predicted to always touch the cylinder wall based on the simulation. However, this assumption is considered in order to get some idea about the leakage area. The calculated sizes of the gap are shown in 6th row of Table 4.12. The range of the size of the gap between the cylinder wall and the piston is 8.4×10^{-4} mm to 2.65×10^{-3} mm.

The gap sizes of the leakage path seem to be possible values as shown in 5th and 6th row of Table 12. Therefore, it can be deduced that the predicted leakage flow rate of CO₂ through the piston ring, 31.3% to 39.6% of CO₂ flow rate, is reasonable.

As shown in Table 4.11, the work produced through the ED-WOW increases with the leakage of CO₂. This is due to the low pressure during the exhaust process. If the

exhaust pressure is small, there is less CO_2 mass remained inside the cylinder and less work is required to sweep out the expanded CO_2 from the cylinder to the inlet of the evaporator. This can be seen in Figure 4.34 and Figure 4.35. Figure 4.34 shows the work produced through the ED-WOW with the assumption of zero leakage. Figure 4.35 illustrates the work with some leakage of CO_2 through the piston ring. The negative work stands for the work produced by the ED-WOW and the positive work indicates the work required to sweep out the expanded CO_2 from the ED-WOW. As shown in the figures, the work produced during the intake and expansion processes are very similar with both assumptions but the works required during the exhaust process are different. As expected, less work is required when the pressure is low during the exhaust process due to the less CO_2 mass. However, there is energy loss due to the CO_2 leakage and the isentropic efficiency of the ED-WOW decreases as shown in Table 4.11. If there is no leakage, less amount of CO_2 is required to achieve the desired low pressure at the end of the expansion process and to obtain the desired work output through the ED-WOW. Therefore, some improvement of the leakage through the piston ring should be considered to increase the efficiency of the ED-WOW.

It can also be seen from Table 4.11 that the predicted works through the ED-WOW (12th row) are much larger than ones in the experiments (5th row). This means that the current method to measure the work produced is very conservative.

Figure 4.36 shows the minimum film thickness of the lubricant under the piston ring with the assumption of some leakage. As shown in this figure, its value is too small and constant over the whole processes. This means that there is always boundary lubrication for all cases. That is, the piston ring always touches the cylinder wall.

Figure 4.37 shows the predicted power loss due to the friction between the piston ring and the cylinder wall with the assumption of some leakage. As shown in the figure, the power loss becomes the largest when the pressure inside the cylinder is the highest, Case 3. This is due to the fact that when the pressure is high, there is much force to push the piston ring in radial direction to the cylinder wall and it results in increase of the friction loss. The calculated values of the power loss are 7.16 W, 7.24 W, and 8.44 W for Case 1, Case 2, and Case 3, respectively.

Table 4.1: Total compression works of the Economizer cycle for low-side pressures.

Low-side pressure (MPa)	Pressure ratio at which the maximum COP occurs	Compression work (kJ/kg)
2.5	1.84	48.383
3.0	1.70	42.017
3.5	1.56	33.249
4.0	1.46	27.330
4.5	1.38	22.575

Table 4.2: Maximum COP values, pressure ratio and high-side pressure at which the maximum COP occurs.

Case	T_H and p_H	Air temperature T_{air} (°C)	Pressure ratio across 1 st compressor	High-side pressure p_{14} (MPa)	COP
1	$T_H=26.7^\circ\text{C}$ $p_H=3.5\text{MPa}$	27.8	1.64	8.0	5.457
2		35	1.78	8.8	4.081
3		40.6	2.06	10.4	3.254
4		46.1	2.32	12.0	2.702
5		51.7	2.34	12.0	2.187
6	$T_H=32.2^\circ\text{C}$ $p_H=3.5\text{MPa}$	35	1.72	8.8	4.146
7		40.6	2.0	10.4	3.307
8		46.1	2.26	12.0	2.749
9		51.7	2.26	12.0	2.246

Table 4.3: Results of thermodynamic analysis for several CO₂ cycles
(For two stage cycles, fixed pressure ratios are considered across compressors)

Operating condition	OC-1	OC-2	OC-3	OC-4	OC-5	OC-6	OC-7	OC-8
T at evaporator (°C)	0	5	10	15	15	15	15	15
T at outlet of gas cooler (°C)	35	35	35	35	40	45	50	55
T at inlet of comp. (°C) (Cases 3 & 4)	24.5	26	27.5	29	32.5	36	39.5	43
P at evaporator (MPa)	3.485	3.969	4.502	5.087	5.087	5.087	5.087	5.087
P at gas cooler (MPa)	10.34	10.34	10.34	10.34	10.34	10.34	10.34	10.34
P intermediate (MPa) (Cases 5 & 6)	9.328	9.399	9.478	9.564	9.564	9.564	9.564	9.564
Results								
Base cycle (Case 1)								
Work of comp. (kJ/kg)	62.752	52.949	43.738	35.098	35.098	35.098	35.098	35.098
Heat cap. of evap (kJ/kg)	143.518	140.106	135.508	129.27	108.115	78.614	43.619	17.208
COP	2.287	2.646	3.098	3.683	3.08	2.24	1.243	0.49
Base + ED-WOW (Case 2)								
Heat cap. of evap (kJ/kg)	150.046	145.742	140.325	133.339	112.954	84.744	51.52	26.624
Work output throu. ED-WOW (kJ/kg)	6.528	5.636	4.817	4.069	4.839	6.13	7.901	9.416
COP without using W of WEOD	2.391	2.753	3.208	3.799	3.218	2.415	1.468	0.759
COP using W of WEOD to run comp.	2.669	3.08	3.605	4.297	3.733	2.925	1.894	1.037
IHX Cycle (Case 3)								
Work of comp. (kJ/kg)	78.623	66.07	54.393	43.552	45.17	46.694	48.142	49.526
Heat cap. of evap (kJ/kg)	179.859	174.761	168.526	160.767	145.597	121.737	92.114	70.861
COP	2.288	2.645	3.098	3.691	3.223	2.607	1.913	1.431
IHX + ED-WOW (Case 4)								
Heat cap. of evap (kJ/kg)	184.619	178.983	172.254	164.044	149.195	126.062	97.627	77.362
Work output throu. ED-WOW (kJ/kg)	4.76	4.222	3.728	3.277	3.598	4.325	5.513	6.502
COP without using W of WEOD	2.348	2.709	3.167	3.767	3.303	2.7	2.028	1.562
COP using W of WEOD to run comp.	2.499	2.894	3.4	4.073	3.589	2.975	2.29	1.798
Intercooler cycle (Case 5)								
Work of 1-st comp. (kJ/kg)	56.058	47.072	38.69	30.883	30.883	30.883	30.883	30.883
Work of 2-nd comp. (kJ/kg)	2.103	1.945	1.772	1.588	1.867	2.556	3.223	3.701
Work of total comp (kJ/kg)	58.161	49.017	40.463	32.471	32.749	33.438	34.106	35.584
Heat cap. of evap (kJ/kg)	143.518	140.106	135.508	129.27	108.115	78.614	43.619	17.208
COP	2.468	2.858	3.349	3.981	3.301	2.351	1.279	0.498
Intercooler + ED-WOW (Case 6)								
Heat cap. of evap (kJ/kg)	150.046	145.742	140.325	133.339	112.954	87.744	51.52	26.624
Work output throu. ED-WOW (kJ/kg)	6.528	5.636	4.817	4.069	4.839	6.13	7.901	9.416
COP without using W of WEOD	2.58	2.973	3.468	4.106	3.449	2.534	1.511	0.77
COP using W of WEOD to run comp.	2.906	3.36	3.937	4.695	4.047	3.103	1.966	1.058
T at outlet of intercooler (°C)	85.245	78.378	71.929	65.844	65.844	65.844	65.844	65.844
Economizer cycle (Case 7)								
Work of 1-st comp. (kJ/kg)	24.266	22.193	20.676	N/A	16.306	7.297	N/A	N/A
Work of 2-nd comp. (kJ/kg)	32.581	27.874	23.918	N/A	18.714	13.724	N/A	N/A
Work of total comp (kJ/kg)	56.847	50.067	44.594	N/A	35.02	21.021	N/A	N/A
Heat cap. of evap (kJ/kg)	138.715	136.538	135.418	N/A	106.772	47.782	N/A	N/A
COP	2.44	2.727	3.037	N/A	3.049	2.273	N/A	N/A
Quality at accumulator	0.174	0.11	0.002	Comp. Liq.	0.025	0.563	Sup. Vapor	Sup. Vapor

Table 4.4: Results of thermodynamic analysis for intercooler and economizer cycles to find pressure ratios across compressors that give maximum system performance.

Operating condition	OC-1	OC-2	OC-3	OC-4	OC-5	OC-6	OC-7	OC-8
T at evaporator (C)	0	5	10	15	15	15	15	15
T at outlet of gas cooler (C)	35	35	35	35	40	45	50	55
P at evaporator (MPa)	3.485	3.969	4.502	5.087	5.087	5.087	5.087	5.087
P at gas cooler (MPa)	10.34	10.34	10.34	10.34	10.34	10.34	10.34	10.34
Results								
Intercooler cycle								
p-ratio across 1st compressor	2.34	2.06	1.82	1.61	1.74	1.78	1.82	1.88
p-ratio across 2nd compressor	1.27	1.26	1.26	1.26	1.17	1.14	1.12	1.08
Intermediate pressure (MPa)	8.155	8.177	8.194	8.19	8.851	9.055	9.258	9.564
Work of 1st compressor (kJ/kg)	47.61	38.773	30.533	22.804	26.803	27.991	29.16	30.882
Work of 2nd compressor (kJ/kg)	5.707	5.554	5.448	5.47	4.613	5.117	4.862	3.701
Total compression work (kJ/kg)	53.317	44.327	35.981	28.273	31.417	33.108	34.022	34.583
Without ED-WOW (Case 8)								
Heat cap. of evaporator (kJ/kg)	143.518	140.106	135.508	129.27	108.115	78.614	43.619	17.208
COP	2.692	3.161	3.766	4.572	3.441	2.374	1.282	0.498
With ED-WOW (Case 9)								
Heat cap. of evaporator (kJ/kg)	150.046	145.742	140.325	133.339	112.954	84.744	51.52	26.624
Work output throu. ED-WOW (kJ/kg)	6.528	5.636	4.817	4.069	4.839	6.13	7.901	9.416
COP without using W of ED-WOW	2.814	3.288	3.9	4.716	3.595	2.56	1.514	0.77
COP using W to run compressor	3.207	3.767	4.503	5.509	4.25	3.141	1.972	1.058
Economizer cycle (Case 10)								
p-ratio across 1st compressor	1.48	1.36	1.26	1.17	1.24	1.28	1.11	1.01
p-ratio across 2nd compressor	2	1.92	1.82	1.74	1.64	1.59	1.83	2.01
Intermediate pressure (MPa)	5.158	5.398	5.673	5.952	6.308	6.511	5.647	5.138
Work of 1st compressor (kJ/kg)	15.367	11.931	8.869	5.919	7.017	5.426	1.11	0.043
Work of 2nd compressor (kJ/kg)	41.079	36.588	32.011	27.597	24.133	21.144	28.58	34.434
Total compression work (kJ/kg)	56.447	48.519	40.88	33.516	31.15	26.57	29.691	34.477
Heat cap. of evaporator (kJ/kg)	139.556	136.546	132.496	127.023	102.401	65.949	37.877	16.655
COP	2.472	2.814	3.241	3.79	3.287	2.482	1.276	0.483

Table 4.5: Input values for simulation of the expansion device producing work.

Parameters	Values	Unit	Parameters	Values	Unit
Engine speed	$S = 120, 400,$ or 600	RPM	Volume at TDC	$V_{TDC} = 1.685$	mm^3
Cylinder bore	$B = 27.7$	mm	Fittings' volume	$V_{fit} = 0.813$	mm^3
Bore radius	$r = 13.85$	mm	Location of expansion	$LOE = 8.01$ (5.21 from TDC)	mm
Crank radius	$R = 11.0$	mm	Diameter of fitting	$D_{fit} = 2.286$	mm
Connecting rod length	$L = 38.8$	mm	Orifice diameter of intake valve	$D_{int} = 1.191$	mm
Composite roughness	$\sigma = 0.37$	μm	Orifice diameter of exhaust valve	$D_{exh} = 2.286$	mm
Piston ring width	$b = 1.067$	mm	Number of intake valves per cylinder	$n_{in} = 2$	-
Ring thickness	$t_r = 1.067$	mm	Number of exhaust valves per cylinder	$n_{exh} = 1$	-
Ring modulus	$E = 70.0$	GN/m^2	Pressure at intake	$p_{in} = 10.3421$	MPa
Ring crown height	$C_R = 14.9$	μm	Desired pressure at exhaust	$p_{exh} = 3.4474$	MPa
Friction coefficient	$f = 0.08$	-	Desired pressure in crank housing	$p_{crk} = 3.4474$	MPa
Lubricant viscosity (CO ₂ at 300 K)	$\mu = 1.50 \times 10^{-5}$	$\text{Pa} \cdot \text{s}$	Temperature at intake	$T_{in} = 322.0$	K
Tangential ring tension	$T = 22.38$	N	Desired temperature at exhaust	$T_{exh} = 298.25$	K
Volume at BDC	$V_{BDC} = 14.952$	mm^3	Time step	$\Delta t = 0.00125,$ 0.0005, or 0.00025	Sec.

Table 4.6: Test conditions to investigate the performance of the ED-WOW.

Case	1	2	3
$T_{\text{indoor}} (^{\circ}\text{C})$	20	20	20
$T_{\text{outdoor}} (^{\circ}\text{C})$	35	35	35
$P_{\text{c,out}} (\text{kPa})$	6620.7	7068.7	7971.3
$P_{\text{c,in}} (\text{kPa})$	2770.9	2637.3	2528.2
$P_{\text{gc,in}} (\text{kPa})$	6603.5	7045.3	7938.2
$P_{\text{gc,out}} (\text{kPa})$	6536.9	6931.5	7845.2
$P_{\text{ED,in}} (\text{kPa})$	6052.1	6392.4	7255.7
$P_{\text{ED,out}} (\text{kPa})$	2921.7	2814.3	2759.8
$P_{\text{evap,out}} (\text{kPa})$	2854.8	2735.7	2657.4
$T_{\text{c,out}} (^{\circ}\text{C})$	87.6	99.4	117.9
$T_{\text{c,in}} (^{\circ}\text{C})$	20.2	19.8	19.6
$T_{\text{gc,in}} (^{\circ}\text{C})$	68.0	77.6	93.7
$T_{\text{gc,out}} (^{\circ}\text{C})$	36.0	36.2	36.7
$T_{\text{ED,in}} (^{\circ}\text{C})$	26.0	27.9	31.4
$T_{\text{evap,out}} (^{\circ}\text{C})$	12.5	11.0	10.3
$\dot{m}_{\text{CO}_2} (\text{g/s})$	9.7	11.6	13.5
$\omega_{\text{ED}} (\text{RPM})$	114	120	120
$\Delta t_{\text{intake}} (\text{s})$	0.129	0.123	0.123

Table 4.7: Results of the experiments with ED-WOW in a transcritical CO₂ cycle.

Case	1	2	3
$P_{ED,in}$ (kPa)	6052.1	6392.4	7255.7
$P_{ED,out}$ (kPa)	2921.7	2814.3	2759.8
$T_{ED,in}$ (°C)	26.0	27.9	31.4
\dot{Q}_{isenth} (W)	425.6	570.7	1030
\dot{Q}_{ED} (W)	448.7	599.4	1064
\dot{W}_{comp} (W)	567.6	773.1	1110
\dot{W}_{ED} (W)	23.18	28.70	34.77
COP_{EXV}	0.7498	0.7382	0.9279
COP_{ED-1}	0.7905	0.7753	0.9586
COP_{ED-2}	0.8242	0.8052	0.9896
$\epsilon_{s,ED}$ (%)	10.47	9.97	10.27

Table 4.8: Increases of the evaporator capacity and COP.

Case	1	2	3
\dot{Q}_{isenth} (W)	425.6	570.7	1030
\dot{Q}_{ED} (W)	448.7	599.4	1064
Increase of evaporator capacity (%)	5.43	5.03	3.30
COP_{EXV}	0.7498	0.7382	0.9277
COP_{ED-1}	0.7905	0.7753	0.9586
Increase of COP with enthalpy effect only (%)	5.43	5.03	3.30
COP_{ED-2}	0.8242	0.8052	0.9896
Increase of COP with enthalpy & work output effects (%)	9.92	9.08	6.67

Table 4.9: Uncertainties of measurements.

Variable	Uncertainty value
Flow meter	0.5% of mass flow rate
T-type thermocouple	0.5°C
Pressure transducer	43.1 kPa
Vacuum pressure gage	4.1 kPa (0.6 psi)
Static pressure gage	13.8 kPa (2 psi)
Rotameter	0.09 m ³ /hr (0.4 GPM)
Torquemeter	0.085 N-m
Tachometer	50 ⁽¹⁾ RPM

Note: ⁽¹⁾ The uncertainty value of the Tachometer is assumed.

Table 4.10: Calculated Results and associating uncertainties (Case 3).

Item	Measure or calculated value	Absolute uncertainty	Relative uncertainty
Work generated through the ED-WOW	34.77 W	10.69 W	30.74 %
Isentropic efficiency of the ED-WOW	10.27 %	3.16 %	30.79 %
Evaporator capacity	1030 W	5.43 W	0.5 %
Compression work	1110 W	44.23 W	3.98 %
COP _{ED-2}	0.9896	0.004972	0.5 %

Table 4.11: Results of the ED-WOW simulation for the experimental test conditions.

Case		1	2	3	
Experiment	$P_{ED,in}$ (kPa)	6052.1	6392.4	7255.7	
	$P_{ED,out}$ (kPa)	2921.7	2814.3	2759.8	
	\dot{m}_{CO_2} (g/s)	9.7	11.58	13.48	
	\dot{W}_{ED} (W)	23.18	28.70	34.77	
Simulation	Zero leakage	$P_{ED,out}$ (kPa)	3657.4	3889.5	4569.3
		\dot{m}_{CO_2} (g/s)	6.16	6.80	9.0
		\dot{W}_{ED} (W)	94.28	98.01	104.53
		Isentropic efficiency (%)	56.9	53.9	46.0
	Some leakage	$P_{ED,out}$ (kPa)	2710	2589.9	3546.5
		\dot{m}_{CO_2} (g/s)	9.71	11.54	13.45
		\dot{W}_{ED} (W)	135.6	154.4	149.2
		\dot{m}_{CO_2-leak} (g/s)	3.27	4.57	4.21
		Rate of leakage (%)	33.67	39.6	31.28
		Isentropic efficiency (%)	33.7	28.8	29.2

Table 4.12: Calculation of leakage area of CO₂ through the piston ring for Case 3.

Parameters	Vapor quality, $x = 0.9$		Vapor quality, $x = 0.5$	
	$p_1 = 7$ MPa	$p_1 = 4$ MPa	$p_1 = 7$ MPa	$p_1 = 4$ MPa
Mass velocity, G , (kg/s-m ²)	28718.3	11724.2	22337.4	9119.2
Flow area (mm ²)	0.146248	0.358233	0.188025	0.460566
Leakage area (mm ²)	0.073124	0.179116	0.094013	0.230283
Gap between the ends of the piston ring (mm)	0.0685	0.1679	0.0881	0.2158
Gap between the cylinder wall and the piston ring (mm)	0.00084	0.00206	0.00108	0.00265

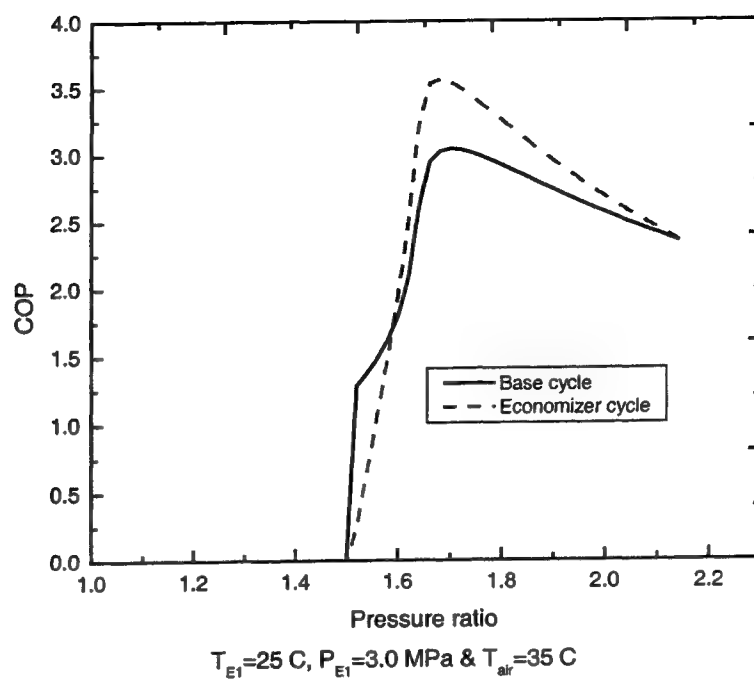


Figure 4.1: Comparison of COPs of Economizer cycle and Base cycle.

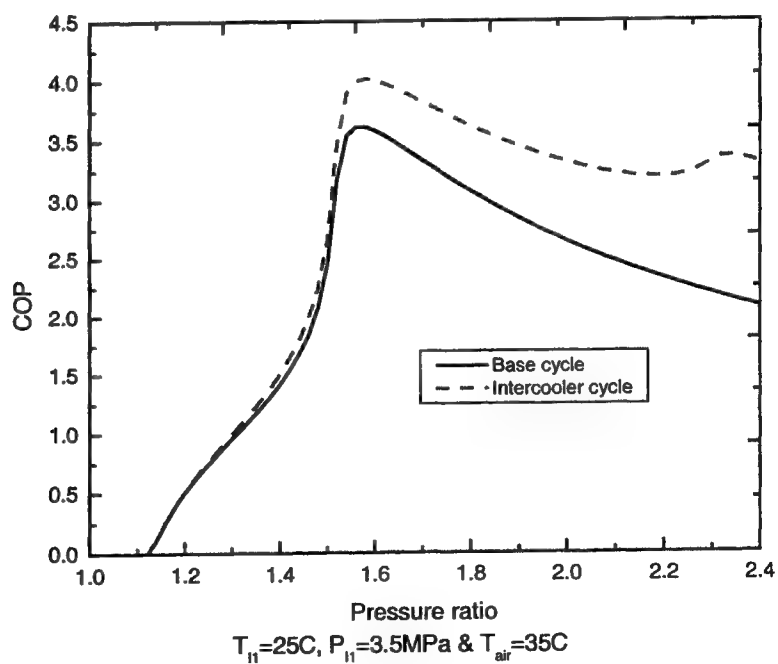


Figure 4.2: Comparison of COPs of Intercooler cycle and Base cycle.

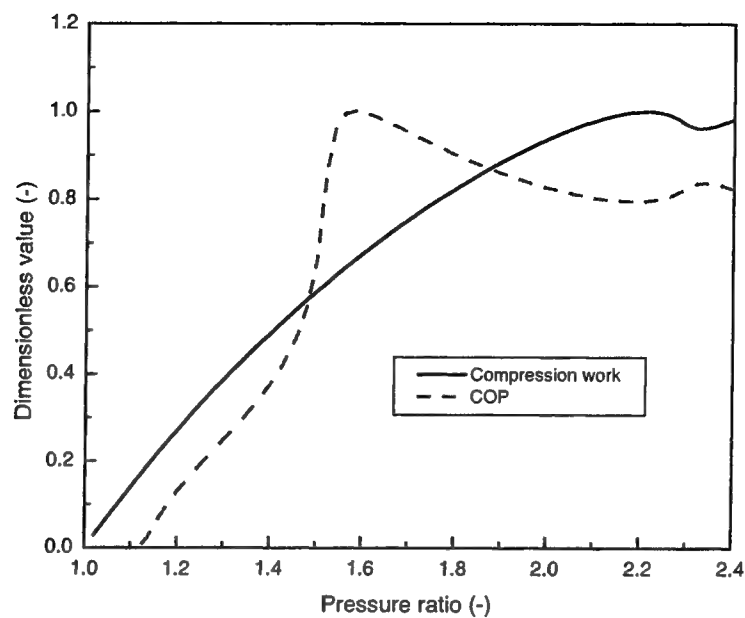


Figure 4.3: COP and compression work of Intercooler cycle.

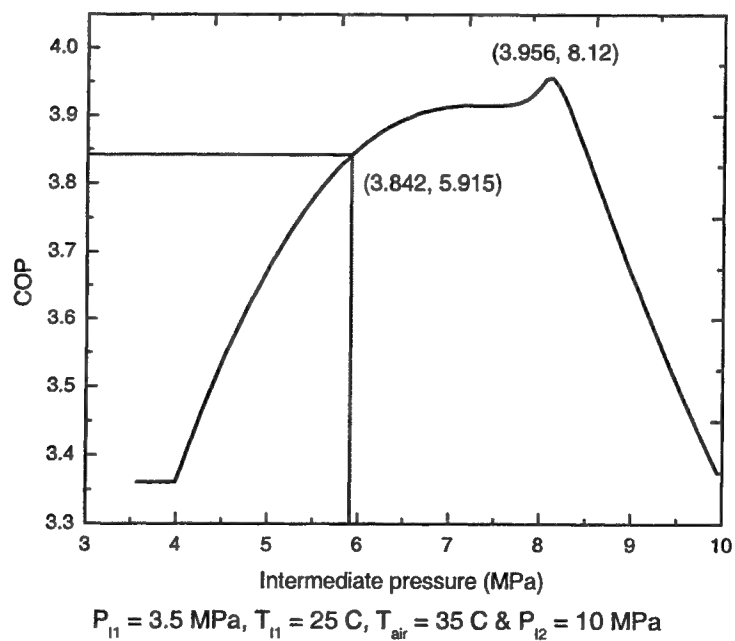


Figure 4.4: COP of Intercooler cycle with different pressure ratios across the 1st-stage and 2nd-stage compressors.

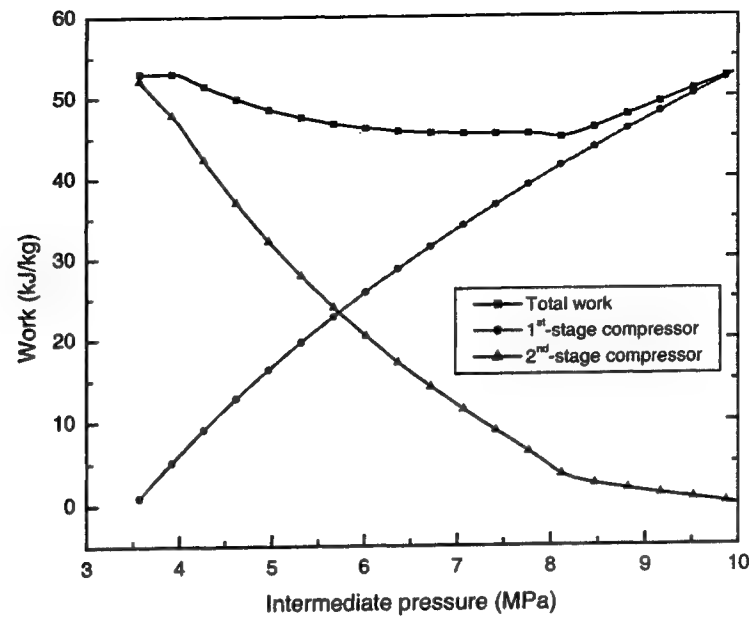


Figure 4.5: Behavior of compression works of Intercooler cycle over intermediate pressure.

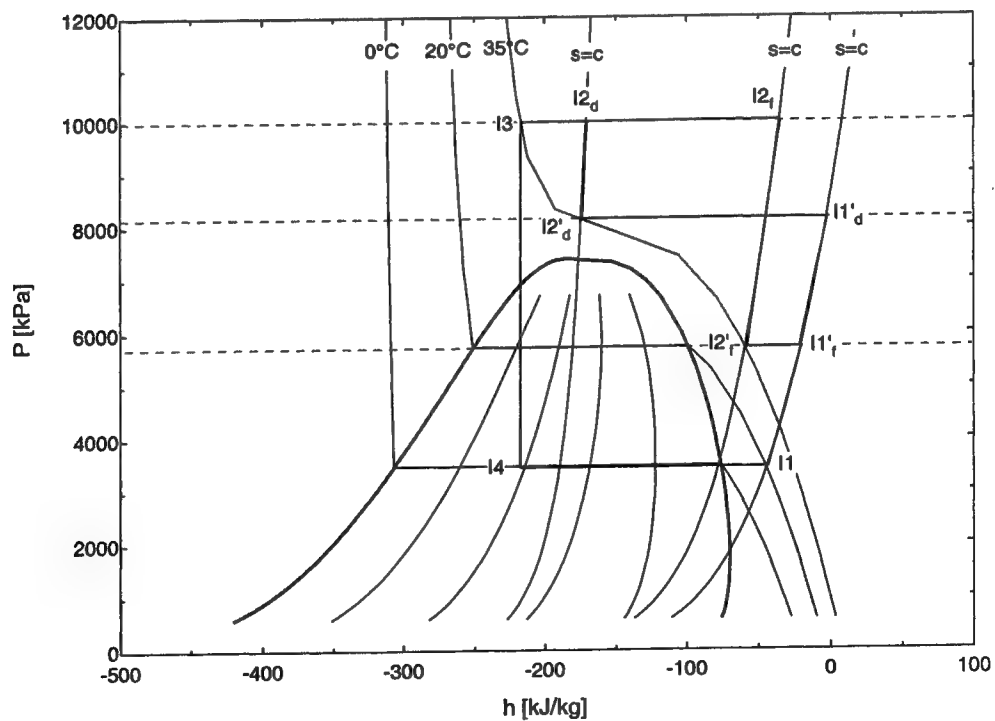


Figure 4.6: Processes of Intercooler cycle on pressure-enthalpy diagram.

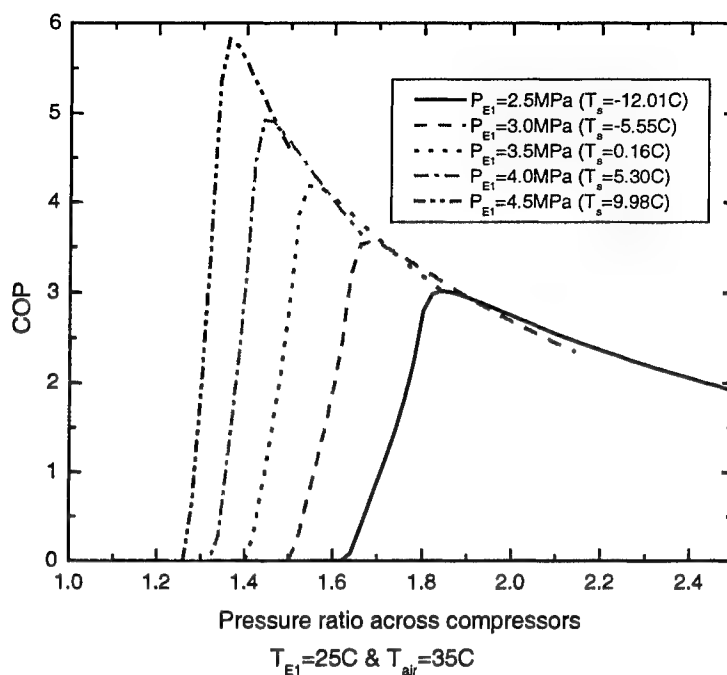


Figure 4.7: Effect of pressure at the inlet to the evaporator on COP of Economizer cycle.

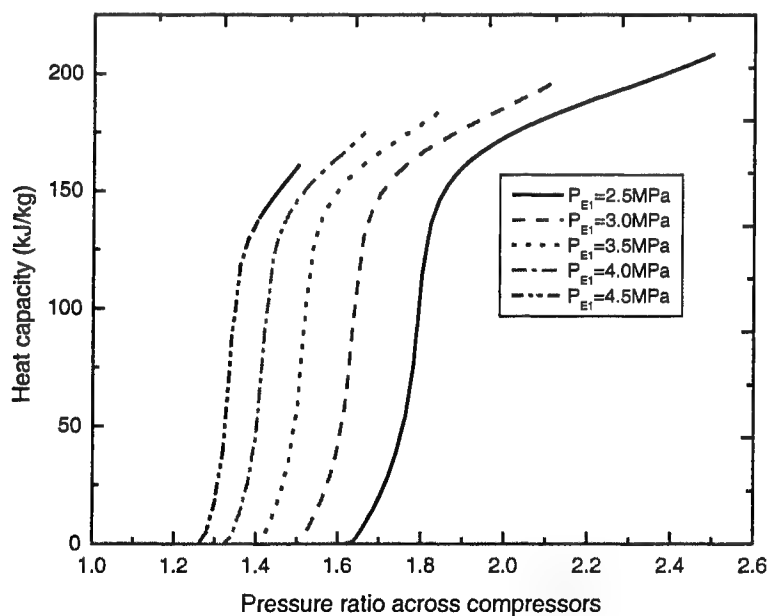


Figure 4.8: Effect of pressure at the inlet to the evaporator on heat removal capacity of Economizer cycle.

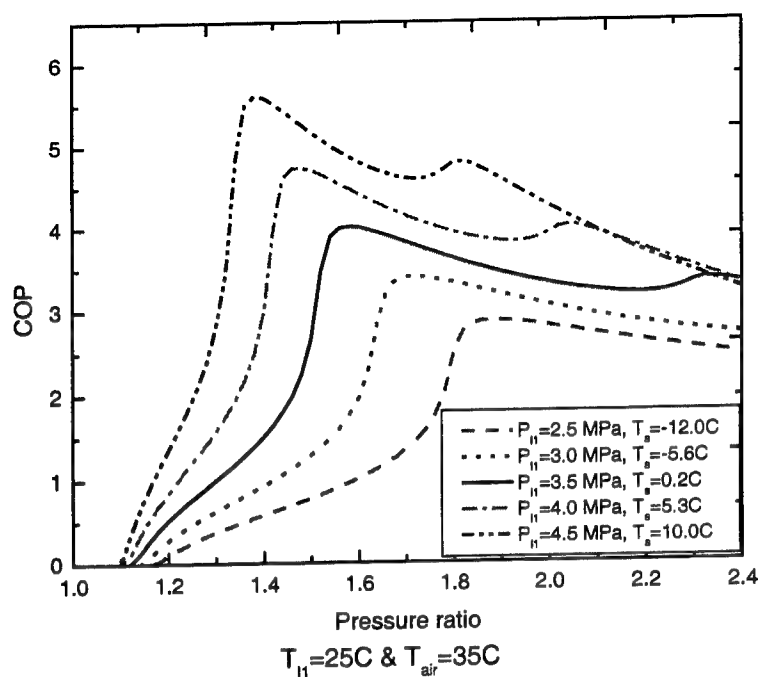


Figure 4.9: Effect of pressure at the inlet to the evaporator on COP of Intercooler cycle.

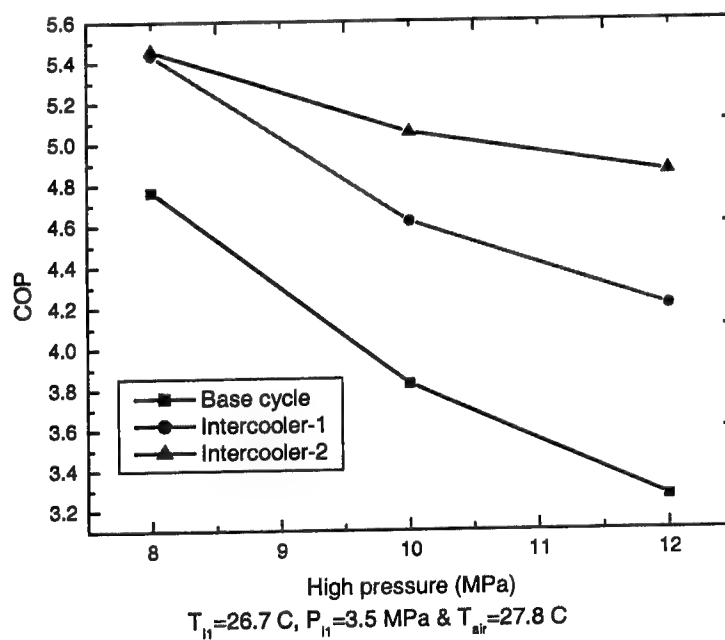


Figure 4.10: Comparison of COPs of transcritical CO_2 cycles for $T_H=26.7^\circ\text{C}$ and $T_{\text{air}}=27.8^\circ\text{C}$.

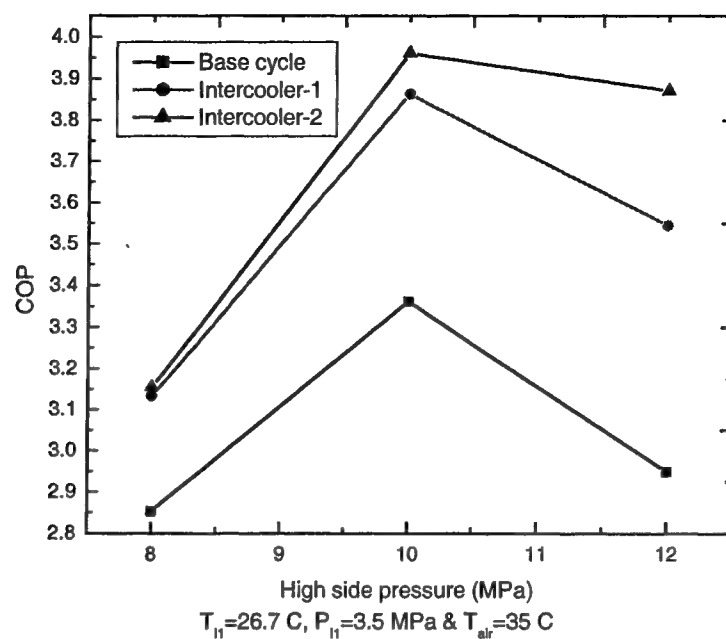


Figure 4.11: Comparison of COPs of transcritical CO₂ cycles for $T_H = 26.7^\circ\text{C}$ and $T_{air} = 35.0^\circ\text{C}$.

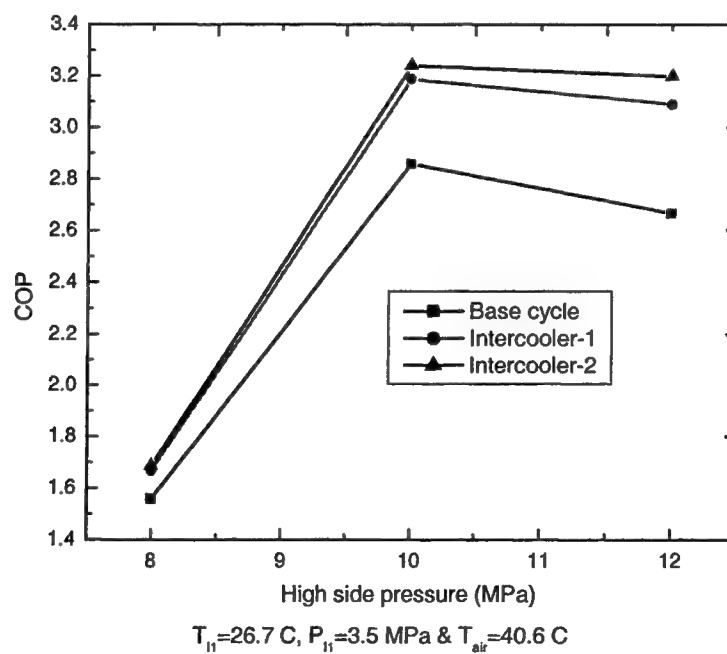


Figure 4.12: Comparison of COPs of transcritical CO₂ cycles for $T_H = 26.7^\circ\text{C}$ and $T_{air} = 40.6^\circ\text{C}$.

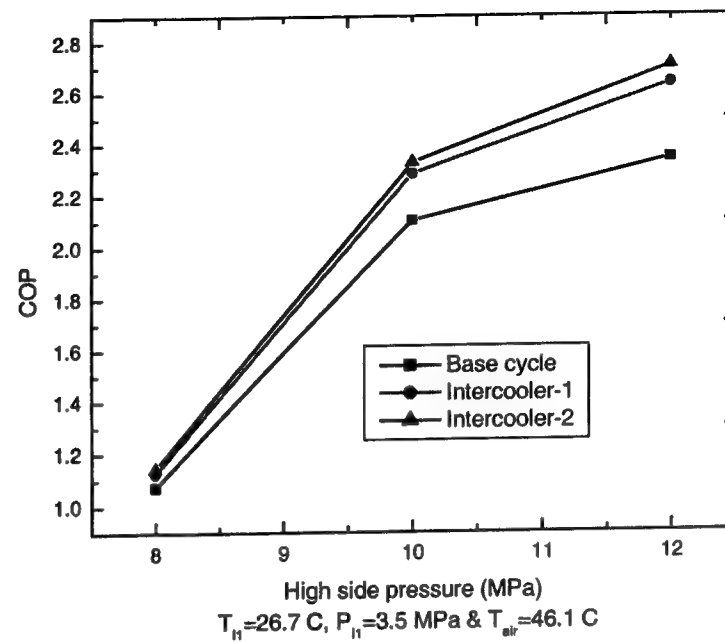


Figure 4.13: Comparison of COPs of transcritical CO_2 cycles for $T_n=26.7^\circ\text{C}$ and $T_{air}=46.1^\circ\text{C}$.

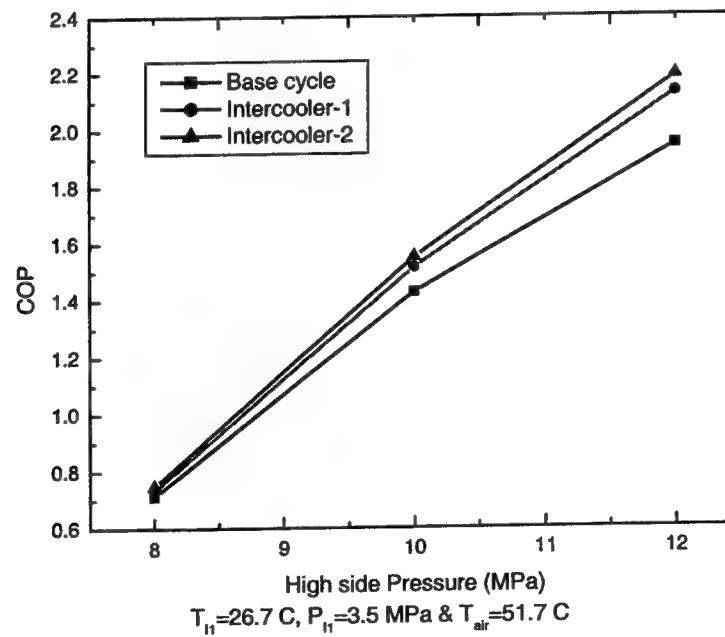


Figure 4.14: Comparison of COPs of transcritical CO_2 cycles for $T_n=26.7^\circ\text{C}$ and $T_{air}=51.7^\circ\text{C}$.

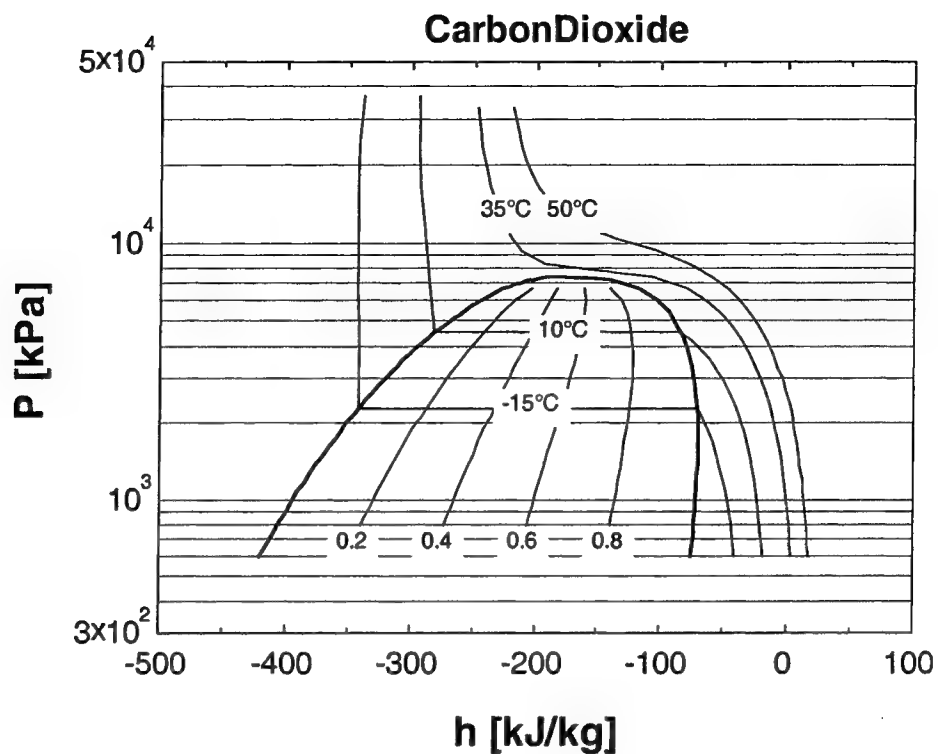


Figure 4.15: Thermodynamic characteristics of CO₂ on P-h diagram.

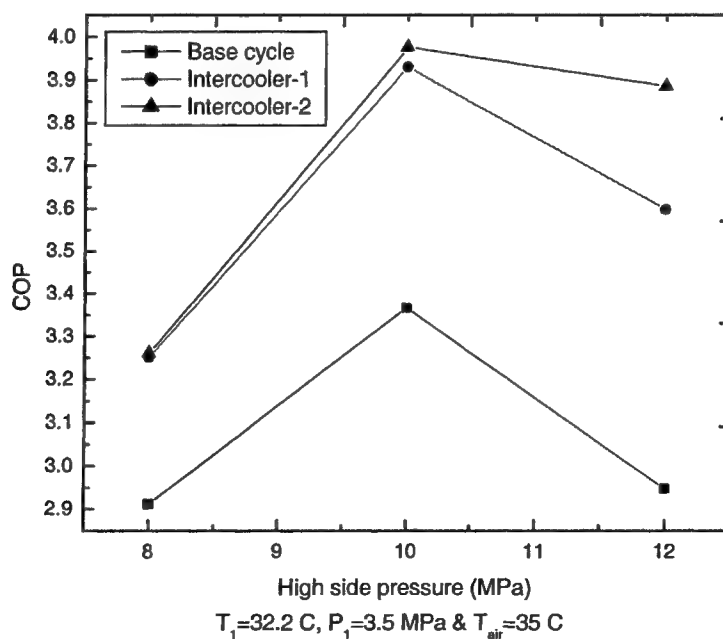


Figure 4.16: Comparison of COPs of transcritical CO₂ cycles for $T_H=32.2^\circ\text{C}$ and $T_{air}=35^\circ\text{C}$.

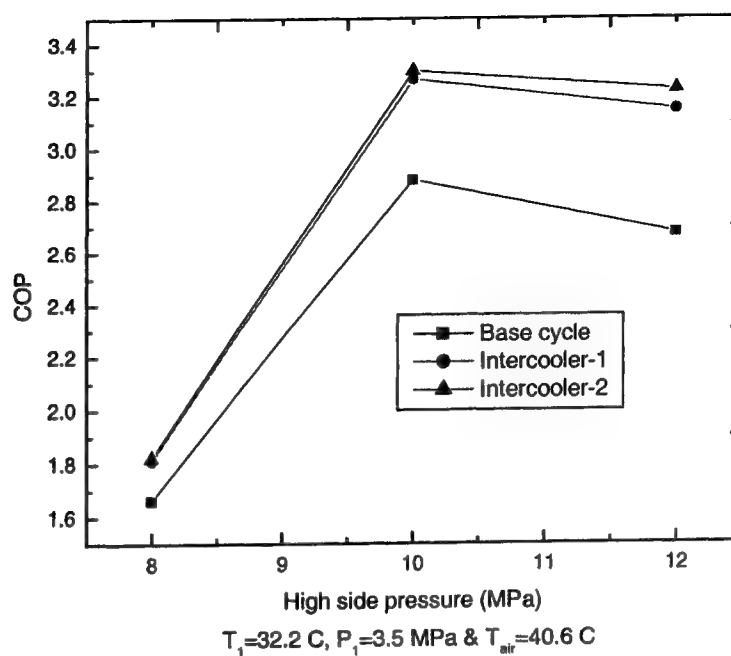


Figure 4.17: Comparison of COPs of transcritical CO₂ cycles for $T_1=32.2^\circ\text{C}$ and $T_{air}=40.6^\circ\text{C}$.

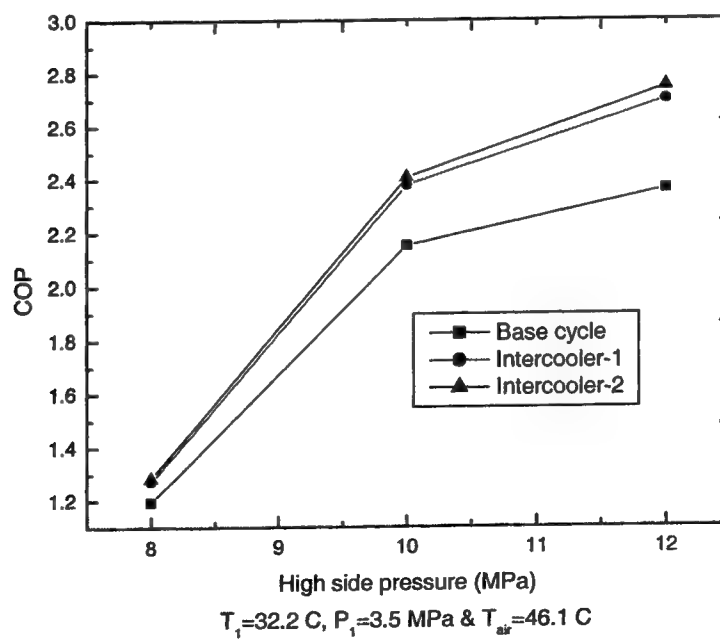


Figure 4.18: Comparison of COPs of transcritical CO₂ cycles for $T_1=32.2^\circ\text{C}$ and $T_{air}=46.1^\circ\text{C}$.

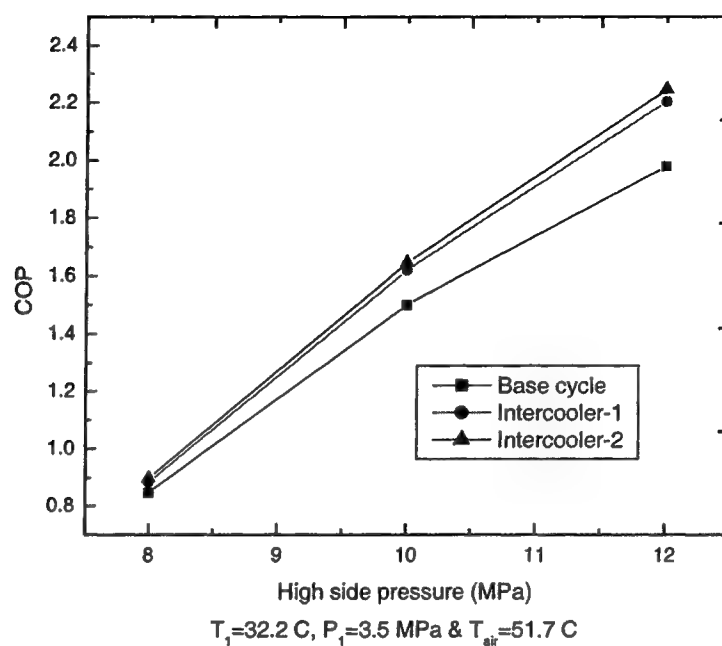


Figure 4.19: Comparison of COPs of transcritical CO_2 cycles for $T_H = 32.2^\circ\text{C}$ and $T_{air} = 51.7^\circ\text{C}$.

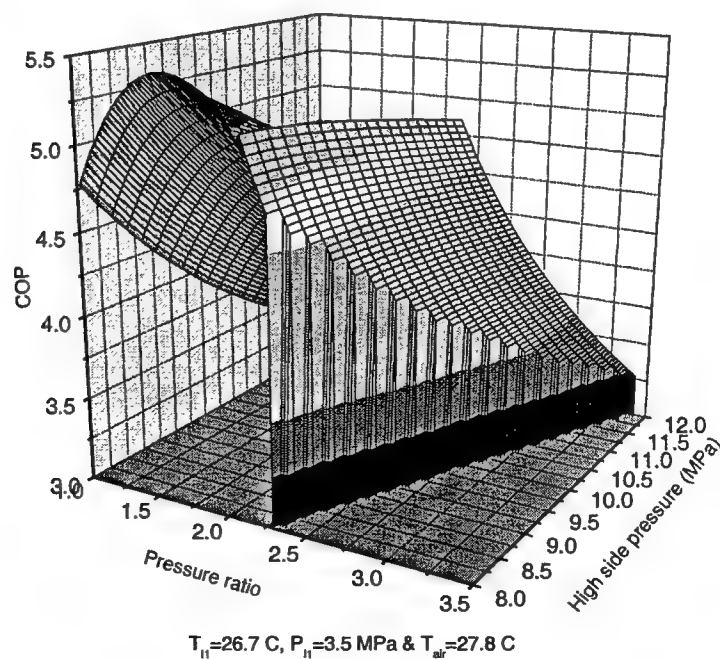


Figure 4.20: Behavior of COP of Intercooler cycle for $T_H = 26.7^\circ\text{C}$ and $T_{air} = 27.8^\circ\text{C}$.

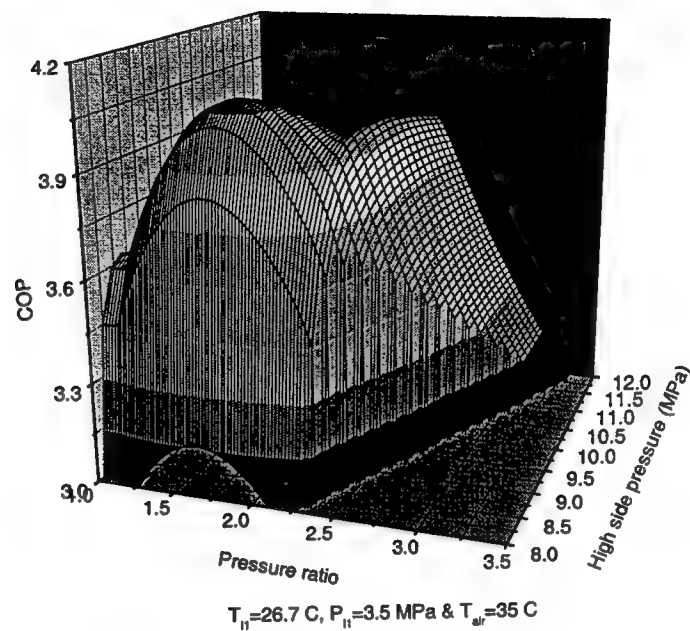


Figure 4.21: Behavior of COP of Intercooler cycle for $T_H = 26.7^\circ\text{C}$ and $T_{air} = 35.0^\circ\text{C}$.

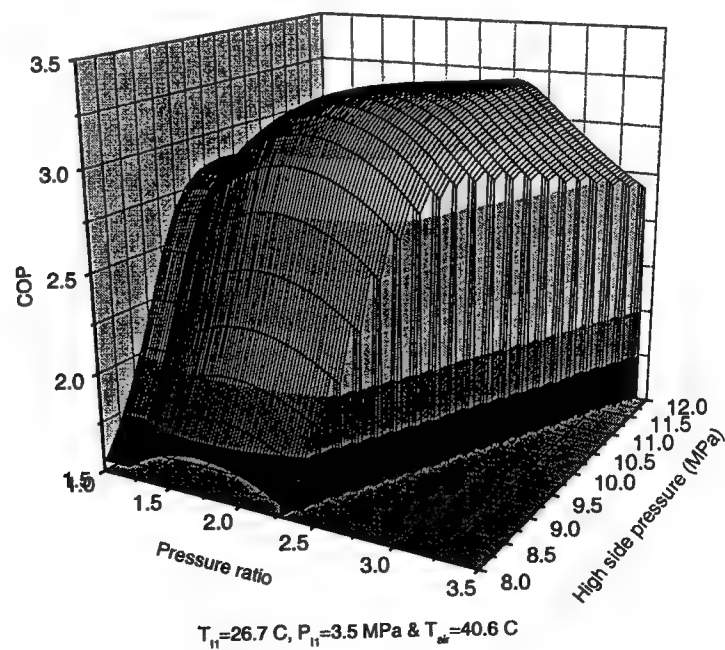


Figure 4.22: Behavior of COP of Intercooler cycle for $T_H = 26.7^\circ\text{C}$ and $T_{air} = 40.6^\circ\text{C}$.

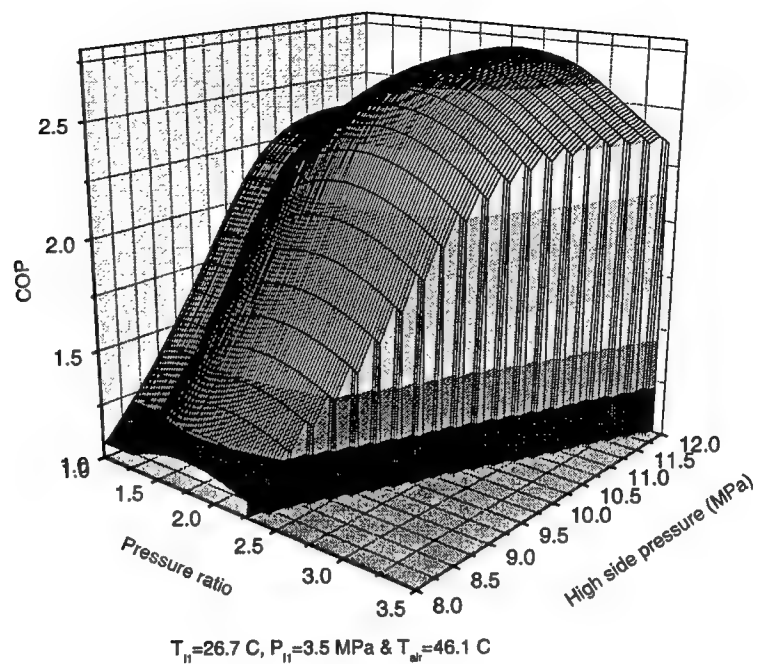


Figure 4.23: Behavior of COP of Intercooler cycle for $T_H=26.7^\circ\text{C}$ and $T_{air}=46.1^\circ\text{C}$.

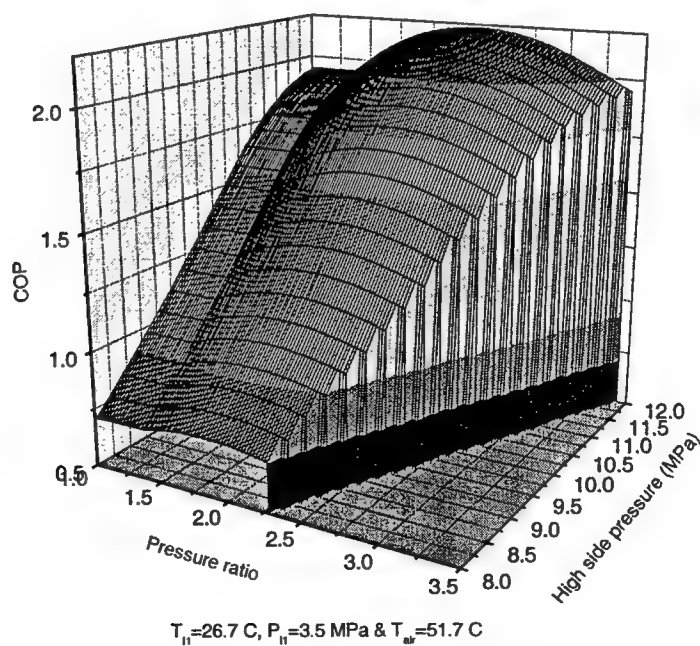


Figure 4.24: Behavior of COP of Intercooler cycle for $T_H=26.7^\circ\text{C}$ and $T_{air}=51.7^\circ\text{C}$.

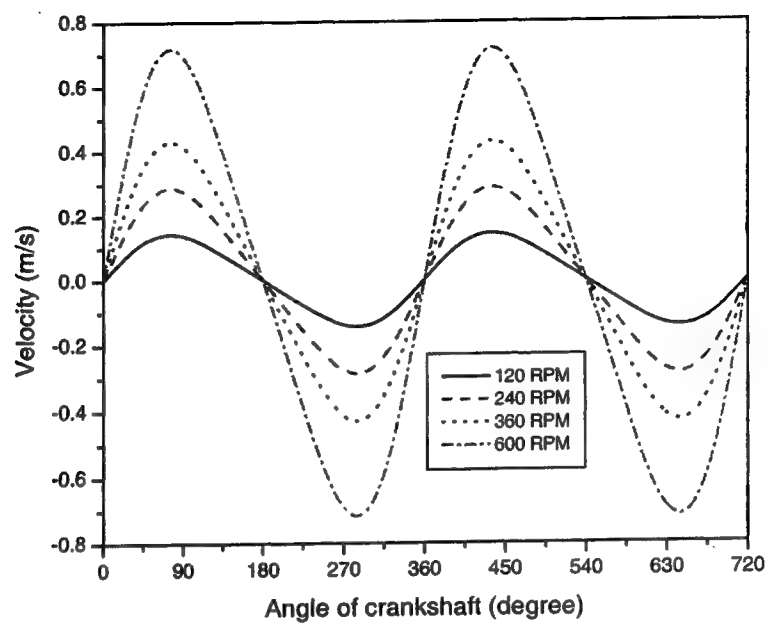


Figure 4.25: Piston speed versus crank angle of the ED-WOW.

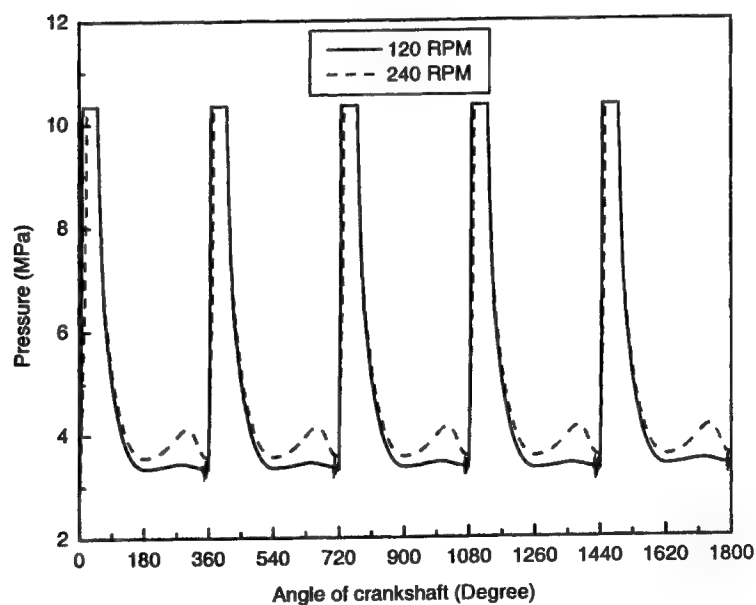


Figure 4.26: Repeat of the same trends of the pressure behavior for 120RPM and 240RPM.

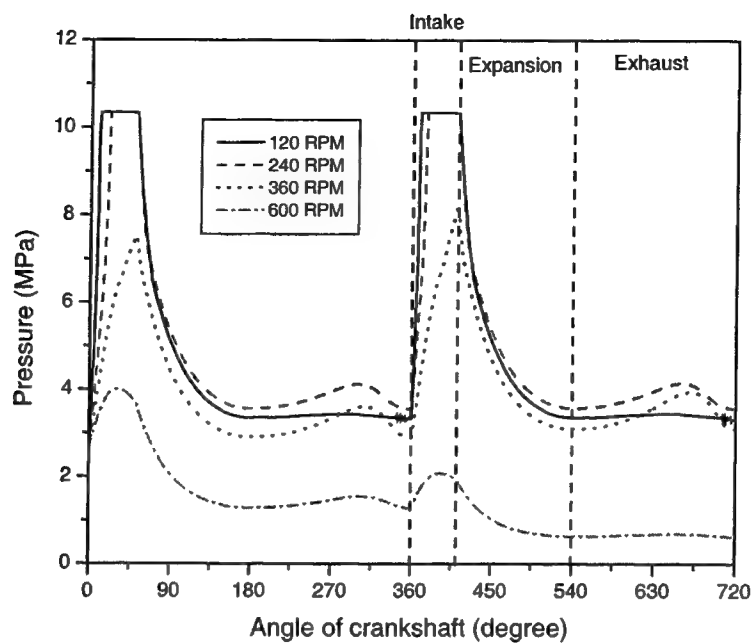


Figure 4.27: CO₂ pressure in the chamber versus crank angle.

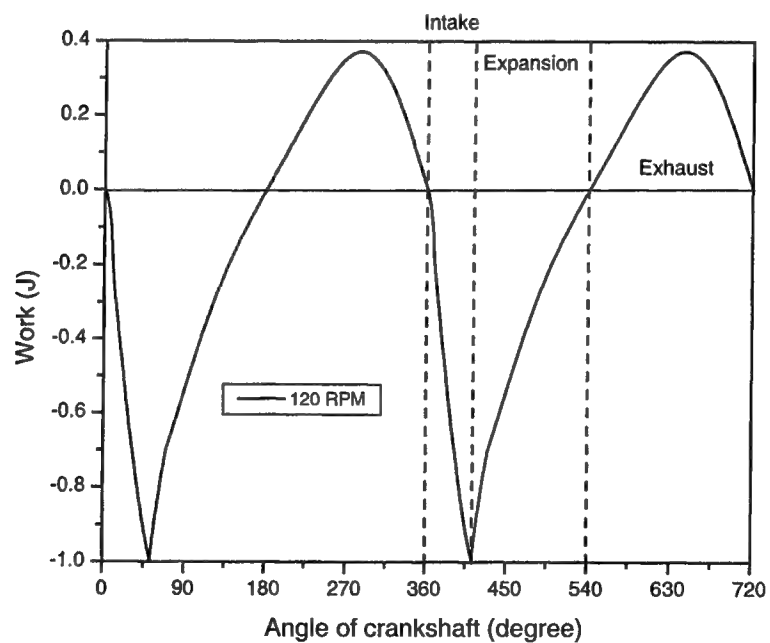


Figure 4.28: Work done by CO₂ versus crank angle (120 RPM).

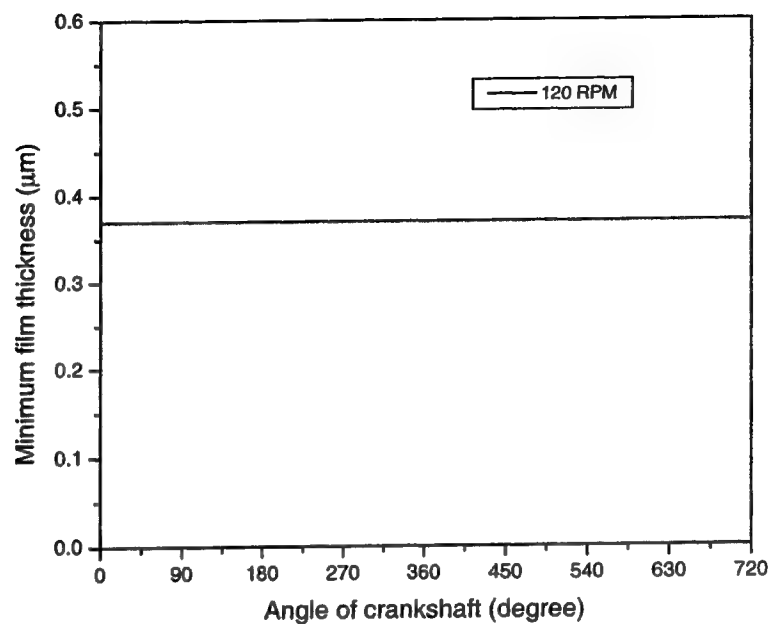


Figure 4.29: Minimum film thickness under the piston ring (120 RPM).

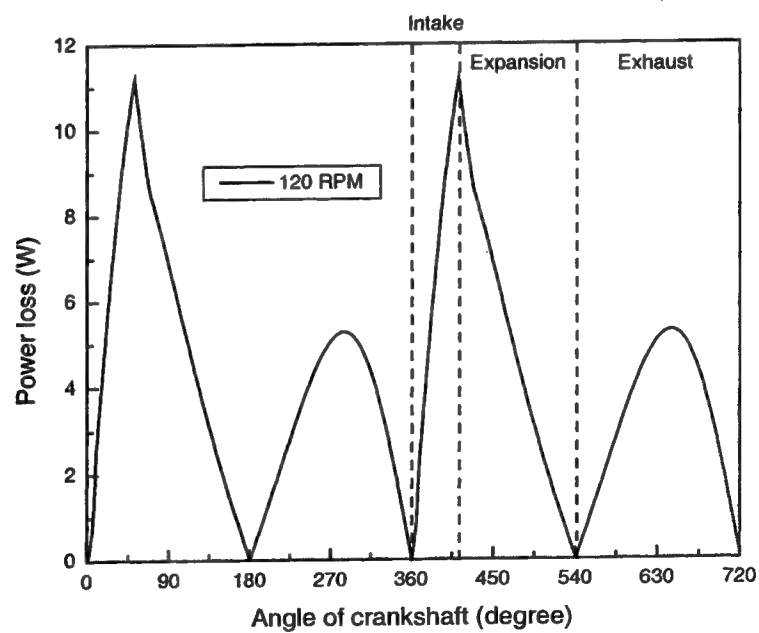


Figure 4.30: Power loss due to friction of the piston ring (120 RPM).

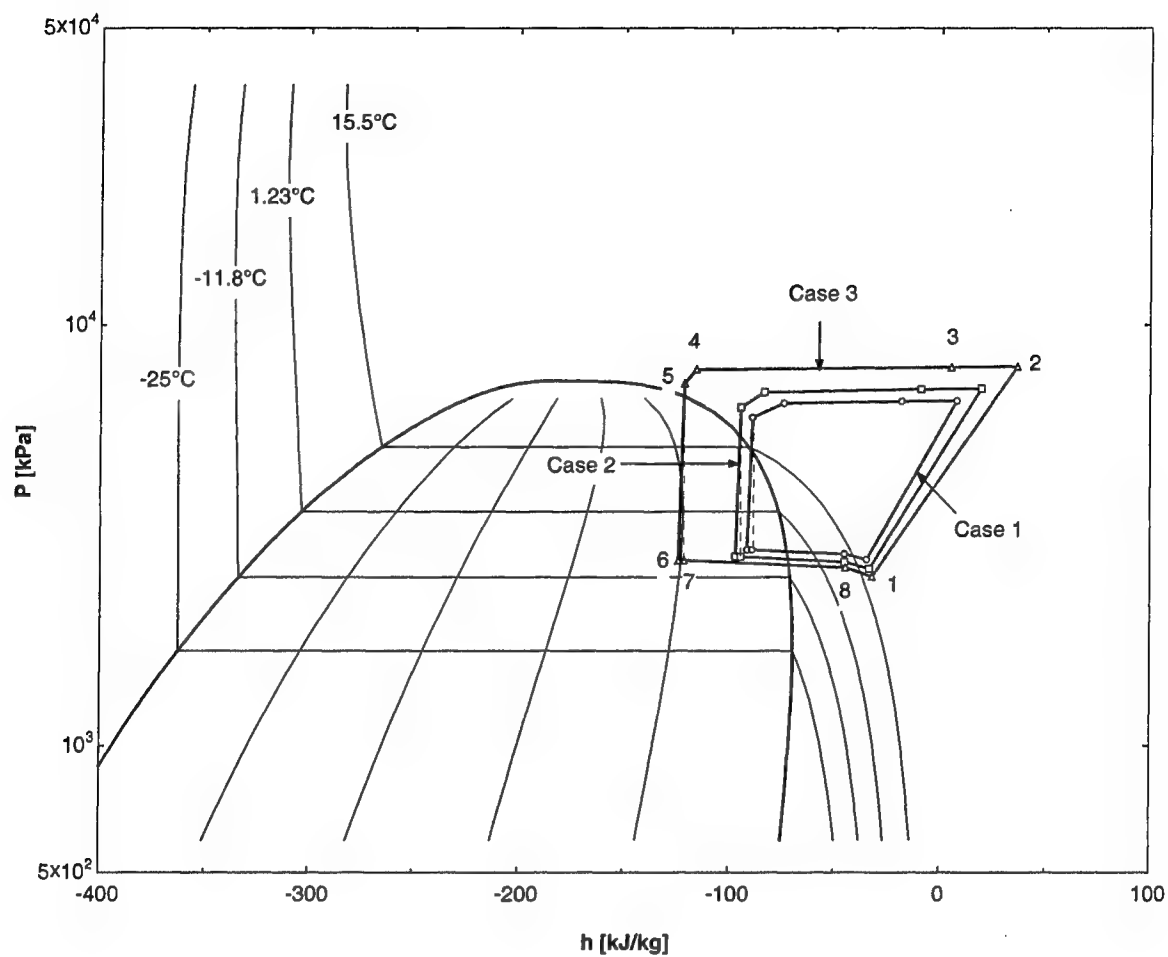


Figure 4.31: Pressure-enthalpy diagram of the processes of the system.

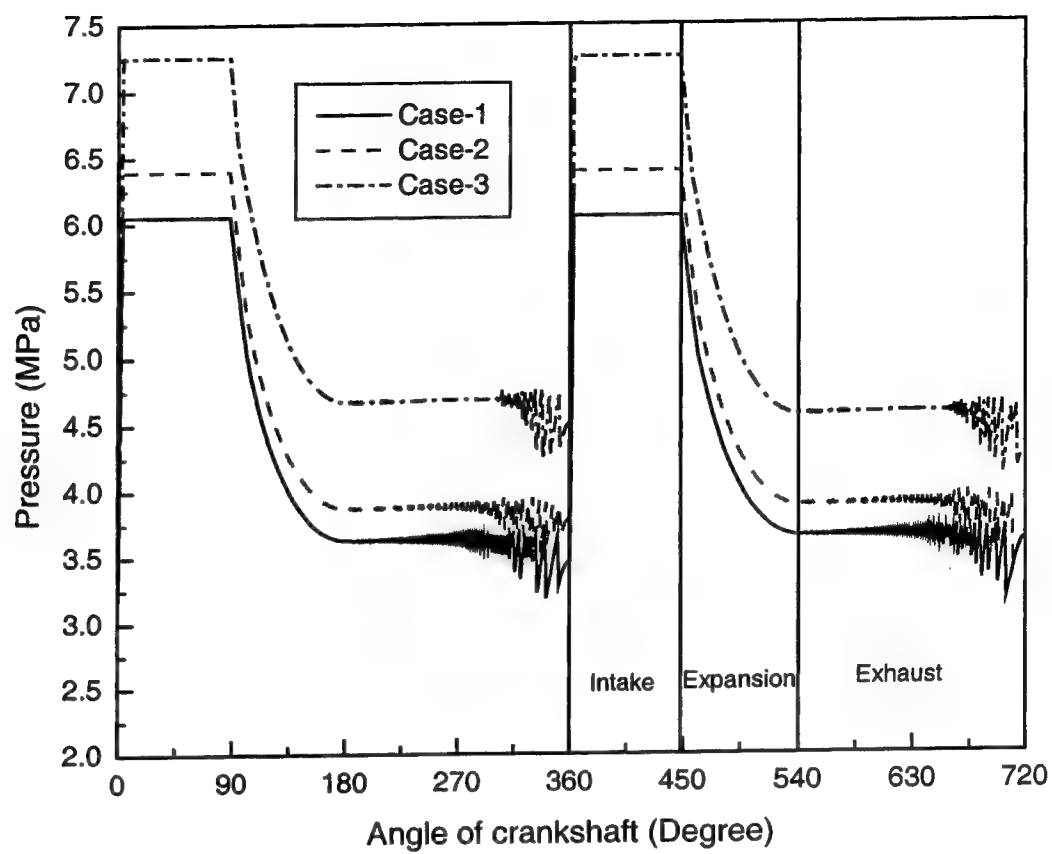


Figure 4.32: Pressure behavior inside the cylinder of the ED-WOW with the assumption of zero leakage of CO_2 .

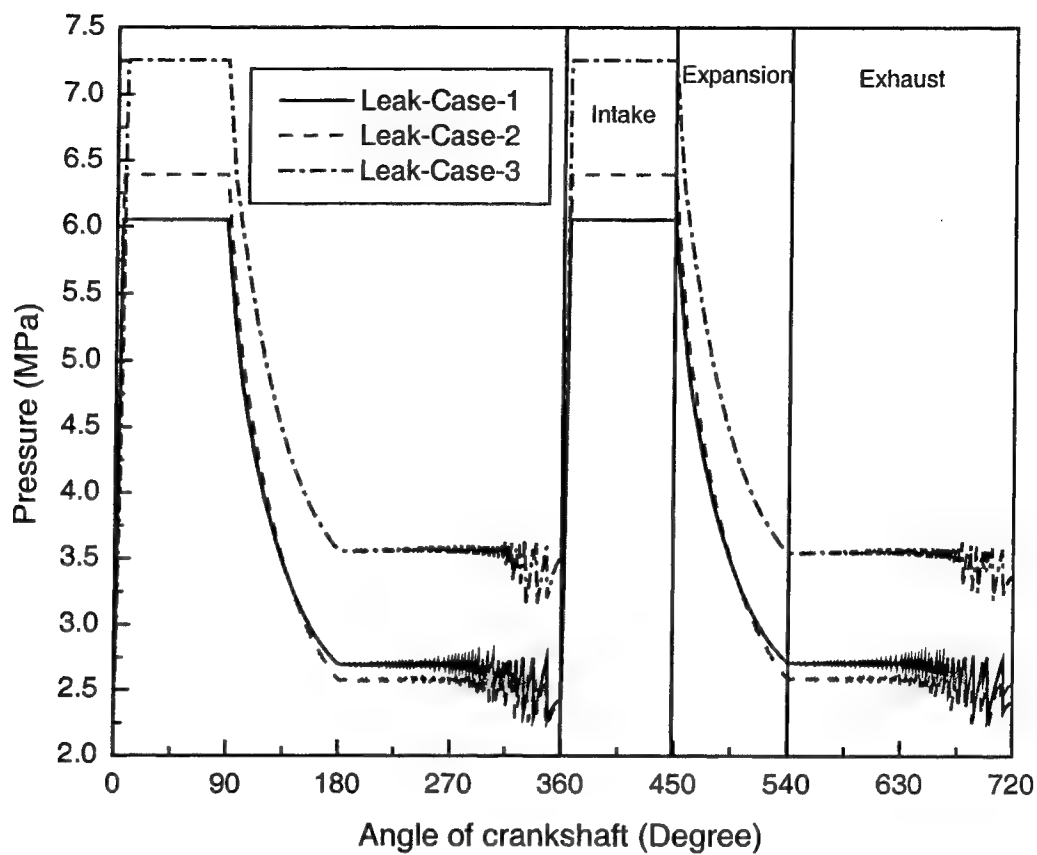


Figure 4.33: Pressure behavior inside the cylinder of the ED-WOW with the assumption of leakage of CO_2 through piston rings.

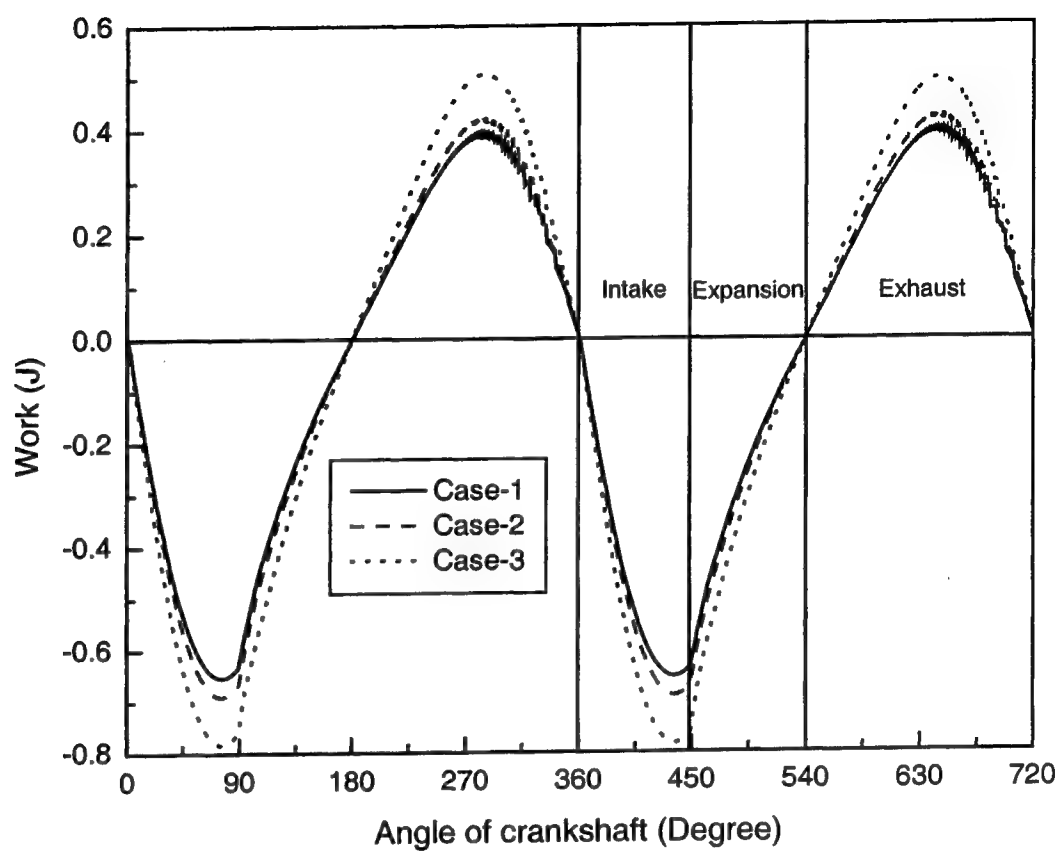


Figure 4.34: Predicted work produced with zero leakage assumption.

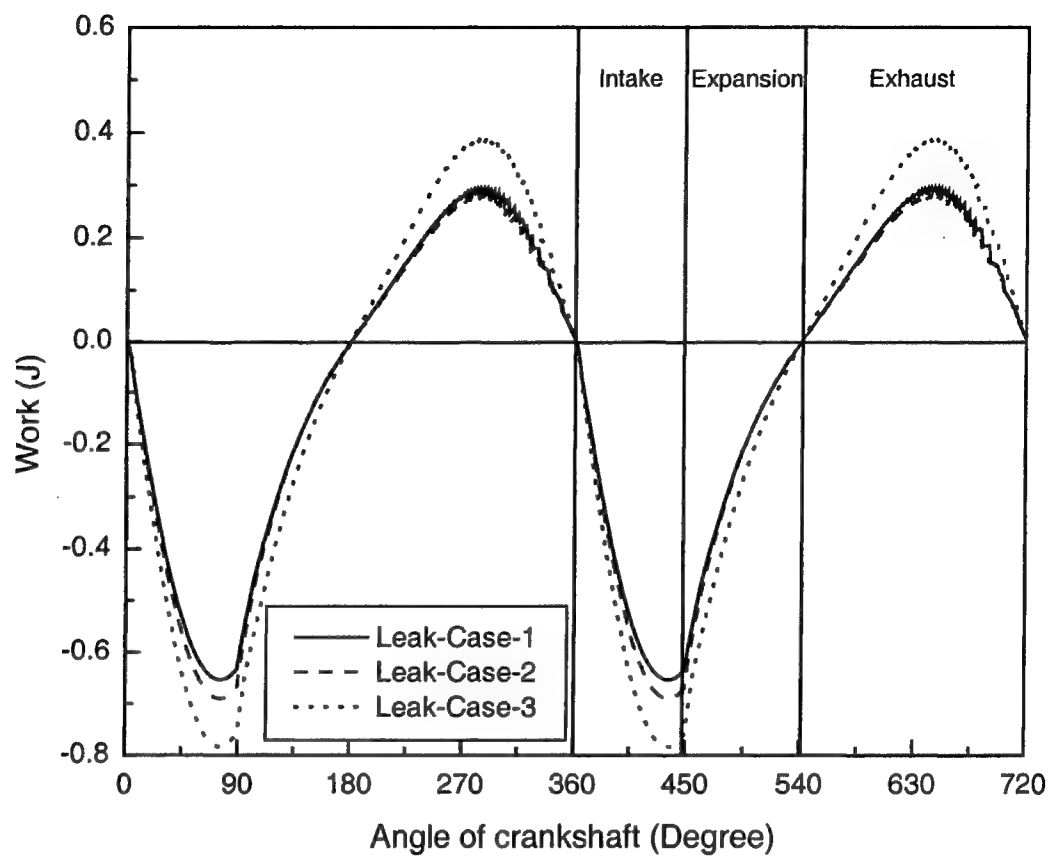


Figure 4.35: Predicted work produced and required with the assumption of leakage.

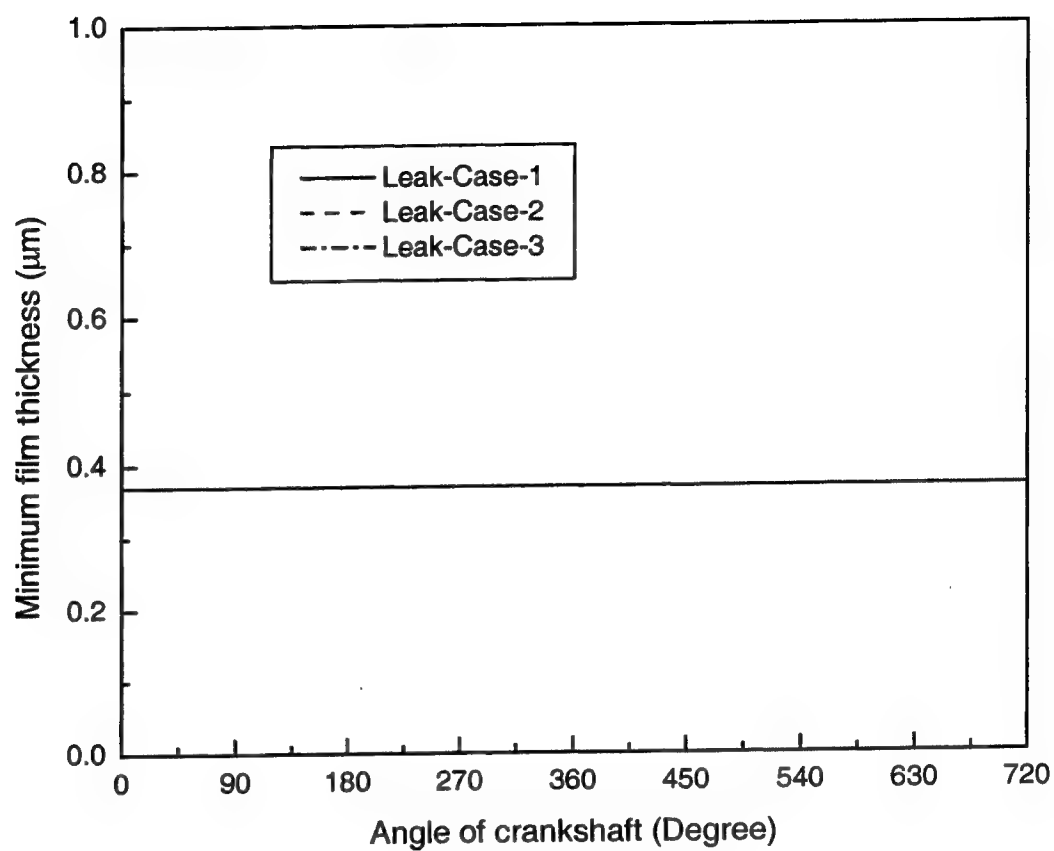


Figure 4.36: Predicted minimum film thickness of the lubricant.

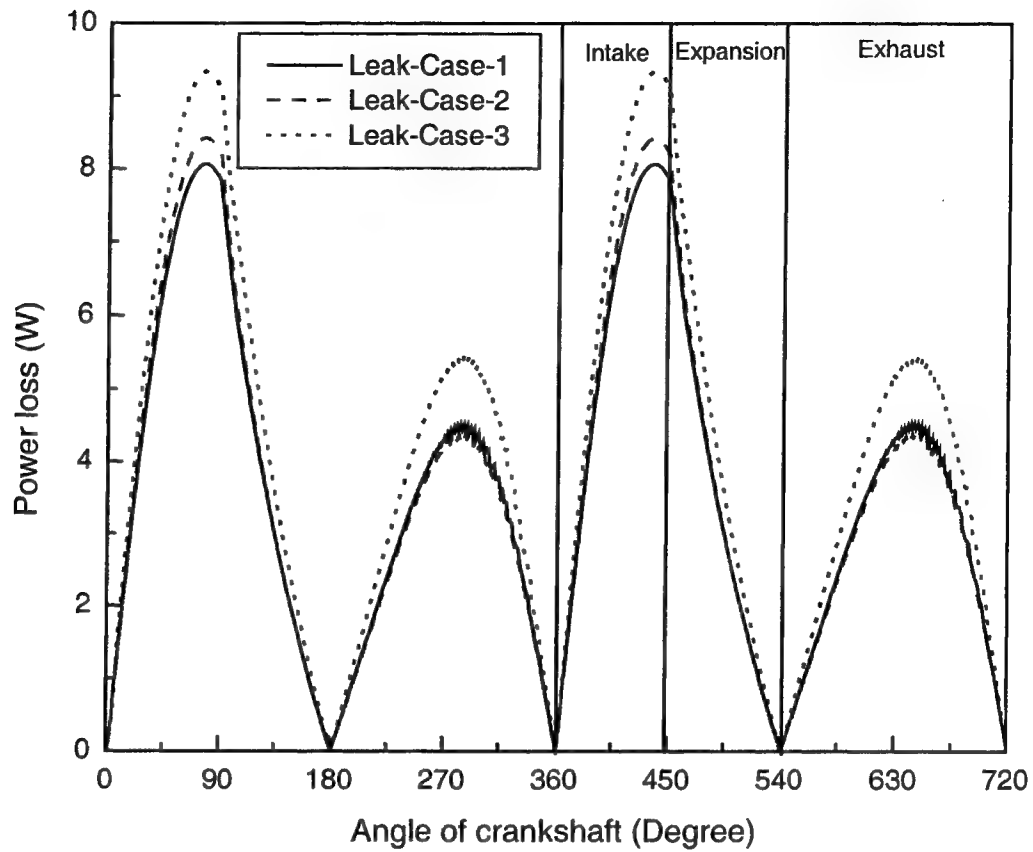


Figure 4.37: Predicted power loss due the friction between the piston ring and the cylinder wall.

5 SUMMARY, CONCLUSIONS, AND RECOMMENDATIONS

A study to increase system performance of a transcritical CO₂ cycle has been conducted. Specifically, an expansion device with output of work (ED-WOW) has been designed, constructed and incorporated into such a cycle. The ED-WOW extracts energy from CO₂ during the expansion process in a transcritical CO₂ cycle which can be used to drive the compression process. In addition, with work extraction reduced enthalpy of the CO₂ can be achieved at the inlet of the evaporator. These two effects of the ED-WOW increase the system performance of CO₂ cycle much. This final chapter will summarize the tasks completed to meet the objectives of this research, make conclusions based on work done, and give some suggestions for future direction of the ED-WOW.

5.1 Summary of Results

Because of high volumetric heat capacity of CO₂, it offers the potential for reduced weight and volume in package system, which is a major focus for the automobile and military applications. However, the overall efficiency of the transcritical CO₂ cycle decreases as the weight and volume of the system decrease. System improvements must be achieved to meet the goals of the reduction of weight and volume and while still retaining competitive cycle efficiency.

5.1.1 Cycle Analysis Conclusions

A thermodynamic analysis was performed for several modified transcritical CO₂ cycles, with a goal of determining the proper configuration to achieve the optimum system performance. The analysis shows that the system efficiency of the transcritical CO₂ cycle can be dramatically increased by modifications of the system configuration, and that the optimum performance is a strong function of the operating conditions.

The system efficiency of the transcritical CO₂ cycle is increased considerably by nearly 100 % when the low-side pressure increases from 2.5 MPa to 4.5 MPa. There is a specific high-side pressure at which the maximum COP occurs in the CO₂ cycle. There are also specific pressure ratios across the compressors for the minimum compression work and the maximum COP for the two-compressor system.

As previously discussed, the employment of a work extraction device in the role of an expander is expected to give the largest improvement of the system efficiency. This device will not only increase the heat removal capacity of the evaporator but also can reduce the compression work. The thermodynamic analysis shows that system efficiency of the transcritical CO₂ cycle is increased by 16% to 112% with the work extraction device compared to the cycle without the device.

5.1.2 Cycle with Work Extraction

A major objective of this research was to design, construct, test, and analyze an expansion device which provides for work extraction (the ED-WOW device). Based on the review of literature and technologies, a piston-cylinder type device was chosen as the ED-WOW. A theoretical model was developed to verify the proper operation of the ED-

WOW in prototype application and to identify loss mechanisms of the ED-WOW. This model bases on the lubrication theory with assumption that the piston ring is a slippery-pad bearing. This model calculates the pressure inside the device, the work done by CO₂, the power loss, etc. After preliminary analysis, the ED-WOW was constructed and installed in a prototype transcritical CO₂ refrigeration system, replacing the simple throttling valve. During cycle tests, the use of the device provided 7% to 10% improvement in COP. These figures are considered to be highly conservative, as the work extraction measurement was biased toward a lower value due to uncertainty in the load device performance.

5.2 Recommendations

Recommendations based on this study are given for the ED-WOW. Some improvements of the design of the ED-WOW can be made to achieve better performance.

5.2.1 Design Improvements

Presented below are some suggestions to achieve better performance or optimize the design of the ED-WOW, which may be topic of future research using the ED-WOW:

- The rotational speed of the ED-WOW needs to be increased, reducing the torque loading on the device. This can be achieved with larger intake and exhaust ports, and either a mechanically driven valve train or faster-acting solenoid valves.
- Improvement of the piston ring reducing the leakage of CO₂ through it should be considered.

- A hermetically sealed device should be constructed, eliminating the need for a large enclosure and reducing the device weight.
- Heat transfer needs to be considered in the simulation model. The current simulation model does not have the capacity to calculate the heat transfer between the CO₂ inside the device and the atmosphere through the body of the ED-WOW. As the CO₂ expands from high pressure and temperature inside the device, the temperature of CO₂ decreases and it becomes much lower than the atmospheric temperature. Therefore, heat will be transferred from the atmosphere to the CO₂ inside the device.

LIST OF REFERENCES

LIST OF REFERENCES

1. Alvarez, Carlos A., 1999, "Turbine Design for a Refrigeration Application," Senior Project Report, Purdue University.
2. ASHRAE, 1997, "ASHRAE Fundamentals Handbook", American Society of Heating, Refrigerating and Air-Conditioning Engineers, Inc., 1997 Edition.
3. G. K. Aue, 1953, "Some Investigations into Piston ring Behavior", *Sulzer Technical Review*, No. 4, pp. 10-20.
4. G. K. Aue, 1974, "On the Mechanism of a Piston Ring Seal", *Sulzer Technical Review*, pp. 3-18.
5. G. K. Aue, 1975, "Piston Ring Scuffing – General Review", *Proceeding of Conference Sponsored by the Tribology Group, the Combustion Engines Group, and the Automobile Division of the Institution of Mechanical Engineers*, pp. 1-7, London.
6. A.J.S. Baker, D. Dowson and P. Strachan, 1973, "Dynamic Operating Factors in Piston Rings", *International Symposium on Marine Engineering (ISME)*, pp. 2-5-47 – 2-5-58, Tokyo.
7. Balje, O.E., 1981, "Turbomachines, A Guide to Design, Selection, and Theory", John Wiley & Sons, New York.
8. J. F. Booker, 1989, "Basic Equations for Fluid Films with Variable Properties", *Journal of Tribology*, Vol. 111, pp. 475-483.
9. R. Byron Bird, Warren E. Stewart and Edwin N. Lightfoot, 1960, "Transport Phenomena", John Wiley & Sons.
10. J.O. Cermak, J. J. Jicha, and R. G. Lightner, 1964, "Two-Phase Pressure Drop across Vertically Mounted Thick Plate Restrictions", *Journal of Heat Transfer*, pp.227-239.
11. John G. Collier, 1972, "Convective Boiling and Condensation", 2nd Edition, McGraw-Hill.

12. Crane, 1976, "Flow of Fluids through Valves, Fittings, and Pipe", Crane Co. Technical paper No. 410-C, 16th Edition.
13. Jack B. Evett and Cheng Liu, 1987, "Fundamentals of Fluid Mechanics", McGraw-Hill.
14. J. K. Ferrel and J. W. McGee, 1966, "Two-Phase Flow through Abrupt Expansions and Contractions", TID-23394, Vol. 3, Rayleigh N.C. Department of Chemical Engineering, North Carolina State University.
15. Robert W. Fox and Alan T. McDonald, 1992, "Introduction to Fluid Mechanics", 4th Edition, John Wiley & Sons.
16. Shoichi Furuhashi, 1959, "A Dynamic Theory of Piston-Ring Lubrication", 1st Report – Calculation, *Bulletin of JSME*, Vol. 2, No. 7, pp. 423-428.
17. G. E. Geiger and W. M. Rohrer, 1966, "Sudden Contraction Losses in Two-Phase Flow", *Journal of Heat Transfer*, pp. 1-9.
18. Eckhard A. Groll and Douglas M. Robinson, 2000, "Theoretical Investigation of the Transcritical Carbon Dioxide Cycle Using an Economizer", *Internal Report of Herrick Laboratory*, Purdue University.
19. P. Heyl, 2000, "Untersuchungen transkritischer CO₂-Prozesse mit arbeitsleistender Entspannung - Prozeßberechnungen, Auslegung und Test einer Expansions-Kompressions-Maschine", DKV-Forschungsbericht Nr. 62, ISBN 3-932715-65-9.
20. P. Heyl, W. E. Kraus, and H. Quack, 1988, "Expander-Compressor for a More Efficient Use of CO₂ as Refrigerant", *Proceedings of the '98 IIR-Gustav Lorentzen Conference on Natural Working Fluids*, pp. 240-248, Oslo, Norway.
21. Joe D. Hoffman, 1992, "Numerical Methods for Engineers and Scientists", McGraw-Hill.
22. Yeau-Ren Jeng, 1992, "Theoretical Analysis of Piston Ring Lubrication, Part I – Fully Flooded Lubrication", *Tribology Transactions*, Vol. 35, pp. 696-706.
23. Yeau-Ren Jeng, 1992, "Theoretical Analysis of Piston Ring Lubrication, Part II – Starved Lubrication and its Application to a Complete Ring Pack", *Tribology Transactions*, Vol. 35, pp. 707-714.
24. S. J. Kline and F. A. McClintock, 1953, "Describing Uncertainties in Single-Sample Experiments", *Mechanical Engineering*, Vol. 75, No. 1, pp. 3-8.

25. G. Knoll, H. Peeken, R. Lechtape-Gruter, and J. Lang, 1996, "Computer-Aided Simulation of Piston and Piston Ring Dynamics", *Journal of Engineering for Gas Turbine and Power*, Vol. 118, pp. 880-886.
26. Budugur Lakshminarayana, 1996, "Fluid Dynamics and Heat Transfer of Turbomachinery", John Wiley & Sons.
27. D. Li, J. S. Baek, E. A. Groll, and P.B. Lawless, 2000, "Thermodynamic Analysis of Vortex Tube and Work Output Expansion Device for the Transcritical Carbon Dioxide Cycle", 4th IIR – Gustav Lorentzen Conference on Natural Working Fluids at Purdue, Joint Conference of the International Institute of Refrigeration, Section B and E, Purdue University, USA.
28. D. Li and Eckhard A. Groll, 2001, "Experimental Investigation of Carbon Dioxide-Based Environmental Control Units to Replace HCFC-22 Units", *Internal Report of Ray W. Herrick Laboratory*, Purdue University.
29. G. Lorentzen and J. Pettersen, 1993, "A New, Efficient and Environmentally Benign System for Car Air Conditioning", *International Journal of Refrigeration*, 16(1): 4-12.
30. T. Maurer and T. Zinn, 1999, "Experimentelle Untersuchung von Entspannungsmaschinen mit mechanischer Leistungsauskopplung fuer die transkritische CO₂-Kaeltemaschine", DKV-Tagungsbericht Berlin, 19. Jahrgang, Band II.2, pp. 264-278.
31. O. J. Mendler, A. S. Rathbun, N. E. Van Huff, and A. Weiss, 1961, "Natural-Circulation Tests with Water at 800 to 2000 psia under Nonboiling, Local Boiling, and Bulk Boiling Conditions", *Journal of Heat Transfer*, pp. 261-273.
32. Michael J. Moran and Howard N. Shapiro, 1992, "Fundamentals of Engineering Thermodynamics", 2nd Edition, John Wiley & Sons.
33. R. L. Panton, 1996, "Incompressible Flow", 2nd Edition, John Wiley & Sons.
34. Ashok S. Patil, 1998, "Natural Working Fluids – Military Advantages and Opportunities", IIR – Gustav Lorentzen Conference, Joint Meeting of the International Institute of Refrigeration, Section B and E, Oslo, Norway.
35. M. Petrick and B. S. Swanson, 1959, "Expansion and Contraction of an Air-Water Mixture in Vertical Flow", *A.I.Ch.E. Journal*, pp. 440-445.
36. D.J. Radakovic and M.M. Khonsari, 1997, "Heat Transfer in a Thin-Film Flow in the Presence of Squeeze and Shear Thinning: Application to Piston Rings", *Journal of Heat Transfer*, Vol. 119, pp. 249-257.

37. B. E. Richardson, 1958, "Some Problems in Horizontal Two-Phase Two-Component Flow", ANL-5949.
38. Douglas M. Robinson, 2000, "Modeling of Carbon Dioxide Based Air-to-Air Air Conditioners", Ph.D. Thesis, Purdue University.
39. D. M. Robinson and E. A. Groll, 1998, "Efficiencies of Transcritical Carbon Dioxide Cycles with and without an Expansion Turbine", *International Journal of Refrigeration*, Vol. 21(3): pp. 577-589.
40. D. M. Robinson and E. A. Groll, 1998, "Heat Transfer Analysis of Air-to-Carbon-Dioxide Two-Phase Heat Absorption and Supercritical Heat Rejection", *HVAC&R Research*, Vol. 4, No. 4, pp. 327-345.
41. D. M. Robinson and E. A. Groll, 2000, "Theoretical Performance Comparison of CO₂ Transcritical Cycle Technology Versus HCFC-22 Technology for a Military Packaged Air Conditioner Application", *HVAC&R Research*, Vol. 6, No. 4: pp. 325-348.
42. S.M. Rohde and K.W. Whitaker, 1979, "A Study of the Effects of Piston Ring and Engine Design Variables on Piston Ring Friction", *Energy Conservation through Fluid Film Lubrication Technology: Frontiers in Research and Design, The Winter Annual Meeting of the American Society of Mechanical Engineers*, New York.
43. Richard L. Scheaffer and James T. McClave, 1990, "Probability and Statistics for Engineers", 3rd Edition, PWS-KENT.
44. Joseph Edward Shigley and John Joseph Uicker, Jr., 1995, "Theory of Machines and Mechanisms", 2nd Edition, McGraw-Hill.
45. R. Span and W. Wagner, 1996, "A New Equation of State for Carbon Dioxide Covering the Fluid Region from the Triple-Point Temperature to 110 K at Pressure up to 800 MPa", *Journal of Physical and Chemical Reference Data*, 25,;1509-1597.
46. Murray R. Spiegel, 1996, "Mathematical Handbook for Formulas and Tables", Schaum's Outline Series, McGraw-Hill.
47. Victor L. Streeter, 1961, "Handbook of Fluid Dynamics", McGraw-Hill.
48. D. C. Sun, 1990, "A Subroutine Package for Solving Slider Lubrication Problems", *Journal of Tribology*, Vol. 112, pp. 84-91.

49. Thiruvengadam, A., 1966, "Erosion by Cavitation or Impingement", 69th Annual Meeting of the American Society for Testing and Materials, Atlantic City, NJ, June 26-July 1.
50. L.L. Ting and J.E. Mayer, Jr., 1974, "Piston Ring Lubrication and Cylinder Bore Wear Analysis, Part I – Theory", *Journal of Lubrication Technology*, pp. 305-314.
51. Simon C. Tung and Simon S. Wang, 1991, "Friction Reduction from Electrochemically Deposited Films", *Tribology Transactions*, Vol. 34, pp. 23-34.
52. G.T. Voorhees, 1979, "Dual Effect Compression System", In R. Thevenot, editor, *A History of Refrigeration Throughout the World*, page 466, Paris, International Institute of Refrigeration.
53. Yutaro Wakuri and Sinsuke Ono, 1973, "Experimental Studies on the Abnormal Wear of Cylinder Liners and Piston Rings in a Marine Diesel Engine", *International Symposium on Marine Engineering (ISME)*, Tokyo.
54. Kenneth Wark, Jr, 1988, "Thermodynamics", 5th Edition, McGraw-Hill.
55. Kenneth Wark, Jr, 1995, "Advanced Thermodynamics for Engineers", McGraw-Hill.
56. Frank M. White, 1986, "Fluid Mechanics", 2nd Edition, McGraw-Hill.
57. Jeong Eui Yun and Yooseok Chung, 1996, "The Influence of Piston Ring Assembly Design on Blowby and Friction in a SI Engine", *International Journal of Vehicle Design*, Vol. 17, No. 2, pp. 147-162.
58. Maurice J. Zucrow and Joe D. Hoffman, 1976, "Gas Dynamics", John Wiley & Sons.

APPENDICES

APPENDIX A: Reynolds Equation

The simplified equations appropriate for lubrication theory are known as Reynolds equation. Figure A.1 shows flow of a lubricant under a piston ring. For simplicity let the piston ring have only a vertical velocity, $V(t)$, which may be a function of time, and the lower wall (cylinder wall) a steady horizontal velocity, U . Assumptions are as follows:

- The flow is axisymmetric. That means $\frac{\partial}{\partial \theta} = 0$.
- Diameter of the cylinder is very large compared to the thickness of the piston ring so that x-y coordinate can be applied.
- The origin of the coordinate is fixed as shown in the figure.
- The width of the piston ring, b , is very large compared to the film thickness of the lubricant, h , so that $\frac{h}{b} \sim 0$.
- Body force of the lubricant is negligible.
- The lubricant behaves as a Newtonian fluid.
- Viscosity is uniform over the ring thickness.

The following scales are appropriate:

$$\begin{aligned}
 x &\sim b \\
 u &\sim U = R\omega \\
 y &\sim h_{\infty}
 \end{aligned}
 \tag{A-1}$$

R and ω stand for crank radius and revolutionary speed in the equation above, respectively. Continuity equation is

$$\frac{\partial u}{\partial x} + \frac{\partial v}{\partial y} = 0. \tag{A-2}$$

The terms have the following sizes (omitting the order symbol):

$$\frac{U}{b} + \frac{v}{h_{\infty}} = 0. \tag{A-3}$$

The size of the y-component of the velocity becomes

$$v = \frac{Uh_{\infty}}{b}. \tag{A-4}$$

The x-component of the momentum equation is

$$\rho u \frac{\partial u}{\partial x} + \rho v \frac{\partial u}{\partial y} = -\frac{\partial p}{\partial x} + \mu \left[\frac{\partial^2 u}{\partial x^2} + \frac{\partial^2 u}{\partial y^2} \right]. \tag{A-5}$$

The sizes of the terms (omitting the order symbol) are

$$\rho U \frac{U}{b} + \rho \frac{h_{\infty} U}{b} \frac{U}{h_{\infty}} = -\frac{\partial p}{\partial x} + \mu \frac{U}{b^2} + \mu \frac{U}{h_{\infty}^2}. \tag{A-6}$$

Reorganizing above equation gives

$$\rho \frac{U^2}{b} + \rho \frac{U^2}{b} = -\frac{\partial p}{\partial x} + \mu \frac{U}{b^2} + \mu \frac{U}{h_{\infty}^2}. \tag{A-7}$$

By multiplying above equation by h_{∞} and considering the limit $\frac{h_{\infty}}{b} \rightarrow 0$, the following equation is obtained:

$$0 = -\frac{\partial p}{\partial x} + \mu \frac{\partial^2 u}{\partial y^2}. \quad (\text{A-8})$$

The y-component of the momentum equation is

$$\rho u \frac{\partial v}{\partial x} + \rho v \frac{\partial v}{\partial y} = -\frac{\partial p}{\partial y} + \mu \left[\frac{\partial^2 v}{\partial x^2} + \frac{\partial^2 v}{\partial y^2} \right]. \quad (\text{A-9})$$

The sizes of the terms (omitting the order symbol) for above equation are

$$\rho U \frac{U h_{\infty}}{b} + \rho \frac{h_{\infty} U}{b} \frac{U h_{\infty}}{h_{\infty}} = -\frac{\partial p}{\partial y} + \mu \frac{U h_{\infty}}{b^2} + \mu \frac{U h_{\infty}}{h_{\infty}^2}. \quad (\text{A-10})$$

Reorganizing above equation gives

$$\rho \frac{U^2}{b} \frac{h_{\infty}}{b} + \rho \frac{U^2}{b} \frac{h_{\infty}}{b} = -\frac{\partial p}{\partial y} + \mu \frac{U}{b^2} \frac{h_{\infty}}{b} + \mu \frac{U}{h_{\infty}^2} \frac{h_{\infty}}{b}. \quad (\text{A-11})$$

Each term of Equation (A-11) contains $\frac{h_{\infty}}{b}$. By considering the limit $\frac{h_{\infty}}{b} \rightarrow 0$, Equation

(A-11) can be reduced as follow:

$$\frac{\partial p}{\partial y} = 0. \quad (\text{A-12})$$

Meaning of Equation (A-12) is that there is no pressure gradient in y-direction.

Boundary conditions for the flow are

$$\begin{aligned} u(y=0) &= U \\ u(y=h(t)) &= 0 \end{aligned} \quad (\text{A-13})$$

Partial integration of Equation (A-8) over y produces

$$u = \frac{1}{2\mu} \frac{\partial p}{\partial x} y^2 + C_1 y + C_2. \quad (\text{A-14})$$

Applying the boundary conditions gives

$$u(y) = \frac{1}{2\mu} \frac{\partial p}{\partial x} (y^2 - yh) + U \left(1 - \frac{y}{h} \right). \quad (\text{A-15})$$

Integrating the continuity equation (Equation (A-2)) over y gives

$$\int_0^h \frac{\partial u}{\partial x} dy + \int_0^h \frac{\partial v}{\partial y} dy = 0. \quad (\text{A-16})$$

Rearranging Equation (A-16) produces

$$\int_0^h \frac{\partial u}{\partial x} dy = - \int_0^h \frac{\partial v}{\partial y} dy = -[v(h) - v(0)] = -V(t). \quad (\text{A-17})$$

From Leibnitz's theorem [Panton, 1996]

$$\frac{\partial}{\partial x} \int_0^h u dy = \int_0^h \frac{\partial u}{\partial x} dy + \underbrace{\frac{\partial h}{\partial x} u(h)}_0 - \underbrace{\frac{\partial 0}{\partial x} u(0)}_0. \quad (\text{A-18})$$

The 2nd and 3rd terms of Equation (A-18) are zero because $u(h) = 0$ and $\frac{\partial 0}{\partial x} = 0$.

Substituting Equation (A-17) into Equation (A-18) produces

$$\frac{\partial}{\partial x} \int_0^h u dy = \int_0^h \frac{\partial u}{\partial x} dy = -V(t). \quad (\text{A-19})$$

Integration of Equation (A-15) gives

$$\begin{aligned} \int_0^h u dy &= \left[\frac{1}{2\mu} \frac{\partial p}{\partial x} \left(\frac{y^3}{3} - \frac{y^2}{2} h \right) + U \left(y - \frac{y^2}{2h} \right) \right]_0^h = \frac{1}{2\mu} \frac{\partial p}{\partial x} \left(-\frac{h^3}{6} \right) + U \frac{h}{2} \\ &= -\frac{h^3}{12\mu} \frac{\partial p}{\partial x} + \frac{Uh}{2} \end{aligned} \quad (\text{A-20})$$

By substituting Equation (A-20), Equation (A-19) becomes

$$\frac{\partial}{\partial x} \int_0^h u dy = \frac{\partial}{\partial x} \left[-\frac{h^3}{12\mu} \frac{\partial p}{\partial x} + \frac{Uh}{2} \right] = -V(t). \quad (\text{A-21})$$

Reorganizing Equation (A-21) produces the Reynolds equation for lubrication theory as follows:

$$\frac{1}{\mu} \frac{\partial}{\partial x} \left(h^3 \frac{\partial p}{\partial x} \right) = 6U \frac{\partial h}{\partial x} + 12V(t). \quad (\text{A-22})$$

APPENDIX B: Analytical Integrations of the Terms in the Lubrication Theory

Results for the analytical integrations of the terms in Equations (2-56) and (2-57) are presented here. The profile of the face of the piston ring is expressed as:

$$h_s(x) = \frac{4C_R}{b^2} x^2. \quad (\text{B-1})$$

The mathematical expression for the film thickness is

$$h(x, t) = h_m(t) + h_s(x). \quad (\text{B-2})$$

$\frac{4C_R}{b^2}$ is a constant and let it be k here for manipulation convenience.

$$I_1 = \int \frac{1}{h^2} dx = \int \frac{1}{(h_m + kx^2)^2} dx = \frac{x}{2h_m[h_m + kx^2]} + \frac{\tan^{-1}\left[\sqrt{\frac{k}{h_m}}x\right]}{2h_m^{3/2}\sqrt{k}} \quad (\text{B-3})$$

$$I_2 = \int \frac{x}{h^3} dx = \int \frac{x}{(h_m + kx^2)^3} dx = \frac{-1}{4k(h_m + kx^2)^3} \quad (\text{B-4})$$

$$I_3 = \int \frac{1}{h^3} dx = \int \frac{1}{(h_m + kx^2)^3} dx = \frac{x}{4h_m(h_m + kx^2)^2} + \frac{3x}{8h_m^2(h_m + kx^2)} + \frac{3 \tan^{-1}\left[\sqrt{\frac{k}{h_m}}x\right]}{8\sqrt{k}h_m^{5/2}} \quad (\text{B-5})$$

APPENDIX C: Program to Control Solenoid Valves

This program has been developed to control the solenoid valves. There are four groups of the valves which should be controlled separately. Those are 1st Intake Valve, 1st Exhaust Valve, 2nd Intake Valve, and 2nd Exhaust Valve, respectively. The revolution speed of the ED-WOW is assumed to be 120 RPM.

The encoder generates 2048 pulses per revolution. The intake valves open 10 pulses after the top dead center (TDC) of the piston and for 60 pulses. The opening time is very short because the time delay for the input signal of closing is about 0.053 s. The exhaust valves are closed 10 pulses after TDC and open 10 pulses before the bottom dead center (BDC) of the piston. This means that the exhaust valves are closed for 1004 pulses.

The time delay is considered only for the closing of the intake valves in the program. The time delays for the opening of all the valves and the closing of the exhaust valves are not considered.

The program below shows the source program written in 'Visual C++' to control the solenoid valves based on the discussion above.

```

/*****
*
* Program:
*   Control.c
*
* Description:
*   Generation of a retriggerable delayed pulse after each transition
*   on the gate input.
*
* All valves (Intake and Exhaust valves) are considered at the same time.
*
* The intake valves are open 10 pulses after TDC.
*
* The exhaust valves are open 10 pulses before TDC and close
*   10 pulses after TDC.
*
* Encoder generates 2048 pulses per revolution. 1024 pulses indicates
*   1 stroke of piston (down or up).
*
* *** This program was created by J. S. Baek on November 13, 2001. ***
*
*****/
/*
* Includes:
*/

#include "nidaqex.h"

/*
* Main:
*/

void main(void)
{
    /*
    * Local Variable Declarations:
    */

    /* 1st Intake Valves */
    u32 ulLOWcount0 = 10;    // Valves are closed for 10 pulses after TDC.
    u32 ulHIGHcount0 = 60;   // Valves are open for the next 60 pulses and then closed.

    /* 1st Exhaust Valve */
    u32 ulLOWcount1 = 10;    // Valves are open for 10 pulses after TDC.
    u32 ulHIGHcount1 = 1004; // Valves are closes for the next 1004 pulses and then open.

    /* 2nd Intake Valves */
    u32 ulLOWcount2 = 1034;  // Valves are closed for 1034 pulses after TDC.
    u32 ulHIGHcount2 = 60;   // Valves are open for the next 60 pulses and then closed.

    /* 2nd Exhaust Valve */
    u32 ulLOWcount3 = 1034;  // Valves are open for 1034 pulses after TDC.
    u32 ulHIGHcount3 = 1004; // Valves are closes for the next 1004 pulses and then open.

    i16 iStatus = 0;
    i16 iRetVal = 0;
    i16 iDevice = 1;

```

```

u32 ulGpctrNum0 = ND_COUNTER_0;
u32 ulGpctrOutput0 = ND_GPCTR0_OUTPUT;
u32 ulGpctrNum1 = ND_COUNTER_1;
u32 ulGpctrOutput1 = ND_GPCTR1_OUTPUT;
u32 ulGpctrNum2 = ND_COUNTER_2;
u32 ulGpctrOutput2 = ND_GPCTR2_OUTPUT;
u32 ulGpctrNum3 = ND_COUNTER_3;
u32 ulGpctrOutput3 = ND_GPCTR3_OUTPUT;

i16 iIgnoreWarning = 0;
i16 iYieldON = 1;

/* ----- 1st Intake valves ----- */
iStatus = GPCTR_Control(iDevice, ulGpctrNum0, ND_RESET);

iRetVal = NIDAQErrorHandler(iStatus, "GPCTR_Control/RESET", iIgnoreWarning);

iStatus = GPCTR_Set_Application(iDevice, ulGpctrNum0, ND_RETRIG_PULSE_GNR);

iRetVal = NIDAQErrorHandler(iStatus, "GPCTR_Set_Application", iIgnoreWarning);

iStatus = GPCTR_Change_Parameter(iDevice, ulGpctrNum0, ND_SOURCE, ND_PFI_39); // counter input source

iRetVal = NIDAQErrorHandler(iStatus, "GPCTR_Change_Parameter/SOURCE", iIgnoreWarning);

iStatus = GPCTR_Change_Parameter(iDevice, ulGpctrNum0, ND_COUNT_2, ulHIGHcount0);

iRetVal = NIDAQErrorHandler(iStatus, "GPCTR_Change_Parameter/COUNT1", iIgnoreWarning);

iStatus = GPCTR_Change_Parameter(iDevice, ulGpctrNum0, ND_COUNT_1, ulLOWcount0);

iRetVal = NIDAQErrorHandler(iStatus, "GPCTR_Change_Parameter/COUNT2", iIgnoreWarning);

/* Each time a pulse arrives in the gate, a new value will be
   latched into the counter and sent to the data buffer. */

iStatus = GPCTR_Change_Parameter(iDevice, ulGpctrNum0, ND_GATE, ND_PFI_38);

iRetVal = NIDAQErrorHandler(iStatus, "GPCTR_Change_Parameter/GATE", iIgnoreWarning);

/* To output a counter pulse, you must call Select_Signal. */
iStatus = Select_Signal(iDevice, ulGpctrOutput0, ulGpctrOutput0, ND_LOW_TO_HIGH);

iRetVal = NIDAQErrorHandler(iStatus, "Select_Signal/GpctrOutput", iIgnoreWarning);

// iStatus = GPCTR_Change_Parameter(iDevice, ulGpctrNum0, ND_OUTPUT_POLARITY, ND_NEGATIVE);

// iRetVal = NIDAQErrorHandler(iStatus, "GPCTR_Change_Parameter/ND_OUTPUT_POLARITY",
// iIgnoreWarning);

// ----- 1st Exhaust valve -----
iStatus = GPCTR_Control(iDevice, ulGpctrNum1, ND_RESET);

iRetVal = NIDAQErrorHandler(iStatus, "GPCTR_Control/RESET", iIgnoreWarning);

```

```

iStatus = GPCTR_Set_Application(iDevice, ulGpctrNum1, ND_RETRIG_PULSE_GNR);
iRetVal = NIDAQErrorHandler(iStatus, "GPCTR_Set_Application", iIgnoreWarning);

iStatus = GPCTR_Change_Parameter(iDevice, ulGpctrNum1, ND_SOURCE, ND_PFI_35); // counter input source
iRetVal = NIDAQErrorHandler(iStatus, "GPCTR_Change_Parameter/SOURCE", iIgnoreWarning);

iStatus = GPCTR_Change_Parameter(iDevice, ulGpctrNum1, ND_COUNT_1, ulLOWcount1);
iRetVal = NIDAQErrorHandler(iStatus, "GPCTR_Change_Parameter/COUNT1", iIgnoreWarning);

iStatus = GPCTR_Change_Parameter(iDevice, ulGpctrNum1, ND_COUNT_2, ulHIGHcount1);
iRetVal = NIDAQErrorHandler(iStatus, "GPCTR_Change_Parameter/COUNT2", iIgnoreWarning);

// Each time a pulse arrives in the gate, a new value will be latched into the counter and sent to the data buffer.

iStatus = GPCTR_Change_Parameter(iDevice, ulGpctrNum1, ND_GATE, ND_PFI_34);
iRetVal = NIDAQErrorHandler(iStatus, "GPCTR_Change_Parameter/GATE", iIgnoreWarning);

// To output a counter pulse, you must call Select_Signal.

iStatus = Select_Signal(iDevice, ulGpctrOutput1, ulGpctrOutput1, ND_LOW_TO_HIGH);
iRetVal = NIDAQErrorHandler(iStatus, "Select_Signal/GpctrOutput", iIgnoreWarning);

iStatus = GPCTR_Change_Parameter(iDevice, ulGpctrNum1, ND_OUTPUT_POLARITY, ND_NEGATIVE);
iRetVal = NIDAQErrorHandler(iStatus, "GPCTR_Change_Parameter/ND_OUTPUT_POLARITY",
iIgnoreWarning);

// ----- 2nd Intake valves -----
iStatus = GPCTR_Control(iDevice, ulGpctrNum2, ND_RESET);
iRetVal = NIDAQErrorHandler(iStatus, "GPCTR_Control/RESET", iIgnoreWarning);

iStatus = GPCTR_Set_Application(iDevice, ulGpctrNum2, ND_RETRIG_PULSE_GNR);
iRetVal = NIDAQErrorHandler(iStatus, "GPCTR_Set_Application", iIgnoreWarning);

iStatus = GPCTR_Change_Parameter(iDevice, ulGpctrNum2, ND_SOURCE, ND_PFI_31); // counter input source
iRetVal = NIDAQErrorHandler(iStatus, "GPCTR_Change_Parameter/SOURCE", iIgnoreWarning);

iStatus = GPCTR_Change_Parameter(iDevice, ulGpctrNum2, ND_COUNT_1, ulLOWcount2);
iRetVal = NIDAQErrorHandler(iStatus, "GPCTR_Change_Parameter/COUNT1", iIgnoreWarning);

iStatus = GPCTR_Change_Parameter(iDevice, ulGpctrNum2, ND_COUNT_2, ulHIGHcount2);
iRetVal = NIDAQErrorHandler(iStatus, "GPCTR_Change_Parameter/COUNT2", iIgnoreWarning);

// Each time a pulse arrives in the gate, a new value will be latched into the counter and sent to the data buffer.

iStatus = GPCTR_Change_Parameter(iDevice, ulGpctrNum2, ND_GATE, ND_PFI_30);

```

```

iRetVal = NIDAQErrorHandler(iStatus, "GPCTR_Change_Parameter/GATE", iIgnoreWarning);

// To output a counter pulse, you must call Select_Signal.

iStatus = Select_Signal(iDevice, ulGpctrOutput2, ulGpctrOutput2, ND_LOW_TO_HIGH);
iRetVal = NIDAQErrorHandler(iStatus, "Select_Signal/GpctrOutput", iIgnoreWarning);

// ----- 2nd Exhaust valve -----
iStatus = GPCTR_Control(iDevice, ulGpctrNum3, ND_RESET);
iRetVal = NIDAQErrorHandler(iStatus, "GPCTR_Control/RESET", iIgnoreWarning);
iStatus = GPCTR_Set_Application(iDevice, ulGpctrNum3, ND_RETRIG_PULSE_GNR);
iRetVal = NIDAQErrorHandler(iStatus, "GPCTR_Set_Application", iIgnoreWarning);
iStatus = GPCTR_Change_Parameter(iDevice, ulGpctrNum3, ND_SOURCE, ND_PFI_27); // counter input source
iRetVal = NIDAQErrorHandler(iStatus, "GPCTR_Change_Parameter/SOURCE", iIgnoreWarning);
iStatus = GPCTR_Change_Parameter(iDevice, ulGpctrNum3, ND_COUNT_2, ulHIGHcount3);
iRetVal = NIDAQErrorHandler(iStatus, "GPCTR_Change_Parameter/COUNT1", iIgnoreWarning);
iStatus = GPCTR_Change_Parameter(iDevice, ulGpctrNum3, ND_COUNT_1, ulLOWcount3);
iRetVal = NIDAQErrorHandler(iStatus, "GPCTR_Change_Parameter/COUNT2", iIgnoreWarning);

// Each time a pulse arrives in the gate, a new value will be latched into the counter and sent to the data buffer.
iStatus = GPCTR_Change_Parameter(iDevice, ulGpctrNum3, ND_GATE, ND_PFI_26);
iRetVal = NIDAQErrorHandler(iStatus, "GPCTR_Change_Parameter/GATE", iIgnoreWarning);

// To output a counter pulse, you must call Select_Signal.

iStatus = Select_Signal(iDevice, ulGpctrOutput3, ulGpctrOutput3, ND_LOW_TO_HIGH);
iRetVal = NIDAQErrorHandler(iStatus, "Select_Signal/GpctrOutput", iIgnoreWarning);
iStatus = GPCTR_Change_Parameter(iDevice, ulGpctrNum3, ND_OUTPUT_POLARITY, ND_NEGATIVE);
iRetVal = NIDAQErrorHandler(iStatus, "GPCTR_Change_Parameter/ND_OUTPUT_POLARITY",
iIgnoreWarning);

// -----
// NOTE: On USB devices, this call takes longer than normal, so
// you may not be able to output a pulse as short as 1ms.

iStatus = GPCTR_Control(iDevice, ulGpctrNum0, ND_PROGRAM);
iStatus = GPCTR_Control(iDevice, ulGpctrNum1, ND_PROGRAM);
iStatus = GPCTR_Control(iDevice, ulGpctrNum2, ND_PROGRAM);
iStatus = GPCTR_Control(iDevice, ulGpctrNum3, ND_PROGRAM);

iRetVal = NIDAQErrorHandler(iStatus, "GPCTR_Control/PROGRAM", iIgnoreWarning);

```

```

// HINT: If you don't see pulses at the OUTPUT of your counter, check your connections.

printf(" Hit any key to stop.\n");

iRetVal = NIDAQWaitForKey(0.0);

//Reset GPCTR.

iStatus = GPCTR_Control(iDevice, ulGpctrNum0, ND_RESET);
iStatus = GPCTR_Control(iDevice, ulGpctrNum1, ND_RESET);
iStatus = GPCTR_Control(iDevice, ulGpctrNum2, ND_RESET);
iStatus = GPCTR_Control(iDevice, ulGpctrNum3, ND_RESET);

// Disconnect GPCTR0_OUTPUT.

// Note that this will cause the output to be high impedance which
// will most likely bring the logic level HIGH if there is a pull-up
// resistor on this pin. (Check your hardware user manual.) If you do
// not want this behavior, comment out the next line.

iStatus = Select_Signal(iDevice, ND_GPCTR0_OUTPUT, ND_NONE, ND_DONT_CARE);
iStatus = Select_Signal(iDevice, ND_GPCTR1_OUTPUT, ND_NONE, ND_DONT_CARE);
iStatus = Select_Signal(iDevice, ND_GPCTR2_OUTPUT, ND_NONE, ND_DONT_CARE);
iStatus = Select_Signal(iDevice, ND_GPCTR3_OUTPUT, ND_NONE, ND_DONT_CARE);

printf(" Single pulse has been generated at GPCTR0_OUTPUT!\n");

}

/* End of program */

```